Correlative Computed Tomography, Magnetic Resonance Imaging and Cross-sectional Anatomy of Selected Regions of the Canine Body

Lieve De Rycke

Thesis submitted in fulfilment of the requirements
for the Degree of Doctor in Vet. Med. Sciences (PhD).
2007

Promotor : Prof. Dr. H. van Bree
Mede-Promotor : Prof. Dr. P. Simoens

Department of Medical Imaging
Faculty of Veterinary Medicine
Ghent University
Salisburylaan 133, B-9820 Merelbeke, Belgium

TABLE OF CONTENTS

List of abbreviations ……………………………………………………………………….. 5

GENERAL INTRODUCTION : Review of literature

1. TECHNICAL ASPECTS OF COMPUTED TOMOGRAPHY ……………………………………. 9
2. TECHNICAL ASPECTS OF MAGNETIC RESONANCE IMAGING …………………………….. 25
3. CLINICAL APPLICATIONS OF COMPUTED TOMOGRAPHY AND MAGNETIC RESONANCE IMAGING IN SMALL ANIMALS ……………………………………………. 43

SCIENTIFIC AIMS ………………………………………………………………………………… 63

RESULTS

CHAPTER 1 CROSS-SECTIONAL ANATOMY OF THE HEAD ……………………………..… 69

1.1. The brain

1.1.1. COMPUTED TOMOGRAPHY AND CROSS SECTIONAL ANATOMY OF THE NORMAL CANINE BRAIN .. …………………………………………………………… 75

1.1.2. MAGNETIC RESONANCE IMAGING OF THE NORMAL CANINE BRAIN ……. 105

1.2. The nasal cavities and frontal sinuses

1.2.1. MAGNETIC RESONANCE IMAGING, COMPUTED TOMOGRAPHY AND CROSS-SECTIONAL ANATOMY OF NORMAL NASAL CAVITIES AND PARANASAL SINUSES IN MESATICEPHALIC DOGS ……………………………. 119

CHAPTER 2 CROSS-SECTIONAL ANATOMY OF THE TRUNK ……………………… 145

2.1. COMPUTED TOMOGRAPHY AND CROSS SECTIONAL ANATOMY OF THE NORMAL CANINE THORAX ………………………………………………………. 149

2.2. THORACOSCOPIC ANATOMY OF DOGS POSITIONED IN LATERAL RECUMBENCY ………………………………………………………………………. 191

2.3. COMPUTED TOMOGRAPHIC ANATOMY OF THE NORMAL CANINE THORAX versus THORACOSCOPY ………………………………………………………211

CHAPTER 3 CROSS-SECTIONAL ANATOMY OF THE LIMBS ……………………………. 217

3.1. The elbow

3.1.1. COMPUTED TOMOGRAPHY OF THE NORMAL CANINE ELBOW JOINT……… 221

3.1.2. MAGNETIC RESONANCE IMAGING OF THE NORMAL CANINE ELBOW JOINT …………………………………………………………………………….. 249

3.2. The tarsus

3.2.1. COMPUTED TOMOGRAPHY OF THE NORMAL CANINE TARSAL JOINT ……. 263

3.2.2. MAGNETIC RESONANCE IMAGING OF THE NORMAL CANINE TARSAL JOINT ………………. 291

GENERAL DISCUSSION …………………………………………………………………………………... 299

SUMMARY……………………………………………………………………………………………….… 309

SAMENVATTING ………………………………………………………………………………………… 315

DANKWOORD …………………………………………………………………………………………. 323

CURRICULUM VITAE ………………………………………………………………………………... 327

3D	three-dimensional
BW	body weight
C	Carbon
Ca	Calcium
CO_2ET	carbon dioxide-end tidal percentage
CSF	cerebrospinal fluid
CNS	central nervous system
CT	computed tomography
DJD	degenerative joint disease
FCP	fragmented coronoid process
Gd-DPTA	Gadolinium diethylenetriamine penta-acetic acid
H	hydrogen
Hg	mercury
HRCT	high-resolution computed tomography
HU	Hounsfield Units
IM	intramuscular(ly)
IV	intravenous(ly)
kg	kilogram
kV	kilovolts
kVp	peak kilovoltage
L	liter
Na	Sodium
mA	milliamperes
mAs	milliamperes seconds
MCP	medial coronoid process
mg	milligram
mm	millimeter
mL	milliliter
n	number
MR	magnetic resonance imaging
O	oxygen
OCD	osteochondritis dissecans

PaO_2	arterial oxygen pressure
$PaCO_2$	arterial carbon dioxide pressure
PD	proton density
TE	echo time
TR	repetition time
μg	microgram
W	watt
WL	window level
WW	window width

In human medicine, computed tomography (CT) and magnetic resonance imaging (MR) have become established as important imaging tools with many applications in various clinical disciplines.
Both techniques are also becoming readily available to veterinarians during the last years and subsequently commonly used for the diagnosis of several disorders in small animals.

In this general introduction a brief description is given of

- the physical principles and techniques of CT
- the physical principles and techniques of MR
- the clinical applications of both techniques in the dog

-

1. TECHNICAL ASPECTS OF COMPUTED TOMOGRAPHY : review of literature

Adapted from

I. Gielen, H. van Bree. Kompendium der Allgemeinen Veterinärchirurgie 2003; 3. Bildgebende Verfahren, c. Computertomographie, Kramer M. (ed.), Schlütersche Verlag, Hannover, Deutschland.

And

I. Gielen, A. Van Caelenberg, H. van Bree. Computed tomography in small animals. Part 1: Technical aspects. Vlaams Diergeneeskundig Tijdschrift 2003.

Introduction

Computed tomography (CT) is a cross-sectional imaging technique using x-rays and computers[1,2]. The tomographic nature of CT images provides accurate anatomic evaluation of tissue planes and regions which are often impossible to visualize with conventional radiography. The ability to image cross-sections makes it possible to build up a three-dimensional picture which is invaluable for understanding normal anatomy and for planning surgical or radiotherapy treatment. High contrast and spatial resolution account for its unsurpassed imaging of bone structure in the clinical setting. Differentiation between fluid and solid tissues and assessment of the internal structure of soft tissues is also possible with CT [3] but better results are achieved with MR imaging.

Several types of CT scanners are used. Third- (as used in this study) and fourth-generation units employ a rotating x-ray tube with movable or stationary detectors (Figure 1). Scan time with these units is only a few seconds. Advances in CT technology with reduced scan times (1-2 seconds) and improved reconstuction algorithms combined with thin section CT (1-2 mm section thickness) is known as high-resolution computed tomography (HRCT). With its superior contrast resolution HRCT allows structures as small as 200µm to be visualized.

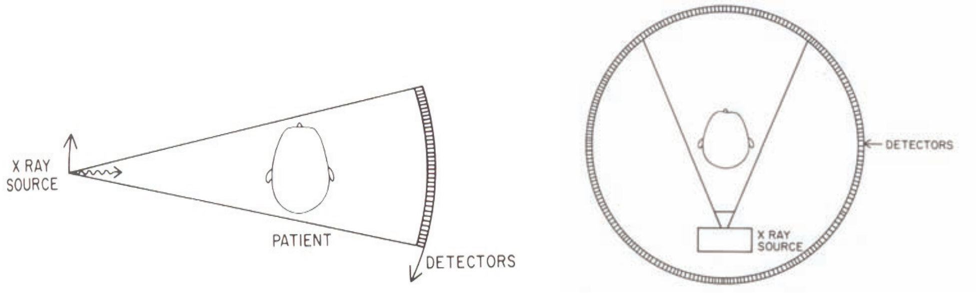

(A) **(B)**

Figure 1: Rotation scanner of the third generation with movable detectors (A) and of the fourth generation with stationary detectors (B).

The fifth-generation scanners were developed primarily for high speed scanning (Figure 2). With the use of spiral CT, the scan time of data acquisition has been dramatically reduced, resulting in a much quicker overall examination, which is especially important in the investigation of small animals in reducing the number of motion artefacts. Thinner slices and faster imaging times are now possible, resulting in increased image resolution[3,5].

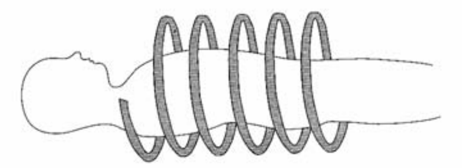

Figure 2 : Helical scanning : spiral motion of the x-ray tube around the patient as the patient continuously moves through the gantry. As a result of these two motions, all points in the patient are interrogated by the x-rays.

The newest development in CT-scanners is the multislice CT or the multirow-detector CT scanners. These scanners produce multiple (2, 4 and 16) spiral acquisition slices simultaneously and gather a large data set of the scanned volume. This information can be processed in order to provide images of slices in all planes and directions. The newest multislice CT-scanners permit submillimeter collimation slice-width, and can provide an isotropic data set which allows not only an optimal in plane resolution but also an identical spatial resolution of multiplanar-reformatting in all directions: these ‘isotropic’ image voxels have equal size in all directions[6].

General principles

THE CT IMAGE

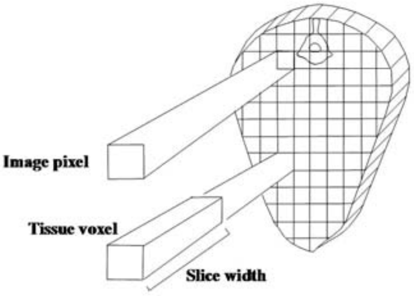

Figure 3 : Composition of the CT image: the smallest square unit of a CT image is the pixel. Each pixel is a two-dimensional representation of a three-dimensional volume of tissue (voxel) from the body slice.

In classic sequential CT, multiple projections of a particular slice of tissue are made and information from all projections is combined to create a single tomographic (slice) image. A complete CT scan consists of a number of slices or images, usually contiguous, through the area of interest. The CT image is composed of a matrix of small tiny squares, called pixels. Each pixel is a two-dimensional representation of a three-dimensional volume of tissue, the voxel. The third dimension of this volume of tissue is the thickness of the slice of the tissue (Figure 3).

The matrix may vary from 256x256 to 1024x1024 pixels. The more pixels in a matrix, the less the transition between the different pixels is visible and) the better the spatial resolution[2,7].
The colours that are used are black, white and shades of gray. CT systems can record thousands of grey shades and separate densities ranging from air to high-density metal can be visualised. For every degree of absorption of a particular tissue or object, there is a corresponding shade of grey (see further for window settings). Each tissue has its own characteristic attenuation coefficient[1].

THE CT PROCESS

In CT images, the shade of grey in the pixels represents the linear attenuation coefficient of the tissues in that voxel. The process of CT determines this linear attenuation coefficient to make a useful image[8]. Therefore, all the components of the CT equipment are used: the gantry and the patient table, the computer and display console, and the camera for hard copies (Figure 4).

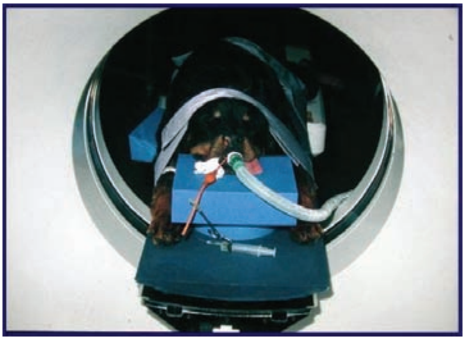

Figure 4 : A dog lying in ventral recumbency on the patient table in the gantry of the CT scanner.

The gantry contains the x-ray tube, x-ray collimators and x-ray detector. A CT scanner gantry can, within limits, be tilted to angle the scan plane. In CT, the choice of peak kilovoltage (kVp) is usually limited and a high kVp technique is always used. The kVp should be increased for very thick and dense body parts to ensure adequate penetration, and for very dense objects to minimise beam hardening. Because of the limitations of thermal tube capacities with a given focal spot size, the choice of milliamperes seconds (mAs) also depends on the selected kVp. High mAs will increase image detail because it reduces image noise. When thin sections are made, an increase in mAs can compensate for otherwise interfering image noise associated with narrow slice collimation[9].

Scan time is the time necessary for the x-ray tube to rotate around the patient while making the exposure. A longer scan time may result in improved image detail since the number of projections can be higher, but may cause motion artefacts (including respiratory motion) and can eventually cause x-ray tube heating[10].

Effects of breathing motion are not a significant problem when scanning joints. Obviously, patient motion should be minimised by using general anaesthesia. Because CT scanners use ionising radiation, the anaesthesiologist must take the appropriate radioprotective precautions. Therefore, monitoring of the patient should be done with acoustic monitors or with monitors that have displays that can be seen from a distance[11]. For protective reasons, the operator site is also behind a protective shield.

The patient lies horizontally on a movable table, in a way that images are transverse to the long axis of the body. First a scout view of the object is obtained by moving the table through the gantry as the x-rays are being emitted while the tube and detectors remain stationary. A scout view is similar to a plain radiograph and is in fact a digital radiograph. The scout view is used to verify patient positioning and to assist the operator in planning the number and location of slices that are required[12].

During CT scanning, an x-ray tube emits the x-ray beam and rotates 360° around the patient. A first collimator, located between the tube and the patient, determines the thickness of the slice (1-10 mm). A second collimator located between the patient and the detector, also influences the slice thickness and limits the interference of scattered x-rays. The thinner the slice, the higher the spatial resolution, but an increased number of slices requires more scan time. Thick slices may result in small lesions remaining undetected because the attenuation information within each tomographic slice is averaged (partial volume effect). Slices of 10 mm are used when scanning the entire thorax or abdomen. In brain CT, 5 mm thick slices are normally used. When it is essential to image the entire object, continuous slices are required. This leads to an increased overall scanning time and tube load. Therefore, thicker slices are often chosen instead. On the other hand, there are body parts and conditions where continuous scanning is not essential. In these circumstances, scannning with a thin slice width and a few mm interval is often a better alternative[1]. One must be aware of information gaps between the different sections.

Depending on the kind of tissue and the thickness of the slices, the x-ray beam is absorbed or scattered. The x-ray photons emerging from the patient are absorbed by the x-ray detectors, converted to an electrical signal, amplified and converted into a number (numeric value). This number is relative to the intensity of the beam as it emerges from the patient, and is equivalent to the attenuation. This number is processed in the computer. The x-ray tube circles around the patient and data are collected from all angles. In this way, different numbers are obtained and a mathematical method is used to determine a specific number, the CT number, for each pixel[1]. The range of these numbers assigned to the various tissues is from more than +1000 to –1000 Hounsfield Units (HU), where +1000 is assigned to cortical bone, -1000 to air and 0 to water. Thus the more radiopaque the tissue, the more attenuation occurs within that voxel, the higher the CT number and the whiter that area of the image. Groups of CT numbers are awarded to a particular scale of gray. The operator controls the tissue contrast. One can also choose the central grey colour (window level (WL)) and the range above and below the window level (window width (WW)). When the computer receives a CT number above or below the window width, a white or black density is outlined (Figure 5).

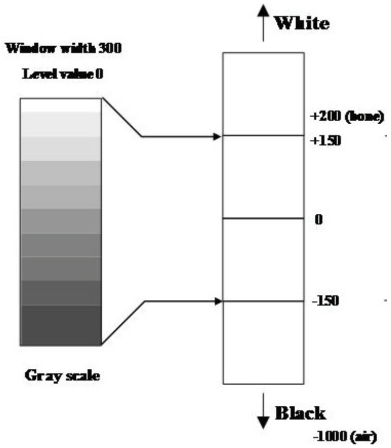

Figure 5 : For the final CT image, the CT numbers of the Hounsfield scale are converted to a gray scale. In the Hounsfield scale, +1000 is assigned to cortical bone, -1000 to air and 0 to water. The central grey colour (window level) and the range below and above this level (window width) can be choosen.

A narrow WW maximises tissue contrast between tissues with a small difference in attenuation coefficient (soft tissue window). A wide WW is selected to view bony structures so that the bones stand out from the soft tissues (bone window)[1,3,13]. Appropriate window levels and window widths are crucial for the proper interpretation of CT images and must be adapted to the tissue type and area of interest[3]. This correct window and image contrast must be selected prior to making a printed hard copy of the CT scan[8]. When reviewing CT images using computers and computer screens (‘soft copy reviewing’) WW and WL can be adjusted interactively.

Image manipulation can be done after the exposure as the image is on the display screen. Regions of interest can be selected and various data computed and displayed regarding them, including size and CT number average and range.

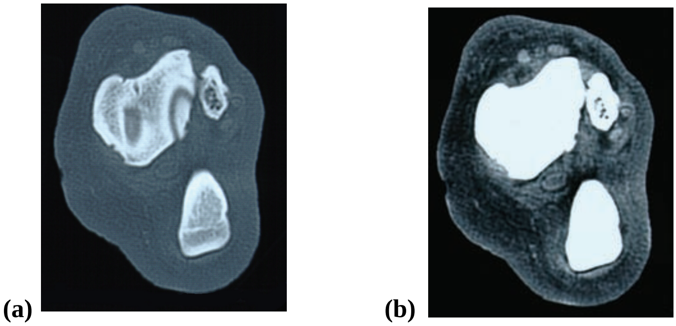

Figure 6 : After the scan examination, the window level and window width can be manipulated. Using a bone window (a) the subchondral details in tibia, fibula and calcaneus are nicely visible. On a soft tissue window (b), the details of tendons and vessels are more clearly visible.

Comparison of CT numbers between different areas on an image is sometimes useful, particularly regarding to relative differences in density[10] (Figure 6).

Image reconstrucions

After the scan examination, images in other planes can be produced using computer reformatting. Using data from the transverse slices, images are produced in other planes (Figure 7). It is easier to appreciate the extent of a lesion when it can be studied in multiple planes[3,14].

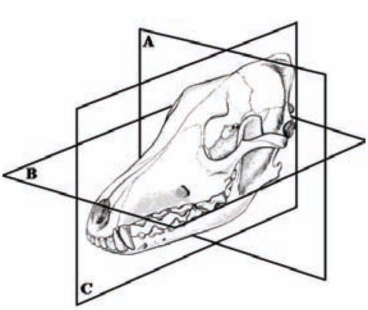

Figure 7 : After the scan examination images can be reconstructed in different planes. A. transversal plane
B. dorsal plane
C. sagittal plane

Three-dimensional (3D) reconstruction is useful in selected cases for obtaining a panoramic view of a lesion and its extent of involvement, particularly in regard to bone lesions. By instructing the computer to eliminate soft-tissue CT numbers, a 3D surface image can be produced and rotated (Figure 8)[9,10].

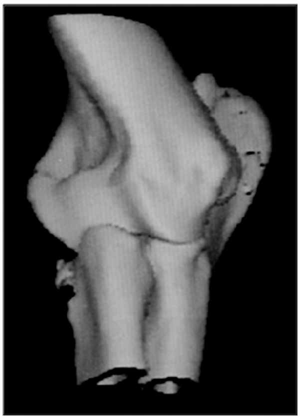

Figure 8 : 3D reconstruction of a canine elbow

Contrast studies

To increase the amount of soft tissue information, negative (air) and positive contrast agents, such as radiopaque iodine can be used. The use of non-ionic contrast agents is advantageous because of their lower incidence of side-effects but they are more expensive than the ionic forms. The ionic, high osmolality contrast agents are less expensive and, in general, adverse reactions are a minimal problem in these cases and especially in veterinary medicine[15]. Ionic contrast agents are good for providing positive contrast enhancement of fluid filled cavities e.g. intrathecal injection in CT-myelography, and also for gastro-intestinal and urogenital studies. Intravenous positive contrast is used to differentiate between normal and abnormal tissue[16]. Contrast agents can be injected either as a bolus or as an infusion[15,17].

Positive contrast techniques are the most important tools in veterinary medicine e.g. for demonstrating brain tumours. Normally, water soluble, iodinated contrast media do not cross the intact blood barrier, but where this barrier is damaged by a lesion, the contrast medum will enter in the interstitium and enhance the radioabsorption of that area. Normal brain enhances only 2-4 HU after the administration of intravenous contrast medium injection (caused by small vascular structures) (Figure 8), but the density of a lesion will increase by 20-40 HU.

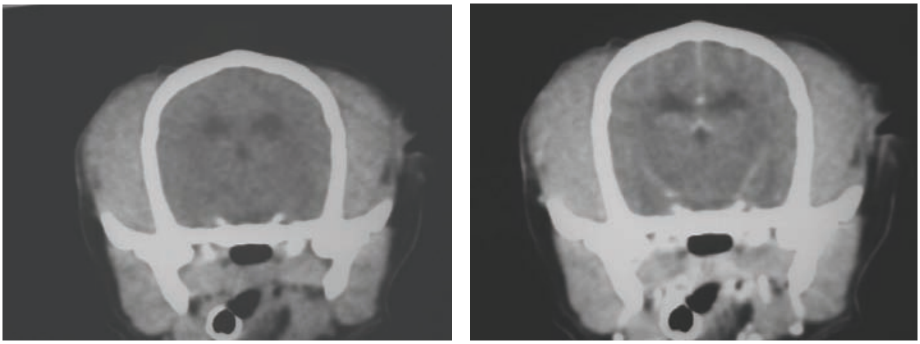

Figure 8 : Plain CT image of the skull of a dog (left) and corresponding image after administration of IV contrast medium (right). The vascular structures become visible and the overall density of the brain parenchyma increases.

This enhancement reflects not only vascularity but leakage (transition) of the contrast medium in the intercellular space as well (damaged blood-brain barrier). This phenomenon can be useful for delineating areas of necrosis[3].

CT guided biopsies

It is possible to obtain biopsies under CT guidance, a procedure which can be accurately performed when additional information is needed for diagnosis, staging or therapy planning. This approach can be of value for investigating mass lesions resulting from neoplasia of infections. Besides their use in the brain, CT guided biopsies in dog and cat appear to be particularly useful for lesions involving the retrobulbar space, the paranasal cavities, the vertebrae and ribs, the pelvis, and the lung and mediastinum[18-29]. Although stereotactic devices and guidance devices improve the accuracy, free-hand techniques are commonly used. CT guided percutaneous biopsy can be performed using a fine aspiration needle, a tru-cut needle to obtain tissue core samples, or a bone biopsy needle. When performing CT guided needle biopsies, precise needle tip localisation is an essential skill[27].

The retrobulbar region is directly accessible to biopsy due to the incomplete bony orbit of the dog. Care must be taken not to damage the optic nerve and the external ophthalmic artery[30]. A percutaneous CT guided needle biopsy of deep lesions such as a vertebral body or intervertebral disc can be performed in a safe and accurate way[28,31].

CT guided aspiration in the thoracic cavity of lymph nodes or pulmonary masses may result in a cytological diagnosis. Intravenous injection of contrast medium delineates vessels immediately adjacent to a mass. During the puncture procedure, vessels can be avoided and the safety of CT guided biopsies in the thorax can be improved[29].

Stereotactic devices are normally used for obtaining brain biopsies. They are rather expensive and complicated, as they have to be adaptable to the different possible skull sizes in dogs. Because most of the time the CT findings do not allow an exact histological diagnosis, biopsies are extremely useful in treatment planning[32,33].

Radiation therapy

Radiation therapy is used to treat inoperable tumors that have not spread to other sites in the body. It works by sterilizing cells, which keeps them from being able to undergo successful division.

The classic method for developing the beam geometry for radiation therapy planning is to use a conventional ‘simulator’, i.e. a radiographic/fluoroscopic system that is geometrically equivalent to the linear accelerator used for treatment[34]. The linear accelerator can be programmed to produce photons or electrons in order to treat deep or superficial tumors, respectively. The planning data include therapeutic beam angles, shapes and isocenters. The fluoroscopic imaging of a conventional simulator provides the physician with views of the patient’s internal anatomy, but due to limitations in soft-tissue visualization the tumor itsself is often not shown[34].

With the advent of CT simulation the use of conventional simulators has diminished significantly. CT simulation can create synthetic X-ray projections from CT image volumes, referred to as Digitally Reconstructed Radiographs. These enable the radiation oncologist to simulate treatment with the added benefit of better soft-tissue visualization. The CT volumetric data also facilitates planning the 3D distribution of the radiation dose[34].

The main objective of external beam radiation therapy, including the more advanced 3D conformal radiation therapy, is to apply a local radiation dose, prescribed by a radiation oncologist, to a solid tumor within the planned treatment volume. In addition, the dose to nearby organs and critical structures must be minimized in order to avoid treatment related complications[34].

Respiratory motion, i.e. excursion, is one factor that adversely affects the objectives outlined above. Recently, new visualization methods have been developed for radiation therapy planning with respiratory gated, multiphasic CT data sets. The system enables the visualization of respiratory movements, helps to identify patients with minimal tumor movement, and reduces the tumor margins needed to keep the tumor in the treatment beam[34].

References

1. Hathcock J, Stickle R. Principles and concepts of computed tomography. Vet Clin North Am: Small Anim Pract 1993;23:399-415.

2. Huygens W, Baert A. Axiale computertomografie. In: Radiologische onderzoeksmethoden, eerste editie, Acco, Leuven, Belgium 1983, pp119-126.

3. Dennis R. An introduction to veterinary CT and MR scanning. Vet Ann 1996;36:16-40.

4. Wegener O, Fassel R, Welger D. Techniques of computed tomography. In: Weber S. (ed). Whole body computed tomography, second edition, Blackwell Scientific Publications, Mass, USA 1993, pp 3-9.

5. Seeram E. Data acquisition concepts. In : Wilke J. (ed). Computed tomography: physical principles, clinical applications, and quality control, second edition, WB Saunders, Philadelphia, USA 2001, pp 75-95.

6. Seeram E. Multislice spiral/helical computed tomography: physical principles and instrumentation. In : Wilke J. (ed). Computed tomography: physical principles, clinical applications, and quality control, second edition, WB Saunders, Philadelphia, USA 2001, pp 245-265.

7. Feeney D, Fletcher T, Hardy R. Abdomen and pelvis. In: Mills L. (ed). Atlas of correlative imaging anatomy of the normal dog, ultrasound and computed tomography, WB Saunders, Philadelphia, USA 1991, pp 219-333.

8. Assheuer J, Sager M. Principles of imaging techniques. In : Assheuer J., Sager M. (eds). MRI and CT atlas of the dog, Blackwell Science Ltd, Berlin 1997, pp 449-453.

9. Seeram E. Computed tomography of the head, neck and spine. In : Wilke J. (ed). Computed tomography: physical principles, clinical applications, and quality control, second edition, WB Saunders, Philadelphia, USA 2001, pp 325-340.

10. Stickle R, Hathcock J. Interpretation of computed tomographic images. Vet Clin North Am: Small Anim Pract 1993;23:417-429.

11. Robertson S. Newer diagnostic and surgical techniques and their impact on anesthesia. Vet Clin North Am: Small Anim Pract 1999;29:665-682.

12. Wortman J. Principles of X-ray computed tomography and magnetic resonance imaging. Semin Vet Med Surg (Small Anim) 1986;1:176-184.

13. Lee S, Rao K, Zimmerman R. Physics and instrumentation: computed tomography. In: Cranial MRI and CT, fourth edition, McGraw-Hill, New York, USA 1999, pp 1-41.

14. Jeffery N, Thakkar C, Yarrow T. Introduction to computed tomography of the canine brain. J Small Anim Pract 1992;33:2-10.

15. Holland M. Contrast agents, diagnostic imaging. Vet Clin North Am: Small Anim Pract 1993;23:269-277.

16. Seeram E. Computed tomography of the body. In : Wilke J. (ed). Computed tomography: physical principles, clinical applications, and quality control, second edition, WB Saunders, Philadelphia, USA 2001, pp 341-361.

17. Burgener F, Hamlin D. Contrast enhancement in abdominal CT: bolus vs infusion. Am J Roentgenol 1981;137:351-358.

18. Anor S, Sturges B, Lafranco L, et al. Systemic phaeohyphomycosis (cladophialophora bantiana) in a dog – clinical diagnosis with stereotactic computed tomographic-guided brain biopsy. J Vet Int Med 2001;15:257-261.

23. Flegel T, Podell M, March P, et al. Use of a disposable real-time CT stereotactic navigator device for minimally invasive dog brain biopsy through a mini-burr hole. Am J Neuroradiol 2002;23:1160-1163.

24. Garbagnati F, Lutman R, Valvassori L, et al. Nonpulmonary thoracic biopsy. Eur J Radiol 1989;9:214-216.

25. Giroux A, Jones J, Bohn J, et al. A new device for stereotactic CT-guided biopsy of the canine brain : design, construction, and needle placement accuracy. Vet Radiol Ultrasound 2002;43:229-236.

26. Harari J, Moore M, Leathers C et al. Computed tomographic-guided free-hand needle biopsy of brain tumors in dogs. Prog in Vet Neuro 1993;4:41-44.

27. Koblik P, LeCouteur R, Higgins R, et al. Modification and application of a Pelorus Mark III Stereotactic System for CT-guided brain biopsy in 50 dogs. Vet Radiol Ultrasound 1999;40:424-433.

28. Koblik P, LeCouteur R, Higgins R, et al. CT-guided brain biopsy using a modified Pelorus Mark III Stereotactic System: experience with 50 dogs. Vet Radiol Ultrasound 1999;40:434-440.

29. Moissonnier P, Blot S, Devauchelle P, et al. Stereotactic CT-guided brain biopsy in the dog. J Small Anim Pract 2002;43:115-123.

30. Moissonnier P, Bordeau W, Delisle F, et al. Accuracy testing of a new stereotactic CT-guided brain biopsy device in the dog. Res Vet Sci 2000;68:243-247.

31. Tidwell A, Johnson K. Computed tomography-guided percutaneous biopsy: criteria for accurate needle tip identification. Vet Radiol Ultrasound 1994;35:440-444.

32. Risselada M, Saunders J, Bhatti S, et al. CT-geleid aspiratie biopt van een geïnfecteerde tussenwervelschijf. Vlaams Diergen Tijdschr 2001;70:59-64.

33. Tidwell A, Johnson K. Computed tomography-guided percutaneous biopsy in the dog and cat: description of technique and preliminary evaluation in 14 patients. Vet Radiol Ultrasound 1994;35;445-456.

34. Penninck D, Daniel G, Brawer R, et al. Cross-sectional imaging techniques in veterinary ophthalmology. Clin Techn Small Anim Pract 2001;16:22-39.

35. Moore G, Mathey W, Eggers J, et al. Osteosarcoma in adjacent lumbar vertebrae in a dog. J Am Vet Med Assoc 2000;217:1038-1040.

36. Lecouteur R. Current concepts in the diagnosis and treatment of brain tumours in dogs and cats. J Small Anim Pract 1999;40:411-416.

37. Moissonnier P, Devauchelle P, Delisle F, et al. Stereotactic CT-guided brain biopsy in the dog. J Small Anim Pract 2002;43:115-123.

38. Klahr P, Subramanian P, Yanof J. Respiratory-correlated multislice CT for radiation therapy planning : imaging and visualization methods. MedicaMundi 2005;49(3):34-37.

2. TECHNICAL ASPECTS OF MAGNETIC RESONANCE IMAGING:

Review of literature

Introduction

In 1980, Holland et al. reported on their first experiences with magnetic resonance imaging (MR)[1] and the technique became available for clinical use in 1983[2]. The MR imaging principle fundamentally differs from CT, using radio waves and magnetism to measure nuclear magnetic resonance emitted from protons instead of x-rays attenuated in tissue[1]. MR had several advantages over CT, due to its inherently high sensitivity to soft tissue contrast, its ability to manipulate the signal intensity of various soft tissues by the use of a different pulse sequence, and its ability to generate images in different planes directly, rather than by reformatting, in transverse, dorsal, and any other plane desired[3].

Initially, MR was used almost exclusively for evaluation of central nervous system (CNS) lesions[2]. Its chief advantage over CT in this region was the ability to image the caudal fossa of the brain without the artifacts frequently seen with CT scans of this area, the improved detail of the images, the ability to acquire images oriented in any plane, and to differentiate extravascular blood from surrounding structures[3]. However, shortly afterwards, it became clear that MR was alsovery well suited for evaluation of the musculoskeletal system[2]. For evaluation of the disorders of various structures of the musculoskeletal system, including bone marrow, muscles, tendon ligaments, fat tissue, articular cartilage, menisci, intervertebral disks in the cervical and thoracic region, and for spinal cord and nerve roots, it is a useful diagnostic imaging modality[2]. MR also shows superior anatomic detail of soft-tissue structures in case of abdominal disorders. Motion artifacts on images involving the chest cavity are considerable, but new breath-hold sequences and cardiac gating techniques have improved the ability to image this region.

It is now evident that MR probably represents the most significant advance in diagnostic medicine since the discovery of x-rays, and each year brings new hardware and software advances[4]. The technique has almost totally supplanted some of the classic diagnostic modalities such as arthroscopy, and is now seriously challenging angiography[2].

General principles

IMAGE ACQUISITION

Components of the system include the magnet, coil, and computer station. The magnet surrounds the gantry and allows the establishment of a magnetic field. A copper coil is positioned in the gantry, parallel to the external magnetic field, and surrounds the region to be imaged. The function of the coil is to detect radiofrequency signals produced by changes in the animal’s magnetic field[5].

The computer station allows the programmer to set parameters for the image study, formulates and transmits instruction for the production of a radiofrequency pulse sequence directed at the region of interest, and analyzes the sampled data to produce the image[5,6].

Figure 1. MR scanner with the patient table and the gantry containing a magnet and a copper coil.

MR represents the unstable portion of an animal's own magnetic field, and images are produced through the interaction of radiofrequency waves and hydrogen ions of tissue within a magnetic field. Nuclei of elemental substances are composed of protons and neutrons.

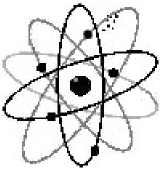

Figure 2 : Nucleus of an atom surrounded by protons and neutrons

The moving or spinning of electrically charged particles (protons) creates the magnetic field of the nuclei. These structures are in constant motion, spinning about the internal axis of the atom, giving the particles angular momentum(= magnetic capacities).

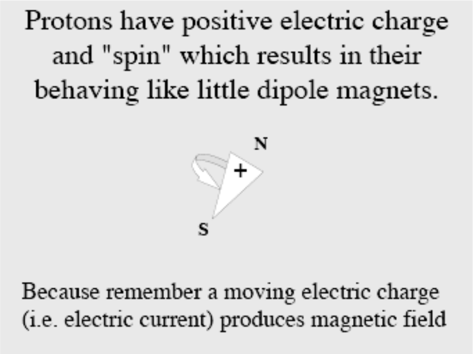
Protons have positive electric charge and "spin" which results in their behaving like little dipole magnets.

Because remember a moving electric charge (i.e. electric current) produces magnetic field

However, not all atoms possess spin. When evenly paired (same number of each particle type), the spin of a particle is opposite that of its paired particle, and the nucleus has a net angular momentum of zero. When the total number of particles is odd (1,3,5, etc) the unpaired particle's spin yields the angular momentum force for the nuclei. Tissue components with spin can be measured with MR; those without spin cannot. Hydrogen (^{1}H), for example, has an atomic number of 1 and only a single proton, possesses spin, and is a common component of biologic tissue. Sodium (^{23}Na) and phosphorus (^{31}P) also possess spin; whereas carbon (^{12}C), oxygen (^{16}O), and calcium (^{40}Ca) do not have spin. In summary, with conventional MR, tissue with high hydrogen content (e.g., water, fat) are imaged; regions of bone or air appear void[3].

Within the bore of the magnet, the external magnetic field is considerably stronger than the biologic field, causing the biologic field to align with the external field. Within the bore of the magnet, the biologic field and the external magnetic field are in a state of equilibrium.

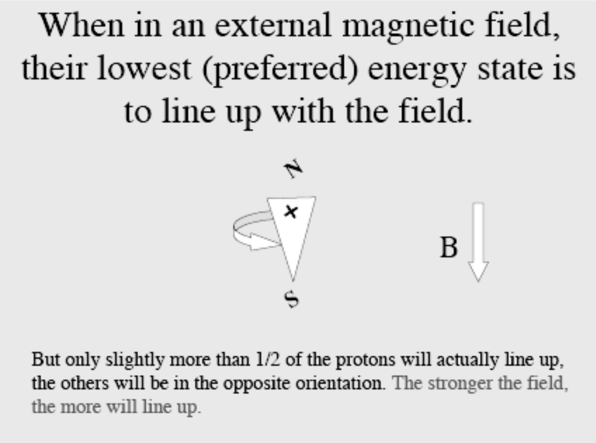
When in an external magnetic field, their lowest (preferred) energy state is to line up with the field.

But only slightly more than 1/2 of the protons will actually line up, the others will be in the opposite orientation. The stronger the field, the more will line up.

To measure the animal's magnetic field and avoid interference from the external field, it is necessary to disturb the biologic field. This alteration of the biologic field is accomplished using a specified sequence of magnetic pulses and taking advantage of the resonance phenomenon.*

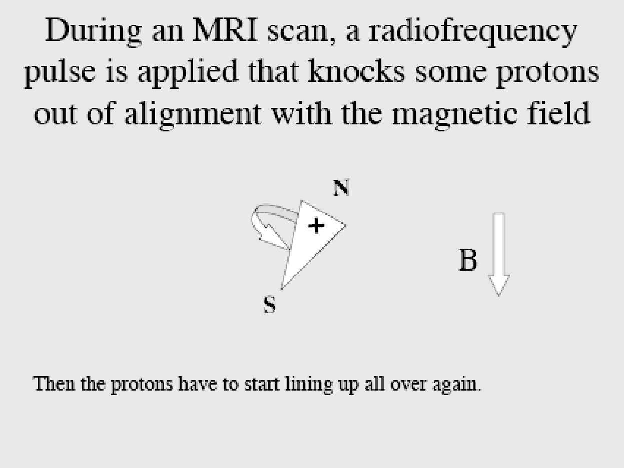

During an MRI scan, a radiofrequency pulse is applied that knocks some protons out of alignment with the magnetic field

Then the protons have to start lining up all over again.

This additional magnetic field (magnetic pulse sequence) is applied as a cyclic force at the natural frequency of the animal’s nuclear field (spin) and perpendicular to the external magnetic field. The effect is a "tipping" or nutating of the animal's nuclear magnetic field. The degree of nutating is governed by the strength and duration of the magnetic pulse[5].

Application of a magnetic pulse sequence imparts minute amounts of energy to atomic nuclei. If the particle possess spin, it precesses around the external field, in a manner similar to that of a gyroscope. Particles without spin simply fall back to the external field with each cessation of the magnetic pulse. The rate of precession for a particle is called the Larmor frequency and is determined by the gyroscopic properties of the atomic field and the strength of the external field. In MR, magnetic pulse sequences are applied perpendicular to the external magnetic field and at the Larmor frequency for (^{1}H) hydrogen (42.58 MHz/T; T = tesla, a measurement of external magnetic field strength). As a result the patient’s (biologic) magnetic field undergoes two simultaneous Larmor precessions: one around the external magnetic field and one around the rotating (cyclic)

**A system's response to an external cyclic force applied at the system's natural frequency of cyclic motion will be larger than for any other frequency of an external cyclic force[5].*

magnetic field applied in the pulse sequence. This allows the steady tipping or nutation of the biologic field. If a different frequency is applied, nutation does not occur[5].

After nutating the biologic field to the desired degree or angle, the magnetic pulse is discontinued, and the biologic field realigns with the external field. Application of specific strengths and durations of the magnetic pulse results in the production of measurable radiofrequency waves created by realignment of the nuclear field (=relaxation). Only the tissue components with the same natural cyclic motion (spin) frequency as the applied magnetic pulse (cyclic force) create these measurable radiofrequency waves.

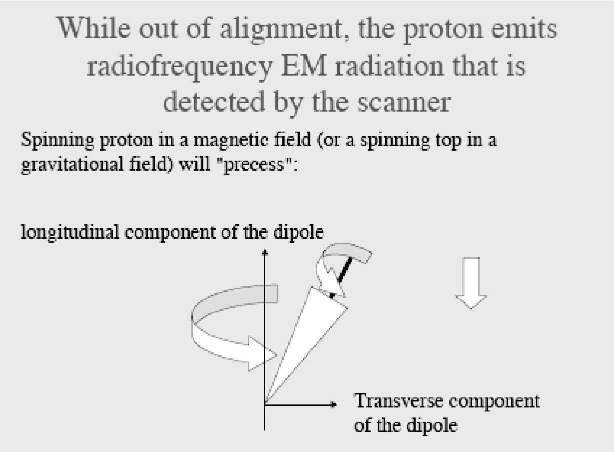

While out of alignment, the proton emits radiofrequency EM radiation that is detected by the scanner

Spinning proton in a magnetic field (or a spinning top in a gravitational field) will "precess":

A coil, placed parallel to the external magnetic field, detects the radiofrequency waves, which are transmitted to a computer station. The computer analyses the data received, using for example a Fourier transformation, to construct the resultant image[5].

The production of a MR image from biologic tissue involves the process just described. The natural frequency at which the cyclic force is applied is that of the ^{1}H (hydrogen) ion. The most often used magnetic pulse sequence for imaging is the spin echo pulse sequence[5,6]. The magnetic pulse is initially applied to mutate the nuclear field 90° and, after specified time, a second pulse produces a 180° rotation in the transverse plane.

A delay occurs before the next 90° pulse, and during the delay the radiofrequency waves (=echos) are sampled by the coil. The time between the 90° pulse and the detection of the radiofrequency waves by the coil is termed the echo time or TE. The time lapse between each 90° pulse is termed the repetition time or TR[5-7].

Image contrast is mainly controlled by the TR and TE. The proper TR and TE combinations are selected to produce image contrast related to differences in proton (^{1}H) density, Tl-relaxation time (see further), and T2-relaxation time (see further). A marked change occurs in the magnitude of the magnetic field during the relaxation phase of the realignment process (following cessation of a magnetic pulse). During relaxation, the magnetic field contains two components termed longitudinal and transverse magnetization.

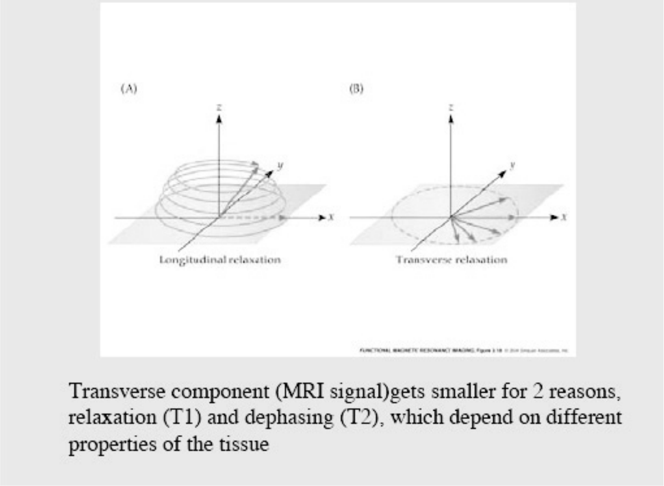

Transverse component (MRI signal)gets smaller for 2 reasons, relaxation (T1) and dephasing (T2), which depend on different properties of the tissue

Relaxation times are related to the rate at which a given tissue can absorb or release radiofrequency waves. Tl-relaxation concerns the spin-lattice interaction, this refers to the change of energy by protons (spinners) with surrounding nonproton structures. The movement of the longitudinal field back to an equilibrium point occurs at a rate specific for each tisue and is called the T1-value for that tissue. The time needed to restore 63% of the original longitudinal magnitude is called the T1-relaxation time. Contrast related to Tl-differences in tissue is controlled by the TR. Images that are Tl-weighted are equated with short TR times to make the differences between tissues with different T1-relaxation times more clearly. Tissues with short Tl-relaxation time e.g fat (fast change of energy to the surrounding tissue and fast relaxation) are brighter (more intense), and tissues with longer Tl-relaxation time e.g. CSF (cerebrospinal fluid) are darker (less intense).

There is a difference between free (urine, CSF, cysts) and bound (brain, pancreas, liver) water: Free water moves quickly, so the energy-transfer is difficult. Longitudinal relaxation is slow. T1-values

are slightly longer. Bound water (intra- and extracellular) will transfer the energy in an easier way to the surroundings, there is more recovery with a certain TR, the T1-values are slightly shorter. Most benign tumors have large intracellular spaces containing bound water, so its T1-values are shorter as is urine/csf. Most malignant tumors have large, bad organized cells, containing more free intracellular water and extracellulair water; its T1 is longer!
TE is also kept short so T2-values will not be able to influence the signal.

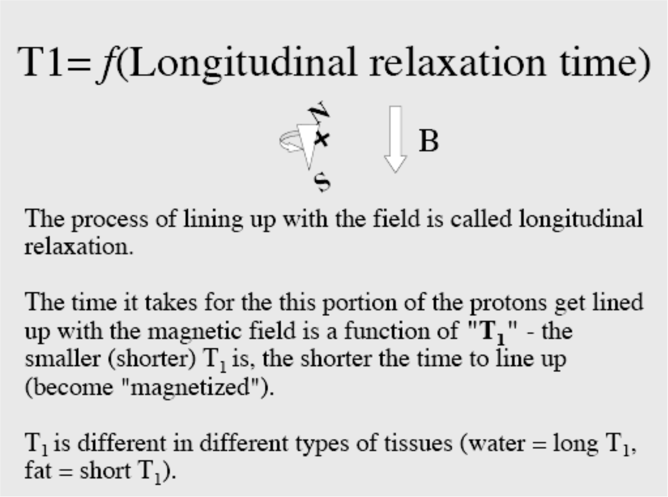

T1=*f*(Longitudinal relaxation time)

The process of lining up with the field is called longitudinal relaxation.

The time it takes for the this portion of the protons get lined up with the magnetic field is a function of "$\mathbf{T_1}$" - the smaller (shorter) T_1 is, the shorter the time to line up (become "magnetized").

T_1 is different in different types of tissues (water = long T_1, fat = short T_1).

There is another possibility to make an image. Take a long TR (all tissues relaxed) a short TE (no T2) so the picture will depend on the amount of protons in this tissue. Much protons give high signal, less protons low signal. This proton density (PD) is tissue specific. (The PD of muscle is 100, as is white matter; fat 98, liquor 96, blood 90, bone 1-10, air <1). The difference between T1 and PD imaging: T1 is depending on the speed of relaxation in the longitudinal direction, PD is depending on the maximum relaxation of the tissue. That´s why for T1, the TR is short and for PD the TR is long. (TR 3 times the T1 value of the tissue will produce PD contrast). The TE must be short (T2 influences).

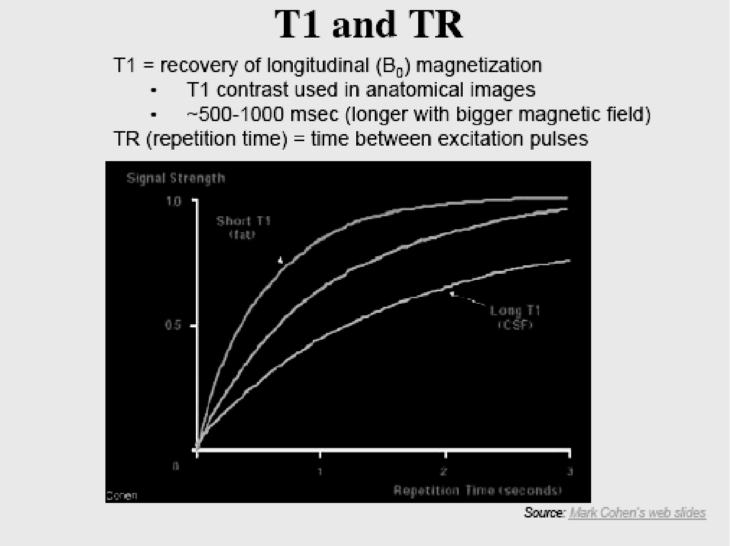

T1 and TR

T1 = recovery of longitudinal (B_0) magnetization
- T1 contrast used in anatomical images
- ~500-1000 msec (longer with bigger magnetic field)

TR (repetition time) = time between excitation pulses

Source: Mark Cohen's web slides

Concurrently, the transverse field decays toward zero during relaxation at a rate proportional to the magnitude of the tissue, the time needed to let the protons(tissue) dephase for 37% is called T2-relaxation time. T2-relaxation concerns the spin-spin interaction, which refers to the exchange of energy by protons with other protons[5]. The more protons that have a magnetic resonance component in the transverse plane, the higher the signal.

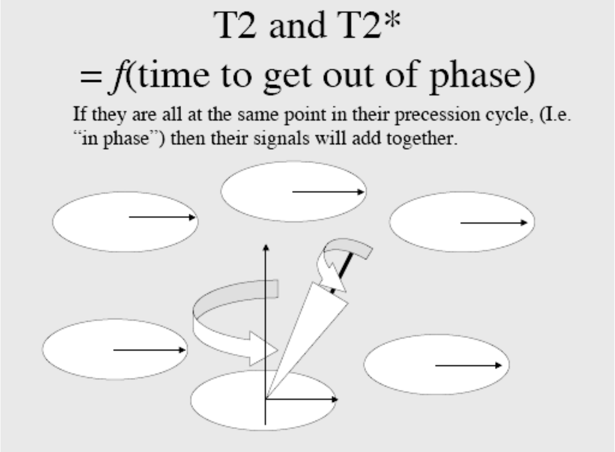

T2 and T2*

= *f*(time to get out of phase)

If they are all at the same point in their precession cycle, (I.e. "in phase") then their signals will add together.

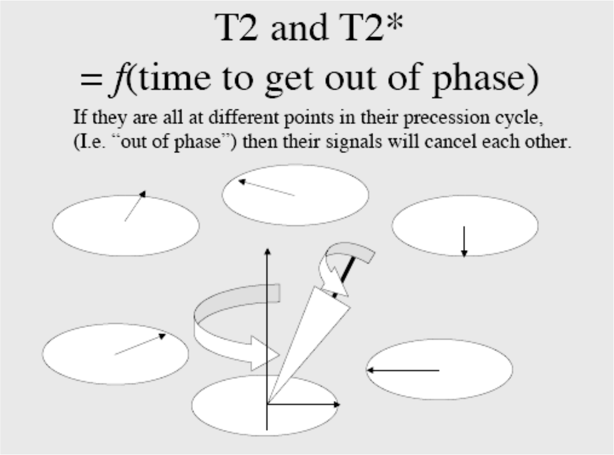

T2 and T2*

= *f*(time to get out of phase)

If they are all at different points in their precession cycle,
(I.e. "out of phase") then their signals will cancel each other.

The contrast related to the T2 differences in tissue are controlled by the TE. With a short TE the difference in signal intensity is less pronounced than after a longer TE.

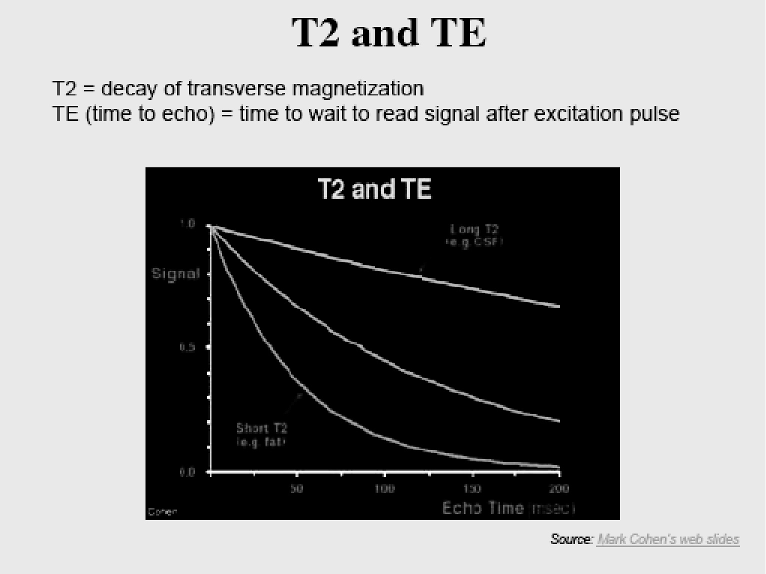

T2 and TE

T2 = decay of transverse magnetization
TE (time to echo) = time to wait to read signal after excitation pulse

Source: Mark Cohen's web slides

The T2-weighted image is produced by a longer TE but also by a longer TR[5]. TR is long so all tissue protons can go back to the transverse plane with the next RF pulse. Tissue with longer T2-times is brighter (more intense), and tissue with shorter T2 times is darker (less intense). For example : the spin-spin energy transfer of water is more difficult because of fluctuating molecules (=long T2-relaxation time, bright). Fat will dephase faster than water (short T2, dark), so the water signal is more T2-weighted.

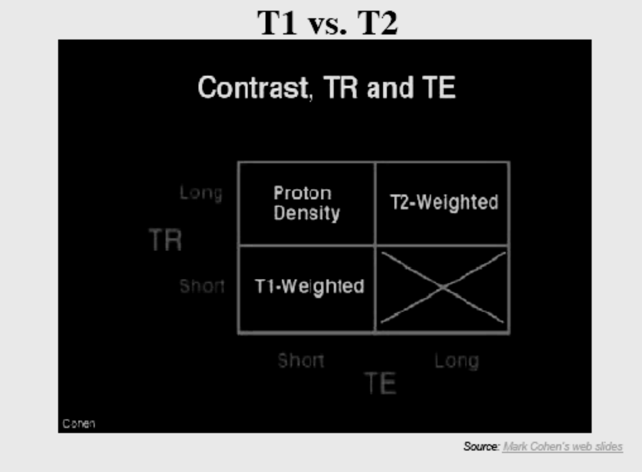

T1 vs. T2

Contrast, TR and TE

Source: Mark Cohen's web slides

With short TE and long TR, the picture is depending on the amount of protons in the tissue (PD weighted).

TR: 250-700 ms = SHORT   TR: >2000 ms = LONG
TE: 10- 25 ms = SHORT   TE: > 60 ms = LONG

For spin echo images, the following apply: Tl and T2 effects occur simultaneously, but Tl effects dominate Tl-weighted images and T2 effects dominate T2-weighted images[5].

The MR examination :

IMAGE ORIENTATION

The MR examination usually consists of acquisition of Tl-weighted and T2-weighted images of an anatomic region (e.g., brain) in one or more planes. Images may be oriented in sagittal, transverse (axial), or dorsal (coronal) planes. MR acquisition can be oriented in any plane, regardless of patient orientation inside the magnet. This property of MR does not require computer generated reformatting of data obtained in one plane and can therefore be performed without sacrifice of image quality[7].

DATA ACQUISITION

A multislice acquisition technique is used, allowing simultaneous acquisition of image data from several tissue slices within the chosen field of view. Slice thickness is chosen based on the purpose of the examination and the area being imaged. For a MR brain scan in a dog, one author has used a 4 mm slice thickness[9]. Thinner slices offer better resolution, but image quality suffers because the signal produced is related to the volume of tissue being pulsed (signal-to-noise ratio). Volume coverage also is reduced[5,6].

Field of view and matrix size are additional parameters to be addressed. Smaller fields of view may increase the spatial resolution, but at the expense of signal-to-noise ratio. An increase in matrix size will also increase spatial resolution, but with loss of signal-to-noise ratio. Most scans are performed using a 256 x 256 matrix size[6].

The TR and TE times vary with the desired image characteristics, the tissue being imaged, and the strength of the magnet. Most magnets in use at human imaging centers are 1 to 1.5 T in strength. T1-weighted images are obtained at a TR of 300 to 600 msec and a short TE of 20 to 30 msec and for the T2-weighted image, TR = 2000 to 3000 msec and TE = 60 to 80 msec is used[5,6,10].

Other parameters are important in the operation of the MR scanner, such as imaging gradients, but are beyond the scope of this review and are best addressed in the references listed.

PATIENT PREPARATION

The animal is, dependant on the area of interest, positioned in ventral or dorsal recumbency, with the head entering the gantry first. Consistent positioning for all imaging procedures facilitates image interpretation and identification of right and left sides. Near perfect symmetry aids in the ability to correctly interpret the images. If one side of the head is rotated more rostrally than the other, for example, many structures (e.g., lateral ventricles) will appear asymmetrical on the scans, and this could lead to an erroneous diagnosis[7]. An assymetric position of the patient can also be corrected on the MR-images by adjusting the image plane on the scanogram.

A scout film is initially made to determine patient position in the gantry and to identify the region to be imaged. Slice thickness and the number of scans necessary for the study are determined before continuing the procedure. This ensures that the area of interest is contained in the completed study[7].

IMAGE CHARACTERISTICS AND PRINCIPLES OF INTERPRETATION

Unlike conventional radiologic and CT techniques, which are almost completely dependent on differences in electron density of tissue, MR reflects complex interactions of the T1- and T2-times and proton (^{1}H) density. T1 and T2 are intrinsic tissue characteristics and are representative of the relative content of water molecules[5,6]. Subtle changes in the blood-brain barrier can be reflected in T2-weighted images as abnormal accumulations of water, well before being evident on T1-weighted images, T1-weighted contrast images, or CT[10]. Tissue contrast is considered the most clinically relevant attribute of MR[5]. T2-weighted images are considered the most sensitive in this regard, whereas T1-weighted images show more specificity in anatomic structure.

Like CT images, MR images are representations of each voxel, constructed from an array of numbers representing computer data, and displayed as two-dimensional structures termed pixels[5,6]. A fundamental difference exists, however, in the pixels of CT and the pixels in MR. CT scanners are calibrated so that pure water has a zero value (CT number or HU) and air has a value of -1000. Other structures have values based on these calibration units as determined by their relative electron density. With MR, pixel values have no absolute values, and the same structure imaged on different scanners or on the same scanner on two seperate occasions may have very different signal intensities, even if the TR, TE and other parameters remain the same. However, relative differences in tissue density (for instance, CSF versus white matter) will remain constant, but other factors such as patient positioning within the coil and how the scanner is tuned are often responsible for the differences in the signal intensity[6].

Rapid flow, e.g. of blood or CSF, creates a signal void. This is because the hydrogen containing components of the fluid, present at the time of the radiofrequency pulse in the slice being imaged, do not remain within the voxel long enough to encounter both the 90° and 180° pulses and therefore do not produce a signal. Slower-moving fluid can produce the opposite effect and appear bright. This occurs because the slower-moving fluid is less saturated with signal produced from multiple radiofrequency pulses, and all tissue loses some signal from this process. The slower-moving fluid encounters fewer total radiofrequency pulses, loses far less signal from saturation, and produces a higher signal intensity[6].

Increased water content of tissue (CSF, edema) results in an increased signal intensity on T2-weighted scans and a decreased signal intensity on T1-weighted scans (Figure 3). Increased signal intensity on T1-weighted scans is noted with the presence of fat, melanine, manganese, some calcifications and methemoglobin (e.g. cerebral hemorrhage during day 7-21). Decreased signal intensity noted on gradient echo T2-weighted images may suggest flow or intracellular degradation products of hemoglobin (cerebral hemorrhage during all stages)[6].

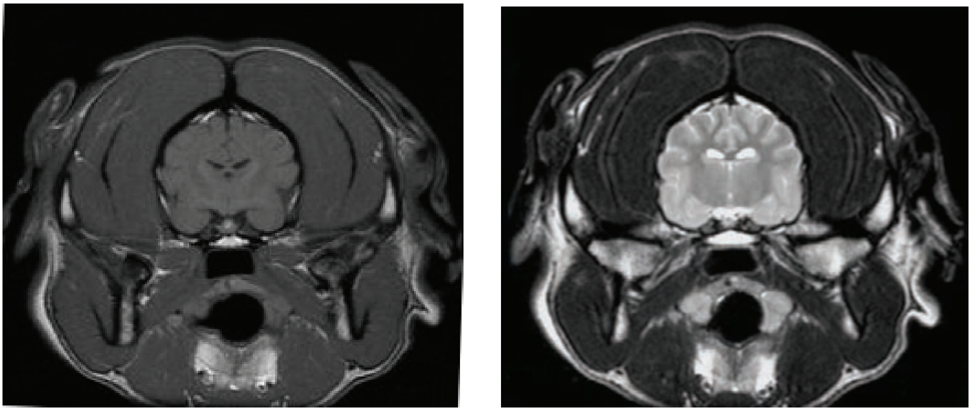

Figure 3 : T1-weighted (left) and T2-weighted (right) transverse images of the canine brain at the pituitary level. Note the increased signal intensity of the CSF on the T2-weighted image. (With permission of R. Dennis, New Market, UK.)

Interpretation of MR scans begins, as with any radiologic technique, with a thourough knowledge of the anatomy of the imaged structure. Additional considerations are the ability of MR to image any plane and the need to recognize structures imaged using sagittal, transverse, or dorsal planes.

Contrast studies

In addition to Tl- and T2-weighted images, and depending on the purpose of the examination, the Tl study may be repeated with the intravenous injection of gadolinium-DTPA (Gd-DTPA) for contrast enhancement[6,8] (Figure 4). Gd-DPTA is a paramagnetic substance, having an unpaired electron which magnetic moment is 700 times stronger than the one of the proton, and due to dipole-dipole interactions it causes adjacent hydrogen nuclei to relax more quickly[6,8]. On Tl studies, the image of tissues containing the contrast agent appears more hyperintense. This provides more sensitive detection of various lesions, especially in the central nervous system, better defines margins of the lesions and allows more accurate differentiation of lesions[6,8]. The resultant effect is much the same as for iodinated contrast agents used in computed tomography imaging studies[6].

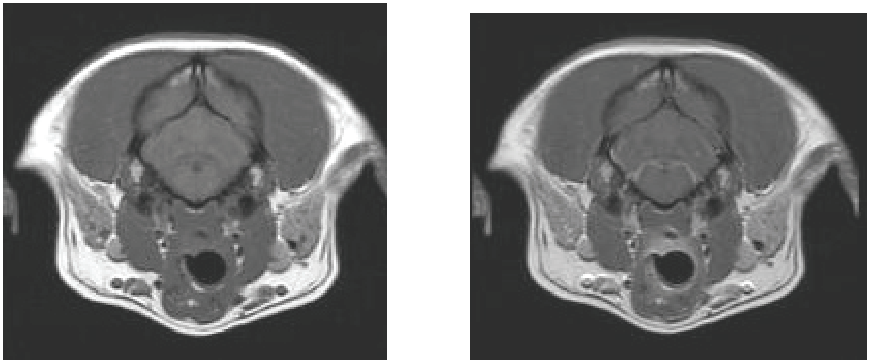

Figure 4 : Pre- (left) and postcontrast (right) T1-weighted images of the canine brain. Tissues containing the contrast agent appear hyperintense. (With permission of R. Dennis, New Market, UK.)

Acknowledgement

I wanted to thank Professor Susan M. Courtney-Faruquee (Johns Hopkins University, Department of Psychological and Brain Sciences, Baltimore) and Professor Mark S. Cohen (UCLA Brain Mapping Center, Los Angeles) for disposing some figures of their website.
These figures are incorporated in the general introduction on pages 25 to 32.

References

1. Assheuer J, Sager M. Introduction. In : Assheuer J, Sager M, (eds). MRI and CT atlas of the dog. Berlin: Blackwell Science, 1997.

2. Firooznia H, Golimbu C, Rafii Mahvash et al. In : Patterson A. (ed). MRI and CT of the musculoskeletal system. St. Louis: Mosby –Year book, Inc, 1992.

3. Shores A. Magnetic resonance imaging. Vet Clin North Am: Small Anim Pract 1993;23:437-459.

4. Westbrook C. In : Westbrook C. (ed). Introduction. Handbook of MRI technique. 2nd ed. Oxford: Blackwell Science, 2003.

5. Friedman B, Jones J, Chaves-Munoz G, et al. In : Friedman B, Jones J, Chaves-Munoz G, et al. (eds). Principles of MRI. New York, McGraw-Hill, Inc, 1989.

6. Aisen A. Basics of image interpretation (Prepared handout). Ann Arbor, MI, University of Michigan School of Medicine.

7. Shores A. Diagnostic capabilities of computed tomography and magnetic resonance imaging. In: August J (ed). Consultations in Feline Medicine, ed 2. Philadelphia, WB Saunders.

8. Kuriashkin I, Losonsky J. Contrast enhancement in magnetic resonance imaging using intravenous paramagnetic contrast media: a review. Vet Radiol Ultrasound 2000;41:4-7.

9. Barber D, Oliver J, Mayhew I. Neuroradiography. In: Oliver J, Hoerlein B, Mayhew I. (eds). Veterinary Neurology. Philadelphia, WB Saunders, 1987, p65.

10. Modic M, Beale S. Magnetic resonance imaging of supratentorial neoplasms. In : Wilkins R, Rengachary S. (eds). Neurosurgery Update I. New York, McGraw-Hill, 1990, p57.

3. CLINICAL APPLICATIONS OF COMPUTED TOMOGRAPHY AND MAGNETIC RESONANCE IMAGING IN SMALL ANIMALS :

Review of literature

Detection of lesions in animals on CT and MR images is possible by virtue of displacement or deformity of normal landmarks (mass effect) or by changes in tissue composition due to pathological processes such as oedema, haemorrhage, necrosis, calcification and osteolysis[1].

In small animals, CT and MR are particularly valuable for the detection and diagnosis of brain disorders[2-71]. The fact that some intracranial lesions may not be visible on CT is due to diffuse distribution, attenuation levels similar to those of the surrounding normal tissue, and minimal or absent contrast enhancement. CT and MR are also very helpful in the investigation of spinal cord lesions in the event of doubtful radiographic and/or myelographic findings[72-91] and in the detection of disorders of the peripheral nerves[92-96]. Musculoskeletal CT and MR[97-116] may be helpful in clinical cases in which standard radiography and ultrasonography are negative or inconclusive, even though there is a high suspicion of pathology. For example in the diagnosis of fragmented coronoid process, CT has been proven to be superior to radiology[117]. For the detection and description of masses, malformations and fluid collections in the thoracic cavity[118-128], CT is the best imaging modality and is considered the most sensitive method for the detection of pulmonary metastases[124]. CT and MR of the abdomen[129-137] give excellent anatomic images of the organs and vessels, but as a consequence of the overall availability of ultrasound the demand for abdominal CT and MR studies is low.

In evaluating the localisation and the extent and in characterising of lesions of the nasal cavities, paranasal sinuses, orbita, jaws, temporomandibular joints and tympanic bullae, CT and MR are more accurate than conventional radiography[138-161]. CT appears to be remarkably accurate in revealing the location, extent and origin of nasal diseases and neoplasia[140,152,155,159], and is also superior to conventional radiography for detecting middle ear diseases[146].

Besides for the diagnosis and delineation of the extent of the lesions, CT and MR are also useful in small animals for tumor-staging, planning surgery[95,162] and radiation therapy[151], and as a guide for biopsies of bone or soft tissues[163-174]. External landmarks and depth measurements are used to localise the lesions.

References

1. Dennis R. An introduction to veterinary CT and MR scanning. Vet Ann 1996;36:16-40.

2. Adamo P, Clinkscales J. Cerebellar meningioma with paradoxical vestibular signs. Prog in Vet Neuro 1991;2:137-142.

3. Bergman R, Jones J, Lanz O, et al. Post-operative computed tomography in two dogs with cerebral meningioma. Vet Radiol Ultrasound 2000;41:425-432.

4. Bertroy E, Feldman E, Nelson R, et al. Magnetic resonance imaging of the brain in dogs with recently diagnosed but untreated pituitary-dependent hyperadrenocorticism. J Am Vet Med Assoc 1995;206:651-656.

5. Brunetti A, Fatone G, Cuomo A, et al. Meningomyelocele and hydrocephalus in a Bulldog. Prog in Vet Neuro 1993;4:54-59.

6. Buback J, Schulz K, Walker M, et al. Magnetic resonance imaging of the brain for diagnosis of neurocysticercosis in a dog. J Am Vet Med Assoc 1996;208:1846-1848.

7. DeHaan C, Kraft S, Gavin P, et al. Normal variation in size of lateral ventricles of the Labrador retriever dog as assessed by magnetic resonance imaging. Vet Radiol Ultrasound 1994;35:83-86.

8. Ducoté J, Johnson K, Dewey C, et al. Computed tomography of necrotizing meningoencephalitis in 3 Yorkshire Terriers. Vet Radiol Ultrasound 1999;40:617-621.

9. Duesburg C, Feldman E, Nelson R, et al. Magnetic resonance imaging for diagnosis of pituitary macro-tumors in dogs. J Am Vet Med Assoc 1995;206:657-662.

10. Esteve-Ratsch B, Kneissl S, Gabler C. Comparative evaluation of the ventricles in the Yorkshire Terrier and the German shepherd dog using low-fields MRI. Vet Radiol Ultrasound 2001;42:410-413.

11. Fike J, Cann C, Turowski K, et al. Differentiation of neoplastic from non-neoplastic lesions in dog brain using quantitative CT. Vet Radiol 1986;27:121-128.

12. Fike J, LeCouteur R, Cann C, et al. Computerized tomography of brain tumors of the rostral and middle fossas in the dog. Am J Vet Res 1981;42:275-281.

13. Fransson B, Kippenes H, Silver G, et al. Magnetic resonance diagnosis: cavernous sinus syndrome in a dog. Vet Radiol Ultrasound 2000;41:536-538.

14. Graham J, Newell S, Voges A, et al. The dural tail sign in the diagnosis of meningiomas. Vet Radiol Ultrasound 1998:39:297-302.

15. Hammer A, Cuoto C, Getzy D. Magnetic resonance imaging in a dog with a choroid plexus carcinoma. J Small Anim Pract 1990;31:341-344.

16. Hathcock J. Low field magnetic resonance imaging characteristics of cranial vault meningiomas in 13 dogs. Vet Radiol Ultrasound 1996:37:257-263.

17. Hause W, Helphrey M, Green R, et al. Cerebral arteriovenous malformation in a dog. J Am Anim Hosp Assoc 1982;18:601-607.

18. Iwamoto K, Norman A, Freshwater D, et al. Diagnosis and treatment of spontaneous canine brain tumors with a CT scanner. Radiother Oncol 1993;26:76-78.

19. Jeffery N, Thakkar C, Yarrow T. Introduction to computed tomography of the canine brain. J Small Anim Pract 1992;33:2-10.

20. Kärkäinen M, Mero M, Nummi P, et al. Low field magnetic resonance imaging of the canine central nervous system. Vet Radiol 1991;32:71-74.

21. Kärkkäinen M. Low- and high-field strength magnetic resonance imaging to evaluate the brain in one normal dog and two dogs with central nervous system disease. Vet Radiol Ultrasound 1995;36:528-532.

22. Kent M, Delahunta A, Tidwell A. MR imaging findings in a dog with intravascular lymphoma in the brain. Vet Radiol Ultrasound 2001;42:504-510.

23. Kii S, Taura Y, Nakaichi M, et al. Developmental change of lateral ventricular volume and ratio in Beagle-type dogs up to 7 months of age. Vet Radiol Ultrasound 1998;39:185-189.

24. Kii S, Uzuka Y, Taura Y, et al. Magnetic resonance imaging of the lateral ventricles in beagle-type dogs. Vet Radiol Ultrasound 1997;38:430-433.

25. Kitagawa M, Kanayama K, Satoh T, et al. Cerebellar focal granulomatous meningoencephalitis in a dog : clinical findings and MR imaging. J Vet Med A Physiol Pathol Clin Med 2004;51:277-279.

26. Klopp L, Hathcock J, Sorjonen D. Magnetic resonance imaging features of brain stem abscessation in two cats. Vet Radiol Ultrasound 2000;41:300-307.

27. Kraft S, Gavin P, DeHaan C, et al. Retrospective review of 50 canine intracranial tumors evaluated by magnetic resonance imaging. J Vet Intern Med 1997;11:218-225.

28. Kraft S, Gavin P, Moore M, et al. An MR diagnosis of canine meningioma. Vet Radiol 1990;31:65-67.

29. Lang J, Huber P, Vandevelde M. Erfahrungen mit der Computertomographie in der Kleintierneurologie. Schweiz Arch Tierheilk 1988;130:167-183.

30. LeCouteur R, Fike J, Cann C, et al. Computed tomography of brain tumors in the caudal fossa of the dog. Vet Radiol 1981;22:244-251.

31. LeCouteur R, Fike J, Cann C, et al. X-ray computed tomography of brain tumors in cats. J Am Vet Med Assoc 1983;183:301-305.

32. LeCouteur R. Current concepts in the diagnosis and treatment of brain tumours in dogs and cats. J Small Anim Pract 1999;40:411-416.

33. Lipsitz D, Levitski R, Chauvet A. Magnetic resonance imaging of a choroid plexus carcinoma and meningeal carcinomatosis in a dog. Vet Radiol Ultrasound 1999;40:246-250.

34. Lobetti R, Rearson J. Magnetic resonance imaging in the diagnosis of focal granulomatous meningoencephalitis in two dogs. Vet Radiol Ultrasound 1996;37:424-427.

35. Lotti D, Capucchio MT, Gaidolfi E, et al. Necrotizing encephalitis in a Yorkshire terrier: clinical, imaging, and pathologic findings. Vet Radiol Ultrasound 1999;40:622-626.

36. Mariani C, Platt S, Newell S, et al. Magnetic resonance imaging of cerebral cortical necrosis (polioencephalomalacia) in a dog. Vet Radiol Ultrasound 2001;42:524-531.

37. Mellema L, Koblik P, Kortz G, et al. Reversible magnetic resonance imaging abnormalities in dogs following seizures. Vet Radiol Ultrasound 1999;40:588-595.

38. Mellema L, Samii V, Vernau K, et al. Meningeal enhancement on magnetic resonance imaging in 15 dogs and 3 cats. Vet Radiol Ultrasound 2002;43:10-15.

39. Millner R, Engela J, Kirberger R. Arachnoid cyst in cerebellar pontine area of a cat - diagnosis by magnetic resonance imaging. Vet Radiol Ultrasound 1996;37:34-36.

40. Morozumi M, Miyahara K, Sato M, et al. Computed tomography and magnetic resonance findings in two dogs and a cat with intracranial lesions. J Vet Med Sci 1997;59:807-810.

41. Morozumi M, Sasaki N, Oyama Y, et al. Computed tomography and magnetic resonance findings of meningeal syndrome in a leukemic cat. J Vet Med Sci 1993;55:1035-1037.

42. Norton F. Cerebral infarction in a dog. Prog Vet Neuro 1992;3:120-125.

43. Nykamp S, Scrivani P, de Lahunta A, et al. Chronic subdural hematomas and hydrocephalus in a dog. Vet Radiol Ultrasound 2001;42:511-514.

44. Nykamp S, Steffey M, Scrivani P, et al. Computed tomographic appearance of epidural empyema in a dog. Can Vet J 2003;44:729-731.

45. Panciera D, Duncan I, Messing A, et al. Magnetic resonance imaging in two dogs with central nervous system disease. J Small Anim Pract 1987;28:587-596.

46. Platt S, Graham J, Chrisman C, et al. Canine intracranial epidermoid cyst. Vet Radiol Ultrasound 1999;40:454-458.

47. Plummer S, Wheeler S, Thrall D, et al. Computed tomography of primary inflammatory brain disorders in dogs and cats. Vet Radiol Ultrasound 1992;33:307-312.

48. Regnier A, Ducos de Lahitte M, Delisle M, et al. Dandy-Walker syndrome in a kitten. J Am Anim Hosp Assoc 1993;29:514-518.

49. Saito M, Sharp N, Munana K, et al. CT findings of intracranial blastomycosis in a dog. Vet Radiol Ultrasound 2002;43:16-21.

50. Sato M, Sharp N, de Lahunta A, et al. Magnetic resonance imaging features of lissencephaly in 2 Lhasa Apsos. Vet Radiol Ultrasound 2002;43:331-337.

51. Sato T, Ikebata Y, Koie H, et al. Magnetic resonance imaging and pathological findings in a cat with brain contusions. J Vet Med A Physiol Pathol Clin Med 2003;50:222-224.

52. Saunders J, Poncelet L, Clercx C, et al. Probable trigeminal nerve schwannoma in a dog. Vet Radiol Ultrasound 1998;39:539-542.

53. Schoeman J, Stidworthy M, Penderis J, et al. Magnetic resonance imaging of a cerebral cavernous haemangioma in a dog. J South Afr Vet Assoc 2002;73:207-210.

54. Seiler G, Cizinauskas S, Scheidegger J, et al. Low-field magnetic resonance imaging of a pyocephalus and a suspected brain abscess in a German Shepherd dog. Vet Radiol Ultrasound 2001;42:417-422.

55. Speciale J, Van Winkle T, Steinberg S, et al. Computed tomography in the diagnosis of focal granulomatous meningoencephalitis: retrospective evaluation of three cases. J Am Anim Hosp Assoc 1992;28:327-332.

56. Stewart W, Parent J, Towner R, et al. The use of MRI in the diagnosis of neurologic diseases. Can Vet J 1992;33:585-590.

57. Swengel J. Computerized tomography for diagnosis of brain tumor in a dog. J Am Vet Med Assoc 1982;181:605.

58. Targett M, McInnes E, Dennis R, et al. Magnetic resonance imaging of a medullary dermoid cyst with secondary hydrocephalus in a dog. Vet Radiol Ultrasound 1998;40:23-26.

59. Thomas W, Adams W, McGavin D, et al. Magnetic resonance imaging appearance of intracranial hemorrhage secondary to cerebral vascular malformation in a dog. Vet Radiol Ultrasound 1997;38:371-375.

60. Thomas W, Wheeler S, Kramer R, et al. Magnetic resonance imaging features of primary brain tumors in dogs. Vet Radiol Ultrasound 1996;37:20-27.

61. Thomson C, Kornegay J, Burn R, et al. Magnetic resonance imaging - a general overview of principles and examples in veterinary neurodiagnosis. Vet Radiol Ultrasound 1993;34:2-17.

62. Tidwell A, Mahony O, Moore R, et al. Computed tomography of an acute hemorrhagic cerebral infarct in a dog. Vet Radiol Ultrasound 1994;35:290-296.

63. Tipold A, Tipold E. Computertomographische Untersuchungen des Zentralnervensystems bei Kleintieren. Tierärztl Prax 1991;19:183-191.

64. Turrel J, Fike J, LeCouteur R, et al. Computed tomographic characteristics of primary brain tumors in 50 dogs. J Am Vet Med Assoc 1986;188:851-856.

65. van Bree H. Visual diagnosis of the brain in the aging dog. Prakt Tierarzt 2003;84:196-199.

66. Vernau K, Kortz G, Koblik P, et al. Magnetic resonance imaging and computed tomography characteristics of intracranial intra-arachnoid cysts in 6 dogs. Vet Radiol Ultrasound 1997;38:171-176.

67. Vink-Nooteboom M, Junker K, Van den Ingh T, et al. Computed tomography of cholesterinic granulomas in the choroid plexus of horses. Vet Radiol Ultrasound 1998;39:512-516.

68. Vite C, Insko E, Schotland H, et al. Quantification of cerebral volume in English Bulldogs. Vet Radiol Ultrasound 1997;38:437-443.

69. Vullo T, Korenman E, Manzo R, et al. Diagnosis of cerebral ventriculomegaly in normal adult beagles using quantitative MRI. Vet Radiol Ultrasound 1997;38:277-281.

70. Wolf M, Pedroia V, Higgings R, et al. Intracranial ring enhancing lesions in a dog: a correlative CT scanning and neuropathologic study. Vet Radiol Ultrasound 1995;36:16-20.

71. Woods J, Cuddon P, Schenkman D. Prefrontal cortical and diencephalic cavernous hemangioma in a dog. Prog in Vet Neuro 1992;3:126-130.

72. Adams W, Daniel G, Pardo A, et al. Magnetic resonance imaging of the caudal lumbar and lumbosacral spine in 13 dogs (1990-1993). Vet Radiol Ultrasound 1995;36:3-13.

73. Asperio R, Marzola P, Zibellini E, et al. Use of magnetic resonance imaging for diagnosis of a spinal tumor in a cat. Vet Radiol Ultrasound 1999;40:267-270.

74. Bagley R, Harrington M, Tucker R, et al. Occipital dysplasia and associated cranial spinal cord abnormalities in two dogs. Vet Radiol Ultrasound 1996;37:359-362.

75. Dabanoglu I, Kara M, Turan E, et al. Morphometry of the thoracic spine in German shepherd dog : a computed tomographic study. Anat Histol Embryol 2004;33:53-58.

76. Drost W, Love N, Berry C. Comparison of radiography, myelography and computed tomography for the evaluation of canine vertebral and spinal cord tumors in sixteen dogs. Vet Radiol Ultrasound 1996;37:28-33.

77. Fraser J, Garosi L, Dennis R, et al. Imaging of a spinal nephroblastoma in a dog. Vet Radiol Ultrasound 2003;44:537-541.

78. Galloway A, Curtis N, Sommerlad S, et al. Correlative imaging findings in seven dogs and one cat with spinal arachnoid cysts. Vet Radiol Ultrasound 1999;40:445-452.

79. Gnirs K, Ruel Y, Blot S, et al. Spinal subarachnoid cysts in 13 dogs. Vet Radiol Ultrasound 2003;44:402-408.

80. Gonzalo-Orden J, Altonaga J, Orden A, et al. Magnetic resonance, computed tomographic and radiologic findings in a dog with discospondylitis. Vet Radiol Ultrasound 2000;41:142-144.

81. Jones J, Sorjonen D, Simpson S, et al. Comparison between computed tomographic and surgical findings in nine large-breed dogs with lumbosacral stenosis. Vet Radiol Ultrasound 1996;37:247-256.

82. Jones J, Inzana K. Subclinical CT abnormalities in the lumbosacral spine of older large-breed dogs. Vet Radiol Ultrasound 2000;41:19-26.

83. Kraus M, Mahaffey M, Girard E, et al. Diagnosis of C5-C6 spinal luxation using three-dimensional computed tomographic reconstruction. Vet Radiol Ultrasound 1997;38:39-41.

84. Levitsky R, Lipitz D, Chauvet A. Magnetic resonance imaging of the cervical spine in 27 dogs. Vet Radiol Ultrasound 1999;40:332-341.

85. Lipitz D, Levitski R, Chauvet A, et al. Magnetic resonance imaging features of cervical stenotic myelopathy in 21 dogs. Vet Radiol Ultrasound 2001;42:20-27.

86. Olby N, Munana K, Sharp N, et al. The computed tomographic appearance of acute thoracolumbar intervertebral disc herniations in dogs. Vet Radiol Ultrasound 2000;41:396-402.

87. Pease A, Berry C, Mott J, et al. Radiographic, computed tomographic and histopathologic appearance of a presumed spinal chordoma in a dog. Vet Radiol Ultrasound 2002;43:338-342.

88. Penderis J, Dennis R. Use of traction during magnetic resonance imaging of caudal cervical spondylomyelopathy (‘wobbler syndrome’) in the dog. Vet Radiol Ultrasound 2004;45:216-219.

89. Sharp N, Cofone M, Robertson I, et al. Computed tomography in the evaluation of caudal cervical spondylomyelopathy of the Doberman Pinscher. Vet Radiol Ultrasound 1995;36:100-108.

90. Tidwell A, Specht A, Bleaser L, et al. Magnetic resonance imaging features of extradural hematomas associated with intervertebral disc herniation in a dog. Vet Radiol Ultrasound 2002;43:319-324.

91. Van Ham L, van Bree H, Tshamala M, et al. Use of computed tomography and computed tomographic myelography for assessment of spinal tumoral calcinosis in a dog. Vet Radiol Ultrasound 1995;36:115-118.

92. Forterre F, Gutmannsbauer B, Schmahl W, et al. CT-Myelographie zur Diagnose des Plexus-brachialis-Abrisses beim Kleintier. Tierärztl Prax 1998;26:322-329.

93. Lipscomb V, Muir P. Magnetic resonance imaging of a dog with sciatic nerve root signature. Vet Rec 2000;147:393-394.

94. Mellanby R, Jeffery N, Baines E, et al. Magnetic resonance imaging in the diagnosis of lymphoma involving the brachial plexus in a cat. Vet Radiol Ultrasound 2003;44:522-525.

95. McCarthy R, Feeney D, Lipowitz A. Preoperative diagnosis of tumors of the brachial plexus by use of computed tomography in three dogs. J Am Vet Med Assoc 1993;202:291-294.

96. Simpson D, Beck J, Allan G, et al. Diagnosis and excision of a brachial plexus nerve sheath tumour in a dog. Aust Vet J 1999;77:222-224.

97. Armbrust L, Hoskinson J, Biller D, et al. Low-field magnetic resonance imaging of bone marrow in the lumbar spine, pelvis, and femur in the adult dog. Vet Radiol Ultrasound 2004;45:393-401.

98. Baird D, Hathcock J, Kincaid S, et al. Low-field magnetic resonance imaging of early subchondral cyst-like lesions in induced cranial ligament deficient dogs. Vet Radiol Ultrasound 1998;39:167-173.

99. Baird D, Hathcock J, Rumph P, et al. Low-field magnetic resonance imaging of the canine stifle joint: normal anatomy. Vet Radiol Ultrasound 1998;39:87-97.

100. Baird D, Kincaid S, Hathcock J, et al. Effect of hydration on signal intensity of gelatin phantoms using low-field magnetic resonance imaging: possible application in osteoarthritis. Vet Radiol Ultrasound 1999;40:27-35.

101. Banfield C, Morrison W. Magnetic resonance arthrography of the canine stifle joint: technique and applications in eleven military dogs. Vet Radiol Ultrasound 2000;41:200-213.

102. Braden T, Stickle R, Dejardin L, et al. The use of computed tomography in fragmented coronoid disease: a case report. Vet Comp Orthop Trauma 1994;7:40-44.

103. Fitch R, Wilson E, Hathcock J, et al. Radiographic, computed tomographic and magnetic resonance imaging evaluation of a chronic long digital extensor tendon avulsion in a dog. Vet Radiol Ultrasound 1997;38:177-181.

104. Glyde M, Doyle R, McAllister H, et al. Magnetic resonance imaging in the diagnosis and surgical management of sacral osteochondrosis in a mastiff dog. Vet Rec 2004;155:83-86.

105. Newberg AH. Computed tomography of joint injuries. Radiol Clin North Am 1990;28:445–460.

106. Nordberg C, Johnson K. Magnetic resonance imaging of normal canine ligaments. Vet Radiol Ultrasound 1998;39:128-136.

107. Reichle J, Snaps F. The elbow. Clin Techn Small Anim Pract 1999;3:177-186.

108. Rossmeisl J, Rohleder J, Hancock R, et al. Computed tomographic features of suspected traumatic injury to the iliopsoas and pelvic limb musculature of a dog. Vet Radiol Ultrasound 2004;45:388-392.

109. Snaps F, Balligand M, Saunders J, et al. Comparison of radiography, magnetic resonance imaging, and surgical findings in dogs with elbow dysplasia. Am J Vet Res 1997;58:1367-1370.

110. Snaps F, Park R, Saunders J, et al. Magnetic resonance arthroscopy of the cubital joint in dogs affected with fragmented medial coronoid processes. Am J Vet Res 1999;60:190-193.

111. Snaps F, Saunders J, Park R, et al. Comparison of spin-echo, gradient echo, and fat saturation MRI sequence. Vet Radiol Ultrasound 1998;39:518-523.

112. Steffen F, Flückiger M, Montavon P. Traumatic atlanto-occipital luxation in a dog: associated hypoglossal nerve deficits and use of 3-dimensional computed tomography. Vet Surg 2003;32:411-415.

113. Turan E, Erden H. Computed tomography and morphometry of the carpal canal in the dog. Ann Anat 2003;185:173-178.

114. van Bree H, Degryse H, Van Ryssen B, et al. Pathologic correlations with magnetic resonance images of osteochondrosis lesions in canine shoulders. J Am Vet Med Assoc 1993;202:1099-1105.

115. Widmer WR, Buckwalter KA, Braunstein EM, et al. Radiographic and magnetic resonance imaging of the stifle joint in experimental osteoarthrosis of dog. Vet Radiol Ultrasound 1994;35:371-383.

116. Young B, Klopp L, Albrecht M, et al. Imaging diagnosis : magnetic resonance imaging of a cervical wooden foreign body in a dog. Vet Radiol Ultrasound 2004;45:538-541.

117. Carpenter L, Schwarz P, Lowry J, et al. Comparison of radiologic imaging techniques for diagnosis of fragmented medial coronoid process of the cubital joint in dogs. J Am Vet Med Assoc 1993;203:78-83.

118. Burk R. Computed tomography of thoracic diseases in dogs. J Am Vet Med Assoc 1991;199:617-621.

119. Chen Q, Klein J, Gamsu G, et al. High-resolution computed tomography of the mammalian lung. Am J Vet Res 1992;53:1218-1224.

120. Dvir E, Kirberger R, Malleczek D. Radiographic and computed tomographic changes and clinical presentation of spirocercosis in the dog. Vet Radiol Ultrasound 2001;42:119-129.

121. Henninger W. Use of computed tomography in the diseased feline thorax. J Small Anim Pract 2003;44:56-64.

122. Kara M, Turan E, Dabanoglu I, et al. Computed tomographic assessment of the trachea in the German shepherd dog. Ann Anat 2004;186:317-321.

123. Punto L, Nevalainen T, Wiljasalo S, et al. Computed tomography of aspiration pneumonia in a dog. Vet Radiol 1984;25:43-45.

124. Schwarz L, Tidwell A. Alternative imaging of the lung. Clin Techn Small Anim Pract 1999;14:187-206.

125. Schwarz T, Sullivan M, Stork C, et al. Aortic and cardiac mineralization in the dog. Vet Radiol Ultrasound 2002;43:419-427.

126. Spann D, Sellon R, Thrall D, et al. Computed tomographic diagnosis: use of computed tomography to distinguish a pulmonary mass from alveolar disease. Vet Radiol Ultrasound 1998;39:532-535.

127. Tidwell A. Diagnostic pulmonary imaging. Problems. Vet Med 1992;4:239-264.

128. Tidwell A. Uses of computed tomography in cardiopulmonary disease. In: Bonagura JD (ed): Kirk: Current Veterinay Therapy XIII. Philadelphia, PA: Saunders, 2000;709-710.

129. Clifford C, Pretorius E, Weisse C, et al. Magnetic resonance imaging of focal splenic and hepatic lesions in the dog. J Vet Intern Med 2004;18:330-338.

130. Kleiter M, Henninger W, Hirt R, et al. Portosystemischer Shunt bei einem Hund - Diagnosestellung mit Hilfe der Computertomographie. Wien Tierärztl Mschr 1999;86:64-70.

131. Moe L, Lium B. Computed tomography of hereditary multifocal renal cystadenocarcinomas in German Shepherd dogs. Vet Radiol Ultrasound 1997;5:335-343.

132. Muleya J, Taura Y, Nakaichi M, et al. Appearance of canine abdominal tumors with magnetic resonance imaging using low fields permanent magnet. Vet Radiol Ultrasound 1997;6:444-447.

133. Patsikas M, Rallis T, Kladakis S, et al. Computed tomography diagnosis of isolated splenic torsion in a dog. Vet Radiol Ultrasound 2001;42:235-237.

134. Rosenstein D. Diagnostic imaging in canine pheochromocytoma. Vet Radiol Ultrasound 2000;6:499-506.

135. Seguin B, Tobias K, Gavin P, et al. Use of magnetic resonance angiography for diagnosis of portosystemic shunts in dogs. Vet Radiol Ultrasound 1999;3:251-258.

136. Yamazoe K, Ohashi F, Kadosawa T, et al. Computed tomography on renal masses in dogs and cats. J Vet Med Sci 1994;56:813-816.

137. Yasuda D, Fujita M, Yasuda S, et al. Usefulness of MRI compared with CT for diagnosis of mesenteric lymphoma in a dog. J Vet Med Sci 2004;66:1447-1451.

138. Allgoewer I, Lucas S, Schmitz S. Magnetic resonance imaging of the normal and diseased feline middle ear. Vet Radiol Ultrasound 2000;5:413-418.

139. Burk RL. Computed tomographic imaging of nasal disease in 100 dogs. Vet Radiol Ultrasound 1992;33:177-180.

140. Codner E, Lurus A, Miller J, et al. Comparison of computed tomography with radiography as a non-invasive diagnostic technique for chronic nasal disease in dogs. J Am Vet Med Assoc 1993;7:1106-1110.

141. Dvir E, Kirberger R, Terblanche A. Magnetic resonance imaging of otitis media in a dog. Vet Radiol Ultrasound 2000;41:46-49.

142. Hathcock J, Newton J. Computed tomographic characteristics of multilobular tumor of bone involving the cranium in 7 dogs and zygomatic arch in 2 dogs. Vet Radiol Ultrasound 2000;41:214-217.

143. Jones J, Smith M, Sponenberg D, et al. Orbital multilobular tumor of bone in a Basset Hound. Vet Comp Ophtalmol 1997;7:111-116.

144. Lipitz D, Levetski R, Berry W. Magnetic resonance imaging features of multilobular osteochondrosarcoma in 3 dogs. Vet Radiol Ultrasound 2001;42:14-19.

145. Lonosky JH, Abbott LC, Kuriashkin IV. Computed tomography of the normal feline nasal cavity and paranasal sinuses. Vet Radiol Ultrasound 1997;38:251-258.

146. Love N, Kramer R, Spodnick G, et al. Radiographic and computed tomographic evaluation of otitis media in the dog. Vet Radiol Ultrasound 1995;36:375-379.

147. Mathews K, Davidson A, Koblik P, et al. Comparison of topical administration of clotrimazole through surgically placed versus nonsurgically placed catheters for treatment of nasal aspergillosis in dogs: 60 cases (1990-1996). J Am Vet Med Assoc 1998;213:501-506.

148. Mathews K, Koblik P, Richardson E, et al. Computed tomographic assessment of noninvasive intranasal infusions in dogs with fungal rhinitis. Vet Surg 1996;25:309-319.

149. Moore M, Gavin R, Kraft S, et al. MR, CT and clinical features from four dogs with nasal tumors involving the rostral cerebrum. Vet Radiol 1991;32:19-25.

150. Morgan R, Ring R, Ward A, et al. Magnetic resonance imaging of ocular and orbital disease in 5 dogs and a cat. Vet Radiol Ultrasound 1996;37:185-192.

151. Ogilvie G, La Rue S. Canine and feline nasal and paranasal tumors. Vet Clin North Am Small Anim Pract 1992;22:1133-1144.

152. Park R, Beck E, LeCouteur R. Comparison of computed tomography and radiography for detecting changes induced by malignant nasal neoplasia in dogs. J Am Vet Med Assoc 1992;201:1720-1724.

153. Saunders JH, Duchateau L, Stock C, et al. Use of computed tomography to predict final outcome of nasal aspergillosis in dogs. Can Vet J 2003;44:305-311.

154. Saunders JH, van Bree H, Gielen I, et al. Diagnostic value of computed tomography in dogs with chronic nasal disease. Vet Radiol Ultrasound 2003;44:409-413.

155. Saunders JH, van Bree H. Comparison of radiography and computed tomography for the diagnosis of nasal aspergillosis. Vet Radiol Ultrasound 2003;44:414-419.

156. Saunders JH, Zonderland JL, Clercx C, et al. Computed tomographic findings in 35 dogs with nasal aspergillosis. Vet Radiol Ultrasound 2002;43:5-9.

157. Seitz S, Losonsky J, Marretta S. Computed tomographic appearance of inflammatory polyps in three cats. Vet Radiol Ultrasound 1996;37:99-104.

158. Snelling S, Beck C. The surgical management of a chronic inflammatory oropharyngeal lesion utilising magnetic resonance imaging for accurate localisation in a dog. Aust Vet J 2002;80:746-748.

159. Thrall D, Robertson I, McLeod D, et al. A comparison of radiographic and computed tomographic findings in 31 dogs with malignant nasal cavity tumors. Vet Radiol 1989;30:59-66.

160. Tidwell A, Ross L, Kleine L. Computed tomographic and magnetic resonance imaging of cavernous sinus enlargement in a dog with unilateral exophthalmos. Vet Radiol Ultrasound 1997;5:363-370.

161. Voges A, Ackerman N. MR evaluation of intra- and extracranial extension of nasal adenocarcinoma in a dog and cat. Vet Radiol Ultrasound 1995;36:196-200.

162. Moreau P, Moreau J-J, Desnoyer P. Presurgical use of computed tomography in a dog. Comp Contin Educ Pract Vet 1989;11:159-168.

163. Anor S, Sturges B, Lafranco L, et al. Systemic phaeohyphomycosis (cladophialophora bantiana) in a dog – clinical diagnosis with stereotactic computed tomographic-guided brain biopsy. J Vet Int Med 2001;15:257-261.

164. Flegel T, Podell M, March P, et al. Use of a disposable real-time CT stereotactic navigator device for minimally invasive dog brain biopsy through a mini-burr hole. Am J Neuroradiol 2002;23:1160-1163.

165. Garbagnati F, Lutman R, Valvassori L, et al. Nonpulmonary thoracic biopsy. Eur J Radiol 1989;9:214-216.

166. Giroux A, Jones J, Bohn J, et al. A new device for stereotactic CT-guided biopsy of the canine brain : design, construction, and needle placement accuracy. Vet Radiol Ultrasound 2002;43:229-236.

167. Harari J, Moore M, Leathers C, et al. Computed tomographic-guided free-hand needle biopsy of brain tumors in dogs. Prog in Vet Neuro 1993;4:41-44.

168. Koblik P, LeCouteur R, Higgins R, et al. Modification and application of a Pelorus Mark II Stereotactic System for CT-guided brain biopsy in 50 dogs. Vet Radiol Ultrasound 1999;40:424-433.

169. Koblik P, LeCouteur R, Higgins R, et al. CT-guided brain biopsy using a modified Pelorus Mark III Stereotactic System: experience with 50 dogs. Vet Radiol Ultrasound 1999;40:434-440.

170. Moissonnier P, Blot S, Devauchelle P, et al. Stereotactic CT-guided brain biopsy in the dog. J Small Anim Pract 2002;43:115-123.

171. Moissonnier P, Bordeau W, Delisle F, et al. Accuracy testing of a new stereotactic CT-guided brain biopsy device in the dog. Res Vet Sci 2000;68:243-247.

172. Tidwell A, Johnson K. Computed tomography-guided percutaneous biopsy: criteria for accurate needle tip identification. Vet Radiol Ultrasound 1994;35:440-444.

173. Tidwell A, Johnson K. Computed tomography-guided percutaneous biopsy in the dog and cat: description of technique and preliminary evaluation in 14 patients. Vet Radiol Ultrasound 1994;35:445-456.

174. Risselada M, Saunders J, Bhatti S, et al. CT-guided biopsy of an infected intervertebral disk. Vlaams Diergeneesk Tijdschr 2001;70:59-64.

SCIENTIFIC AIMS

CT and MR are novel techniques to perceive anatomical structures on images. On CT and MR pictures, the radiologist is confronted with detailed anatomical cross-sections instead of two-dimensional “shadow pictures” as on conventional radiographs. These new developments have caused difficulties when interpreting CT and MR images, because the knowledge of the normal three-dimensional anatomy and conventional radiographic anatomy could no longer serve as a basis for recognizing structural abnormalities in diseased animals.

To provide an accurate interpretation of CT and MR images and to recognize abnormalities that may be found, knowledge of the cross-sectional anatomy of normal animals is a prerequisite. Therefore a detailed anatomical description of several regions of the body, as revealed by the use of CT and MR, is necessary for the clinician. The aim of this study was to provide a comprehensive atlas of the normal canine body comparing cross-sectional anatomical slices to CT and MR images. Besides the descriptive anatomical aspect of this work, a comparative aspect is added as the results of CT anatomy are compared to those revealed by other imaging techniques such as MR and endoscopy. By combining CT pictures showing the calcified structures with MR scans of the same region, and taking advantage of the MR characteristics of depicting soft tissue in great detail and in superior spatial resolution, a unique atlas has been created.

Several publications on CT and MR anatomy of the dog are already available[1-16]and an atlas of MR and CT of the dog has recently been published[17]. Despite the partial overlap with these previous publications, the present work differs as a large number of matching cross-sectional anatomical colour images is used to clarify the corresponding CT/MR images, which provides more detailed and additional information. Every possible effort was made to label in great detail all anatomical structures depicted on the images.

As a complete cross-sectional description of the entire normal canine body should be too overwhelming, a number of representative and clinically important regions has been selected for this study.

The first part of this study describes and compares the CT and MR anatomy of two regions of the head, i.e., the canine brain (chapter 1.1) and the nasal cavities and frontal sinuses (chapter 1.2).

In the second part of this study the anatomy of the thorax is described as revealed by CT (chapter 2.1.1) and by thoracoscopy (chapter 2.1.2), followed by a comparison between both techniques (chapter 2.1.3).

In the third part of this study, the CT and MR anatomy of the elbow (chapter 3.1) and the tarsus (chapter 3.2) are described, and both techniques are compared for each joint.

REFERENCES

1. Baird D, Hathcock J, Rumph P, et al. Low-field magnetic resonance imaging of the canine stifle joint: normal anatomy. Vet Radiol Ultrasound 1998;39:87-97.

2. Burk RL. Computed tomographic anatomy of the canine nasal passages. Vet Radiol Ultrasound 1992;33:170-176.

3. Drost W, Berry C, Fischer P. Computed tomographic appearance of a normal variant of the canine tentorium cerebelli osseum. Vet Radiol Ultrasound 1996;37:351-353.

4. Feeney D, Fletcher T, Hardy R. Atlas of correlative imaging anatomy of the normal dog. Ultrasound and computed tomography. Philadelphia: WB Saunders Co, 1991.

5. Fike J, Druy E, Zook B, et al. Canine anatomy assisted by computerized tomography. Am J Vet Res 1980;41:1823-1832.

6. Fike J, LeCouteur R, Cann C. Anatomy of the canine brain using high resolution computed tomography. Vet Radiol 1981;22:236-243.

7. Fike J, LeCouteur R, Cann C. Anatomy of the canine orbital region. Multiplanar imaging by CT. Vet Radiol 1984;25:32-36.

8. George T, Smallwood J. Anatomic atlas for computed tomography in the mesaticephalic dog: head and neck. Vet Radiol Ultrasound 1992;33:217-240.

9. Gomez M, Freeman L, Jones J, et al. Computed tomographic anatomy of the canine cervical vertebral venous system. Vet Radiol Ultrasound 2004;45:29-37.

10. Jones J, Cartee R, Bartels J. Computed tomographic anatomy of the canine lumbosacral spine. Vet Radiol Ultrasound 1995;36:91-95.

11. Kraft S, Gavin P, Wendling L, et al. Canine brain anatomy on magnetic resonance images. Vet Radiol Ultrasound 1998;30:147-158.

12. Legrand J, Carlier B. Examen tomodensitométrique de l'encéphale du chien I. Conduite de l'examen et repères anatomiques. Revue Méd Vét 1999;137:193-196.

13. Love N, Fisher P, Hudson L. The computed tomographic enhancement pattern of the normal canine pituitary gland. Vet Radiol Ultrasound 2000;41:507-510.

14. Smallwood J, George T. Anatomic atlas for computed tomography in the mesaticephalic dog : caudal abdomen and pelvis. Vet Radiol Ultrasound 1992;33:143-167.

15. Smallwood J, George T. Anatomic atlas for computed tomography in the mesaticephalic dog: thorax and cranial abdomen. Vet Radiol Ultrasound 1993;34:65-84.

16. Zook B, Hitzelberg R, Fike J, et al. Anatomy of the Beagle in cross-section: Head and neck. Am J Vet Res 1981;42:844-849.

17. Assheuer J, Sager M. Head. In : Assheuer J, Sager M, eds. MRI and CT atlas of the dog. Berlin: Blackwell Science, 1997;50-57.

Cross-sectional anatomy
of the

HEAD

1.1. The brain

The next two chapters concern the investigation of the brain of the clinically normal dog. In the first chapter (chapter 1.1.1) the computed tomographic examination of the brain is described. The second chapter (chapter 1.1.2) briefly handles the magnetic resonance of the brain and gives a comparison between the results of the 2 techniques, CT and MR. .

However, all figures (anatomic, CT and MR sections) of the canine brain are combined in figure 2 of the first chapter (chapter 1.1.1) to make a visual comparison easier and simple.

1.1.1. Computed Tomography and Cross Sectional Anatomy of the Normal Canine Brain

Lieve M. De Rycke*, DVM; Ingrid M. Gielen*, DVM, MSc; Sofie A. Van Meervenne*, DVM;
Paul J. Simoens**, DVM, PhD; Henri J. van Bree*, DVM, PhD.

*Department of Medical Imaging, Faculty of Veterinary Medicine,
Ghent University, Salisburylaan 133, 9820 Merelbeke, Belgium

**Department of Morphology, Faculty of Veterinary Medicine,
Ghent University, Salisburylaan 133, 9820 Merelbeke, Belgium

Adapted from :
De Rycke LM, Gielen IM, van Meervenne SA, Simoens PJ, van Bree H. Computed Tomography and Cross Sectional Anatomy of the Normal Canine Brain. *Am J Vet Res* 2005;66:1743-1756.

SUMMARY

Objective—To provide a detailed anatomic description of brain structures in clinically normal dogs by means of computed tomography (CT).

Animals—4 clinically normal adult German Shepherd Dogs weighing 30 to 35 kg.

Procedure—Each dog was anesthetized and positioned in dorsal recumbency for CT examination of the brain; transverse scans were completed at 2-mm intervals from the cribriform plate of the ethmoid bone to the cranial part of the atlas by use of a third-generation CT scanner. Contrast material was injected IV, and a second series of scans was completed. Images (with or without contrast) from all dogs were reviewed by use of a soft tissue setting (window width, 150 Hounsfield units; window level, 50 Hounsfield units). One of the dogs was euthanatized, and a 3.5% formaldehyde solution was perfused via the common carotid arteries. After fixation, the brain was embedded in gelatin and sectioned into 5-mm-thick transverse sections by use of a stainless-steel knife. Anatomic sections were photographed and compared with the corresponding CT views.

Results—Most features of the brain that were identified on anatomic sections could be identified on the corresponding CT scans despite the low contrast between structures, particularly if adjacent bony structures and cerebrospinal fluid (CSF) were used as landmarks. Additional anatomic structures surrounding the brain were also identifiable on the CT images.

Conclusions and Clinical Relevance—Images obtained in this study could be used as a guide for evaluation of CT images of the brain in dogs with brain diseases.

INTRODUCTION

In human medicine, computed tomography (CT) is an important tool for investigation of intracranial disease. During recent years, the technique has become more available to veterinarians and CT of the brain has supplemented conventional radiography for the diagnosis of intracranial disorders in animals. In horses, dogs, cats, sheep, and goats, several pathologic conditions of the brain, such as congenital abnormalities, acquired hydrocephalus, neoplasia, inflammatory and neurodegenerative disorders, infarction, hemorrhage, and cysts, have been investigated and diagnosed by means of CT.[1-32] In addition to the diagnosis of intracranial disorders, CT can also be used as a presurgical tool[33] and to provide guidance for brain biopsy procedures.[34-40]

To accurately interpret CT scans of a brain, a thorough knowledge of the anatomic features of clinically normal brains is a prerequisite. In the veterinary medical literature, some anatomic features of clinically normal brains of dogs (determined via CT) have been described.[41-49] The purpose of the study reported here was to provide a detailed anatomic description of brain structures in clinically normal dogs by means of CT. Unlike the previous studies, this study was intended to provide cross-sectional images of the anatomic features of the brain (in color) with more detailed labeling of the gross sections and corresponding CT images as a reference guide for other investigations. Subsequently a comparison between the results of this chapter and the results of the MR examination of the brain (chapter 1.1.2) is made.

MATERIAL AND METHODS

Animals—Four clinically normal adult German Shepherd Dogs weighing 30 to 35 kg were used for this study. None of the animals had a history of neurologic disorders, and physical examination of the dogs revealed no pathologic conditions. The animals were maintained and procedures were performed in accordance with the Ethical Committee of the Faculty of Veterinary Medicine, Ghent University.

Computed tomography—Each dog was sedated by use of fentanyl (0.005 to 0.01 mg/kg, IV) and droperidol[a] (0.25 to 0.5 mg/kg, IV); anesthesia was induced via IV administration of thiopental sodium[b] (8 mg/kg). Dogs were intubated and anesthesia was maintained with halothane[c] (1.5% to 2%).

For CT examination, each dog was positioned in dorsal recumbency with the forelimbs extended caudally. A lateral survey view was obtained by use of a third-generation CT scanner.[d] Settings for the CT image technique were 120 kV and 130 mA. Transverse CT scans of the brain were obtained at 2-mm intervals from the cribriform plate of the ethmoid bone to the cranial part of the atlas, perpendicular to the long axis (or hard palate) of the skull. Following this series of scans, iohexol[e] (1 mL/kg) was injected via a catheter in a cephalic vein, and a second series of scans identical to the first series was completed 5 minutes after injection of contrast material. Individual images (obtained before and after contrast administration) from all 4 dogs were reviewed by use of a soft-tissue setting (window width, 150 Hounsfield units; window level, 50 Hounsfield units), formatted on x-ray film,[f] and evaluated by 2 investigators (LMDR and IMG).

Comparison of CT and anatomic images—At the end of CT examination, 1 dog weighing 31 kg was euthanatized while anesthetized for reasons unrelated to neurologic conditions. For euthanasia, a combination[g] of embutramide, mebenzoniumiodide, and tetracaïne (0.3 ml/kg) was injected intravenously during anesthesia. Following euthanasia, a 3.5% solution of formaldehyde was injected via the common carotid arteries until total perfusion of the brain was achieved. Subsequently, the head was separated at the atlantooccipital joint, and the skin, temporal muscles, calvaria, and dura mater were removed. The skull with the exposed brain was placed in a 3.5% solution of formaldehyde for 3 days; the brain was removed and maintained in the same solution for another week. At the end of this period, the brain was embedded in gelatin and sectioned into 5-mm-thick transverse sections by use of a stainless-steel knife. The rostral surface of each anatomic section was photographed; for each photograph, a corresponding CT image was selected on the basis of appearance. Matched pairs of images of the brain were obtained at 17 levels (from rostral to caudal brain regions). One person (LMDR) identified the anatomic structures on the photographs of the sections with the aid of texts on canine anatomy.[50,51] The identified structures were subsequently located on the corresponding CT images (without contrast material), and afterwards, the list of labeled structures was evaluated on CT images of the 3 other dogs. Nomenclature used for designating all structures was in accordance with official anatomic terminology.[52]

RESULTS

Seventeen transverse planes of the canine brain, extending from the cribriform plate of the ethmoid bone to the cranial part of the atlas and perpendicular to the hard palate, were matched with their corresponding anatomic section (Figure 1). Structures identified on the anatomic sections were also identified on the corresponding CT images without contrast material (soft tissue window setting; Figure 2).

Figure 1 – Lateral computed tomography (CT) survey view of the brain of a clinically normal dog indicating the levels (A through Q) at which the CT images were obtained. The CT scans were performed perpendicular to the hard palate.

On anatomic sections, numerous structures of the canine brain were identified, including the lobes of the cerebral hemispheres and the longitudinal cerebral fissure. On the rostral anatomic sections (levels A through G), various parts of the telencephalon such as the fornix, corpus callosum, rostral commissure, septum pellucidum, internal capsule, and the caudate nucleus were very distinct. The olfactory bulbs, peduncles, and tracts could be identified ventral to the cerebral hemispheres. At the level of the diencephalon, the optic chiasm was distinguished.

On the more caudal anatomic sections (levels H through L), identifiable structures of the telencephalon included the piriform lobe, hippocampus, and the hippocampal gyrus and sulcus. Several diencephalic structures such as the thalamus, hypothalamus, mamillary body, infundibulum with infundibular recess, hypophysis, epiphysis, lateral and medial geniculate bodies, and the interthalamic adhesion were observed. From the mesencephalon, the cerebral peduncles with the interpeduncular fossa, the rostral and caudal colliculi, the red nucleus, and the substantia nigra were distinct.

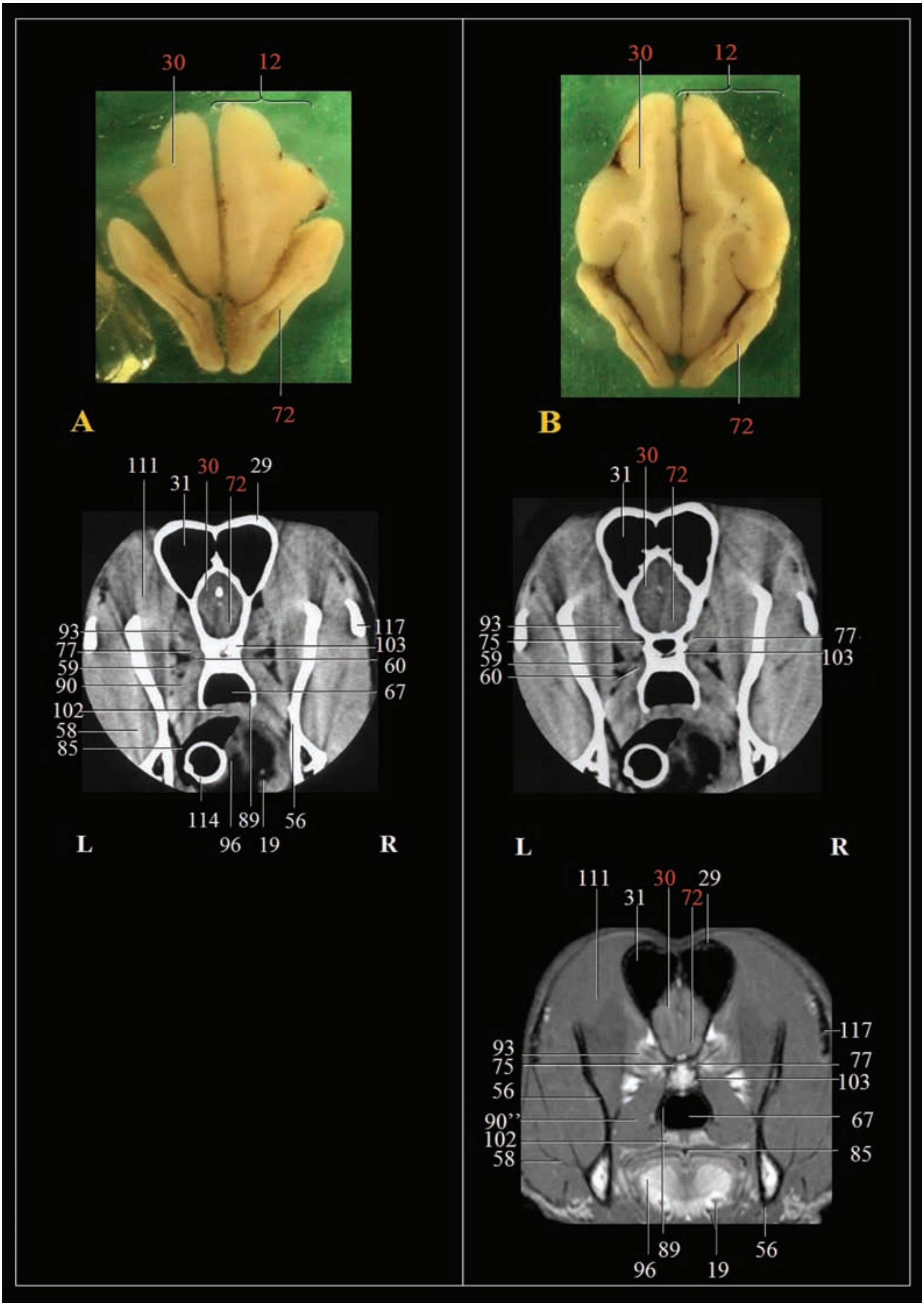
30
12
72
A
111
31
30
72
29
93
77
59
90
102
58
85
117
103
60
67
114
89
56
96
19
L
R
30
12
72
B
30
31
72
93
75
59
60
77
103
L
R
111
30
29
31
72
93
75
56
90''
102
58
117
77
103
67
85
89
56
96
19

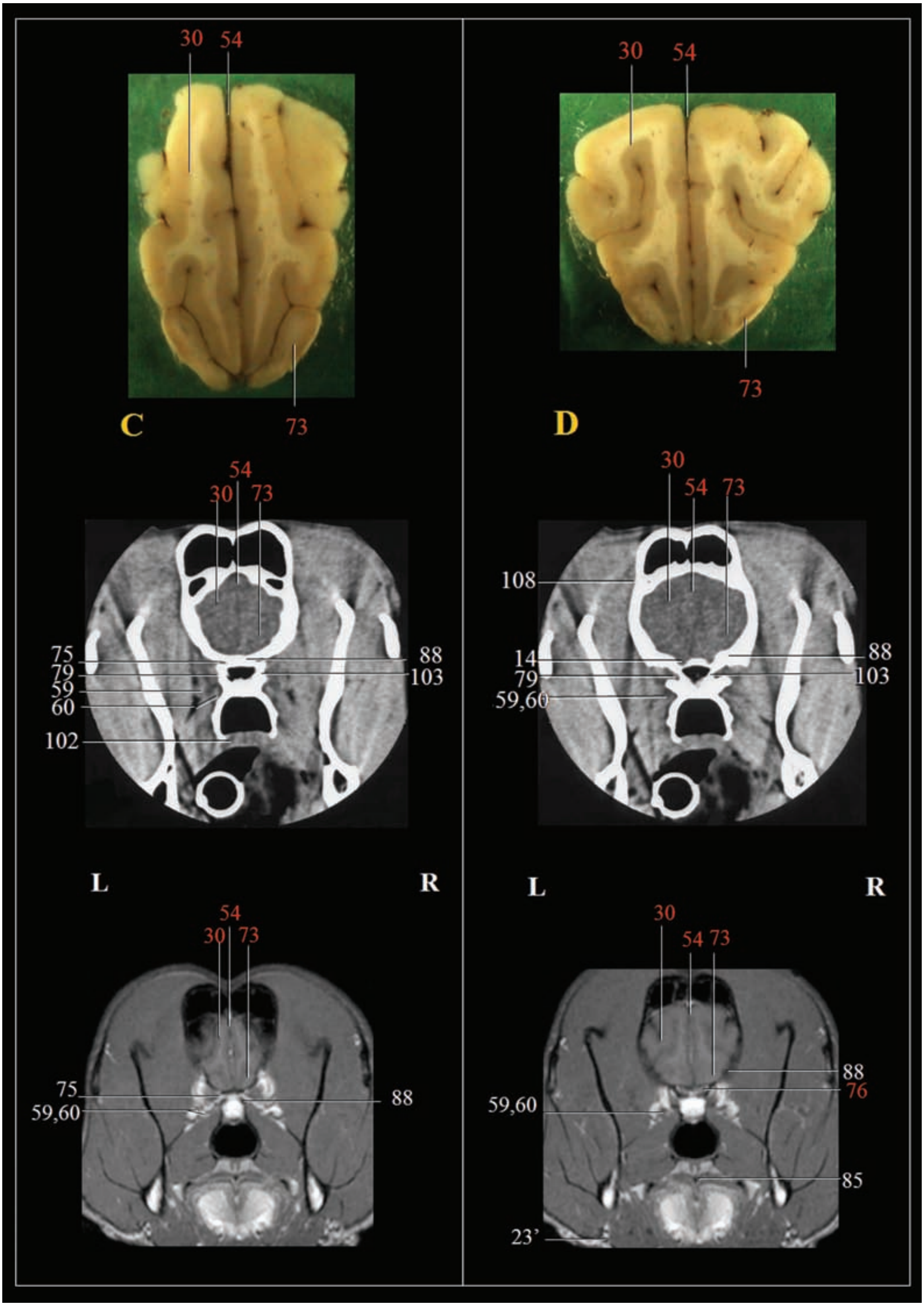
30
54
73
C
30
54
73
D
54
30
73
75
79
59
60
102
88
103
30
54
73
108
14
79
59,60
88
103
L
R
L
R
54
30
73
75
59,60
88
30
54
73
88
76
59,60
85
23'

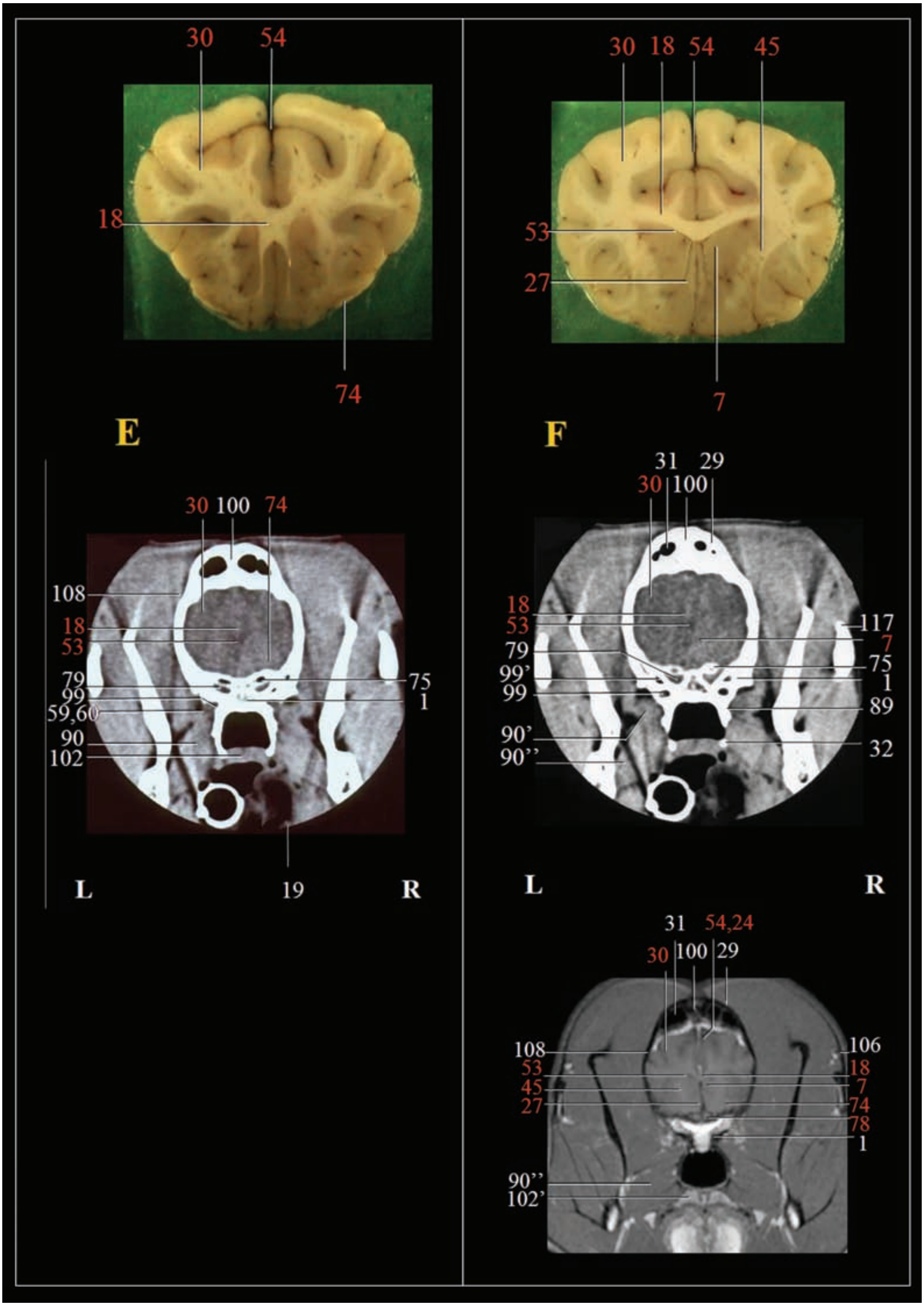
30
54
18
74
E
30
18
54
45
53
27
7
F
30
100
74
108
18
53
79
99
59,60
90
102
75
1
L
19
R
31
29
30
100
18
53
79
99'
99
90'
90''
117
7
75
1
89
32
L
R
31
54,24
30
100
29
108
53
45
27
90''
102'
106
18
7
74
78
1

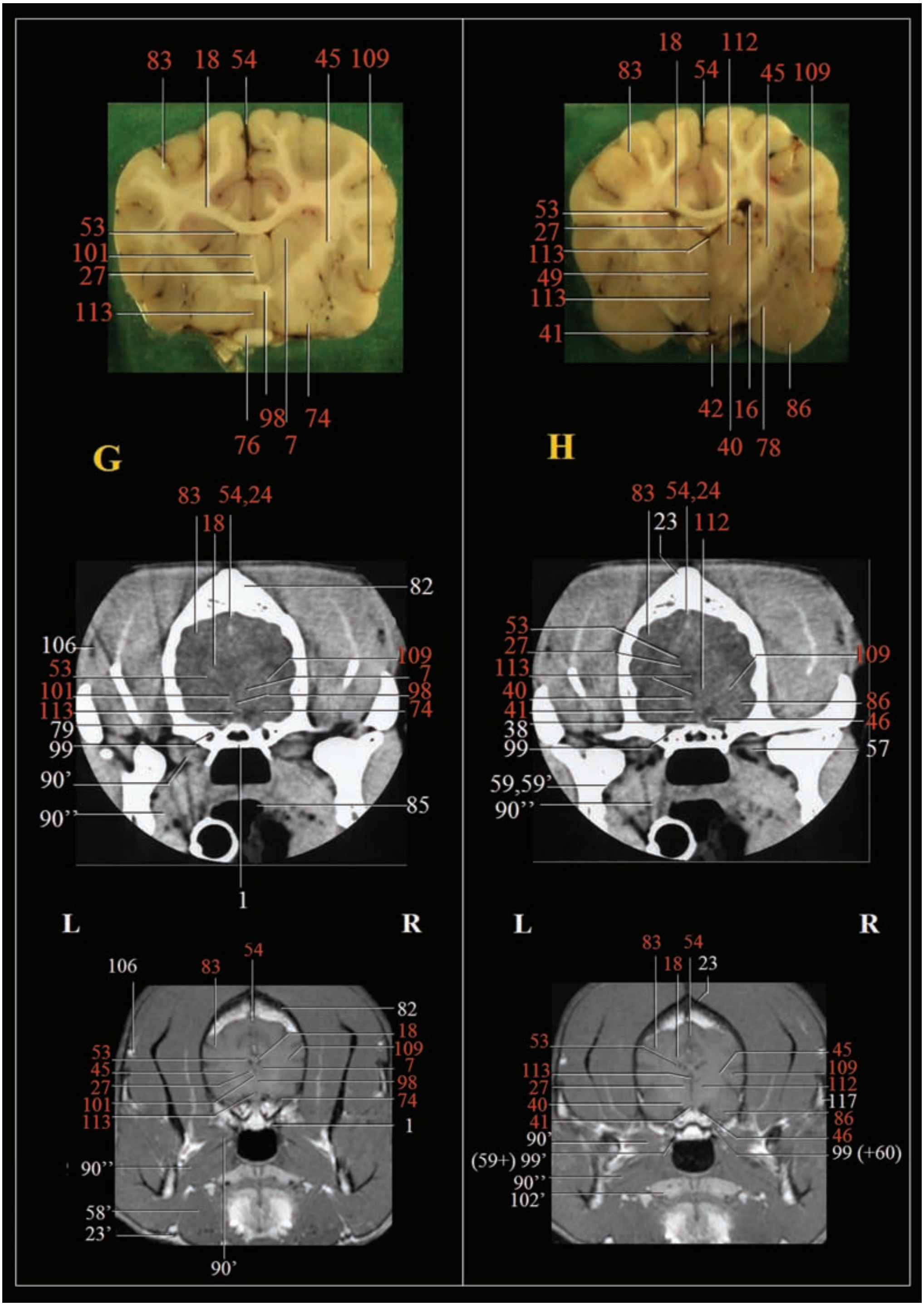
83
18
54
45
109
53
101
27
113
98
74
76
7
G
83
54,24
18
82
106
53
109
7
101
98
113
74
79
99
90’
90’’
85
1
L
R
106
83
54
82
18
109
53
45
7
27
98
101
74
113
1
90’’
58’
23’
90’
18
112
83
54
45
109
53
27
113
49
113
41
42
16
86
40
78
H
83
54,24
23
112
53
27
109
113
40
86
41
46
38
99
57
59,59’
90’’
L
R
83
54
18
23
53
45
113
109
27
112
40
117
41
86
90’
46
(59+) 99’
99 (+60)
90’’
102’

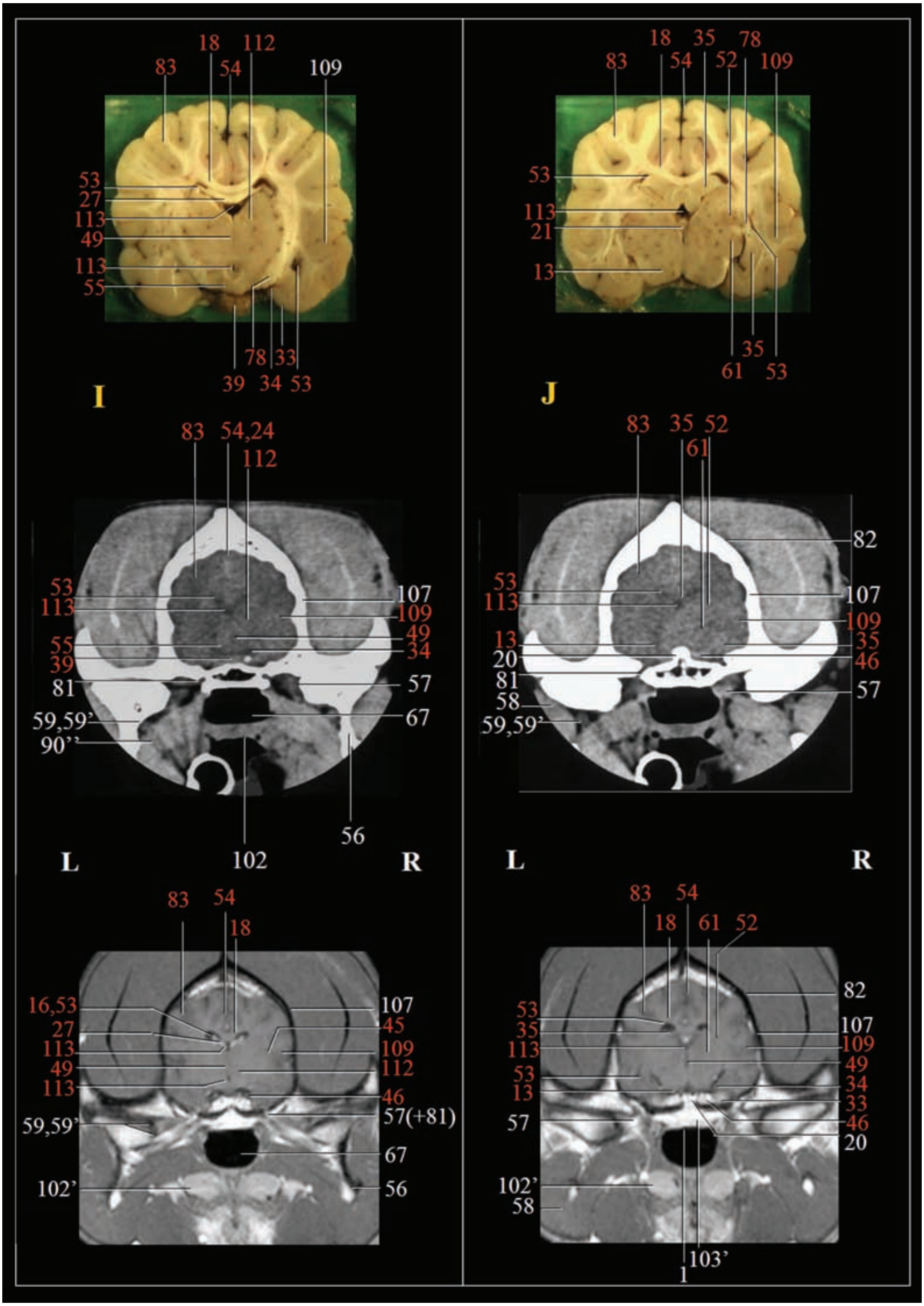
83
18
54
112
109
53
27
113
49
113
55
78
33
39
34
53
I
83
54,24
112
53
113
55
39
81
59,59'
90''
107
109
49
34
57
67
56
102
L
R
83
54
18
16,53
27
113
49
113
59,59'
102'
107
45
109
112
46
57(+81)
67
56
83
18
35
54
78
52
109
53
113
21
13
35
61
53
J
83
35
52
61
82
53
113
13
20
81
58
59,59'
107
109
35
46
57
L
R
83
54
18
61
52
82
53
35
113
53
13
57
102'
58
107
109
49
34
33
46
20
103'
1

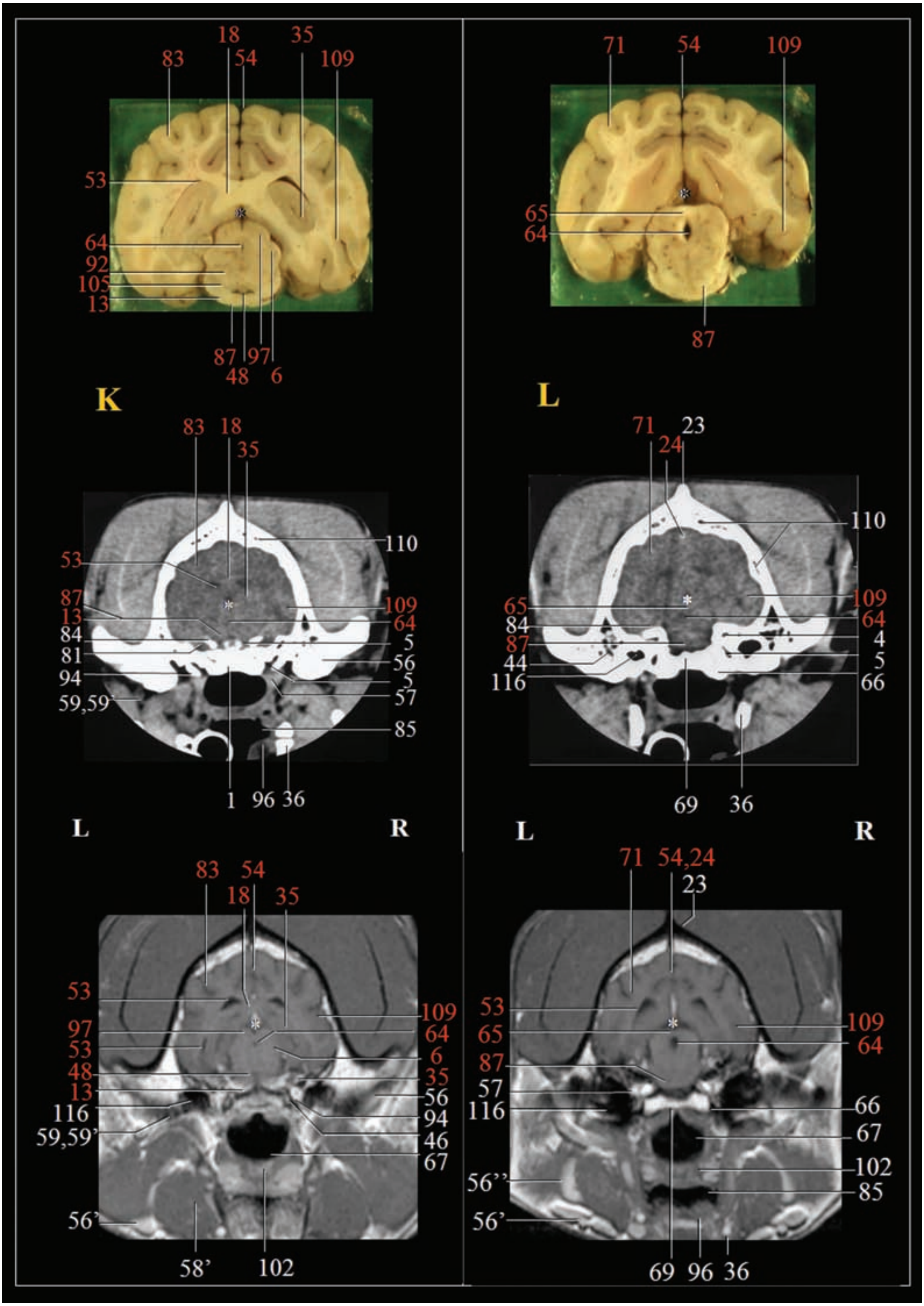
K
83
18
54
35
109
53
64
92
105
13
87
97
48
6
83
18
35
110
53
87
13
84
81
94
59,59'
109
64
5
56
5
57
85
1
96
36
L
R
83
54
18
35
53
97
53
48
13
116
59,59'
109
64
6
35
56
94
46
67
56'
58'
102
L
71
54
109
65
64
87
71
23
24
110
65
84
87
44
116
109
64
4
5
66
69
36
L
R
71
54,24
23
53
65
87
57
116
109
64
66
67
56''
102
85
56'
69
96
36

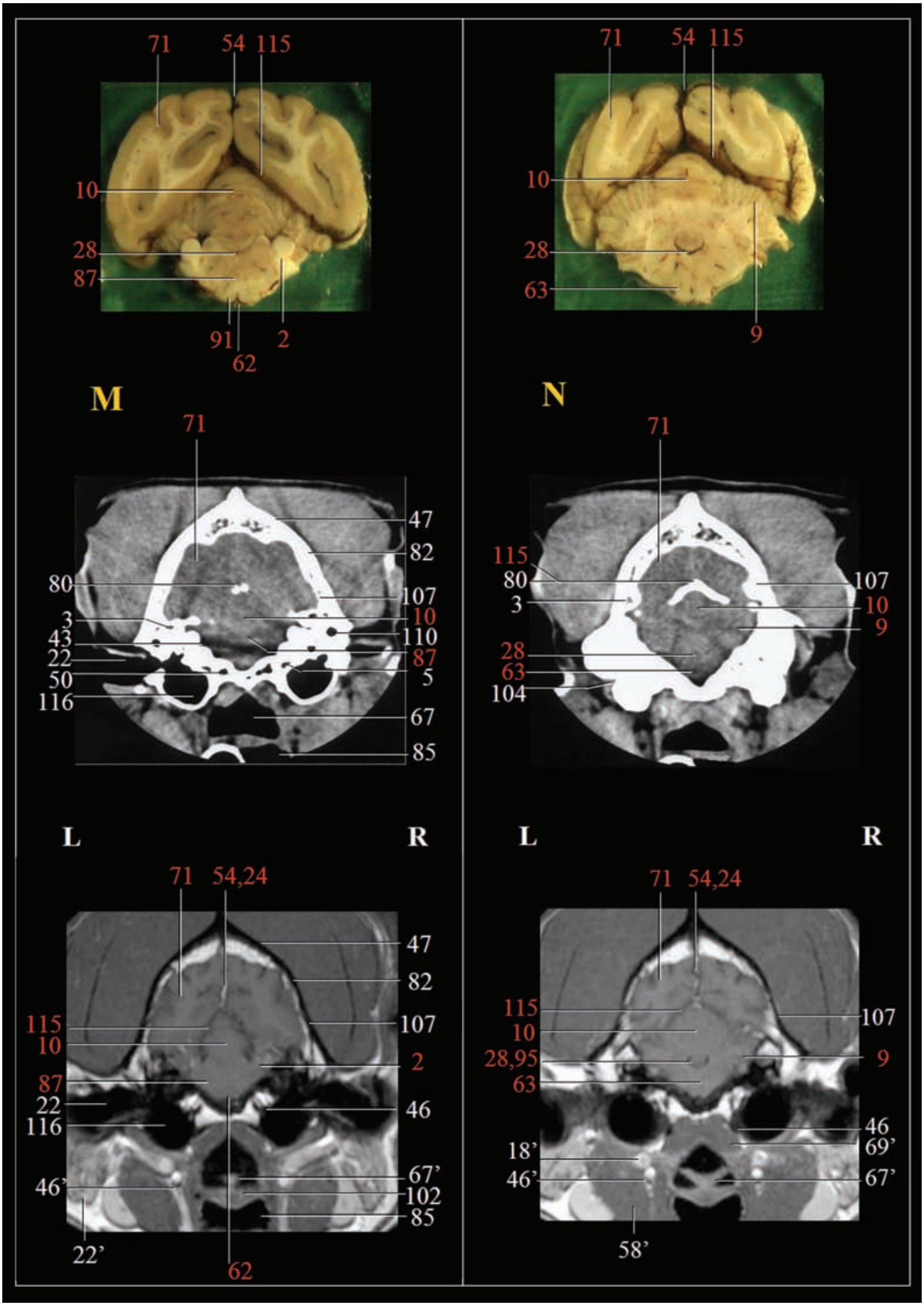
71
54
115
10
28
87
91
62
2
M
71
47
82
80
107
3
10
43
110
22
87
50
5
116
67
85
L
R
71
54,24
47
82
115
107
10
2
87
22
46
116
46'
67'
102
85
22'
62
71
54
115
10
28
63
9
N
71
115
80
107
3
10
9
28
63
104
L
R
71
54,24
115
107
10
28,95
9
63
46
69'
18'
46'
67'
58'

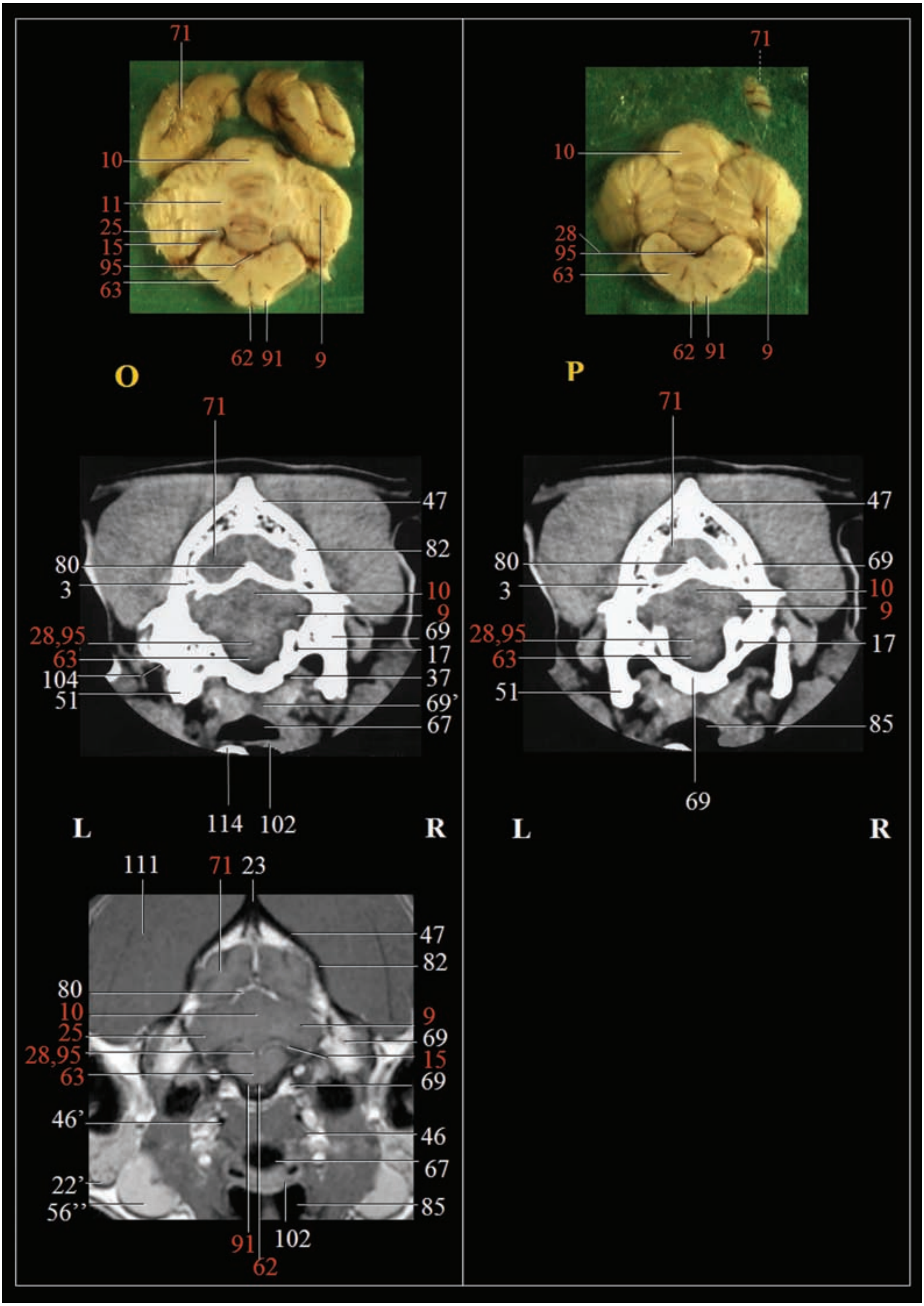
71
10
11
25
15
95
63
62 91 9
O
71
47
82
80
3
10
9
69
28,95
63
17
104
37
51
69'
67
114 102
L R
111 71 23
47
82
80
10
25
9
69
28,95
15
63
69
46'
46
67
22'
56''
85
91 102
62
71
10
28
95
63
62 91 9
P
71
47
80
69
3
10
9
28,95
17
63
51
85
69
L R

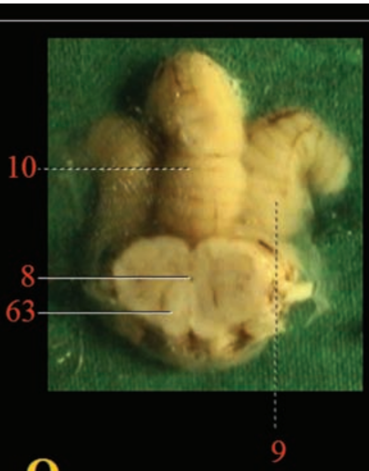

Q

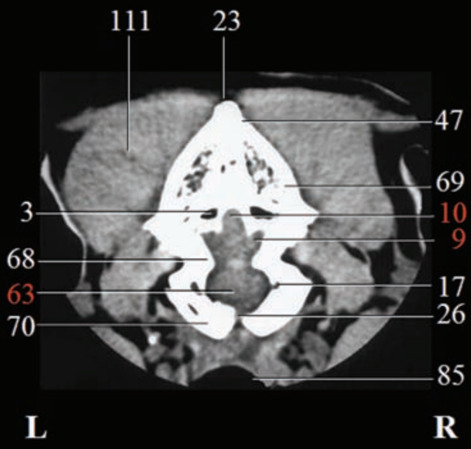

Figure 2 – Photographs of transverse anatomical sections (top), CT images obtained without administration of contrast material (soft tissue window; middle) and T1-weighted weighted MR images (TR = 498msec, TE = 14msec; bottom) of the brain of a clinically normal dog. Images were obtained at sections A through Q as illustrated in figure 1. Numbers in red represent intracranial structures; numbers in white represent skull bones and extracranial structures.

L = Left.
R = Right.
* = Subarachnoidal space.
1 = Basisphenoid bone.
2 = Brachium of pons (middle cerebellar peduncle).
3 = Canal of transverse sinus.
4 = Canal of trigeminal nerve.
5 = Carotid canal.
5’ = Carotid fossa.
6 = Caudal collicle.
7 = Caudate nucleus.
8 = Central canal.
9 = Cerebellar hemisphere.
10 = Cerebellar vermis.
11 = Cerebellar white matter.
12 = Cerebral hemisphere.
13 = Cerebral peduncle.
14 = Chiasmatic sulcus.
15 = Choroid plexus of the fourth ventricle.
16 = Choroid plexus of the lateral ventricle.
17 = Condylar canal.
18 = Corpus callosum.
18’ = Cranial cervical ganglion.
19 = Deep lingual artery and vein.
20 = Dorsum sellae turcicae.
21 = Epiphysis (pineal gland).
22 = External acoustic meatus.
22’ = Parotid salivary gland.
23 = External occipital crest.
23’= Facial vein.
24 = Falx cerebri.
25 = Floccular lobe.
26 = Foramen magnum.
27 = Fornix.
28 = Fourth ventricle.
29 = Frontal bone.
30 = Frontal lobe.
31 = Frontal sinus.
32 = Hamulus of the pterygoid bone.
33 = Hippocampal gyrus.
34 = Hippocampal sulcus.
35 = Hippocampus.
36 = Hyoid bone.
37 = Hypoglossal canal.
38 = Hypophyseal fossa.
39 = Hypophysis (pituitary gland).
40 = Hypothalamus.
41 = Infundibular recess.
42 = Infundibulum.
43 = Internal acoustic pore.
44 = Cochlea.
45 = Internal capsule.
46 = Internal carotid artery (in the cavernous sinus on image H).
46’ = External carotid artery.
47 = Interparietal bone.
48 = Interpeduncular fossa.
49 = Interthalamic adhesion.
50 = Jugular foramen.
51 = Jugular (paracondylar) process.
52 = Lateral geniculate body.
53 = Lateral ventricle.
54 = Longitudinal cerebral fissure.
55 = Mamillary body.
56 = Mandible.
56’ = Mandibular lymphnodes.
56’’ = Mandibular salivary gland.
57 = Mandibular nerve.
58 = Masseter muscle.
58’ = Digastric muscle.
59 = Maxillary artery.
59’ = Maxillary vein.
60 = Maxillary nerve.
61 = Medial geniculate body.
62 = Median ventral fissure.
63 = Medulla oblongata.
64 = Mesencephalic aqueduct.
65 = Mesencephalic tectum.
66 = Muscular tubercle.
67 = Nasopharyngeal cavity.
67’ = Epiglottis.
68 = Nuchal tubercle.
69 = Occipital bone.
69’ = Longus capitis muscle.
70 = Occipital condyle.
71 = Occipital lobe.
72 = Olfactory bulb.
73 = Olfactory peduncle.
74 = Olfactory tract (lateral).
75 = Optic canal.
76 = Optic chiasm.
77 = Optic nerve.
78 = Optic tract.
79 = Orbital fissure.
80 = Osseous tentorium cerebelli.
81 = Oval foramen.
82 = Parietal bone.
83 = Parietal lobe.
84 = Petrosal crest of the temporal bone.
85 = Pharyngeal cavity.
86 = Piriform lobe.
87 = Pons.
88 = Presphenoid bone.
89 = Pterygoid bone.
90 = Pterygoid muscles (90’= lateral, 90’’ = medial).
91 = Pyramid of medulla oblongata.
92 = Red nucleus.
93 = Dorsal and ventral straight muscles of the eye.
94 = Retroarticular process.
95 = Rhomboid fossa.
96 = Root of tongue.
97 = Rostral collicle.
98 = Rostral commissure.
99 = Round foramen (foramen rotundum).
99’ = Alar canal.
100 = Septum of frontal sinuses.
101 = Septum pellucidum including nuclei septi (septal nuclei).
102 = Soft palate.
102’ = Palatine tonsil.
103 = Sphenoid bone (=1+88) (+bone cavity)
104 = Stylomastoid foramen.
105 = Substantia nigra.
106 = Superficial temporal artery and vein.
107 = Temporal bone.
108 = Temporal line.
109 = Temporal lobe.
110 = Temporal meatus.
111 = Temporal muscle.
112 = Thalamus.
113 = Third ventricle.
114 = Tracheotube.
115 = Transverse cerebral fissure.
116 = Tympanic cavity.
117 = Zygomatic arch.

On the most caudal sections (levels M through Q), parts of the metencephalon such as the cerebellar hemispheres, the vermis, and the floccular lobe were clearly visible. Dorsal to the cerebellum, the transverse cerebral fissure formed a major landmark. Prominent ventral structures included the pons, the middle cerebellar peduncle (brachium pontis), and the medulla oblongata with the pyramids flanking the median ventral fissure.

In addition, the various parts of the ventricular system were distinguished. These included the lateral, third, and fourth ventricles; mesencephalic aqueduct; central canal; and choroid plexuses.

On the CT images without contrast material (soft tissue window setting), most of the aforementioned structures could be located by the use of landmarks such as adjacent hypodense CSF and hyperdense bony structures. The position of the longitudinal cerebral fissure was determined by the presence of the hyperdense falx cerebri.

On the rostral CT images (levels A through G), the corpus callosum and caudate nucleus were located adjacent to the hypodense lateral ventricles. The corpus callosum appeared as a moderate hyperdense and V-shaped structure. The fornix, septum pellucidum, and the rostral commissure were identified with reference to the adjacent hypodense third ventricle. It was not possible to distinguish the internal capsule. Several parts of the olfactory system were not distinct but could be identified by their ventral and lateral position in the brain. The hyperdense optic chiasm was identified dorsal to the basisphenoid bone and ventral to the third ventricle.

On the more caudal CT images (levels H through L), the hippocampus was located ventrolateral in the brain and dorsal to the third ventricle and the piriform lobe. The hippocampal gyrus could not be clearly seen. The hypophysis was identified dorsal to the bony hypophyseal fossa. The internal carotid artery was moderately hyperdense and located lateral to the hypophysis; dorsal to the hypophysis, the mamillary bodies and the hypodense hippocampal sulcus were identified. The position of the thalamus could be clearly defined by its margins; however, the optic tract, epiphysis, infundibulum, and tuber cinereum were impossible to distinguish. With regard to the mesencephalon, only the cerebral peduncles could be located lateral to the bony dorsum sellae turcicae. The geniculate bodies were difficult to see but were located dorsal to the cerebral peduncles.

On the most caudal CT images (levels M through Q), the transverse cerebral fissure was identified because of the presence of the hyperdense osseous tentorium cerebelli. Ventral to the tentorium cerebelli, the vermis and the adjacent cerebellar hemispheres were identified. The cerebellar white matter, floccular lobe, and the middle cerebellar peduncle (brachium pontis) could not be distinguished. The pons was determined to be dorsal to the occipital bone, but it was not possible to identify the medial ventral fissure and the pyramids of the medulla oblongata. From the ventricular system, all 4 ventricles and the mesencephalic aqueduct could be located by the presence of radiolucent CSF. In contrast, the central canal and the choroid plexuses of the lateral and fourth ventricles were not detected. The fourth ventricle was not always very distinct because of streak artifacts at the level of the caudal cerebral fossa.

In addition, surrounding bony and soft tissue structures observable on the CT images were also identified and labeled with reference to the anatomic sections and anatomy texts. In the ventral parts of the images, the nasopharyngeal cavity, soft palate, and the root of the tongue were identified. Several cranial muscles (eg, the pterygoid, masseter, retractor bulbi and temporal muscles) were distinguished. Furthermore, numerous blood vessels and nerves were located: the optic nerve surrounded by the retractor bulbi muscle; the superficial temporal artery and vein adjacent to the temporal muscle; the deep lingual artery and vein in the root of the tongue; the mandibular nerve; and the maxillary artery, vein, and nerve situated mediodorsal to the pterygoid muscle. The various cranial bones surrounding the brain were identified, including the parietal and interparietal, pterygoid, temporal, basisphenoid, presphenoid, and occipital bones. Parts of the mandible and the hyoid bone could also be seen.

On the CT images without contrast material from the other 3 dogs, most parts of the brain and almost all bony, muscular, nervous, and vascular structures mentioned were similarly visible. In 2 dogs, a large amount of CSF was present in the ventricular system, which made it possible to locate the rostral and caudal colliculi on the images. The third dog had a small amount of CSF; therefore, it was rather difficult to identify the ventricles, infundibular recess, mesencephalic aqueduct, and the subarachnoidal space. In the same dog, the superficial temporal arteries and veins and the internal carotid arteries could not be identified via CT. In 1 of the other dogs, the maxillary vein and artery could not be located with certainty. The falx cerebri and the longitudinal cerebral fissure were not distinct in images from 1 dog and the canal of the transverse sinus was not identifiable in images from another. The alar canal and the cochlea could not be seen in images from any of the 3 dogs.

On evaluation of the CT images of the 4 dogs obtained after administration of contrast material, only the falx cerebri and the blood vessels were more distinct, compared with the images obtained before administration of contrast material (not shown).

DISCUSSION

The present investigation was carried out to characterize the anatomic features of the brain of clinically normal dogs by use of a high-resolution CT system. In our study, dolichocephalic dogs were used. In a previous study,[47] small interbreed variations of anatomic structures, such as the size of the ventricles or depth of the hypophyseal fossa, as well as important individual variations among dogs of the same breed, have been described.

Numerous structures of the canine brain identified on anatomic sections were also identified on the CT images. For best contrast resolution of the CT images, the window width should be narrow and the window level should be set at a number similar to the mean Hounsfield units of the structure of interest. However, the distinctions among internal brain structures were frequently difficult because of the minor density differences on CT images; therefore, landmarks such as hypodense CSF and bony structures were used for orientation, and standard anatomic texts were used for reference.[41-45,47-49] The presence of CSF in the ventricles and in the subarachnoidal space facilitated the accurate identification of various adjacent structures and tissues that were not discernible on the basis of their appearance or inherent density alone. In 2 dogs of the present study, a relatively large amount of CSF was present; consequently, identification of adjacent structures, such as the caudate nucleus, rostral and caudal colliculi, corpus callosum, fornix, geniculate bodies, hippocampus, mamillary body, rostral commissure, septum pellucidum, thalamus, and interthalamic adhesion, was easier in these images than in the images from the other 2 dogs. In addition, numerous bony landmarks present on the CT images (eg, the osseous tentorium cerebelli, falx cerebri, dorsum sellae turcicae, and chiasmatic sulcus, along with bony foramina and canals) facilitated the identification of important intracranial structures such as the cerebral peduncles and lobes, transverse and longitudinal cerebral fissures, hypothalamus, hypophysis, olfactory peduncle and tract, optic chiasm and nerve, and pons.

Administration of contrast material can be an important part of CT investigations, although it does not necessarily need to be performed in every situation.[11] The use of contrast medium enhances the CT visualization of certain clinically normal brain structures such as the pituitary gland,[48] falx cerebri, and some blood vessels. It is also effective as a high-contrast marker of pathologic changes of the brain, which is especially useful for the diagnosis of brain tumours.[1,2,4-6,9,10,12-14,16,18,20,22,24-26,28-31,33] However, even after administration of contrast, a number of intracranial mass lesions may not be detectable by means of CT, probably because of their diffuse distribution, similar attenuation to surrounding tissue, and minimal or absent contrast enhancement.[15]

It is known that magnetic resonance imaging (MR) provides superior soft tissue detail, compared with that achieved by CT, and allows visualization of subtle changes that accompany diffuse brain lesions that are not easily detected via CT.[15] Also, MR is preferred for imaging structures at the caudal cerebral fossa because these are frequently poorly defined on CT images; this is caused by streak artefacts that are a result of beam hardening in this region.[11] The multiplanar imaging capability of MR permits a better definition of the anatomic relationship of an intracranial lesion and surrounding unaffected structures.[15] However, by use of advanced computer software, it is possible to use original display data to reform CT images in dorsal and sagittal planes,[44] thereby obtaining a 3-dimensional presentation of anatomic features. Visualization of specific morphologic components can be optimized in these multiplanar CT images by varying the CT window and level settings. The combination of multiplanar imaging and selective viewing constitute a unique and flexible means of brain imaging in dogs.[44] If MR is not available, CT is an extremely useful diagnostic procedure in dogs in which intracranial disease is suspected. Because a thorough knowledge of the anatomic features of the brain in clinically normal dogs is a prerequisite for accurate interpretation of CT images in which pathologic changes may be evident, the comprehensive iconography provided in the present study may be a useful tool for diagnosis of neuropathologic conditions of the brains of dogs.

[a] Thalamonal, Janssen Pharmaceutics NV, Beerse, Belgium.
[b] Pentothal, Abott Laboratories, North Chicago, Ill.
[c] Fluothane, AstraZeneca, Wilmington, Del.
[d] CT-scanner Pace Plus, GE Medical Systems, Milkauwee, Wis.
[e] Omnipaque, Nycomed, Brussels, Belgium.
[f] X-ray film, Fuji Photo Film Co, Tokyo, Japan.
[g] T-61, Hoechst Roussel Vet GmbH, Unterschleiβheim, Germany.

REFERENCES

1. Adamo P, Clinkscales J. Cerebellar meningioma with paradoxical vestibular signs. Prog in Vet Neuro 1991;2:137-142.

2. Bergman R, Jones J, Lanz O, et al. Post-operative computed tomography in two dogs with cerebral meningioma. Vet Radiol Ultrasound 2000;41:425-432.

3. Brunetti A, Fatone G, Cuomo A, et al. Meningomyelocele and hydrocephalus in a Bulldog. Prog in Vet Neuro 1993;4:54-59.

4. Ducoté J, Johnson K, Dewey C, et al. Computed tomography of necrotizing meningoencephalitis in 3 Yorkshire Terriers. Vet Radiol Ultrasound 1999;40:617-621.

5. Fike J, LeCouteur R, Cann C, et al. Computerized tomography of brain tumors of the rostral and middle fossas in the dog. Am J Vet Res 1981;42:275-281.

6. Fike J, Cann C, Turowski K, et al. Differentiation of neoplastic from non-neoplastic lesions in dog brain using quantitative CT. Vet Radiol 1986;27:121-128.

7. Gerros T, Mattoon J, Snyder S. Use of tomography in the diagnosis of cerebral abscess in a goat. Vet Radiol Ultrasound 1998;39:322-324.

8. Gonzalo-Orden J, Diez A, Altonaga J, et al. Computed tomographic findings in ovine coenurosis. Vet Radiol Ultrasound 1999;40:441-444.

9. Hause W, Helphrey M, Green R, et al. Cerebral arteriovenous malformation in a dog. J Am Anim Hosp Assoc 1982;18:601-607.

10. Iwamoto K, Norman A, Freshwater D, et al. Diagnosis and treatment of spontaneous canine brain tumors with a CT scanner. Radiother Oncol 1993;26:76-78.

11. Jeffery N, Thakkar C, Yarrow T. Introduction to computed tomography of the canine brain. J Small Anim Pract 1992;33:2-10.

12. Lang J, Huber P, Vandevelde M. Erfahrungen mit der Computertomographie in der Kleintierneurologie. Schweiz Arch Tierheilk 1988;130:167-183.

13. LeCouteur R, Fike J, Cann C, et al. Computed tomography of brain tumors in the caudal fossa of the dog. Vet Radiol 1981;22:244-251.

14. LeCouteur R, Fike J, Cann C, et al. X-ray computed tomography of brain tumors in cats. J Am Vet Med Assoc 1983;183:301-305.

15. LeCouteur R. Current concepts in the diagnosis and treatment of brain tumours in dogs and cats. J Small Anim Pract 1999;40:411-416.

16. Morozumi M, Sasaki N, Oyama Y, et al. Computed tomography and magnetic resonance findings of meningeal syndrome in a leukemic cat. J Vet Med Sci 1993;55:1035-1037.

17. Morozumi M, Miyahara K, Sato M, et al. Computed tomography and magnetic resonance findings in two dogs and a cat with intracranial lesions. J Vet Med Sci 1997;59:807-810.

18. Norton F. Cerebral infarction in a dog. Prog in Vet Neuro 1992;3:120-125.

19. Nykamp S, Scrivani P, de Lahunta A, et al. Chronic subdural hematomas and hydrocephalus in a dog. Vet Radiol Ultrasound 2001;42:511-514.

20. Plummer S, Wheeler S, Thrall D, et al. Computed tomography of primary inflammatory brain disorders in dogs and cats. Vet Radiol Ultrasound 1992;33:307-312.

21. Regnier A, Ducos de Lahitte M, Delisle M, et al. Dandy-Walker syndrome in a kitten. J Am Anim Hosp Assoc 1993;29:514-518.

22. Speciale J, Van Winkle T, Steinberg S, et al. Computed tomography in the diagnosis of focal granulomatous meningoencephalitis: retrospective evaluation of three cases. J Am Anim Hosp Assoc 1992;28:327-332.

23. Swengel J. Computerized tomography for diagnosis of brain tumor in a dog. J Am Vet Med Assoc 1982;184:605.

24. Tidwell A, Mahony O, Moore R, et al. Computed tomography of an acute hemorrhagic cerebral infarct in a dog. Vet Radiol Ultrasound 1994;35:290-296.

25. Tipold A, Tipold E. Computertomographische Untersuchungen des Zentralnervensystems bei Kleintieren. Tierärztl Prax 1991;19:183-191.

26. Turrel J, Fike J, LeCouteur R, et al. Computed tomographic characteristics of primary brain tumors in 50 dogs. J Am Vet Med Assoc 1986;188:851-856.

27. Van Bree H. Visual diagnosis of the brain in the aging dog. Prakt -Tierarzt 2003;84:196-199.

28. Vernau K, Kortz G, Koblik P, et al. Magnetic resonance imaging and computed tomography characteristics of intracranial intra-arachnoid cysts in 6 dogs. Vet Radiol Ultrasound 1997;38:171-176.

29. Vink-Nooteboom M, Junker K, Van den Ingh T, et al. Computed tomography of cholesterinic granulomas in the choroid plexus of horses. Vet Radiol Ultrasound 1998;39:512-516.

30. Wolf M, Pedroia V, Higgings R, et al. Intracranial ring enhancing lesions in a dog: a correlative CT scanning and neuropathologic study. Vet Radiol Ultrasound 1995;36:16-20.

31. Woods J, Cuddon P, Schenkman D. Prefrontal cortical and diencephalic cavernous hemangioma in a dog. Prog in Vet Neuro 1992;3:126-130.

32. Woods P, Walker M, Weir V, et al. Computed tomography of Rambouillet sheep affected with neuronal ceroid lipofuscinosis. Vet Radiol Ultrasound 1993;4:259-262.

33. Moreau P, Moreau J-J, Desnoyer P. Presurgical use of computed tomography in a dog. Comp Contin Educ Pract Vet 1989;11:159-164,168.

34. Anor S, Sturges B, Lafranco L, et al. Systemic phaeohyphomycosis (cladophialophora bantiana) in a dog – clinical diagnosis with stereotactic computed tomographic-guided brain biopsy. J Vet Int Med 2001;15:257-261.

35. Giroux A, Jones J, Bohn J, et al. A new device for stereotactic CT-guided biopsy of the canine brain : design, construction, and needle placement accuracy. Vet Radiol Ultrasound 2002;43:229-236.

36. Harari J, Moore M, Leathers C et al. Computed tomographic-guided free-hand needle biopsy of brain tumors in dogs. Prog in Vet Neuro 1993;4:41-44.

37. Koblik P, LeCouteur R, Higgins R, et al. Modification and application of a Pelorus Mark III Stereotactic System for CT-guided brain biopsy in 50 dogs. Vet Radiol Ultrasound 1999;40:424-433.

38. Koblik P, LeCouteur R, Higgins R, et al. CT-guided brain biopsy using a modified Pelorus Mark III Stereotactic System: experience with 50 dogs. Vet Radiol Ultrasound 1999;40:434-440.

39. Moissonnier P, Bordeau W, Delisle F, et al. Accuracy testing of a new stereotactic CT-guided brain biopsy device in the dog. Res Vet Sci 2000;68:243-247.

40. Moissonnier P, Blot S, Devauchelle P, et al. Stereotactic CT-guided brain biopsy in the dog. J Small Anim Pract 2002;43:115-123.

41. Assheuer J, Sager M. Head. In: Assheuer J, Sager M, eds. MRI and CT atlas of the dog. Berlin: Blackwell Science, 1997;1-81.

42. Drost W, Berry C, Fischer P. Computed tomographic appearance of a normal variant of the canine tentorium cerebelli osseum. Vet Radiol Ultrasound 1996;37:351-353.

43. Feeney D, Fletcher T, Hardy R. Atlas of correlative imaging anatomy of the normal dog. Ultrasound and computed tomography. Philadelphia: WB Saunders Co, 1991.

44. Fike J, LeCouteur R, Cann C. Anatomy of the canine brain using high resolution computed tomography. Vet Radiol 1981;22:236-243.

45. George T, Smallwood J. Anatomic atlas for computed tomography in the mesaticephalic dog : head and neck. Vet Radiol Ultrasound 1992;33:217-240.

46. Hathcock J, Pugh D, Cartee R, et al. Computed tomography of the llama head: technique and normal anatomy. Vet Radiol Ultrasound 1995;36:290-296.

47. Legrand J, Carlier B. Examen tomodensitométrique de l’encéphale du chien I. Conduite de l’examen et repères anatomiques. Revue Méd Vét 1999 ;137 :193-196.

48. Love N, Fisher P, Hudson L. The computed tomographic enhancement pattern of the normal canine pituitary gland. Vet Radiol Ultrasound 2000;41:507-510.

49. Zook B, Hitzelberg R, Fike J, et al. Anatomy of the Beagle in cross-section: Head and neck. Am J Vet Res 1981;42:844-849.

50. Done S, Goody P, Evans S, et al. The head. In: Done S, Goody P, Evans S, et al. eds. *Color Atlas of Veterinary Anatomy, Volume 3*. London: Mosby, 1999;2.78-2.81.

51. Popesco P. Volume I Head and neck. In: Atlas of Topographical Anatomy of the Domestic Animals. Philadelphia:WB Saunders Co, 1977.

52. World Association of Veterinary Anatomists (WAVA). Nomina Anatomica Veterinaria. 4th ed. Ithaca, NY: International Committee on Veterinary Gross Anatomical Nomenclature, 1994;1-198.

1.1.2. Magnetic Resonance imaging of the Normal Canine Brain

Lieve M. De Rycke, DVM

Department of Medical Imaging, Faculty of Veterinary Medicine,
Ghent University, Salisburylaan 133, 9820 Merelbeke, Belgium

SUMMARY

Objective—To provide a detailed anatomic description of brain structures in clinically normal dogs by means of magnetic resonance imaging (MR).

Animals—1 clinically normal adult German Shepherd Dog weighing 30 kg.

Procedure—Immediately after the CT examination of the brain *(see chapter 1.1.1.)* and under the same anesthesia, MR of the brain was performed in one of the German shepherd dogs. The animal was kept in the same position as used on the CT scanning table (dorsal recumbency with the forelimbs extended caudally). Transversal T1-weighted weighted (repetition time (TR) = 498msec, echogenicity time (TE) = 14msec) and T2-weighted images (TR = 7820msec, TE = 104msec) were obtained with a slice thickness of 4 mm, extending from the cribriform plate of the ethmoid bone to the cranial part of the atlas and perpendicular to the hard palate, on a 1.5 closed Tesla MR unit [a]. For this study only the T1-weighted images were used as a good anatomical resolution was most important. After euthanasia, anatomic sections were performed *(see chapter 1.1.1)* and compared with the corresponding MR views. Subsequently the CT images of the previous study *(chapter 1.1.1)* were compared to the MR images.

Results— A lot of brain structures that were visible on the anatomic sections could be identified on the MR images. When comparing the MR images of the brain with the corresponding CT images *(Figure 2, chapter 1.1.1)*, all brain structures and surrounding soft tissue structures identified on the CT images could be much better visualized on the MR images and several additional brain structures were located on the MR images. Only the bony structures of the skull were more distinct on the CT images compared to the MR images.

Conclusions and Clinical Relevance— MR is a non-invasive technique that provides anatomic detail of numerous structures of the canine brain. These results could be used as a basis for evaluation of MR images of the brain of dogs with pathologies of the CNS.

INTRODUCTION

In humans, MR is frequently used for imaging the CNS. This technique has the ability to produce high-detail, high-contrast, two-dimensional grayscale images of the brain, on a non-invasive way and without ionising forms of electromagnetic energy. Consequently, the complex anatomy of the head and brain is better defined with MR than with conventional radiology, scintigraphy or computed tomography (CT)[1]. The superior contrast resolution of soft tissue provided by MR facilitates diagnosis of many CNS lesions, including tumors and other degenerative abnormalities[1].

MR has been increasingly used in veterinary medicine during the last decade. The majority of publications on MR of the brain concern clinical reports of dogs and cats with neurologic disease[2-33], and MR studies of brain structures such as the ventricles[34-39] and the pituitary gland[40].
A few publications on MR anatomy of the normal brain are available. One paper reports the MR of the brain of normal neonatal foals[1] and two others describe the MR of the normal feline brain[41,42]. MR anatomy of the canine brain has been described by one research team[43] and an atlas of MR of the dog has recently been published[44]. However, to date a detailed comparative study using gross anatomic sections to identify all structures visible on MR images of the canine brain has not been reported. Knowledge of normal MR anatomy of the canine brain is a prerequisite for MR diagnosis of abnormalities.
The purpose of this study was to determine normal canine MR neuroanatomy and to make a comparison with corresponding CT images *(Figure 2, chapter 1.1.1).*

MATERIAL AND METHODS

Immediately after the CT examination of the brain *(see chapter 1.1.1.)* and under the same anesthesia, MR of the brain was performed in one of the German shepherd dogs used in the previous study. The animal was kept in the same position as used on the CT scanning table (dorsal recumbency with the forelimbs extended caudally). Transverse T1-weighted weighted (repetition time (TR) = 498msec, echogenicity time (TE) = 14msec) and T2-weighted images (TR = 7820msec, TE = 104msec) were obtained with a slice thickness of 4 mm, extending from the cribriform plate of the ethmoid bone to the cranial part of the atlas and perpendicular to the hard palate, on a 1.5 closed Tesla MR unit [a]. Acquisition matrix was 256 x 256. For this study only the T1-weighted images were used as a good anatomical resolution was most important.

The anatomical sections of the brain *(see chapter 1.1.1.)* were compared with the corresponding transverse MR images. From the collection of matched MR and anatomical images, 13 representative pairs were selected from the rostral to the caudal regions of the brain *(Figure 2 chapter 1.1.1).* The structures identified on the anatomical sections *(see chapter 1.1.1)* were subsequently located on the corresponding MR images.
Afterwards a comparison with the corresponding CT images of the brain was made.

RESULTS

Most of the brain structures that were visible on the anatomic sections could be identified on the MR images, except for some parts of the diencephalon such as the epiphysis, hypophysis with infundibulum and the mamillary body, probably because these structures were not present in one of the sections. The mesencephalic red nucleus and substantia nigra could not been located on the T1-weighted MR images, neither the cerebellar white matter.
When comparing the MR images of the brain with the corresponding CT images *(Figure 2 chapter 1.1.1),* all brain structures and surrounding soft tissue structures identified on the CT images could be much better visualized on the MR images. Moreover several brain structures such as the internal capsule, optic tract, hippocampal gyrus, rostral and caudal collicle, interpeduncular fossa, brachium of the pons, median ventral fissure, floccular lobe, pyramid of the medulla oblongata and the choroid plexuses of the fourth and lateral ventricles could easily be located on the MR images and were unidentifiable on the CT images. Only the bony structures of the skull especially foramina, fossae, canals and the chiasmatic sulcus, were more distinct on the CT images compared to the MR images.

These results are listed in Table 1.

TABLE 1	CT	MR
Intracranial structures		
* = Subarachnoidal space.	+	+
2 = Brachium of pons (middle cerebellar peduncle).	--	+
6 = Caudal collicle.	--	+
7 = Caudate nucleus.	+	+
8 = Central canal.	--	N
9 = Cerebellar hemisphere.	+	+
10 = Cerebellar vermis.	+	+
11 = Cerebellar white matter.	--	--
12 = Cerebral hemisphere.	+	+
13 = Cerebral peduncle.	+	+
15 = Choroid plexus of the fourth ventricle.	--	+
16 = Choroid plexus of the lateral ventricle.	--	+
18 = Corpus callosum.	+	+
21 = Epiphysis (pineal gland).	--	--
24 = Falx cerebri.	+	+
25 = Floccular lobe.	--	+
27 = Fornix.	+	+
28 = Fourth ventricle.	+	+
30 = Frontal lobe.	+	+
33 = Hippocampal gyrus.	--	+
34 = Hippocampal sulcus.	+	+
35 = Hippocampus.	+	+
39 = Hypophysis (pituitary gland).	+	--
40 = Hypothalamus.	+	+
41 = Infundibular recess.	+	+
42 = Infundibulum.	--	--
45 = Internal capsule.	--	+
48 = Interpeduncular fossa.	--	+
49 = Interthalamic adhesion.	+	+
52 = Lateral geniculate body.	+	+
53 = Lateral ventricle.	+	+
54 = Longitudinal cerebral fissure.	+	+
55 = Mamillary body.	+	--
61 = Medial geniculate body.	+	+
62 = Median ventral fissure.	--	+
63 = Medulla oblongata.	+	+
64 = Mesencephalic aqueduct.	+	+
65 = Mesencephalic tectum.	+	+
71 = Occipital lobe.	+	+
72 = Olfactory bulb.	+	+
73 = Olfactory peduncle.	+	+
74 = Olfactory tract (lateral).	+	+
76 = Optic chiasm.	+	+
78 = Optic tract.	--	+
83 = Parietal lobe.	+	+
86 = Piriform lobe.	+	+
87 = Pons.	+	+
91 = Pyramid of medulla oblongata.	--	+
92 = Red nucleus.	--	--
95 = Rhomboid fossa.	+	+
97 = Rostral collicle.	--	+
98 = Rostral commissure.	+	+
101 = Septum pellucidum including nuclei septi (septal nuclei).	+	+

TABLE 1	CT	MR
105 = Substantia nigra.	--	--
109 = Temporal lobe.	+	+
112 = Thalamus.	+	+
113 = Third ventricle.	+	+
115 = Transverse cerebral fissure.	+	+
Bony structures		
1 = Basisphenoid bone.	+	+
3 = Canal of transverse sinus.	+	--
4 = Canal of trigeminal nerve.	+	--
5 = Carotid canal.	+	--
5’ = Carotid fossa	--	+
14 = Chiasmatic sulcus.	+	--
17 = Condylar canal.	+	--
20 = Dorsum sellae turcicae.	+	+
22 = External acoustic meatus.	+	+
23 = External occipital crest.	+	+
26 = Foramen magnum.	+	N
29 = Frontal bone.	+	+
31 = Frontal sinus.	+	+
32 = Hamulus of the pterygoid bone.	+	--
36 = Hyoid bone.	+	--
37 = Hypoglossal canal.	+	--
38 = Hypophyseal fossa.	+	--
43 = Internal acoustic pore.	+	--
44 = Cochlea.	+	--
47 = Interparietal bone.	+	+
50 = Jugular foramen.	+	--
51 = Jugular (paracondylar) process.	+	--
56 = Mandible.	+	+
66 = Muscular tubercle.	+	+
68 = Nuchal tubercle.	+	N
69 = Occipital bone.	+	+
70 = Occipital condyle.	+	N
75 = Optic canal.	+	+
79 = Orbital fissure.	+	--
80 = Osseous tentorium cerebelli.	+	+
81 = Oval foramen.	+	--
82 = Parietal bone.	+	+
84 = Petrosal crest of the temporal bone.	+	+
88 = Presphenoid bone.	+	+
89 = Pterygoid bone.	+	+
94 = Retroarticular process.	+	+
99 = Round foramen (foramen rotundum).	+	+
99’ = Canalis alaris.	+	--
100 = Septum of frontal sinuses.	+	+
103 = Sphenoid bone (=1+88).	+	+
103’ = Sphenoid bone cavity.	+	+
104 = Stylomastoid foramen.	+	--
107 = Temporal bone.	+	+
108 = Temporal line.	+	+
110 = Temporal meatus.	+	--
116 = Tympanic cavity.	+	+
117 = Zygomatic arch.	+	+

TABLE 1	CT	MR
Structures outside the cranial cavity		
18’ = Cranial cervical ganglion.	--	+
19 = Deep lingual artery and vein.	+	+
22’ = Parotid salivary gland .	--	+
46 = Internal carotid artery.	+	+
46’ = External carotid artery.	--	+
56’ = Mandibular lymphnodes	--	+
56’’ = Mandibular salivary gland	--	+
57 = Mandibular nerve.	+	+
58 = Masseter muscle.	+	+
58’ = Digastric muscle	--	+
59 = Maxillary artery.	+	+
59’ = Maxillary vein.	+	+
60 = Maxillary nerve.	+	+
67 = Nasopharyngeal cavity.	+	+
67’ = Epiglottis	--	+
69’ = Longus capitis muscle	+	+
77 = Optic nerve.	+	+
85 = Pharyngeal cavity.	+	+
90 = Pterygoid muscles (90’= lateral, 90’’ = medial).	+	+
93 = Retractor bulbi muscle.	+	+
96 = Root of tongue.	+	+
102 = Soft palate.	+	+
102’ = Palatine tonsil.	--	+
106 = Superficial temporal artery and vein.	+	+
111 = Temporal muscle.	+	+
114 = Tracheotube.	+	N

TABLE 1 : Structures of the canine brain and surrounding structures visible on CT and MR scans

+ = identified, -- = not identified, N = not present on the figures

CONCLUSIONS

MR is a non-invasive technique that provides anatomic detail of numerous structures of the canine brain. The surrounding soft tissue structures of the head such as the muscles, blood vessels and some nerves are also distinct and can easily be identified. On the T1-weighted images fat tissue and bone marrow generate a high signal, wheras muscle and other soft tissue (glands, nerves, brain-parenchyma) demonstrate an intermediate signal. The white matter signal is slightly more hyperintense compared to the signal of the grey matter. Vascular structures, CSF and air show a signal void. Only the bony structures of the skull, which show a signal void on MR images, could be better visualized on the CT images.

The conclusion is that MR provides more details of the brain parenchyma, especially at the caudal cerebral fossa, than CT. Therefore it is the technique of preference in case of brain pathologies. Only if MR is not available, CT can be of useful when intracranial disease is suspected.

These results could be used as a basis for evaluation of MR images of the brain of dogs with pathologies of the CNS.

[a] Symphony, Siemens A.G., Erlangen, Germany

REFERENCES

1. Chaffin K, Walker M, McArthur N, et al. Magnetic resonance imaging of the brain of normal neonatal foals. Vet Radiol Ultrasound 1997;38:102-111.

2. Bertroy E, Feldman E, Nelson R, et al. Magnetic resonance imaging of the brain in dogs with recently diagnosed but untreated pituitary-dependent hyperadrenocorticism. J Am Vet Med Assoc 1995;206:651-656.

3. Buback J, Schulz K, Walker M, et al. Magnetic resonance imaging of the brain for diagnosis of neurocysticercosis in a dog. J Am Vet Med Assoc 1996;208:1846-1848.

4. Duesburg C, Feldman E, Nelson R, et al. Magnetic resonance imaging for diagnosis of pituitary macro-tumors in dogs. J Am Vet Med Assoc 1995;206:657-662.

5. Fransson B, Kippenes H, Silver G, et al. Magnetic resonance diagnosis: cavernous sinus syndrome in a dog. Vet Radiol Ultrasound 2000;41:536-538.

6. Graham J, Newell S, Voges A, et al. The dural tail sign in the diagnosis of meningiomas. Vet Radiol Ultrasound;1998:39:297-302.

7. Hammer A, Cuoto C, Getzy D. Magnetic resonance imaging in a dog with a choroid plexus carcinoma. J Small Anim Pract 1990;31:341-344.

8. Hathcock J. Low field magnetic resonance imaging characteristics of cranial vault meningiomas in 13 dogs. Vet Radiol Ultrasound 1996:37:257-263.

9. Kärkäinen M, Mero M, Nummi P, et al. Low field magnetic resonance imaging of the canine central nervous system. Vet Radiol 1991;32:71-74.

10. Kärkkäinen M. Low- and high-field strength magnetic resonance imaging to evaluate the brain in one normal dog and two dogs with central nervous system disease. Vet Radiol Ultrasound 1995;36:528-532.

11. Kent M, Delahunta A, Tidwell A. MR imaging findings in a dog with intravascular lymphoma in the brain. Vet Radiol Ultrasound 2001;42:504-510.

12. Klopp L, Hathcock J, Sorjonen D. Magnetic resonance imaging features of brain stem abscessation in two cats. Vet Radiol Ultrasound 2000;41:300-307.

13. Kraft S, Gavin P, Moore M, et al. An MR diagnosis of canine meningioma. Vet Radiol 1990;31:65-67.

14. Kraft S, Gavin P, DeHaan C, et al. Retrospective review of 50 canine intracranial tumors evaluated by magnetic resonance imaging. J Vet Intern Med 1997;11:218-225.

15. Lipsitz D, Levitski R, Chauvet A. Magnetic resonance imaging of a choroid plexus carcinoma and meningeal carcinomatosis in a dog. Vet Radiol Ultrasound 1999;40:246-250.

16. Lobetti R, Rearson J. Magnetic resonance imaging in the diagnosis of focal granulomatous meningoencephalitis in two dogs. Vet Radiol Ultrasound 1996;37:424-427.

17. Lotti D, Capucchio MT, Gaidolfi E, et al. Necrotizing encephalitis in a Yorkshire terrier: clinical, imaging, and pathologic findings. Vet Radiol Ultrasound 1999;40:622-626.

18. Mariani C, Platt S, Newell S, et al. Magnetic resonance imaging of cerebral cortical necrosis (polioencephalomalacia) in a dog. Vet Radiol Ultrasound 2001;42:524-531.

19. Mellema L, Koblik P, Kortz G, et al. Reversible magnetic resonance imaging abnormalities in dogs following seizures. Vet Radiol Ultrasound 1999;40:588-595.

20. Mellema L, Samii V, Vernau K, et al. Meningeal enhancement on magnetic resonance imaging in 15 dogs and 3 cats. Vet Radiol Ultrasound 2002;43:10-15.

21. Millner R, Engela J, Kirberger R. Arachnoid cyst in cerebellar pontine area of a cat- diagnosis by magnetic resonance imaging. Vet Radiol Ultrasound 1996;37:34-36.

22. Morozumi M, Sasaki N, Oyama Y, et al. Computed tomography and magnetic resonance fidings of meningeal syndrome in a leukemic cat. J Vet Med Sci 1993;55:1035-1037.

23. Morozumi M, Miyahara K, Sato M, et al. Computed tomography and magnetic resonance findings in two dogs and one cat with intracranial lesions. J Vet Med Sci 1997;59:807-810.

24. Panciera D, Duncan I, Messing A, et al. Magnetic resonance imaging in two dogs with central nervous system disease. J Small Anim Pract 1987;28:587-596.

25. Platt S, Graham J, Chrisman C, et al. Canine intracranial epidermoid cyst. Vet Radiol Ultrasound 1999;40:454-458.

26. Sato M, Sharp N, de Lahunta A, et al. Magnetic resonance imaging features of lissencephaly in 2 Lhasa Apsos. Vet Radiol Ultrasound 2002;43:331-337.

27. Saunders J, Poncelet L, Clercx C, et al. Probable trigeminal nerve schwannoma in a dog. Vet Radiol Ultrasound 1998;39:539-542.

28. Seiler G, Cizinauskas S, Scheidegger J, et al. Low-field magnetic resonance imaging of a pyocephalus and a suspected brain abscess in a German Shepherd dog. Vet Radiol Ultrasound 2001;42:417-422.

29. Stewart W, Parent J, Towner R, et al. The use of MRI in the diagnosis of neurologic diseases. Can Vet J 1992;33:585-590.

30. Targett M, McInnes E, Dennis R, et al. Magnetic resonance imaging of a medullary dermoid cyst with secondary hydrocephalus in a dog. Vet Radiol Ultrasound 1998;40:23-26.

31. Thomas W, Wheeler S, Kramer R, et al. Magnetic resonance imaging features of primary brain tumors in dogs. Vet Radiol Ultrasound 1996;37:20-27.

32. Thomas W, Adams W, McGavin D, et al. Magnetic resonance imaging appearance of intracranial hemorrhage secondary to cerebral vascular malformation in a dog. Vet Radiol Ultrasound 1997;38:371-375.

33. Thomson C, Kornegay J, Burn R, et al. Magnetic resonance imaging - a general overview of principles and examples in veterinary neurodiagnosis. Vet Radiol Ultrasound 1993;34:2-17.

34. De Haan C, Kraft S, Gavin P, et al. Normal variation in size of lateral ventricles of the Labrador retriever dog as assessed by magnetic resonance imaging. Vet Radiol Ultrasound 1994;35:83-86.

35. Esteve-Ratsch B, Kneissl S, Gabler C. Comparative evaluation of the ventricles in the Yorkshire Terrier and the German shepherd dog using low-fields MRI. Vet Radiol Ultrasound 2001;42:410-413.

36. Kii S, Uzuka Y, Taura Y, et al. Magnetic resonance imaging of the lateral ventricles in Beagle-type dogs. Vet Radiol Ultrasound 1997;38:430-433.

37. Kii S, Taura Y, Nakaichi M, et al. Developmental change of lateral ventricular volume and ratio in Beagle-type dogs up to 7 months of age. Vet Radiol Ultrasound 1998;39:185-189.

38. Vite C, Insko E, Schotland H, et al. Quantification of cerebral volume in English Bulldogs. Vet Radiol Ultrasound 1997;38:437-443.

39. Vullo T, Korenman E, Manzo R, et al. Diagnosis of cerebral ventriculomegaly in normal adult Beagles using quantitative MRI. Vet Radiol Ultrasound 1997;38:277-281.

40. Graham J, Roberts G, Newell S. Dynamic magnetic resonance imaging of the normal canine pituitary gland. Vet Radiol Ultrasound 2000;41:35-40.

41. Hudson L, Cauzinille L, Kornegay J, et al. Magnetic resonance imaging of the normal feline brain. Vet Radiol Ultrasound 1995;36:267-275.

42. Yamada K, Miyahara K, Sato M, et al. Magnetic resonance imaging of the central nervous system in the kitten. J Vet Med Sci 1995;57:155-156.

43. Kraft S, Gavin P, Wendling L, et al. Canine brain anatomy on magnetic resonance images. Vet Radiol Ultrasound 1998;30:147-158.

44. Assheuer J, Sager M. Head. Neurocranium. In Assheuer, Sager M, eds. MRI and CT atlas of the dog. Berlin: Blackwell Science, 1997;1-43.

1.2. The nasal cavities and frontal sinuses

1.2.1. Magnetic Resonance Imaging, Computed Tomography and Cross Sectional Anatomy of the normal Canine Nasal Cavities and Paranasal Sinuses in the mesaticephalic Dog

Lieve M. De Rycke*, DVM; Jimmy H. Saunders*, DVM; Ingrid M. Gielen*, DVM, MSc;
Henri J. van Bree*, DVM, PhD; Paul J. Simoens**, DVM, PhD

*Department of Medical Imaging, Faculty of Veterinary Medicine,
Ghent University, Salisburylaan 133, 9820 Merelbeke, Belgium

**Department of Morphology, Faculty of Veterinary Medicine,
Ghent University, Salisburylaan 133, 9820 Merelbeke, Belgium

Adapted from :

De Rycke LM, Saunders JH, Gielen IM, van Bree H, Simoens PJ. Magnetic Resonance Imaging, Computed Tomography and Cross Sectional Anatomy of the normal Canine Nasal Cavities and Paranasal Sinuses in the mesaticephalic Dog. *Am J Vet Res* 2003;64:1093-1098.

SUMMARY

Objective- To use computed tomography (CT) and magnetic resonance imaging (MR) to provide a detailed description of the nasal cavities and paranasal sinuses in clinically normal mesaticephalic dogs.

Animals- Two clinically normal Belgian Shepherd dogs weighing 25 and 35 kg, respectively.

Procedure- The first dog was anesthetized and positioned in ventral recumbency for CT and MR examinations, and transverse slices were obtained from the caudal part of the frontal sinuses to the nares. For MR, T1-weighted, T2-weighted and proton density sequences were obtained. The second dog was anesthetized and positioned in dorsal recumbency with the head perpendicular to the table, and CT and MR examinations were again conducted. At the completion of the MR examination, each dog received an intravenous (IV) injection of heparin and then was euthanatized. A 4% solution of formaldehyde was perfused IV immediately after each dog was euthanized. The skull was prepared, decalcified, embedded with gelatine, and sectioned into 5-mm-thick sections by use of a stainless steel knife. Each anatomic section was photographed and compared with the corresponding CT and MR views.

Results- Structures on the CT and MR views matched with structures on the corresponding anatomic sections. The CT scans provided good anatomic detail of the bony tissues, and MR scans were superior to CT scans for determining soft tissue structures.

Conclusions and Clinical Relevance- CT and MR provide a means for consistent evaluation of all structures of the nasal cavities and frontal sinuses. Both techniques could be useful for evaluation of diseases that affect the nasal region such as fungal rhinitis, nasal tumors, non-specific rhinitis and foreign body rhinitis.

INTRODUCTION

Computed tomography (CT) and magnetic resonance imaging (MR) are reliable noninvasive techniques for use in the diagnosis of nasal diseases in dogs.[1,2] These techniques have been used in dogs with fungal rhinitis, nasal tumors, non-specific rhinitis and foreign body rhinitis.[1-9,a]

CT and MR are superior to radiography for defining the extent and character of lesions in the nasal cavities.[3,6,8,10-12] In addition, these techniques are also useful for staging of tumors and during planning for surgery and radiation treatments; they also have a prognostic value in dogs with nasal aspergillosis. [5,13-15]

In the veterinary literature, there is paucity of publications on the use of CT and MR for determining anatomy of the head of animals. In one report,[16] CTscans of the normal nasal cavities and paranasal sinuses of cats were described, whereas MR views and the cross sectional anatomic features of the normal sinuses and nasal passages of horses were reported in another study.[17] CT scans of the anatomy of the head of dogs have been described[18-23] and an atlas of MR and CT views of dogs has been published[24]. However, to our knowledge, a detailed comparative study of gross anatomic sections to identify all structures visible on CT and MR scans of the nasal cavities and paranasal sinuses of dogs has not been conducted.

Thus, the objective of this study was to provide a comprehensive atlas of the normal nasal cavities and paranasal sinuses in dogs by use of CT and MR.

MATERIAL AND METHODS

Animals - Two healthy Belgian Shepherd Dogs that weighed 25 and 35 kg, respectively, were used in the study. Neither dog had a history of nasal disease, and pathologic conditions were not detected during physical and radiographic examinations. Four radiographic images were obtained for each dog (dorsoventral and lateral radiographs of the entire skull, dorsoventral intraoral radiograph of the nasal cavities and maxilla, and rostrocaudal radiograph of the frontal sinuses).

CT and MR– Dogs were sedated by IV administration of fentanyl (0.005 to 0.01 mg/kg) and droperidol[b] (0.25 to 0.5 mg/kg) Anesthesia was induced by IV administration of thiopental sodium[c]

(8 mg/kg). Dogs were intubated and anesthesia was maintained by administration of halothane[d] 1.5-2%. The CT and MR examinations were then performed on the anesthetized dogs.

The first dog was positioned in ventral recumbency for CT and MR examinations, and transverse slices of the nasal cavities and paranasal sinuses were obtained. First, CT was performed by use of a third generation CT scanner[e]. Technical setttings were 120 kV and 130 mA. Five-millimeter-thick contiguous slices were obtained from the caudal aspect of the frontal sinuses to the nares and perpendicular to the length-axis (or hard palate) of the skull. Hard copies were printed[e] by use of a bone setting (window width = 3,500 Hounsfield units; window level = 500 Hounsfield units). Immediately after CT was completed, MR was performed using commercially available equipment[g]. A series of 5-mm transverse slices was obtained from the caudal aspect of the frontal sinuses to the nares. The T1-weighted (repetition time (TR) = 400msec, echogenicity time (TE) = 19msec), T2-weighted (TR = 4000msec, TE = 80msec) and proton density (TR = 4000msec, TE = 18msec) images were acquired. Acquisition matrix was 256 x 224.

The second dog was positioned in dorsal recumbency with the head perpendicular to the table; this dog was used to obtain dorsal (i.e., horizontal) images from the nasal cavities and paranasal sinuses. The same CT and MR protocol was used in both dogs.

Comparison of CT and MRI images and anatomic structures - At the completion of the MR examination, each dog was injected IV with heparin (via a cephalic vein). The dogs were then euthanatized.

A 4% solution of formaldehyde was perfused IV (via a jugular vein) immediately after each dog was euthanatized. The head of each dog was removed at the atlanto-occipital joint, and the skin of the cranium, mandibles, and temporal muscles were removed. Each skull was placed in a nitric acid solution for decalcification for 2 weeks; skulls were then embedded with gelatin. Each skull was sectioned into 5-mm- thick sections by use of a stainless steel knife. Each anatomic section was photographed and compared with the corresponding CT and MR views. From this collection, 11 (9 transverse and 2 dorsal) representative matched series of images of the nasal cavities and paranasal sinuses were selected from rostral to caudal (9) and dorsal to ventral (2) regions. Bony structures and soft tissues were identified on the anatomic sections. The identified structures were subsequently located on the corresponding CT and MR views. Nomenclature used for designating all structures was in accordance with official anatomic terms.[26]

RESULTS

Nine representative transverse planes extending from the olfactory bulb of the brain to the alar cartilage were selected in the first dog, and 2 dorsal planes of the nasal cavities were selected in the second dog (Fig 1). CT and MR (T1-weighted, T2-weighted and proton-density sequences) scans of the nasal cavities were compared with the corresponding anatomic sections (Figs. 2 and 3).

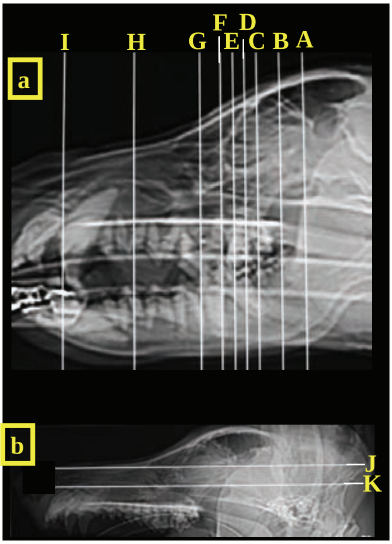

Figure 1 – Lateral computed tomography CT scans of transverse (a) and dorsal (b) views of the nasal cavities and paranasal sinuses of 2 clinically normal mesaticephalic dogs indicating the location (A through K) at which the anatomic sections, CT scans and magnetic resonance scans (MR) were obtained.

Most parts of the nasal cavities and paranasal sinuses could be identified on the anatomic sections. Several adjacent structures that remained on the skull, such as the olfactory bulb of the brain, orbits, canine teeth, nasopharynx, soft palate, salivary glands, and pterygoid muscles were quite distinct. The various facial bones that form the wall of the nasal cavities as well as the nasal conchae, septa, meatuses and all endo- and ectoturbinates could easily be identified. The medial and lateral parts of the frontal sinuses and the maxillary recess were also visible.

On the CT scans it was also possible to identify various structures of the nasal cavities and paranasal sinuses. Only the dorsal, middle and ventral nasal meati and some of the ectoturbinates could not be located. We were also less able to distinguish several surrounding soft-tissue structures on the CT scans such as the different parts of the eye, the pterygoid muscle, the zygomatic salivary gland and the falx cerebri.

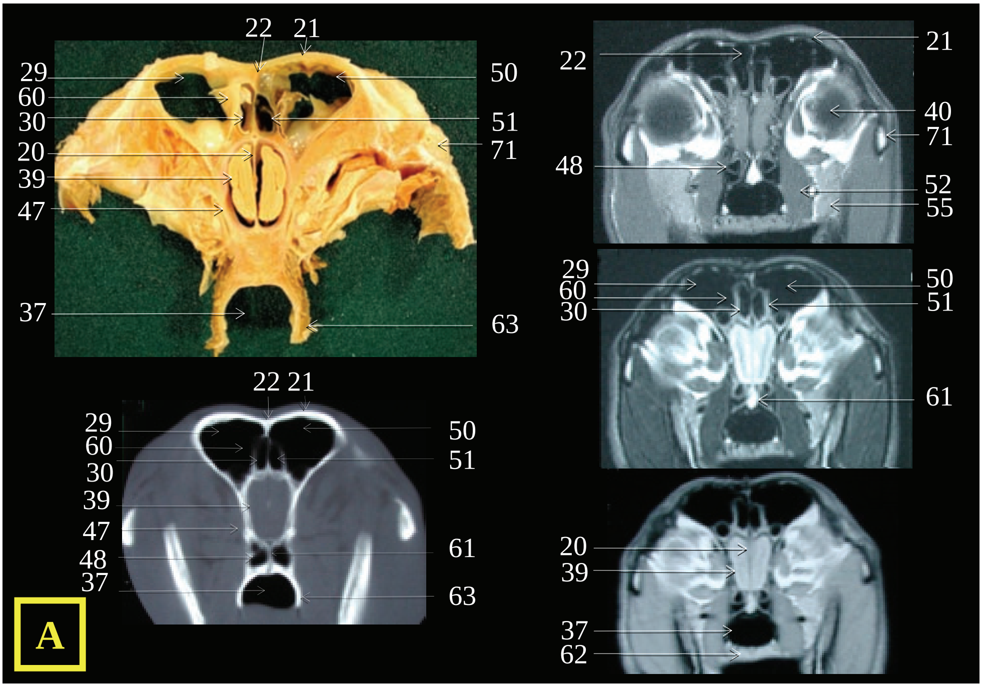
22
21
29
60
30
20
39
47
37
50
51
71
63
22 21
29
60
30
39
47
48
37
50
51
61
63
22
48
21
40
71
52
55
29
60
30
50
51
61
20
39
37
62
A

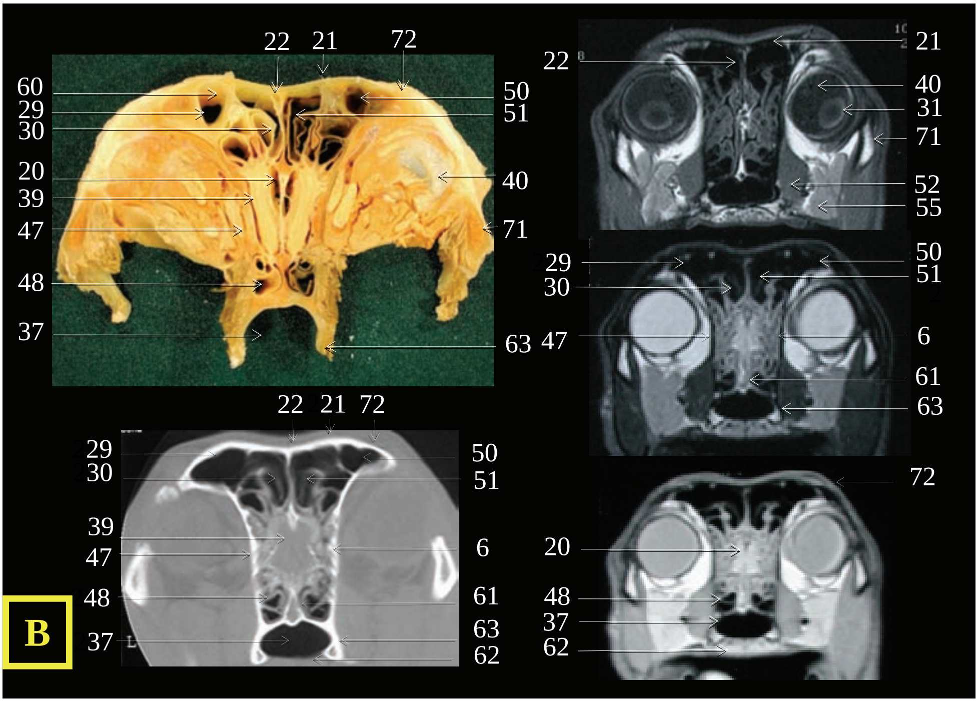
22
21
72
60
29
30
20
39
47
48
37
50
51
40
71
63
22
21
72
29
30
39
47
48
37
50
51
6
61
63
62
22
21
40
31
71
52
55
29
30
47
50
51
6
61
63
72
20
48
37
62
B

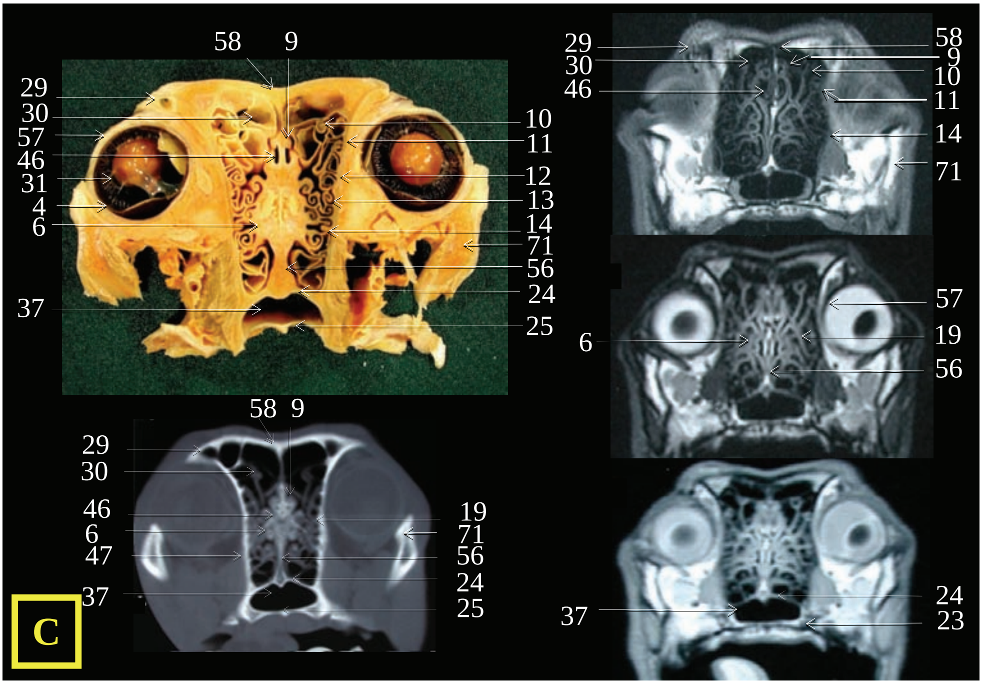
58
9
29
30
57
46
31
4
6
37
10
11
12
13
14
71
56
24
25
58 9
29
30
46
6
47
37
19
71
56
24
25
C
29
30
46
58
9
10
11
14
71
6
57
19
56
37
24
23

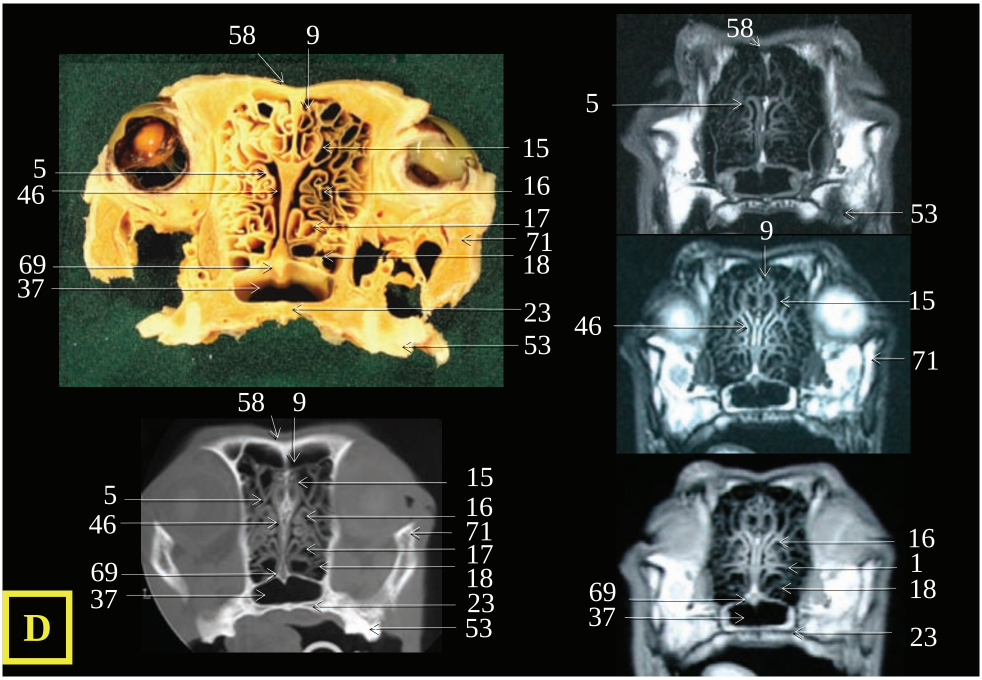
58
9
5
46
69
37
15
16
17
71
18
23
53
58 9
5
46
69
37
15
16
71
17
18
23
53
D
58
5
53
9
46
15
71
69
37
16
1
18
23

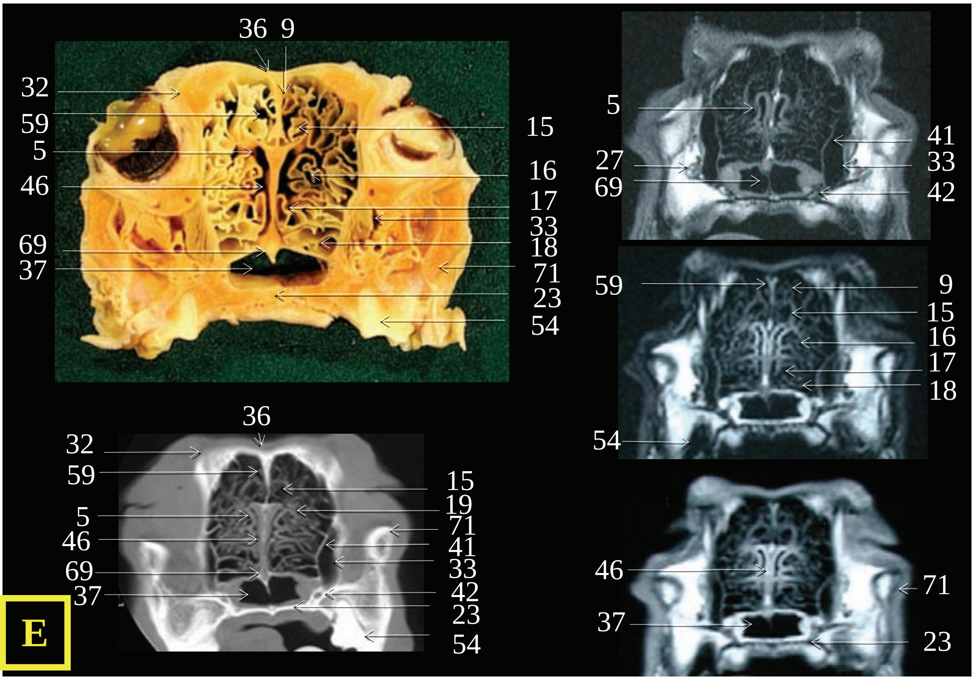
36
9
32
59
5
46
69
37
15
16
17
33
18
71
23
54
36
32
59
5
46
69
37
15
19
71
41
33
42
23
54
E
5
27
69
41
33
42
59
54
9
15
16
17
18
46
37
71
23

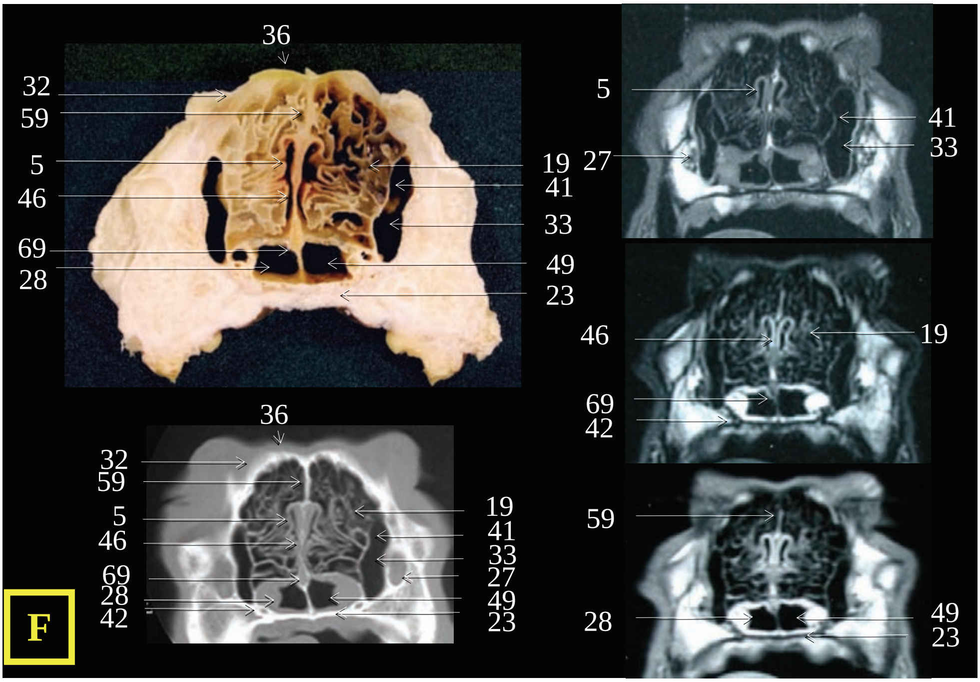
36
32
59
5
46
69
28
19
41
33
49
23
36
32
59
5
46
69
28
42
19
41
33
27
49
23
F
5
27
41
33
46
69
42
19
59
28
49
23

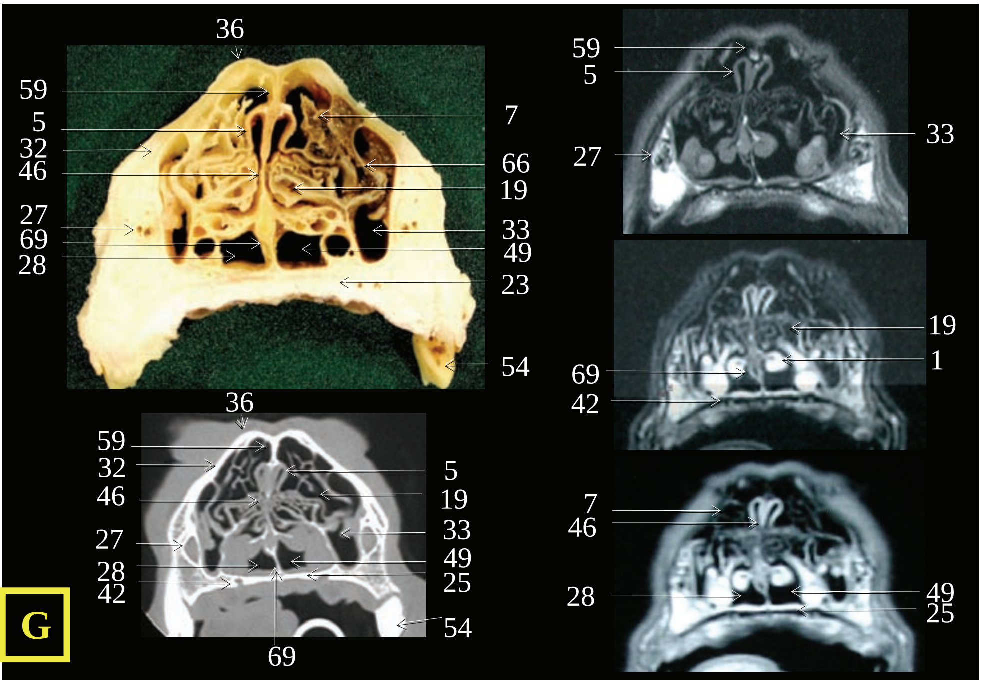
36
59
5
32
46
27
69
28
7
66
19
33
49
23
54
36
59
32
46
27
28
42
5
19
33
49
25
54
69
59
5
27
33
19
1
69
42
7
46
28
49
25

G

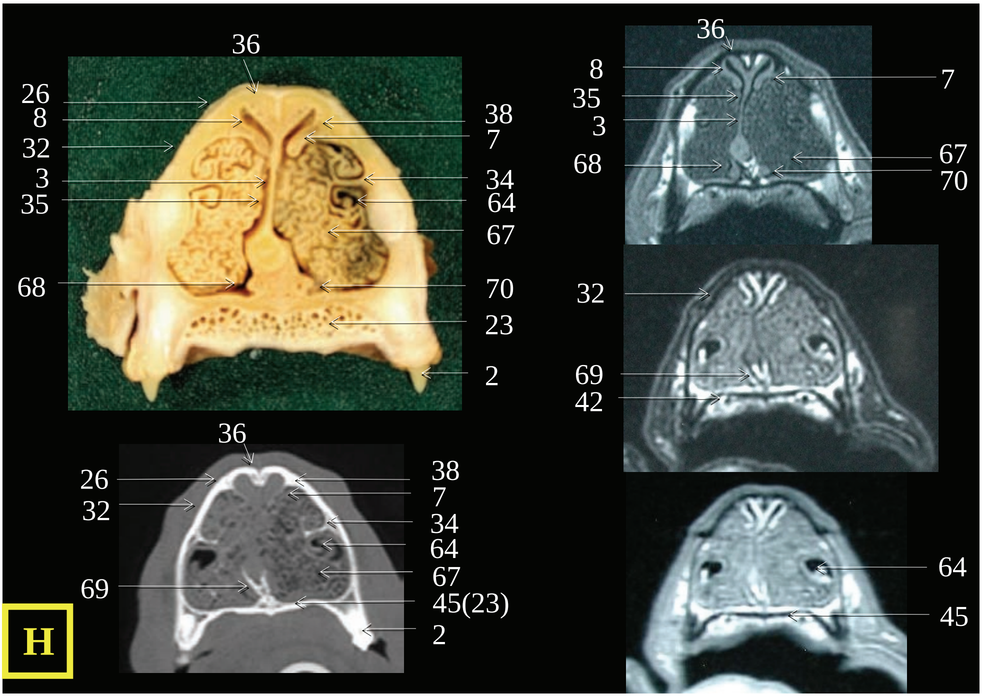
36
26
8
32
3
35
68
38
7
34
64
67
70
23
2
36
26
32
69
38
7
34
64
67
45(23)
2
36
8
35
3
68
7
67
70
32
69
42
64
45

H

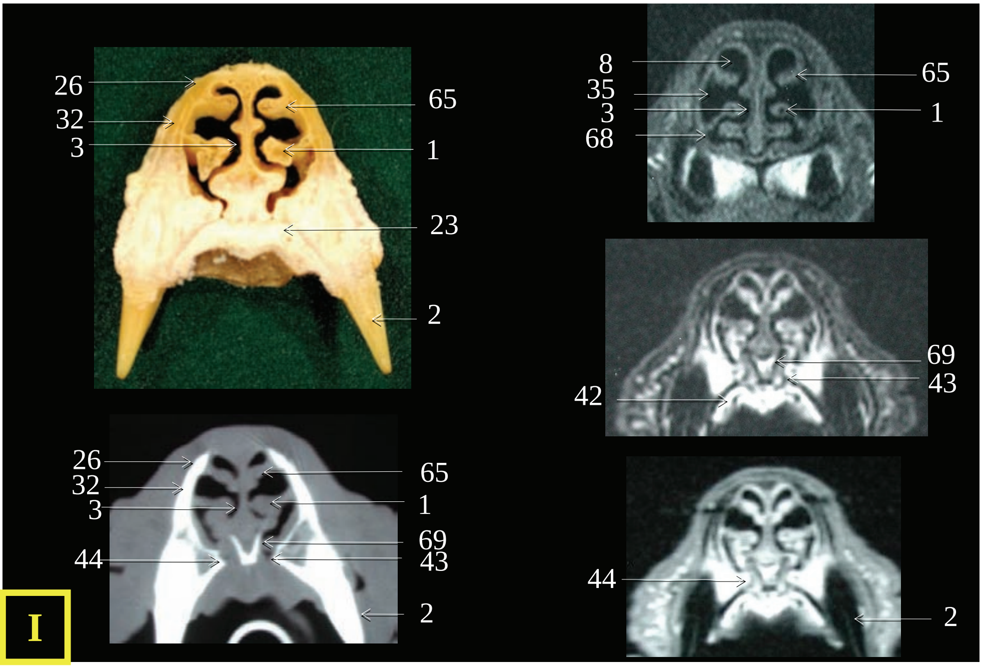

It was difficult to identify facial bones on the MR scans, but most of them could be located due to their void signal. In contrast, the conchae, conchal septa, and turbinates were easy to see because of the distinct mucosal covering. Only some of the ectoturbinates could not be identified. The surrounding soft-tissue structures were clearly visible on MR scans, especially when compared to the CT scans.

Figure 2 – Transverse anatomic sections (upper left), CT scans (lower left), and MR scans (T1-weighted MR (top right), T2-weighted MR (middle right), proton density (bottom right)) of the nasal cavities and paranasal sinuses of clinically normal mesaticephalic dogs. Images were obtained at sections A through I as illustrated in figure 1.

1= Alar fold (ventral nasal concha).
2 = Canine tooth of maxillary dental arch.
3 = Cartilaginous nasal septum.
4 = Ciliary body of the eye.
5 = Common nasal meatus.
6 = Cribriform plate of the ethmoid bone.
7 = Dorsal nasal concha.
8 = Dorsal nasal meatus.
9 = Ectoturbinate 1.
10 = Ectoturbinate 2.
11 = Ectoturbinate 3.
12 = Ectoturbinate 4.
13 = Ectoturbinate 5.
14 = Ectoturbinate 6.
15 = Endoturbinate I.
16 = Endoturbinate II (middle nasal concha).
17 = Endoturbinate III.
18 = Endoturbinate IV.
19 = Ethmoturbinates.
20 = Falx cerebri.
21 = Frontal bone.
22 = Frontal crest between the right and left frontal sinuses.
23 = Hard palate.
24 = Horizontal part (wing) of the vomer bone.
25 = Horizontal part of the palatine bone.
26 = Incisive bone.
27 = Infraorbital canal.
28 = Left choana.
29 = Left frontal sinus – lateral compartment.
30 = Left frontal sinus - medial compartment.
31 = Lens.
32 = Maxilla.
33 = Maxillary recess.
34 = Maxilloturbinate crest (conchal crest).
35 = Middle nasal meatus.
36 = Nasal bone.
37 = Nasopharyngeal meatus.
38 = Nasoturbinate crest (ethmoidal crest).
39 = Olfactory bulb of the brain.
40 = Orbit.
41 = Orbital lamina of the ethmoid bone forming the medial wall of the maxillary recess.
42 = Palatine canal.
43 = Palatine fissure.
44 = Palatine process of the incisive bone.
45 = Palatine process of the maxillary bone.
46 = Perpendicular lamina of the ethmoid bone (ventral part of osseous nasal septum).
47 = Presphenoid bone.
48 = Right caudal diverticle of the right nasal cavity occupied by endoturbinate IV.
49 = Right choana.
50 = Right frontal sinus – lateral compartment.
51 = Right frontal sinus - medial compartment.
52 = Right medial pterygoid muscle.
53 = Right upper molar.
54 = Right upper premolar.
55 = Right zygomatic salivary gland.
56 = Sagittal part of the vomer bone.
57 = Sclera.
58 = Septal process of the frontal bone (dorsal part of osseous nasal septum).
59 = Septal process of the nasal bone (dorsal part of osseous nasal septum).
60 = Septum between the medial and lateral frontal sinuses.
61 = Septum between the caudal diverticles of the nasal cavities.
62 = Soft palate.
63 = Sphenoidal process of the palatine bone.
64 = Spiral lamella of ventral nasal concha.
65 = Straight fold (dorsal nasal concha).
66 = Uncinate process.
67 = Ventral nasal concha.
68 = Ventral nasal meatus.
69 = Vomer.
70 = Vomeronasal organ.
71 = Zygomatic arch.
72 = Zygomatic process of the frontal bone.

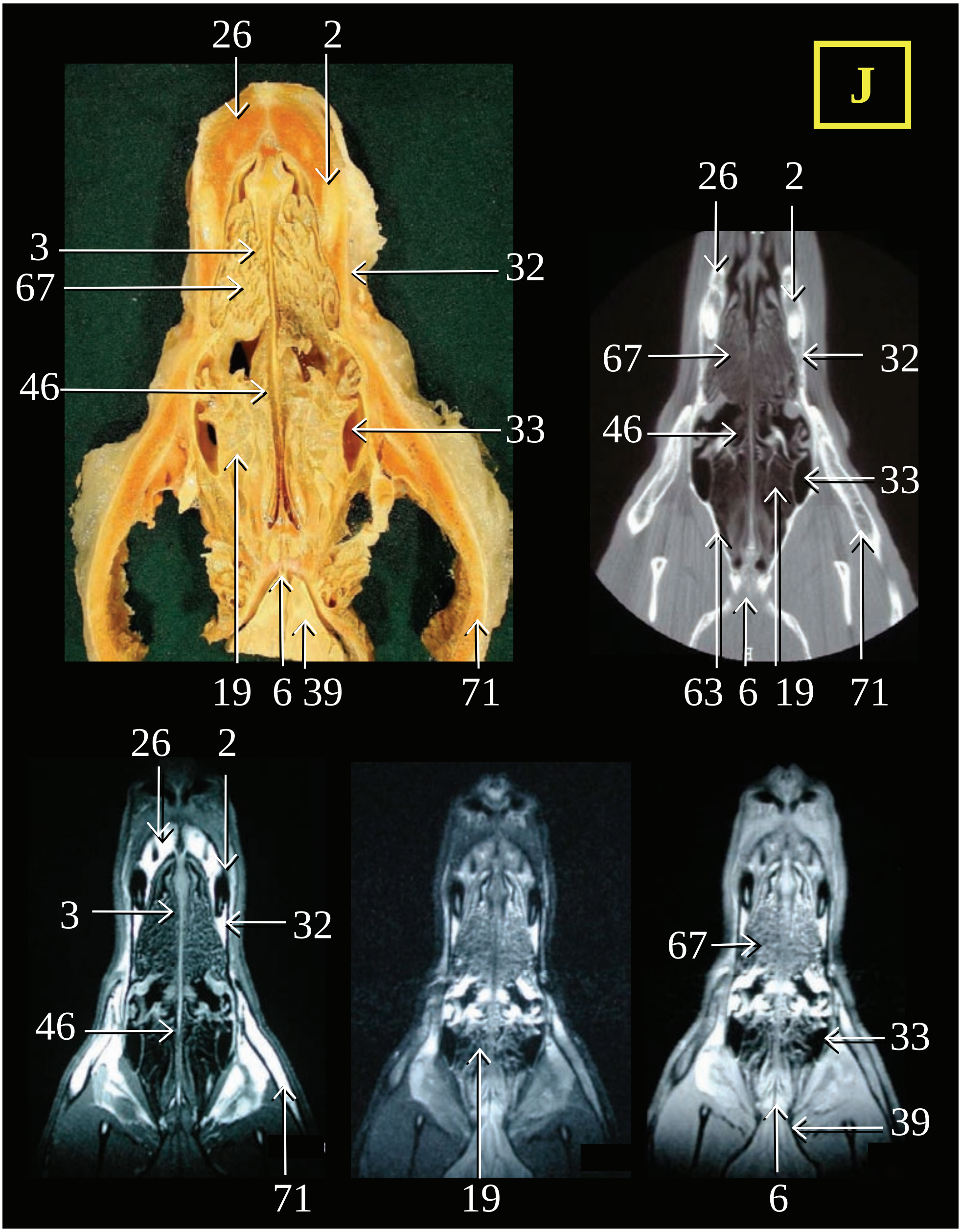

Figure 3a – Dorsal anatomic section (upper left), CT scan (upper right) and MR scans {T1-weighted MR (bottom left), T2-weighted MR (bottem middle), and proton density MR (bottom right)} of the nasal cavities and paranasal sinuses of clinically normal mesaticephalic dogs. Images were obtained at section J as illustrated in Figure 1. See Figure 2 for key

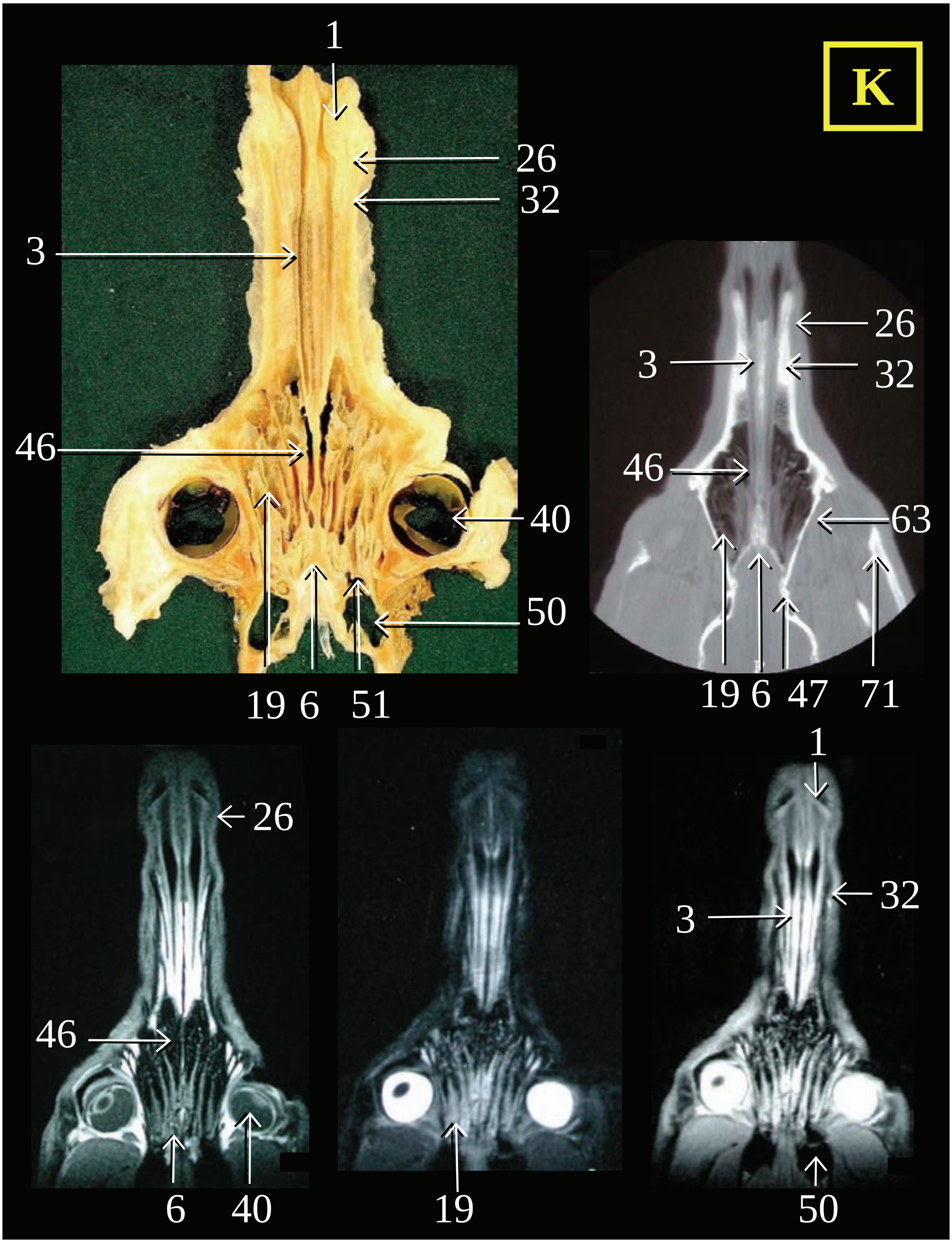

Figure 3b – Dorsal anatomic section (upper left), CT scan (upper right) and MR scans {T1-weighted MR (bottom left), T2-weighted MR (bottem middle), and proton density MR (bottom right)} of the nasal cavities and paranasal sinuses of clinically normal mesaticephalic dogs. Images were obtained at section K as illustrated in Figure 1. See Figure 2 for key.

These results are also listed in Table 1.

	CT	MR
Structures of the nasal cavities and paranasal sinuses		
1= Alar fold (ventral nasal concha).	+	+
3 = Cartilaginous nasal septum.	+	+
5 = Common nasal meatus.	+	+
7 = Dorsal nasal concha.	+	+
8 = Dorsal nasal meatus.	--	+
9 = Ectoturbinate 1.	+	+
10 = Ectoturbinate 2.	+	+
11 = Ectoturbinate 3.	+	+
12 = Ectoturbinate 4.	--	--
13 = Ectoturbinate 5.	--	--
14 = Ectoturbinate 6.	--	--
15 = Endoturbinate I.	+	+
16 = Endoturbinate II (middle nasal concha).	+	+
17 = Endoturbinate III.	+	+
18 = Endoturbinate IV.	+	+
19 = Ethmoturbinates.	+	+
29 = Left frontal sinus – lateral compartiment.	+	+
30 = Left frontal sinus - medial compartiment.	+	+
35 = Middle nasal meatus.	--	+
50 = Right frontal sinus – lateral compartiment.	+	+
51 = Right frontal sinus - medial compartiment.	+	+
64 = Spiral lamella of ventral nasal concha.	+	+
65 = Straight fold (dorsal nasal concha).	+	+
67 = Ventral nasal concha.	+	+
68 = Ventral nasal meatus.	--	+
Surrounding structures of the skull		
2 = Canine tooth of maxillary dental arch.	+	+
4 = Ciliary body of the eye.	--	--
20 = Falx cerebri.	--	+
31 = Lens.	--	+
39 = Olfactory bulb of the brain.	+	+
40 = Orbit.	--	+
52 = Right medial pterygoid muscle.	--	+
53 = Right upper molar.	+	+
54 = Right upper premolar.	+	--
55 = Right zygomatic salivary gland.	--	+
57 = Sclera.	--	+
62 = Soft palate.	+	+
Facial bones		
6 = Cribriform plate of the ethmoid bone.	+	+
21 = Frontal bone.	+	+
22 = Frontal crest between the frontal sinuses.	+	+
23 = Hard palate.	+	+
24 = Horizontal part of the vomer bone.	+	+
25 = Horizontal part of the palatine bone.	+	+ (void)
26 = Incisive bone.	+	+
27 = Infraorbital canal.	+	+
28 = Left choana.	+	+

	CT	MR
32 = Maxilla.	+	+ (void)
33 = Maxillary recess.	+	+
34 = Maxilloturbinate crest (conchal crest).	+	--
36 = Nasal bone.	+	+ (void)
37 = Nasopharyngeal meatus.	+	+
38 = Nasoturbinate crest (ethmoidal crest).	+	--
41 = Orbital lamina of the ethmoid bone	+	+
42 = Palatine canal.	+	+ (vessels)
43 = Palatine fissure.	+	+ (vessels)
44 = Palatine process of the incisive bone.	+	+
45 = Palatine process of the maxillary bone.	+	+ (void)
46 = Perpendicular lamina of the ethmoid bone	+	+
47 = Presphenoid bone.	+	+ (void)
48 = Right caudal recess of the right nasal cavity	+	+
49 = Right choana.	+	+
56 = Sagittal part of the vomer bone.	+	+
58 = Septal process of the frontal bone.	+	+
59 = Septal process of the nasal bone.	+	+
60 = Septum between the medial and lateral frontal sinuses.	+	+
61 = Septum between the caudal recesses of the nasal cavities.	+	+
63 = Sphenoidal process of the palatine bone.	+	+
66 = Uncinate process.	--	--
69 = Vomer.	+	+
70 = Vomeronasal organ.	--	--
71 = Zygomatic arch.	+	+
72 = Zygomatic process of the frontal bone.	+	+ (void)

TABLE 1 : Structures of the nasal cavities and paranasal sinuses visible on the CT and MR scans.
+ = identified, -- = not identified

DISCUSSION

Although information on CT and MR scans of the nasal cavities and frontal sinuses of dogs exists[18,19,24], a detailed anatomic description of those images in clinically normal dogs is lacking. The complexity of radiographs attributable to superimposition of the facial bones and the nasal turbinates can be overcome by use of single-plane images of the nasal cavities and frontal sinuses. Images through the transverse, dorsal, or sagittal plane provide detailed anatomic information. The sagittal plane was not used in this study because it does not permit symmetric comparison between the left and the right sides of the nose. The dorsal plane is most appropriate for use in determining the integrity of the cribriform plate in dogs with nasal tumors or nasal aspergillosis.[11] Images through the dorsal plane also provide a more general view of the entire nasal cavities, allowing easier characterization of the disease processes. This differentiation is also possible by use of transverse images obtained via the transverse plane. Moreover, images for the transverse plane can easily be obtained with a dog positioned in ventral recumbency, and this allows better evaluation of the nasal turbinates, which is essential for the diagnosis of diseases that affect the nasal region. Therefore, the transverse plane is the reference plane for the assessment of nasal pathologic changes.

MR allows investigators to make multiplanar images without repositioning the dog.[2§] It is also possible to obtain dorsal, sagittal and transverse views of the same dog by use of CT, but this requires repositioning of the dog, which may be complicated. An alternative method to achieve CT images in various planes without repositioning the dog is by way of dorsal and sagittal reconstructions, although their quality on a third generation scanner is inferior to that of native images. Recent multidetector helical CT scans are capable of producing isotropic voxels, and multiplanar reconstructions are therefore of the same high quality as the original transverse images.

The CT examinations were reviewed only using bone window settings. The nasal cavities and paranasal sinuses do not contain soft-tissue structures other than the mucosa.[19] Therefore, a soft-tissue window was not used in our anatomic study. A soft-tissue window in combination with examinations conducted by use of contrast agents, may be useful in nasal cavity with pathologic changes to enable differentiation between fluid and soft tissue or to define more accurately the nature of an abnormal soft-tissue structure.[8,12] However, in pathologic conditions, the nasal cavities often contain many structures of different physical densities (ie, bone, cartilage, mucosa, and air) which makes most CT measurements of attenuation values unreliable.[7,27] In contrast to CT, MR allows differentiation between the nasal mucosa and other soft tissues or fluid.

Analysis of results of the study reported here indicates that all nasal structures can be evaluated by use of CT or MR. However, differentiation between the various layers of the nasal mucosa is not possible with these techniques.

CT and MR are increasingly available to veterinarians. Axial CT, MR and radiography require at least 15 minutes for a complete examination and must be performed in anesthetized animals. Using helical CT, the time of the examination is considerably reduced (2 to 4 minutes), and the procedure may be performed in animals that are deeply sedated.[26] Advantages of CT over MR include lower cost and a reduced amount of time to conduct an examination. Advantages of MR over axial CT include the use of multiplanar capabilities.

The information reported here should serve as a baseline reference for evaluation of CT and MR scans of the nasal cavities and paranasal sinuses of dogs. It can be used to assist in interpretation of pathologic conditions of the nasal region.

[a] Schwarz T. Die Rolle der Röntgendiagnostik und der Computertomographie in der Diagnostik klinischer Rhinitiden des Hundes unter besonderer Berücksichtigung von Tumoren und Mykosen der Nasen-Und Nasennebenhöhlen. Diss. Med. Vet. FU Berlin, Journal No 186, 1997;63.

[b] Thalamonal, Janssen Pharmaceutics n.v., Beerse, Belgium

[c] Pentothal, Abbott Laboratories, North Chicago, Ill.

[d] Fluothane, Zeneca, Delaware

[e] CT-scanner Pace Plus, GE Medical Systems, Milwaukee, Wis.

[f] Fuji Photo Film Co, Ltd, Tokyo, Japan

[g] Symphony, Siemens A.G., Erlangen, Germany

REFERENCES

1. Burk RL. Computed tomographic imaging of nasal disease in 100 dogs. Vet Radiol Ultrasound 1992;33:177-180.

2. Saunders JH, van Bree H, Gielen I, et al. Computed tomography in chronic nasal disease in the dog. Vet Radiol Ultrasound. *In Press.*

3. Codner E, Lurus A, Miller J, et al. Comparison of computed tomography with radiography as a non-invasive diagnostic for chronic nasal disease in dogs. J Am Vet Med Assoc 1993;7:1106-1110.

4. Moore M, Gavin R, Kraft S, et al. MR, CT and clinical features from four dogs with nasal tumors involving the rostral cerebrum. Vet Radiol 1991;32:19-25.

5. Saunders JH, Duchateau L, Stock C, et al. Use of computed tomography to predict final outcome of nasal aspergillosis in dogs. Can Vet J 2003;44:305-311.

6. Saunders JH, van Bree H. Comparison of radiography and computed tomography for the diagnosis of nasal aspergillosis. Vet Radiol Ultrasound 2003;44:414-419.

7. Saunders JH, Zonderland JL, Clercx C, et al. Computed tomographic findings in 35 dogs with nasal aspergillosis. Vet Radiol Ultrasound 2002;43:5-9.

8. Thrall D, Robertson I, McLeod D, et al. A comparison of radiographic and computed tomographic findings in 31 dogs with malignant nasal cavity tumors. Vet Radiol 1989;30:59-66.

9. Voges A, Ackerman N. MR evaluation of intra- and extracranial extension of nasal adenocarcinoma in a dog and cat. Vet Radiol Ultrasound 1995;36:196-200.

10. Berry C, Koblik P. Evaluation of survey radiography, linear tomography and computed tomography for detecting experimental lesions of the cribriform plate in dogs. Vet Radiol 1990;31:146-154.

11. Koblik P, Berry C. Dorsal plane computed tomographic imaging of the ethmoid region to evaluate chronic nasal disease in the dog. Vet Radiol 1990;31:92-97.

12. Park R, Beck E, LeCouteur R. Comparison of computed tomography and radiography for detecting changes induced by malignant nasal neoplasia in dogs. J Am Vet Med Assoc 1992;201:1720-1724.

13. Mathews K, Davidson A, Koblik P, et al. Comparison of topical administration of clotrimazole through surgically placed versus nonsurgically placed catheters for treatment of nasal aspergillosis in dogs: 60 cases (1990-1996). J Am Vet Med Assoc 1998;213:501-506.

14. Mathews K, Koblik P, Richardson E, et al. Computed tomographic assessment of noninvasive intranasal infusions in dogs with fungal rhinitis. Vet Surg 1996;25:309-319.

15. Ogilvie G, La Rue S. Canine and feline nasal and paranasal tumors. Vet Clin North Am Small Anim Pract, Update on Respiratory Diseases. Guest Editor Brendan C. McKiernan, Vol 22, No 5 , September 1992.

16. Lonosky JH, Abbott LC, Kuriashkin IV. Computed tomography of the normal feline nasal cavity and paranasal sinuses. Vet Radiol Ultrasound 1997;38:251-258.

17. Arencibia A, Vazquez JM, Jaber R, et al. Magnetic resonance imaging and cross sectional anatomy of the normal equine sinuses and nasal passages. Vet Radiol Ultrasound 2000;41:313-319.

18. Burk RL. Computed tomographic anatomy of the canine nasal passages. Vet Radiol Ultrasound 1992;33:170-176.

19. Feeney D, Fletcher T, Hardy R. Atlas of correlative imaging anatomy of the normal dog, ultrasound and computed tomography, Philadelphia: WB Saunders, 1991.

20. George F, Smallwood J. Anatomic atlas for computed tomography in the mesaticephalic dog: head and neck. Vet Radiol Ultrasound 1992;33:217-240.

21. Fike J, Druy E, Zook B, et al. Canine anatomy assisted by computerized tomography. Am J Vet Res 1980;41:1823-1832.

22. Fike J, LeCouteur R, Cann C. Anatomy of the canine brain using high resolution computed tomography. Vet Radiol 1981;22:236-243.

23. Fike J, LeCouteur R, Cann C. Anatomy of the canine orbital region multiplanar imaging by CT. Vet Radiol 1984;25:32-36.

24. Assheuer J, Sager M. Head. In : AssheuerJ, Sager M, eds. MRI and CT atlas of the dog. Berlin: Blackwell Science, 1997;50-57.

25. World Association of Veterinary Anatomists (WAVA). In*:* Nomina Anatomica Veterinaria. 4th ed. Ithica, NY: International Committee on Veterinary Gross Anatomical Nomenclature, 1994;1-198.

26. Forrest LJ. The head: Excluding the brain and orbit. Clin Techn Small Anim Pract 1999;14:170-176.

27. Williams G., Bydder G.M., Kreel L. The validity and use of computed tomography attenuation values. British Med Bull 1980;36:279-287.

Cross-sectional anatomy of the

TRUNK

2.1. The Thorax

2.1.1. Computed tomography and cross-sectional anatomy of the thorax in clinically normal dogs

Lieve M. De Rycke*, DVM; Ingrid M. Gielen*, DVM, MSc;
Paul J. Simoens**, DVM, PhD; Henri van Bree*, DVM, PhD

*Department of Medical Imaging, Faculty of Veterinary Medicine, Ghent University,
Salisburylaan 133, 9820 Merelbeke, Belgium.

**Department of Morphology, Faculty of Veterinary Medicine, Ghent University,
Salisburylaan 133, 9820 Merelbeke, Belgium.

Adapted from :

De Rycke LM, Gielen IM, van Bree H, Simoens PJ. Computed tomography and cross-sectional anatomy of the thorax in clinically normal dogs. *Am J Vet Res* 2005;66:512-524.

SUMMARY

Objective—To provide a detailed anatomic description of the thorax in clinically normal dogs by means of computed tomography.

Animals—4 clinically normal adult German Shepherd dogs weighing 28 to 37 kg.

Procedure—Dogs were anesthetized and positioned in ventral recumbency for computed tomographic (CT) examination of the thorax. A CT image from the thoracic inlet to the diaphragm was made by use of a third- generation scanner with a slice thickness of 5mm. Individual images were reviewed by use of soft tissue (mediastinal)(window width, 250 Hounsfield units; window level, 35 Hounsfield units) and lung (window width, 1000 Hounsfield units; window level, –690 Hounsfield units) settings. One dog, weighing 28 kg, was euthanatized, bound on a wooden frame in the same position as used for CT examination, and frozen at –14°C until solid. By use of an electric band saw, the frozen thorax was sectioned at 10-mm thick intervals. Slab sections were immediately cleaned, photographed, and compared with corresponding CT images.

Results—Anatomic sections were studied and identified anatomic structures were matched with structures on corresponding CT images. Except for some blood vessels and parts of the heart, most of the bony and soft tissue structures of the thorax discerned on anatomic slices could be found on matched CT images.

Conclusions and Clinical Relevance—Because CT images provide detailed information on most structures of the canine thorax, results of our study could be used as a guide for evaluation of CT images of dogs with thoracic diseases.

INTRODUCTION

Computed tomography (CT) of the thorax has become established as an important radiologic procedure. CT displays of the lungs, mediastinum, pleural cavity, and chest wall in a transverse plane provide unique diagnostic information that is unobtainable with conventional radiographic techniques.[1] Compared with conventional radiography, CT allows better distinction among specific tissue densities in the thorax and detection of subtle changes in organ size, shape, margin contour, and position.[2-4]

In human medicine, use of CT plays a key role in the diagnosis and evaluation of various thoracic syndromes and diseases such as pneumothorax; pleural and pericardial effusion; collapse of a lung lobe; congenital anomalies; pulmonary parenchymal and bronchial diseases; cysts; abscesses; and primary or metastatic neoplasia of the lungs, pleura, mediastinum, lymph nodes, and chest wall.[1,5-23] Furthermore, CT is a useful preoperative technique, a precise staging tool, and improves the use of biopsies by allowing detection of lesions not identifiable by fluoroscopy and determination of the location of high-risk masses that are close to cardiovascular structures.[24,25,a]

The use of CT in diagnosing thoracic diseases in veterinary medicine is in full exploration,[4,26-35] and an increasing number of published clinical reports[3,36-40] are found involving thoracic CT. Accurate interpretation of CT images of the thorax requires a thorough knowledge of cross-sectional anatomy of that region. A few papers[41,42] on CT anatomy of the thorax of clinically normal animals are available. Authors of one paper[41] described the CT and cross-sectional anatomy of the thorax of clinically normal cats and authors[42] of another paper reported the CT anatomy of the thorax of Nubian goats. The purpose of the study reported here was to identify structures that are visible on CT images of the canine thorax by means of a detailed color atlas consisting of a series of labeled anatomic photographs. Although some publications[2,43-46] on cross-sectional CT anatomy of the canine thorax exist, in the present study we combined the study of CT and gross anatomic sections, which provides more detailed and additional information.

MATERIAL AND METHODS

Animals—Four clinically normal adult German shepherd dogs weighing 28 to 37 kg were used for this study. Before the onset of CT examination, a clinical and radiographic examination of the thorax of each dog was performed, which included obtaining right and left lateral radiographic views of the thorax.

Computed tomography—Dogs were sedated by use of medetomidine hydrochloride[b] (40 to 50 µg/kg of body weight, IM), and anesthetized with thiopental sodium[b] (8 mg/kg, IV). After intubation, anesthesia was maintained with 1.5% to 2% halothane[d]. Intermittent positive-pressure ventilation was applied to the lungs to decrease motion artifacts caused by irregular or fast respiration of the dogs. Respiratory rate was set at 6 breaths/minute.

Dogs were positioned in ventral recumbency on the scanning table with forelimbs in extension. A lateral survey view was made by use of a third generation CT scanner[e]. Transverse, 5mm thick contiguous CT images of the thorax from the thoracic inlet to diaphragm were obtained. Settings for the CT image technique were 120 kV and 100 mA. Hard copies were printed[f] on x-ray film by use of a soft tissue setting (window width, 250 Hounsfield units; window level, 35 Hounsfield units) and a lung setting (window width, 1000 Hounsfield units; window level, –690 Hounsfield units).

Comparison of CT and anatomic images—At the end of CT examination 1 dog weighing 28 kg was euthanatized for reasons unrelated to thoracic disease. For euthanasia a combination[g] of embutramide, mebenzoniumiodide, and tetracaïne (0.3 ml/kg of body weight) was injected IV during anesthesia. After euthanasia, the dog was bound on a wooden frame in the same position used for scanning and frozen at –14°C until solid. The frozen cadaver was placed on the movable table of an electric band saw[h], and serial transverse sections were cut approximately 10 mm apart, beginning at the thoracic inlet and ending at the diaphragm. Slices were numbered and gently cleansed of debris with cold tap water and light brushing. They were immersed in water, and the cranial surface of each section was photographed immediately (ie, before thawing). Photographs were studied, and identifiable anatomic structures were labeled with the aid of texts on canine anatomy.[47,48] For each anatomic slice, a corresponding CT image was chosen on the basis of similar appearance. Identified structures were subsequently located on CT images. Nomenclature used for designating all structures was in accordance with official anatomic terminology.[49] From this collection, 24 representative matched pairs of images extending from the level of the sternal manubrium to the most caudal part of the lungs were selected.

RESULTS

The 24 selected levels, at which anatomic sections and their corresponding CT images were made, are indicated on a lateral survey view of the thorax of a German Shepherd (Figure 1). Identifiable anatomic structures are labeled on cadaver sections and corresponding CT images (Figure 2).

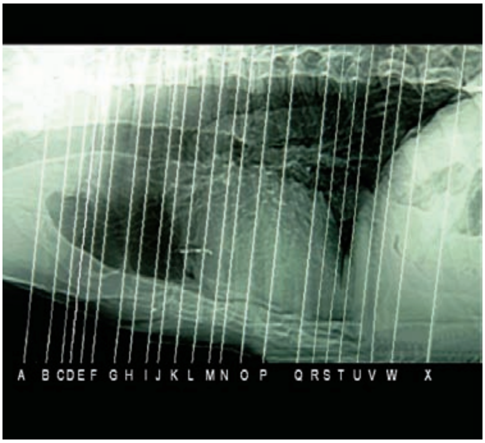

Figure 1—Lateral computed tomographic (CT) survey pilot image of the thorax of a clinically normal dog indicating the levels (A through X) at which the CT images were obtained.

On anatomic sections various structures of the canine thorax could be identified. Respiratory tract structures including the trachea, tracheal bifurcation (with carina), principal bronchi, lobar bronchi, and various lobes of the left and right lungs were clearly visible.

Large vessels such as left and right external jugular veins, brachiocephalic veins, common carotid arteries, subclavian and axillary arteries and veins, costocervical trunks and veins, and the cranial vena cava could readily be seen in the cranial mediastinum. Identification of these vessels could be ascertained by comparing cross-sectional images on successive levels. Other intrathoracic vascular structures including the thick walled aortic arch, ascending and descending aorta, pulmonary arteries and veins (located ventral to corresponding principal bronchi), left coronary artery, internal thoracic arteries and veins ventral to the transversus thoracis muscle, right azygos vein (located dorsal to the esophagus), intercostal veins, vertebral arteries and veins within the transverse canals, and the prominent caudal vena cava were observed.

Intrathoracic structures such as the heart with its chambers and valves, esophagus, longus colli muscle, and transverse thoracic muscle could easily be distinguished. Sternal lymph nodes were identified ventral to the transversus thoracis muscle and dorsal to the manubrium of the sternum. Cranial mediastinal lymph nodes were discerned lateral to the cranial vena cava. Tracheobronchal lymph nodes could be observed ventral to the tracheal bifurcation.

Various parts of the thoracic wall including the sternum, ribs with the intercostal muscles, and thoracic vertebrae enclosing the spinal cord were clearly visible. Other identifiable structures were the scapulae, nuchal ligament, and muscles of the thorax and proximal part of the forelimbs. In caudal sections the liver with portal and hepatic blood vessels, gallbladder, stomach, cranial and descending duodenum, and diaphragm could be discerned.

In the 4 dogs examined most of the previously mentioned structures of the thorax could be identified on CT images at the soft tissue setting. The heart silhouette could be observed, but cardiac chambers, valves, and interventricular septum were not visible.

In any dog, the nuchal ligament, left coronary artery, intercostal veins, vertebral vessels, lobar bronchi, and various lobes of the lungs could not be distinguished. In the cranial mediastinum, the left and right axillary arteries and right costocervical trunk and vein could not be discerned. Furthermore, portal and hepatic vessels, diaphragm, and descending duodenum were not visible in the most caudal CT images of the 4 dogs. The left costocervical trunk and contours of the gallbladder could be discerned in 2 of the 4 dogs. The ascending aorta, left costocervical vein, left and right axillary vein, main bronchus of the accessory lobe of the right lung, and left and right pulmonary veins could be identified in 3 of the 4 dogs by comparing their position on the corresponding anatomic images. In all 4 dogs most parts of the stomach could be seen.

On CT images obtained at the lung setting, only various structures of the respiratory tract and some large vessels were distinct in all dogs. The tracheobronchial tree including the trachea, tracheal bifurcation, principal bronchi, lobar bronchi, and various lobes of the left and right lung could easily

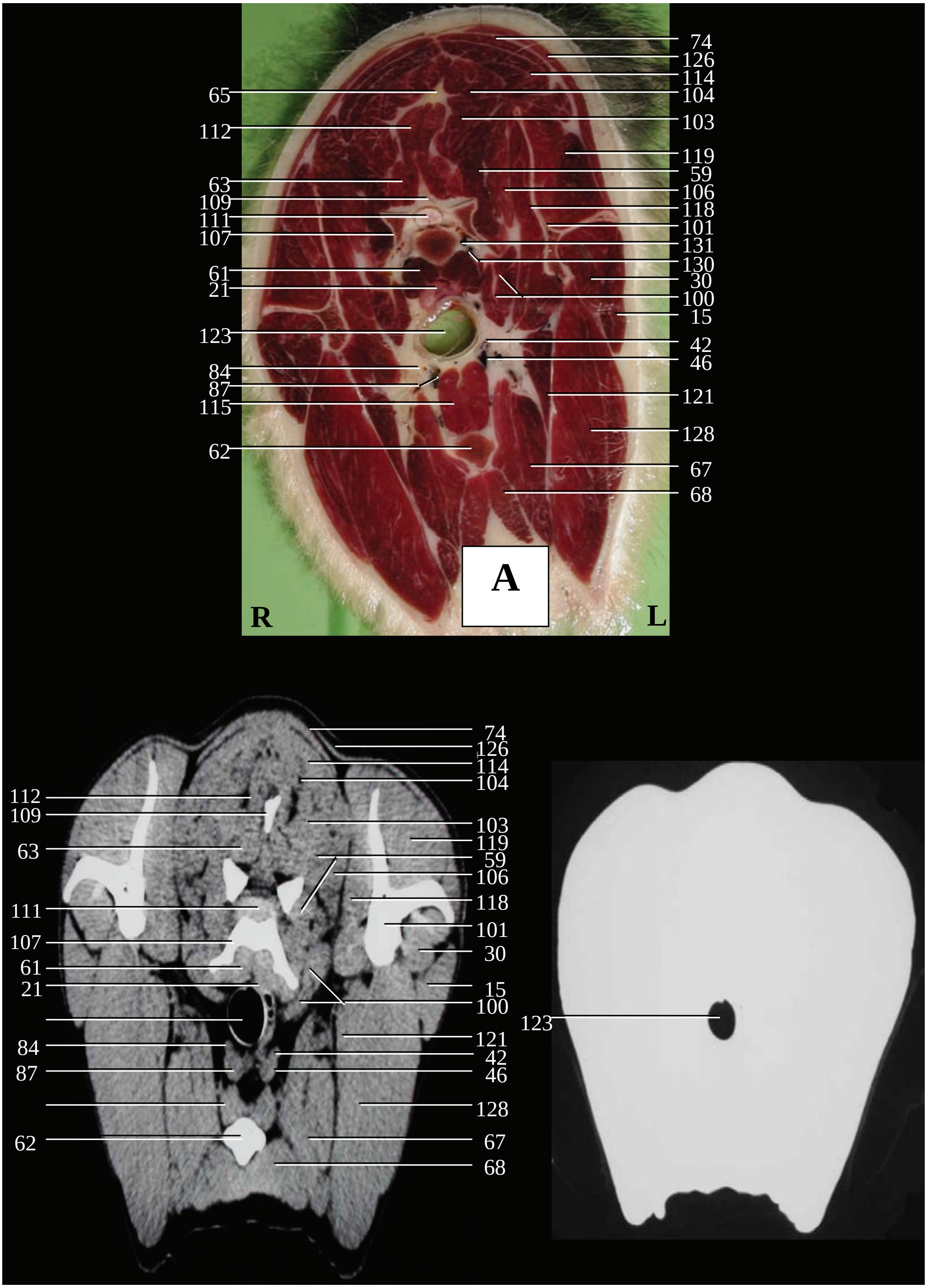
74
126
114
104
65
112
103
119
59
106
118
101
131
130
30
100
15
63
109
111
107
61
21
123
42
46
121
128
67
68
84
87
115
62
A
R
L
74
126
114
104
112
109
103
119
59
106
118
101
30
15
100
121
42
46
128
67
68
63
111
107
61
21
84
87
62
123

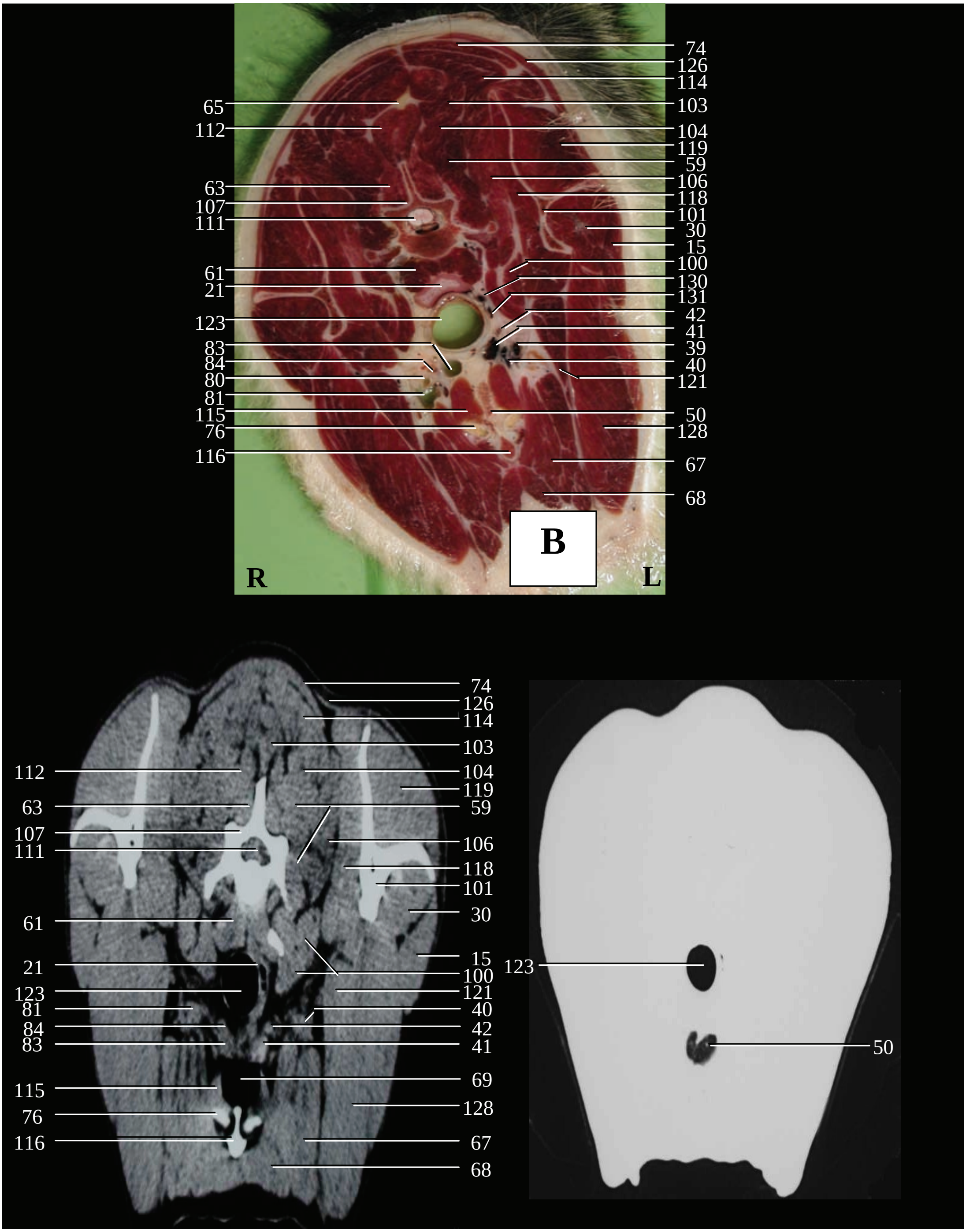
74
126
114
65
103
112
104
119
59
63
106
107
118
111
101
30
15
61
100
21
130
131
123
42
41
83
39
84
40
80
121
81
115
50
76
128
116
67
68
B
R
L
74
126
114
103
112
104
119
63
59
107
106
111
118
101
61
30
21
15
100
123
121
81
40
84
42
83
41
69
115
76
128
116
67
68
123
50

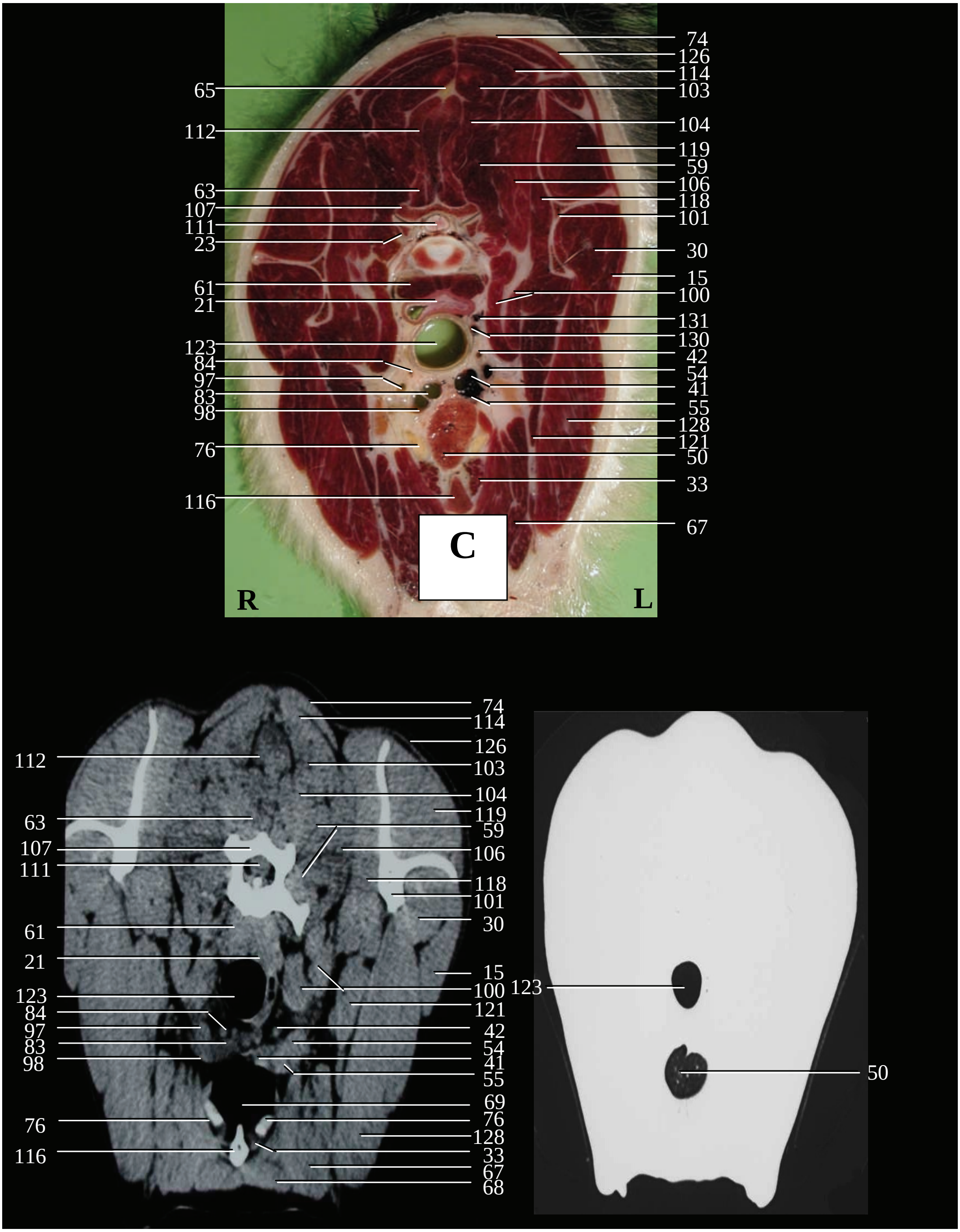
65
112
63
107
111
23
61
21
123
84
97
83
98
76
116
74
126
114
103
104
119
59
106
118
101
30
15
100
131
130
42
54
41
55
128
121
50
33
67
C
R
L
112
63
107
111
61
21
123
84
97
83
98
76
116
74
114
126
103
104
119
59
106
118
101
30
15
100
121
42
54
41
55
69
76
128
33
67
68
123
50

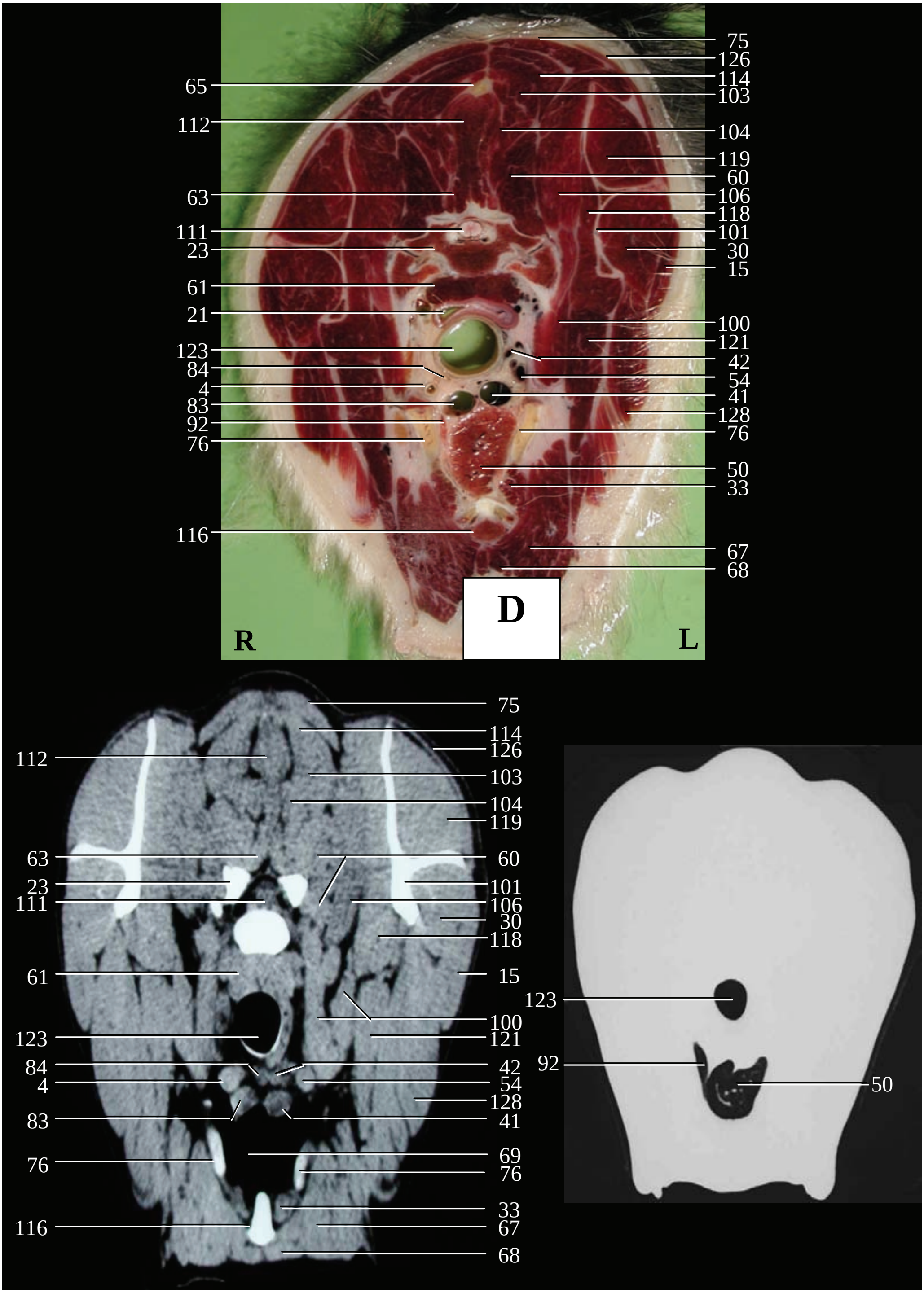
65
112
63
111
23
61
21
123
84
4
83
92
76
116
75
126
114
103
104
119
60
106
118
101
30
15
100
121
42
54
41
128
76
50
33
67
68
D
R
L
112
63
23
111
61
123
84
4
83
76
116
75
114
126
103
104
119
60
101
106
30
118
15
100
121
42
54
128
41
69
76
33
67
68
123
92
50

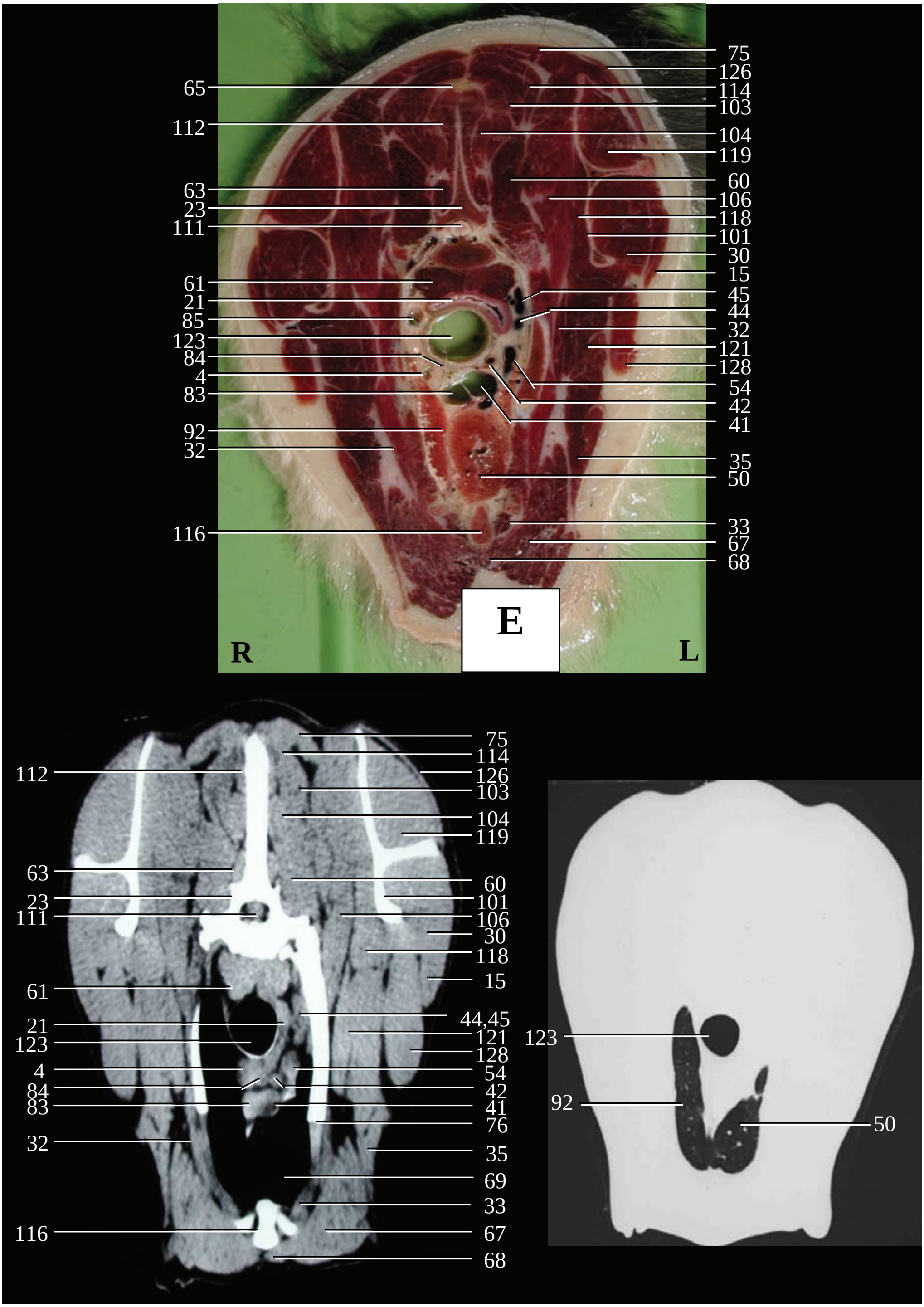
65
112
63
23
111
61
21
85
123
84
4
83
92
32
116
75
126
114
103
104
119
60
106
118
101
30
15
45
44
32
121
128
54
42
41
35
50
33
67
68
E
R
L
112
63
23
111
61
21
123
4
84
83
32
116
75
114
126
103
104
119
60
101
106
30
118
15
44,45
121
128
54
42
41
76
35
69
33
67
68
123
92
50

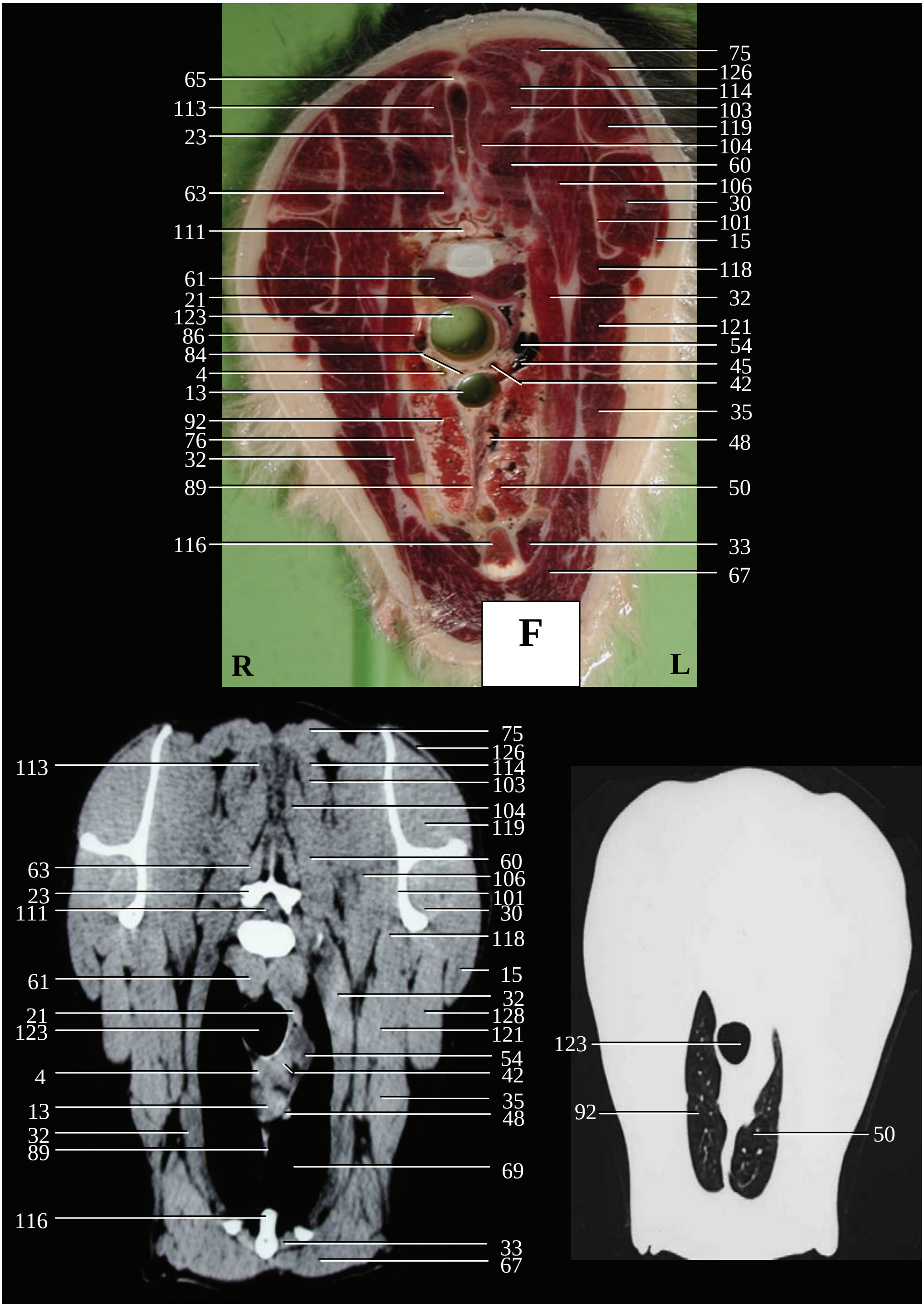
65
113
23
63
111
61
21
123
86
84
4
13
92
76
32
89
116
75
126
114
103
119
104
60
106
30
101
15
118
32
121
54
45
42
35
48
50
33
67
F
R
L
113
63
23
111
61
21
123
4
13
32
89
116
75
126
114
103
104
119
60
106
101
30
118
15
32
128
121
54
42
35
48
69
33
67
123
92
50

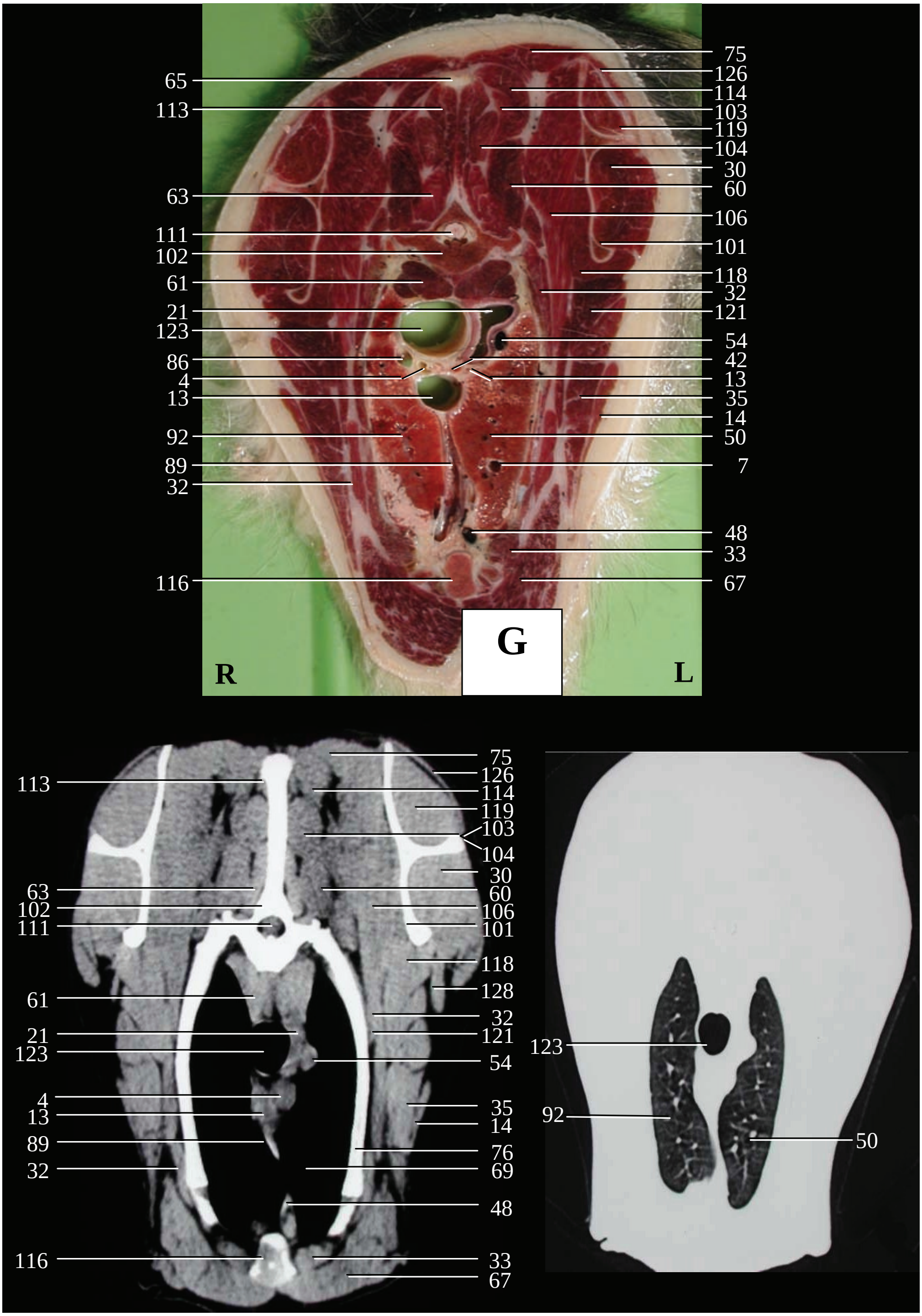
65
113
63
111
102
61
21
123
86
4
13
92
89
32
116
75
126
114
103
119
104
30
60
106
101
118
32
121
54
42
13
35
14
50
7
48
33
67
G
R
L
113
63
102
111
61
21
123
4
13
89
32
116
75
126
114
119
103
104
30
60
106
101
118
128
32
121
54
35
14
76
69
48
33
67
123
92
50

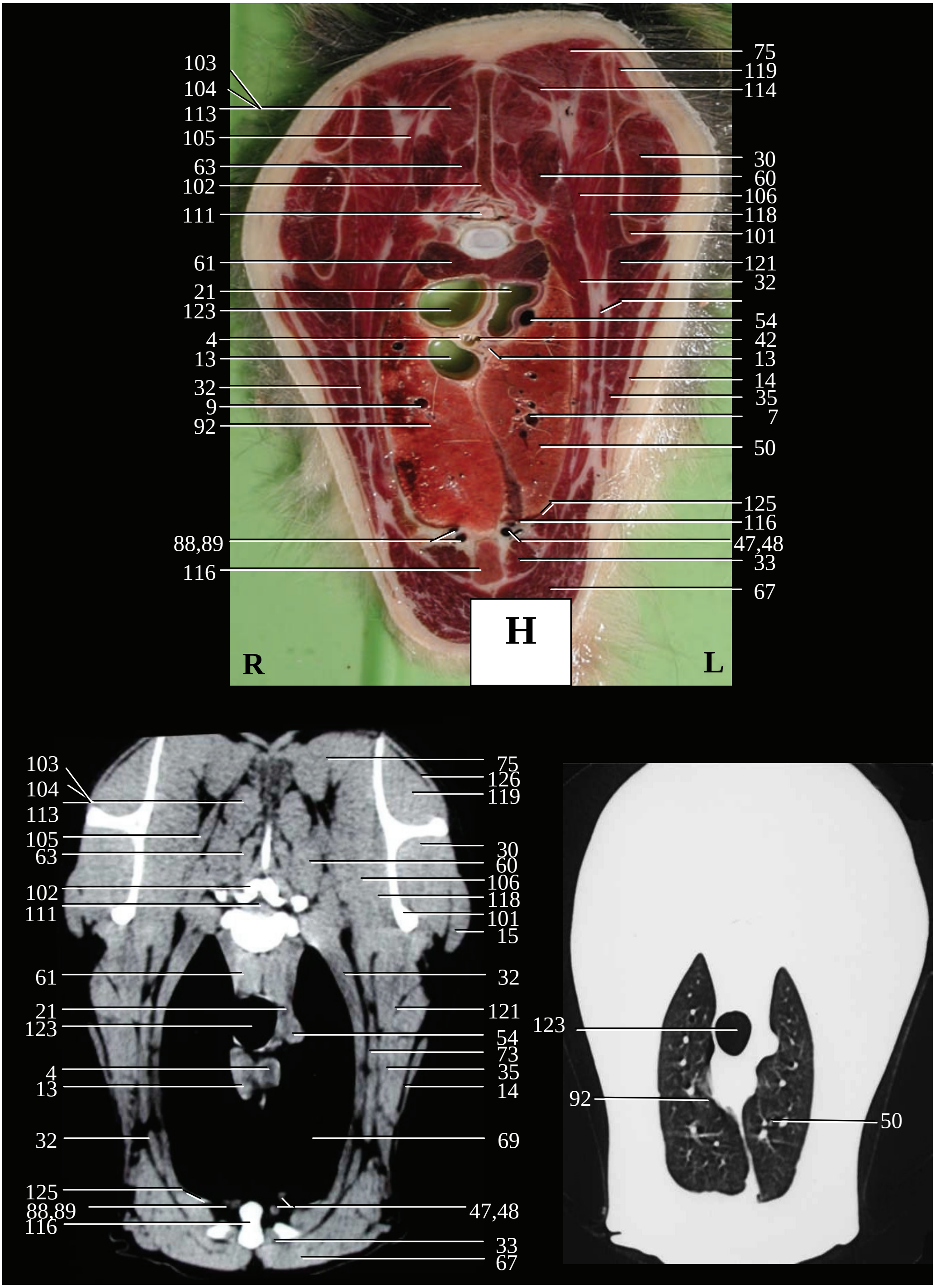
103
104
113
105
63
102
111
61
21
123
4
13
32
9
92
88,89
116
75
119
114
30
60
106
118
101
121
32
54
42
13
14
35
7
50
125
116
47,48
33
67
H
R
L
103
104
113
105
63
102
111
61
21
123
4
13
32
125
88,89
116
75
126
119
30
60
106
118
101
15
32
121
54
73
35
14
69
47,48
33
67
123
92
50

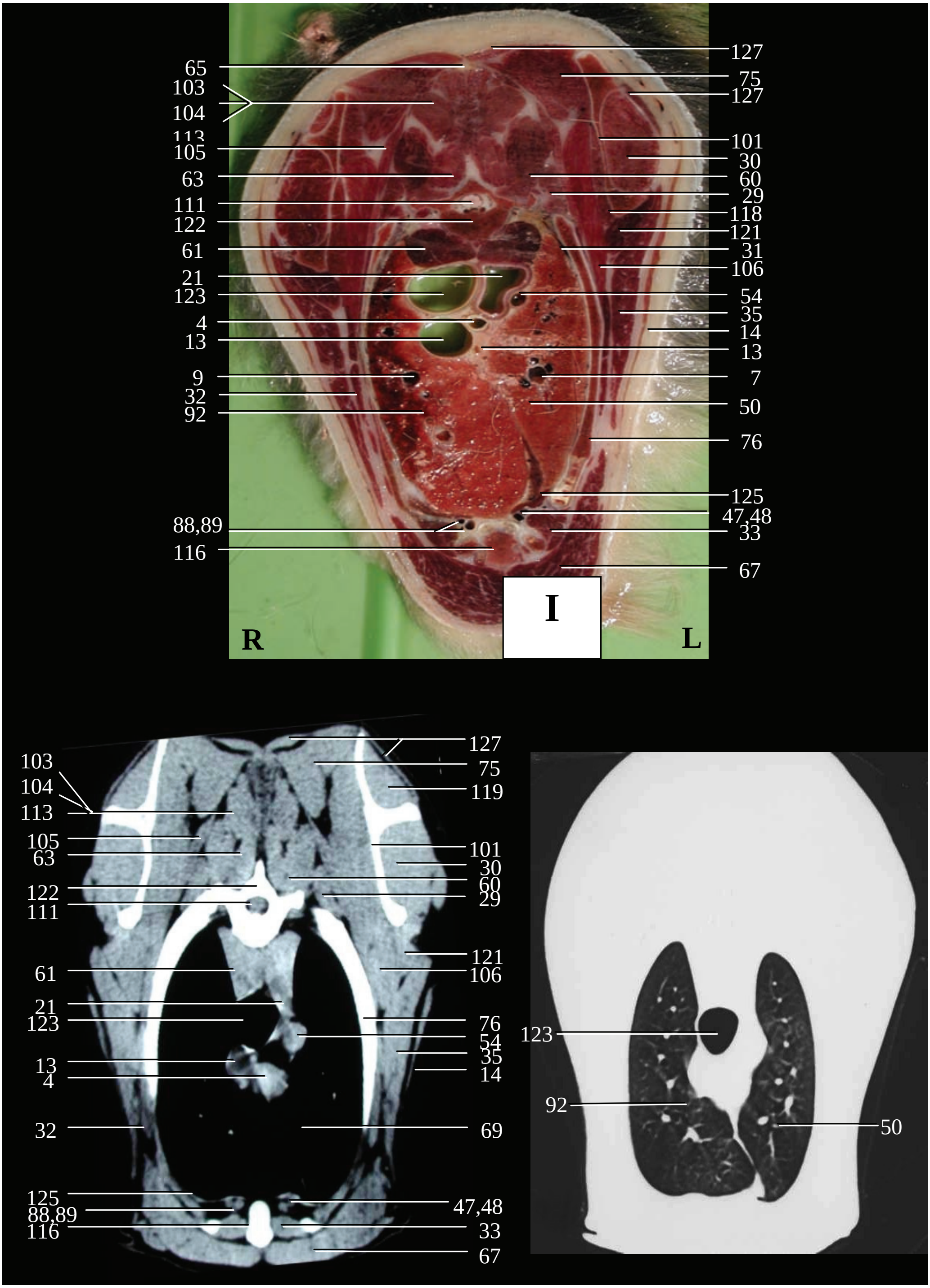
65
103
104
113
105
63
111
122
61
21
123
4
13
9
32
92
88,89
116
127
75
127
101
30
60
29
118
121
31
106
54
35
14
13
7
50
76
125
47,48
33
67
I
R
L
103
104
113
105
63
122
111
61
21
123
13
4
32
125
88,89
116
127
75
119
101
30
60
29
121
106
76
54
35
14
69
47,48
33
67
123
92
50

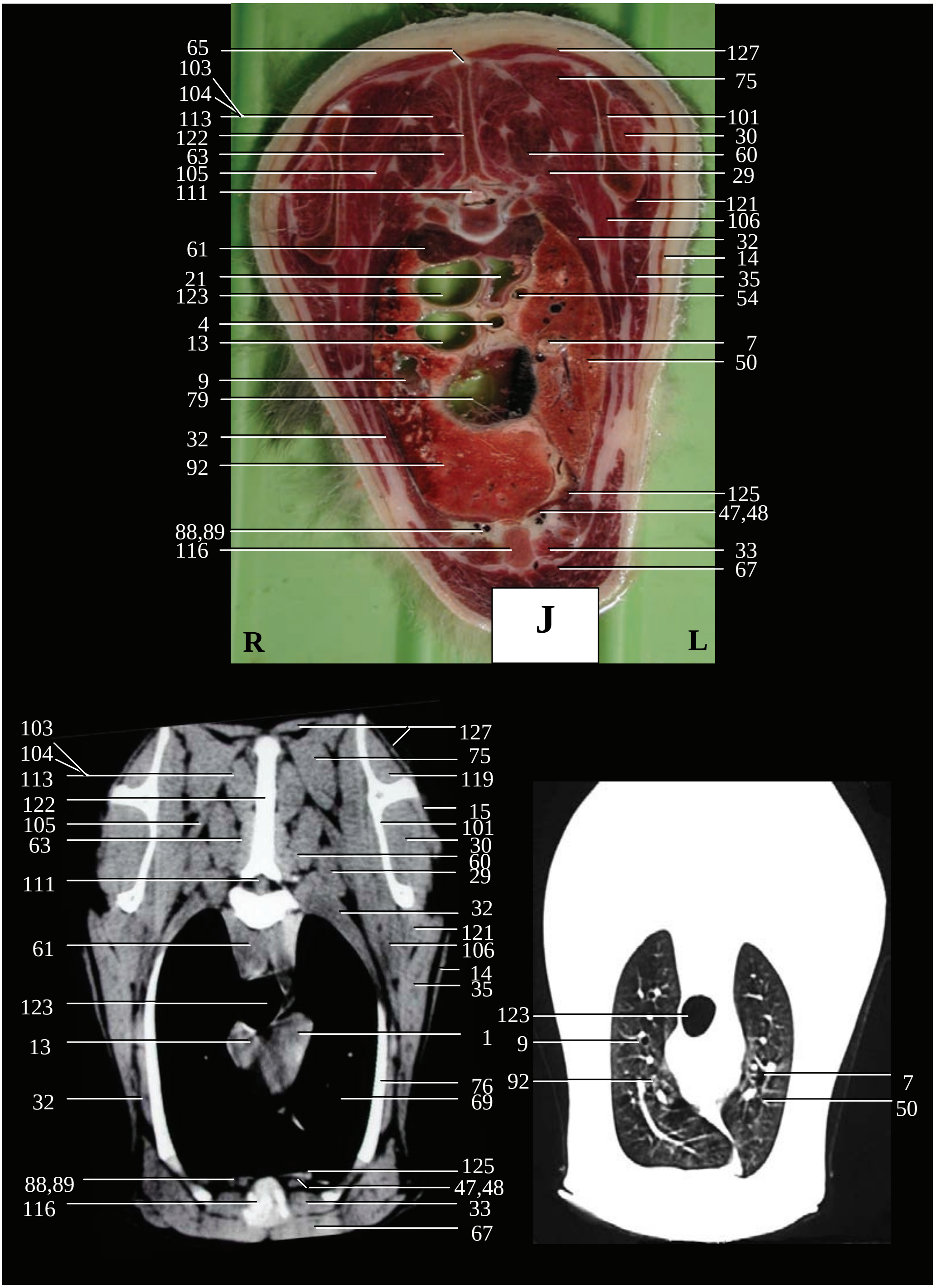
65
103
104
113
122
63
105
111
61
21
123
4
13
9
79
32
92
88,89
116
127
75
101
30
60
29
121
106
32
14
35
54
7
50
125
47,48
33
67
J
R
L
103
104
113
122
105
63
111
61
123
13
32
88,89
116
127
75
119
15
101
30
60
29
32
121
106
14
35
1
76
69
125
47,48
33
67
123
9
92
7
50

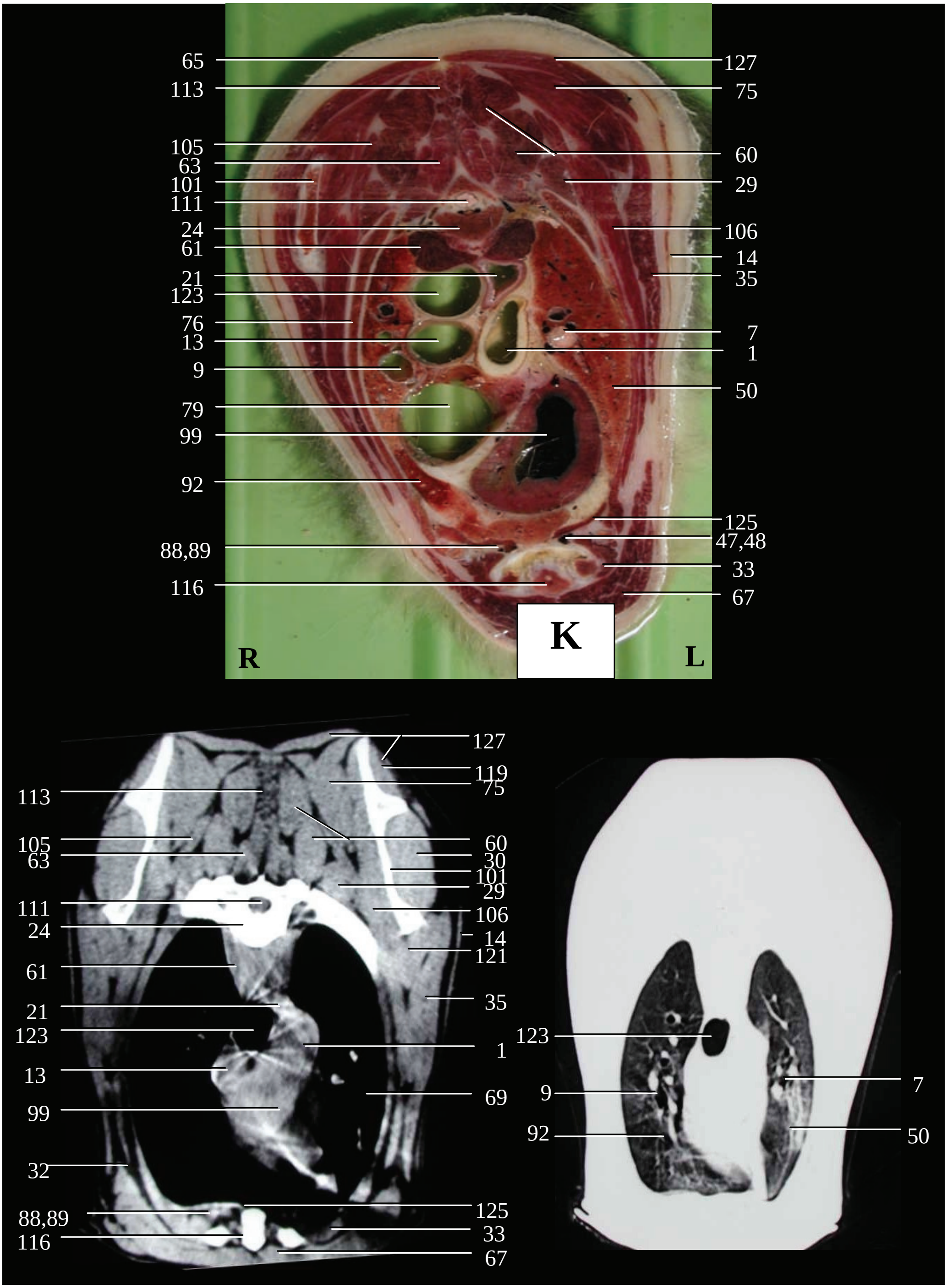
65
113
105
63
101
111
24
61
21
123
76
13
9
79
99
92
88,89
116
127
75
60
29
106
14
35
7
1
50
125
47,48
33
67
K
R
L
113
105
63
111
24
61
21
123
13
99
32
88,89
116
127
119
75
60
30
101
29
106
14
121
35
1
69
125
33
67
123
9
92
7
50

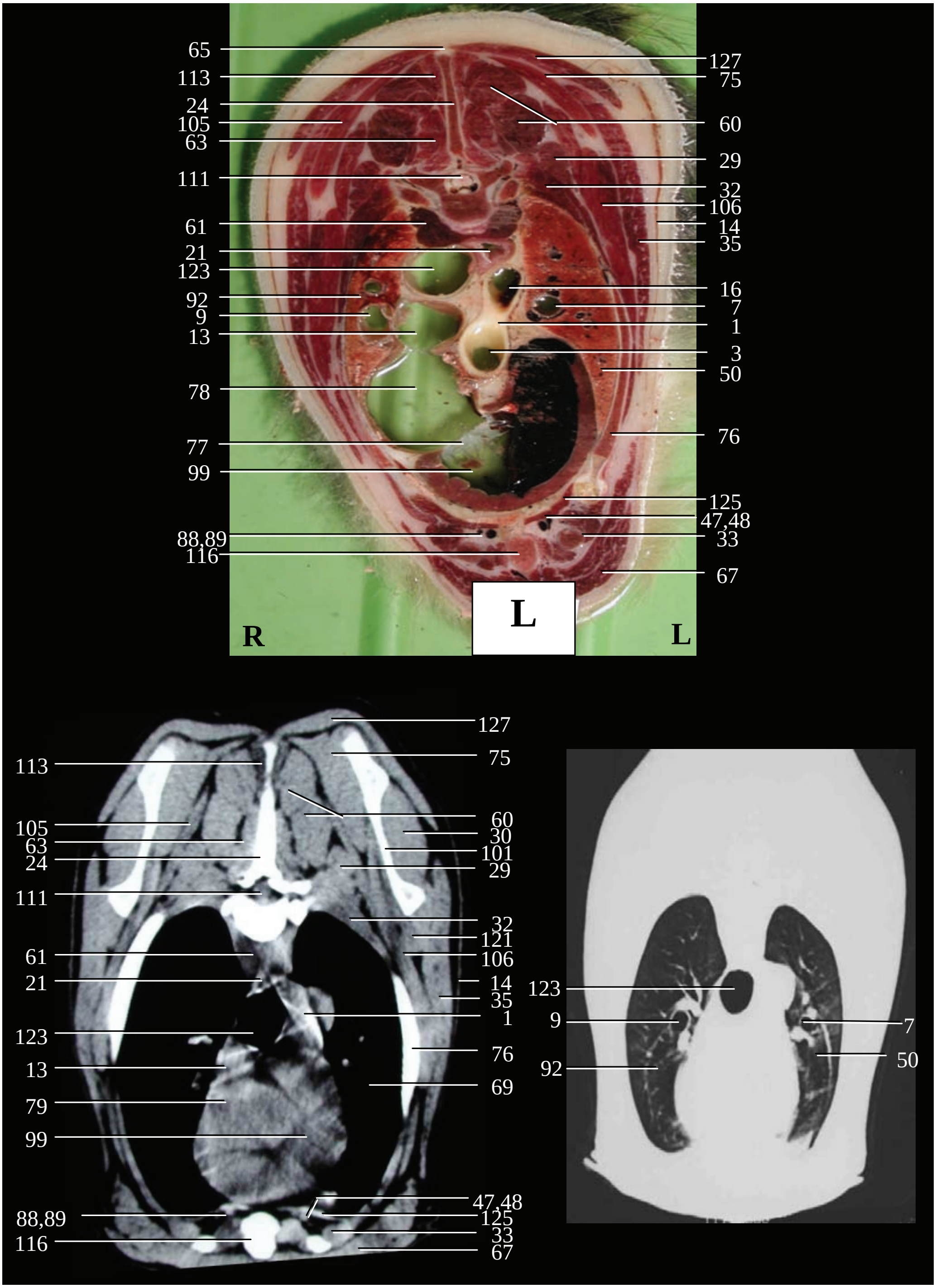
65
113
24
105
63
111
61
21
123
92
9
13
78
77
99
88,89
116
127
75
60
29
32
106
14
35
16
7
1
3
50
76
125
47,48
33
67
L
R
L
127
75
113
105
63
24
60
30
101
29
111
32
121
106
61
21
14
35
1
123
76
13
69
79
99
47,48
88,89
125
33
116
67
123
9
7
50
92

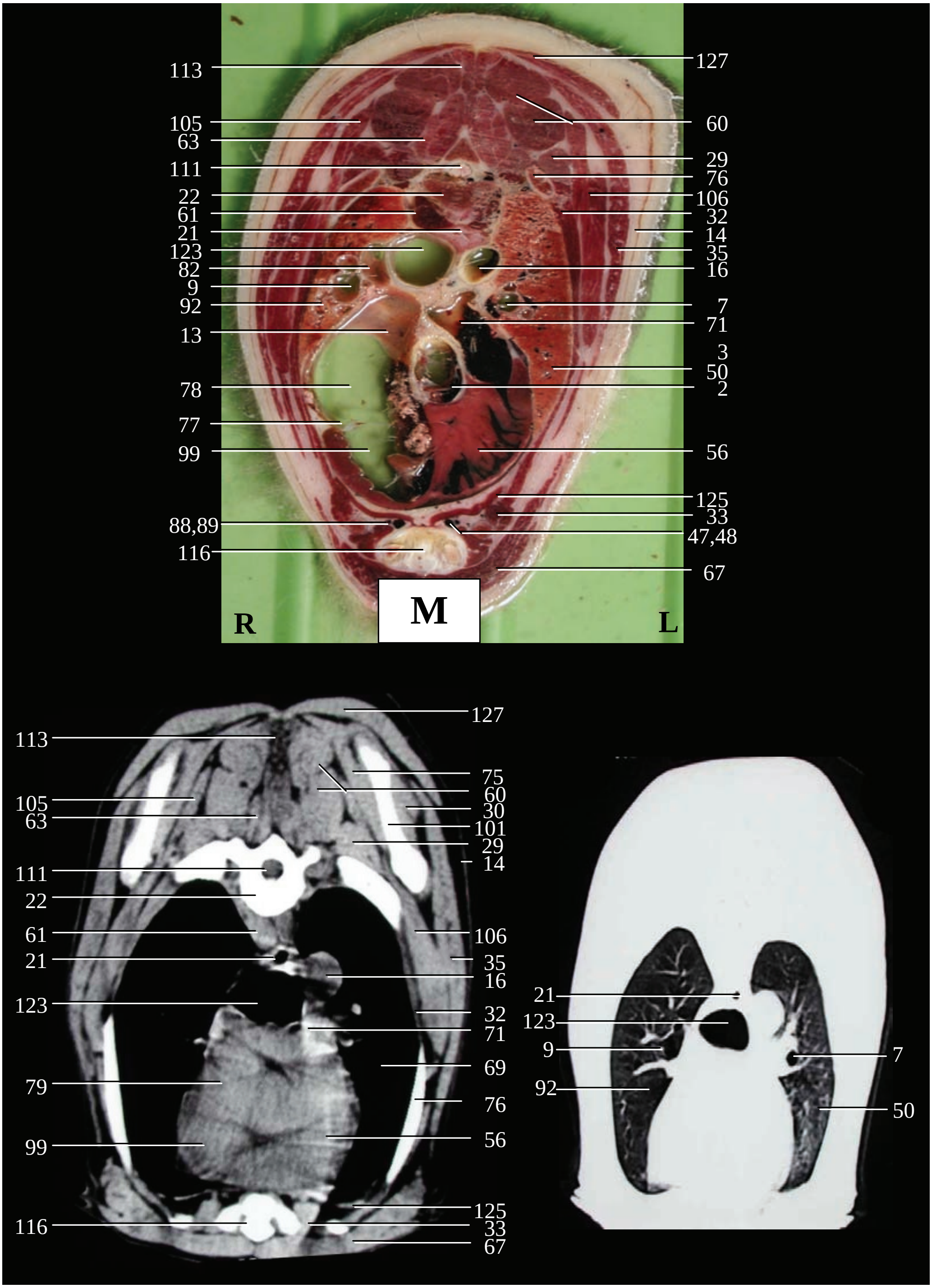
113
105
63
111
22
61
21
123
82
9
92
13
78
77
99
88,89
116
127
60
29
76
106
32
14
35
16
7
71
3
50
2
56
125
33
47,48
67
R
M
L
113
105
63
111
22
61
21
123
79
99
116
127
75
60
30
101
29
14
106
35
16
32
71
69
76
56
125
33
67
21
123
9
92
7
50

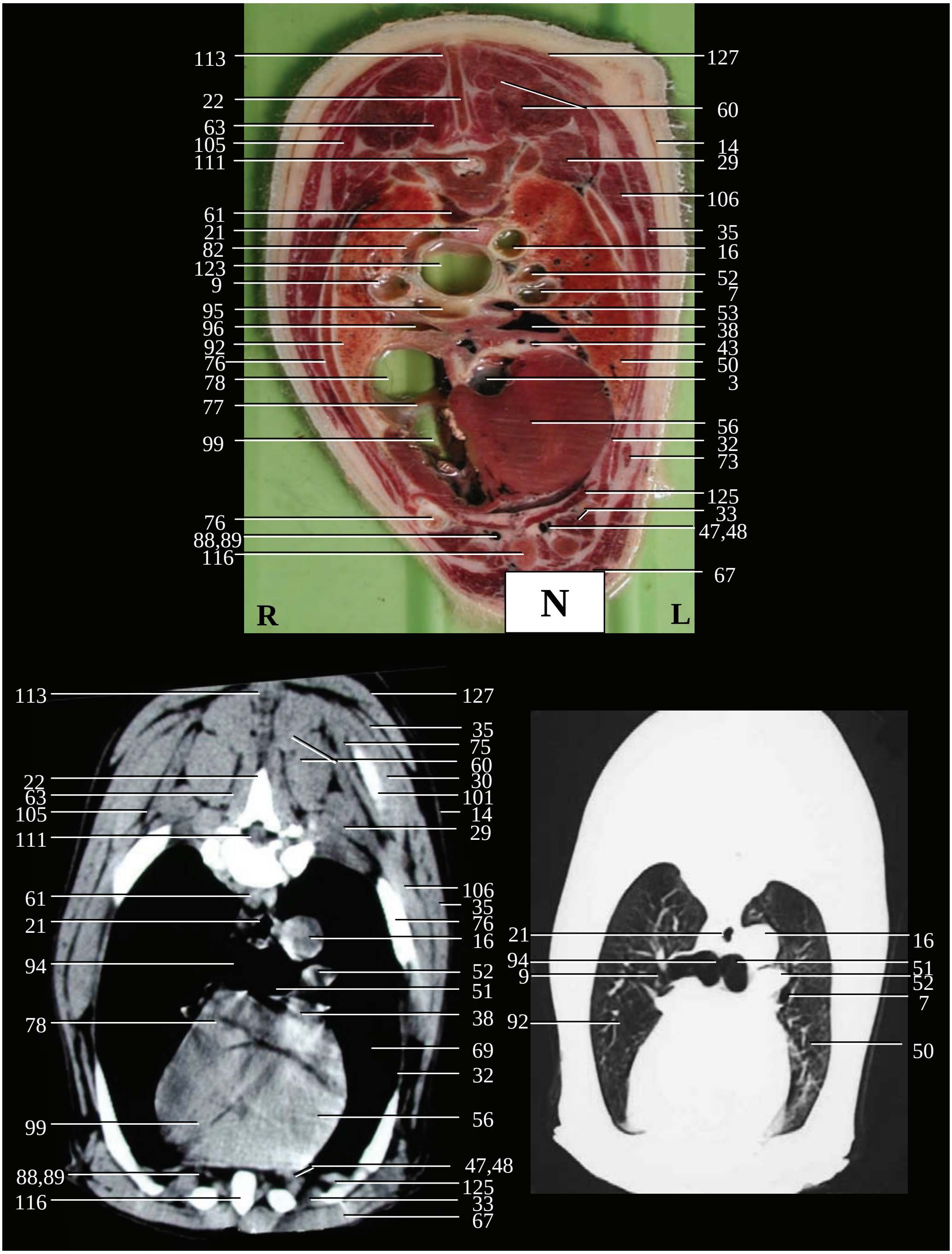
113
22
63
105
111
61
21
82
123
9
95
96
92
76
78
77
99
76
88,89
116
R
127
60
14
29
106
35
16
52
7
53
38
43
50
3
56
32
73
125
33
47,48
67
N
L
113
22
63
105
111
61
21
94
78
99
88,89
116
127
35
75
60
30
101
14
29
106
35
76
16
52
51
38
69
32
56
47,48
125
33
67
21
94
9
92
16
51
52
7
50

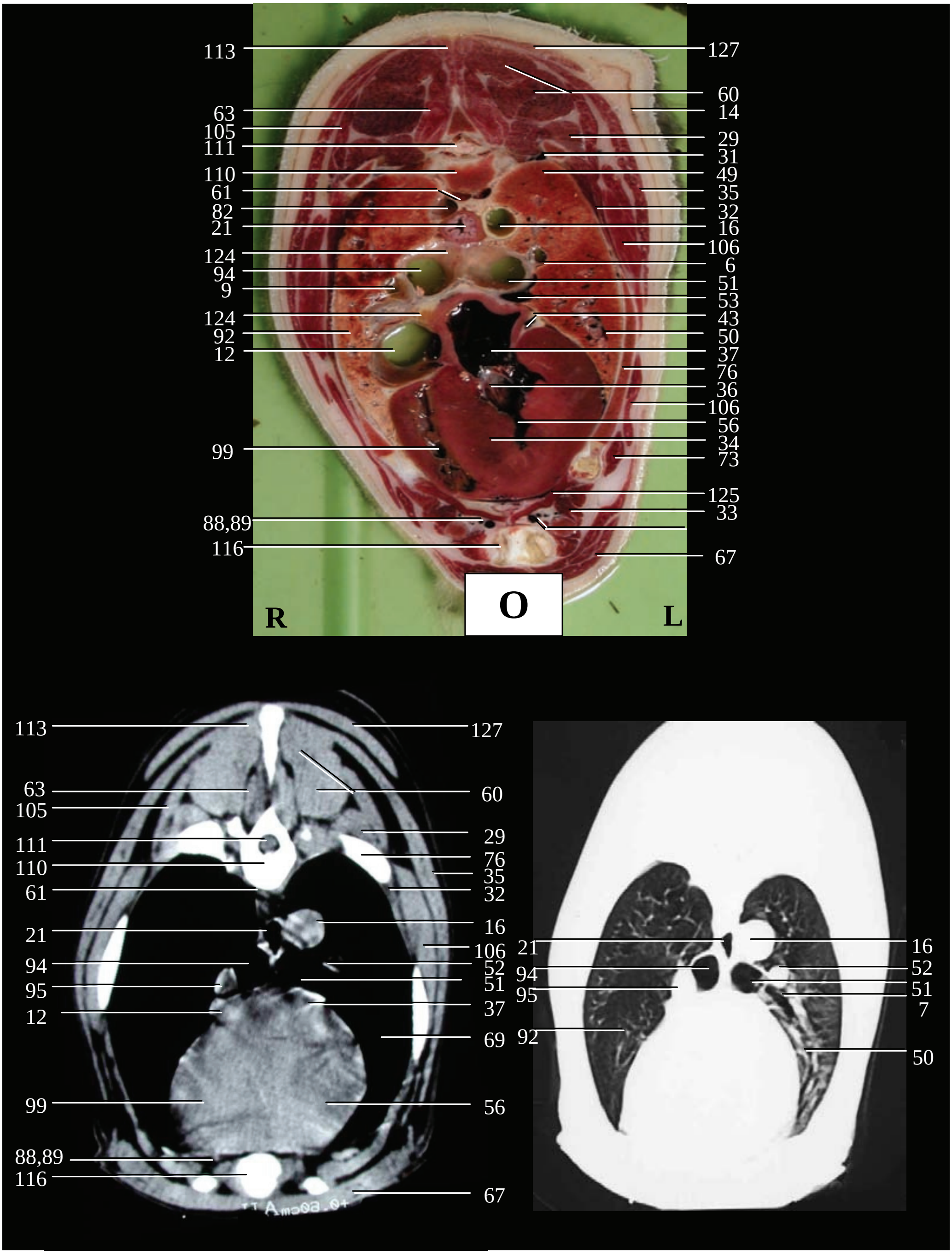
113
127
60
63
14
105
29
111
31
110
49
61
35
82
32
21
16
124
106
94
6
9
51
53
124
43
92
50
12
37
76
36
106
56
99
34
73
125
33
88,89
116
67
R
O
L
113
127
63
60
105
111
29
110
76
35
61
32
21
16
106
94
52
51
95
37
12
69
99
56
88,89
116
67
21
16
94
52
95
51
7
92
50

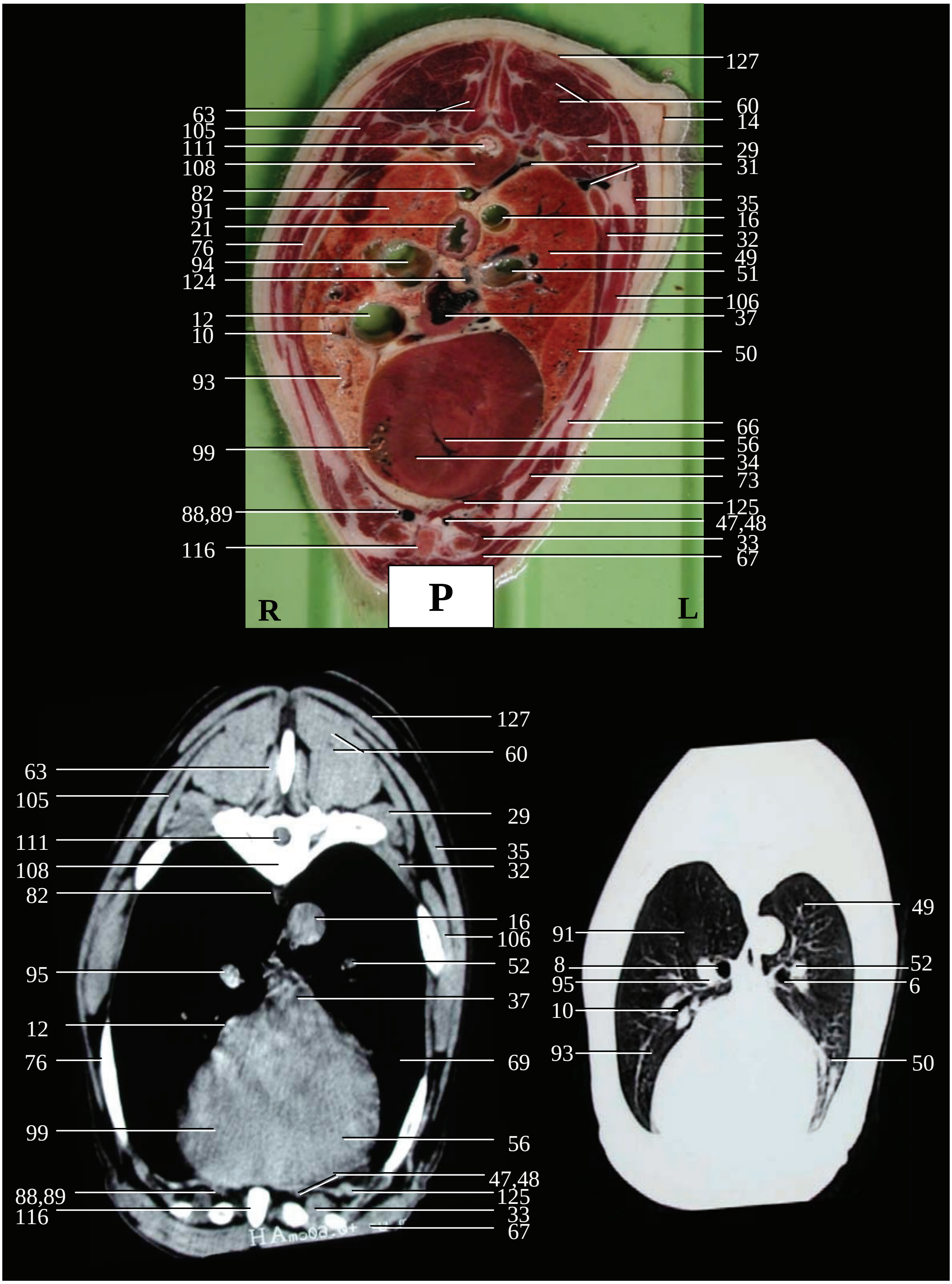
127
63
60
105
14
111
29
108
31
82
35
91
16
21
32
76
49
94
51
124
106
12
37
10
93
50
66
99
56
34
73
88,89
125
47,48
116
33
67
R
P
L
127
60
63
105
29
111
35
108
32
82
16
106
95
52
37
12
76
69
99
56
47,48
88,89
125
116
33
67
49
91
8
52
95
6
10
93
50

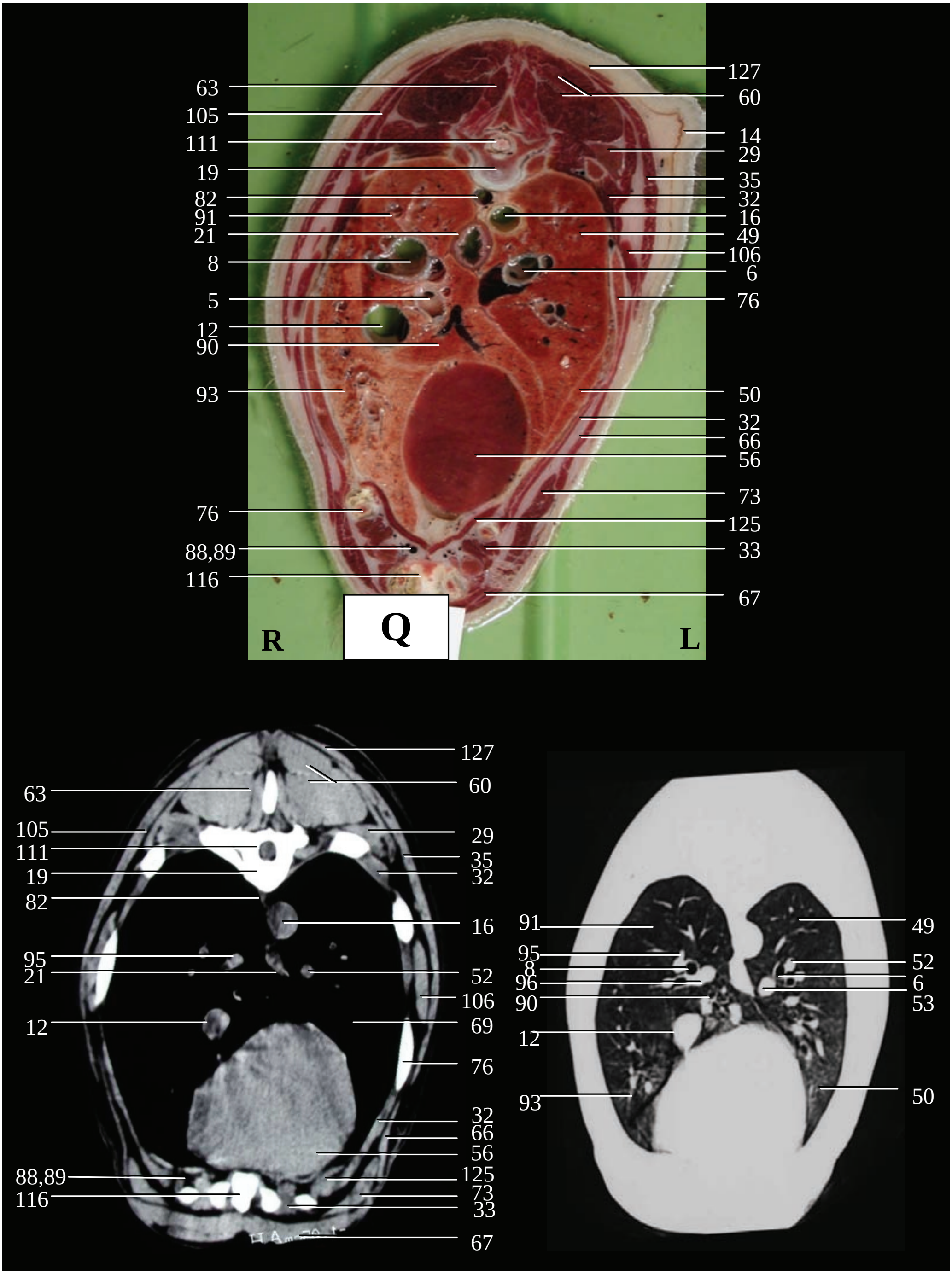
63
105
111
19
82
91
21
8
5
12
90
93
76
88,89
116
127
60
14
29
35
32
16
49
106
6
76
50
32
66
56
73
125
33
67
R
Q
L
127
60
63
105
111
19
82
29
35
32
16
95
21
52
106
12
69
76
32
66
56
88,89
116
125
73
33
67
91
95
8
96
90
12
93
49
52
6
53
50

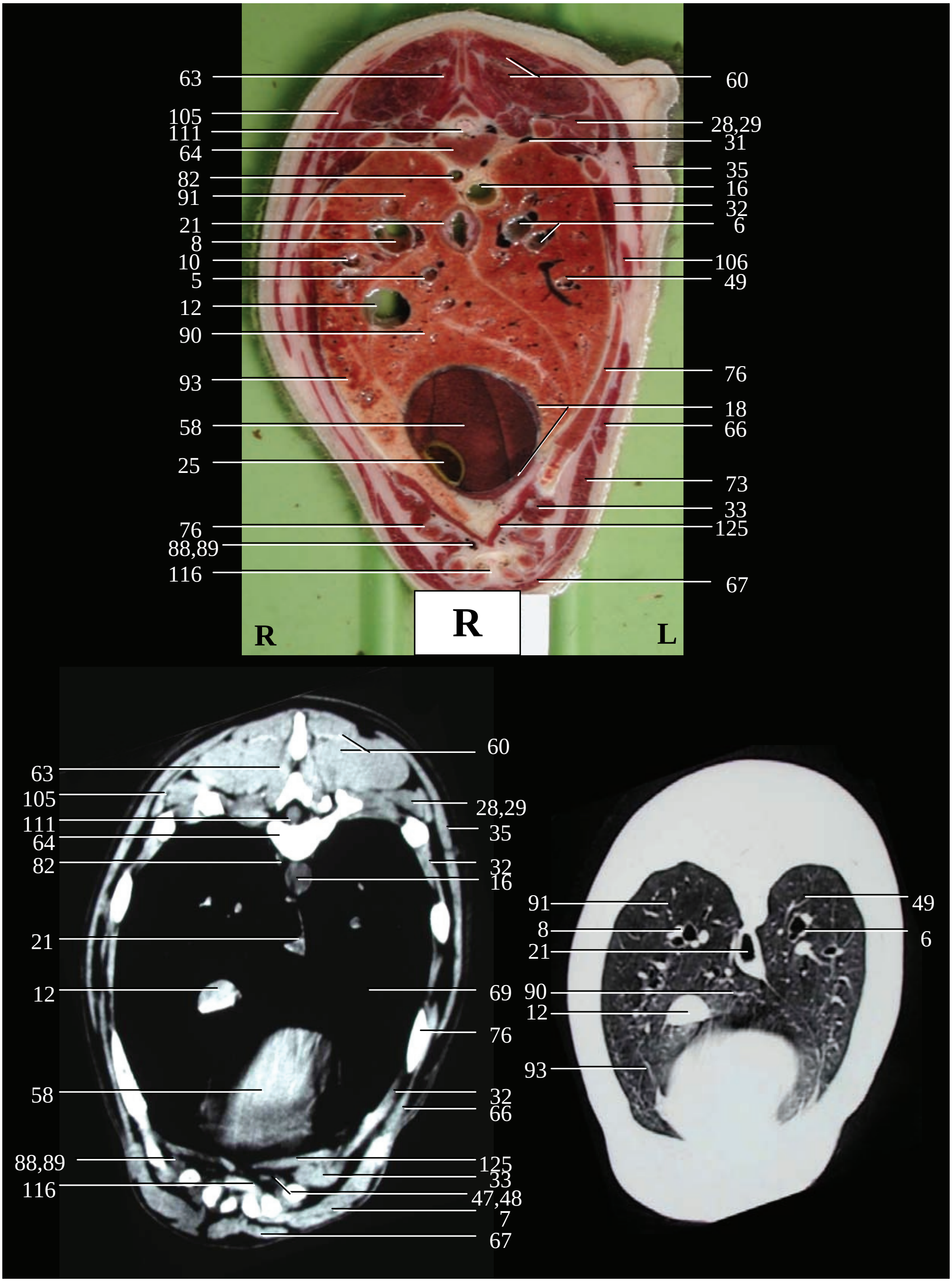
63
60
105
111
28,29
31
64
82
35
16
91
32
21
6
8
10
106
5
49
12
90
76
93
18
58
66
25
73
33
76
125
88,89
116
67
R
R
L
60
63
105
28,29
111
64
35
82
32
16
91
49
8
6
21
21
12
69
90
12
76
93
58
32
66
88,89
125
33
116
47,48
7
67

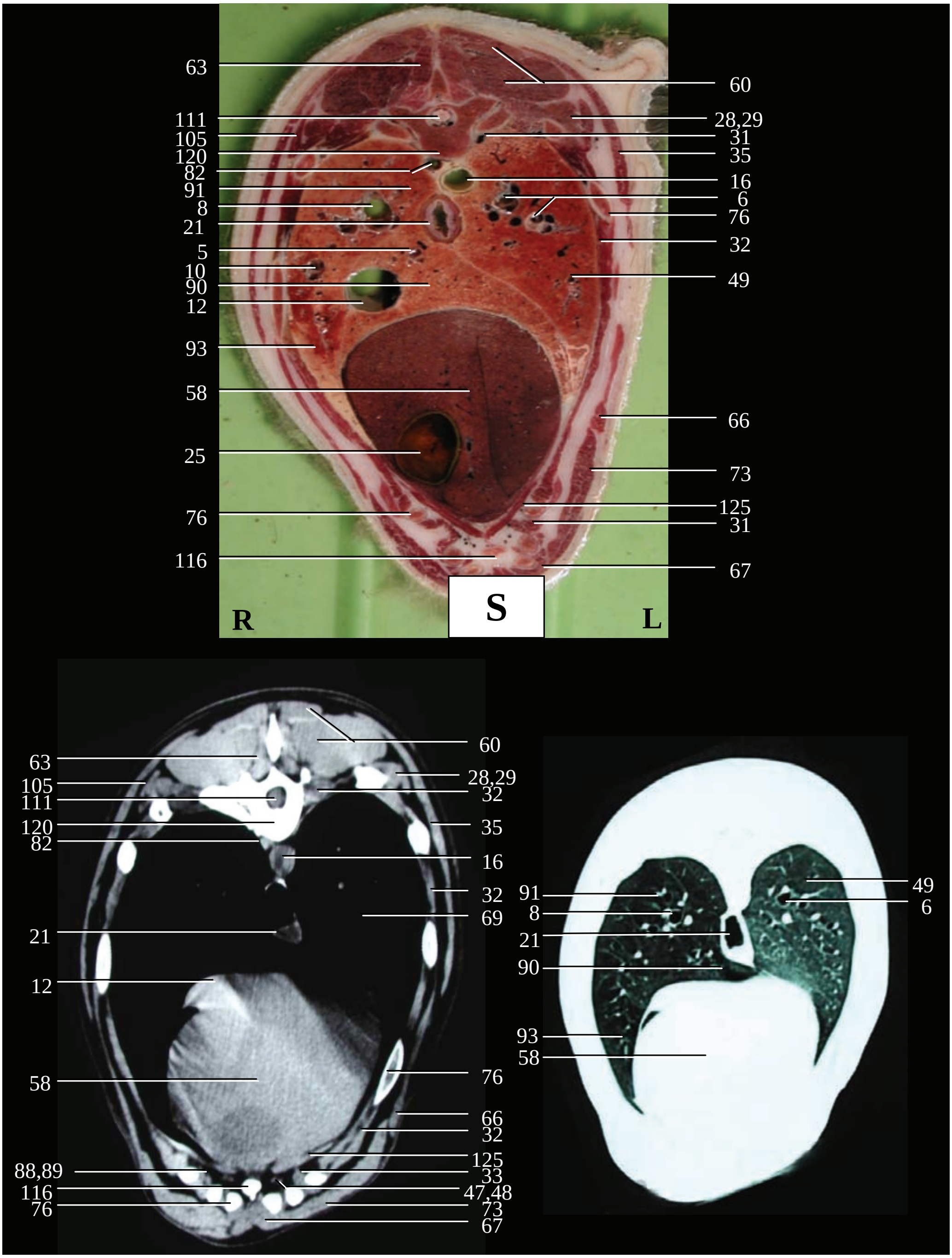
63
111
105
120
82
91
8
21
5
10
90
12
93
58
25
76
116
60
28,29
31
35
16
6
76
32
49
66
73
125
31
67
R
S
L
63
105
111
120
82
21
12
58
88,89
116
76
60
28,29
32
35
16
32
69
76
66
32
125
33
47,48
73
67
91
8
21
90
93
58
49
6

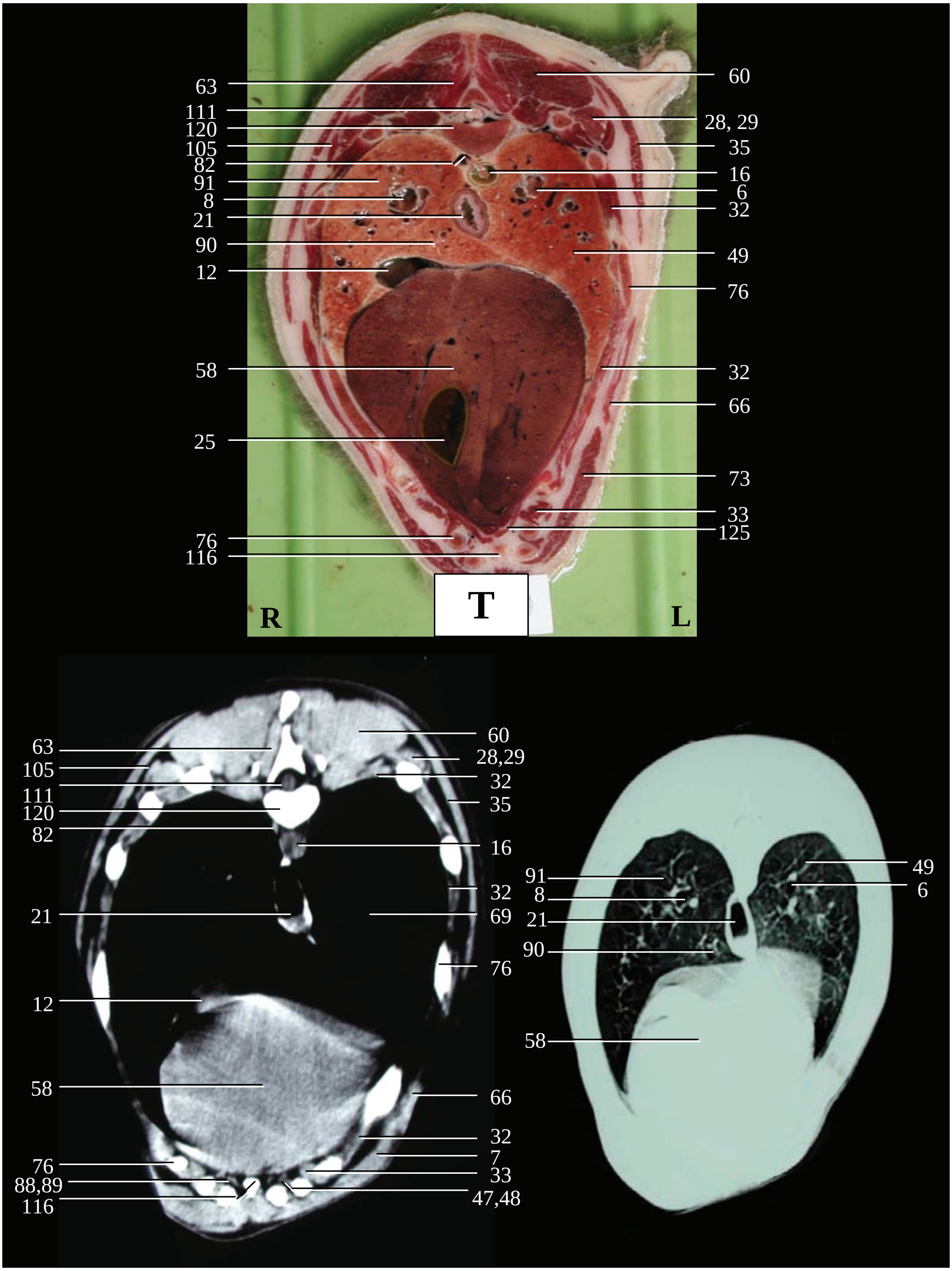
63
111
120
105
82
91
8
21
90
12
58
25
76
116
60
28, 29
35
16
6
32
49
76
32
66
73
33
125
T
R
L
63
105
111
120
82
21
12
58
76
88,89
116
60
28,29
32
35
16
32
69
76
66
32
7
33
47,48
91
8
21
90
58
49
6

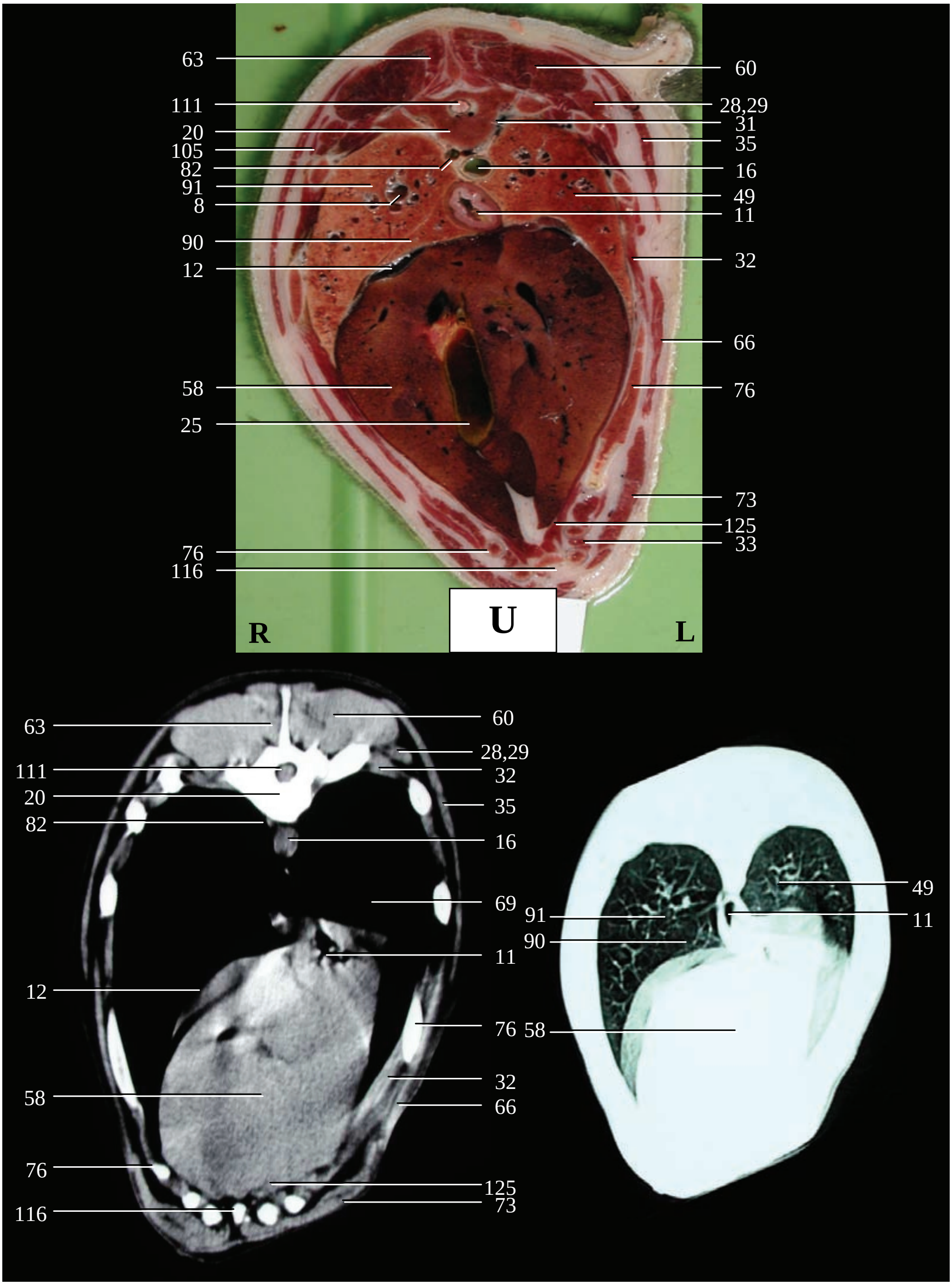
63
111
20
105
82
91
8
90
12
58
25
76
116
60
28,29
31
35
16
49
11
32
66
76
73
125
33
R
U
L
63
111
20
82
12
58
76
116
60
28,29
32
35
16
69
11
76
32
66
125
73
49
91
11
90
58

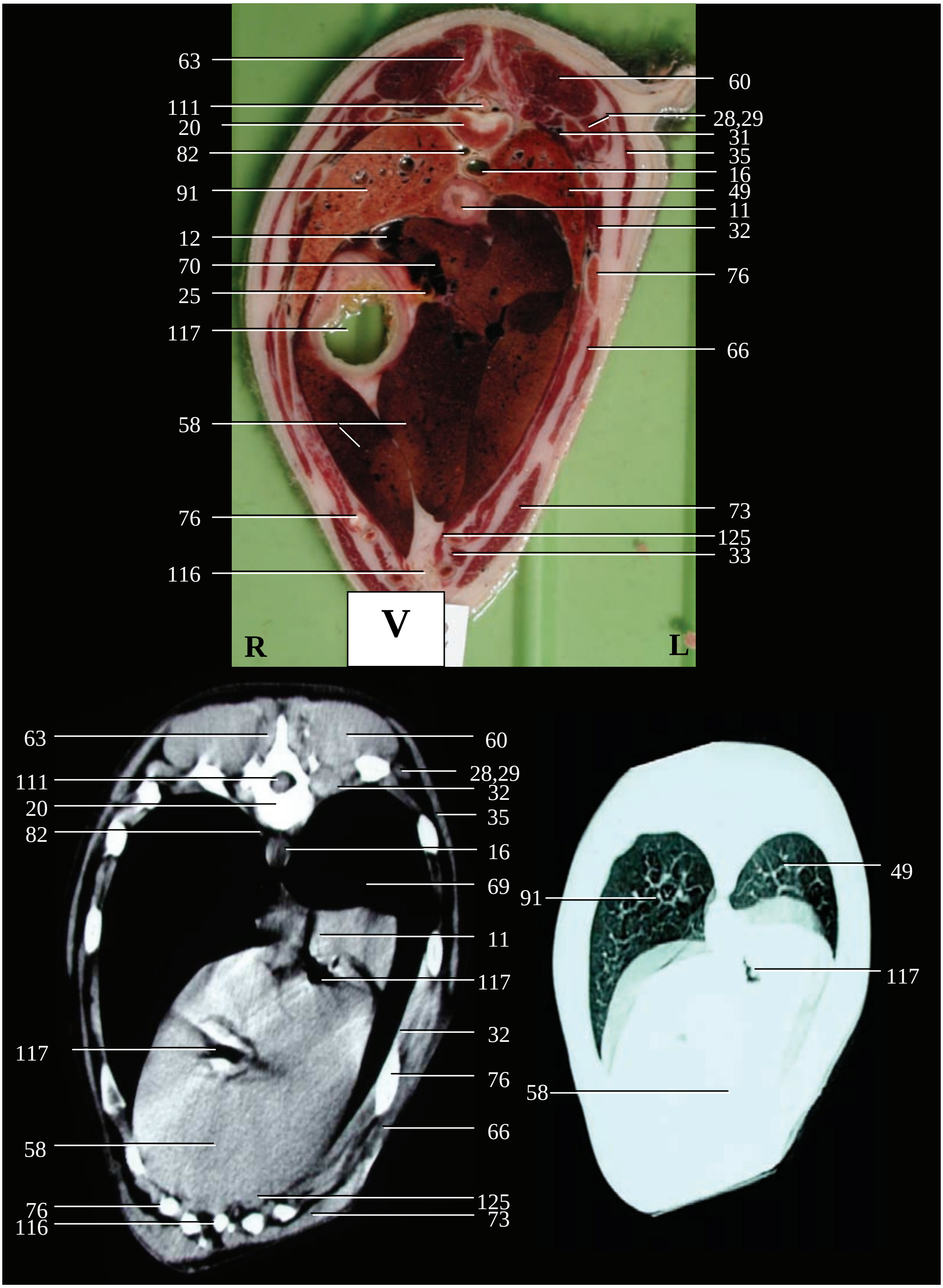
63
111
20
82
91
12
70
25
117
58
76
116
60
28,29
31
35
16
49
11
32
76
66
73
125
33
V
R
L
63
111
20
82
117
58
76
116
60
28,29
32
35
16
69
11
117
32
76
66
125
73
91
58
49
117

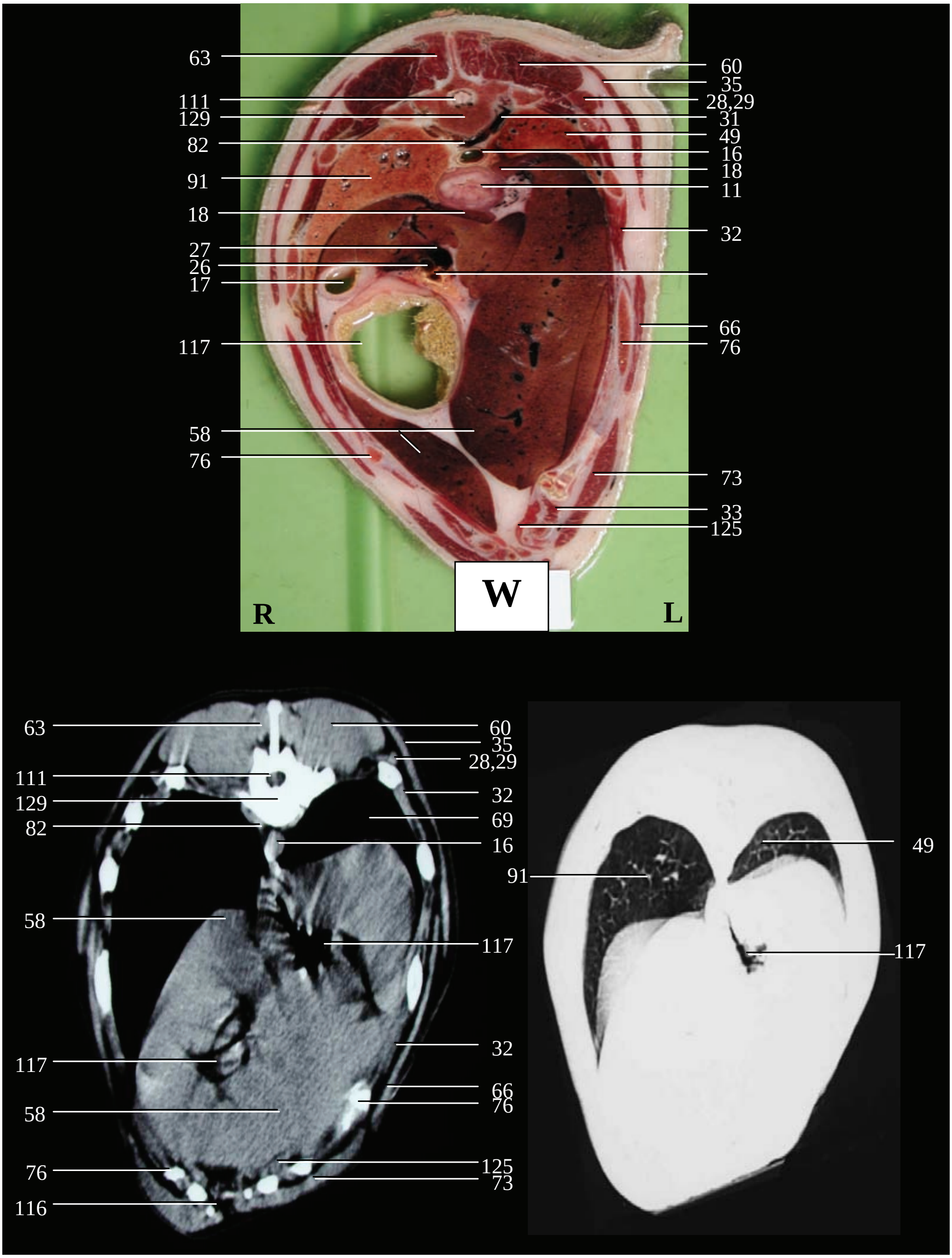
63
111
129
82
91
18
27
26
17
117
58
76
60
35
28,29
31
49
16
18
11
32
66
76
73
33
125
W
R
L
63
111
129
82
58
117
58
76
116
60
35
28,29
32
69
16
117
32
66
76
125
73
91
49
117

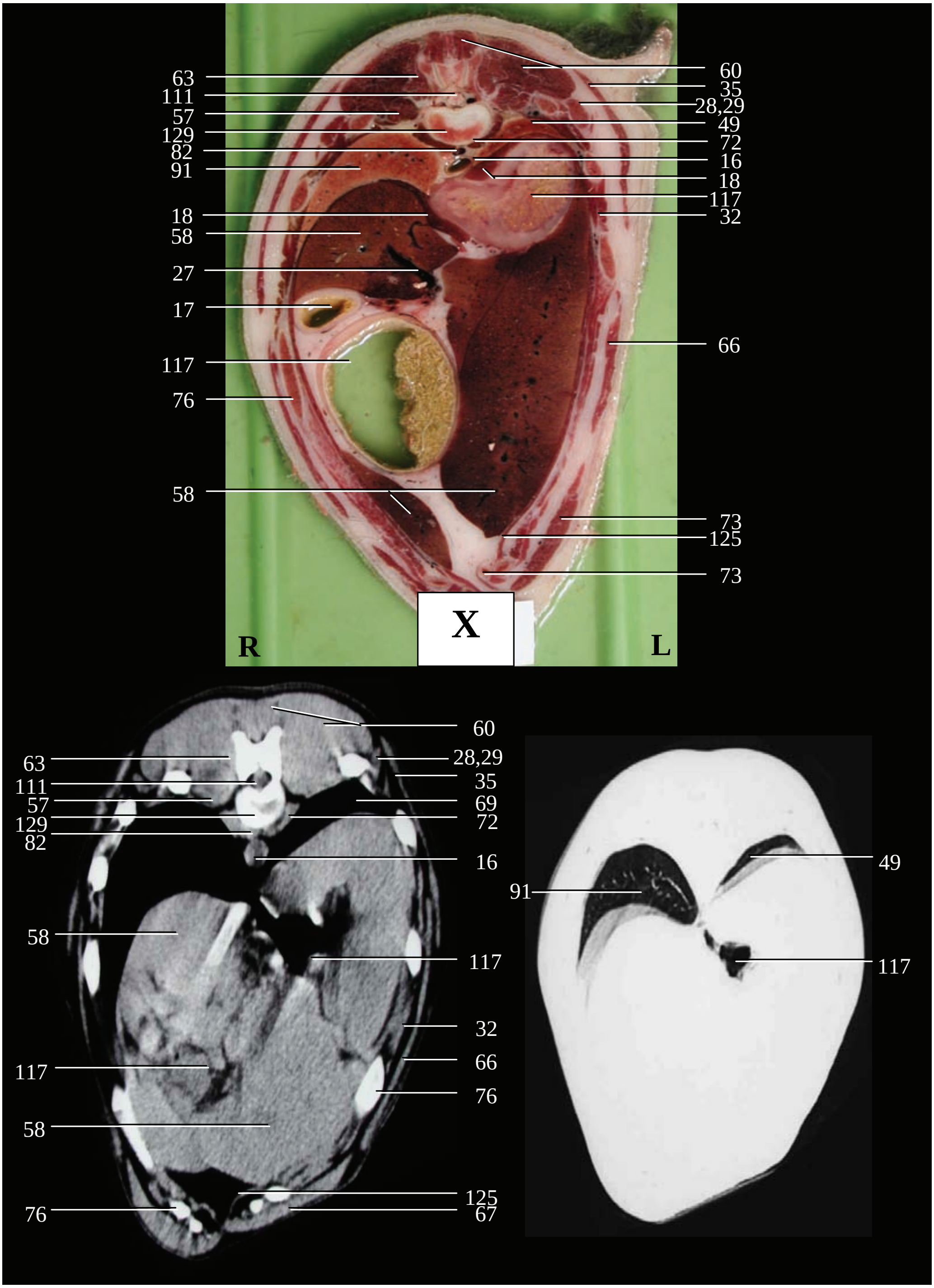
63
111
57
129
82
91
18
58
27
17
117
76
58
60
35
28,29
49
72
16
18
117
32
66
73
125
73
X
R
L
63
111
57
129
82
58
117
58
76
60
28,29
35
69
72
16
117
32
66
76
125
67
91
49
117

Figure 2—Transverse anatomic sections (top), CT soft tissue window images (bottom left), and CT lung window images (bottom right) of the thorax of a clinically normal dog. Images were obtained at sections A through X as illustrated in Fig. 1.

L = Left. R = Right.
1 = Aortic arch.
2 = Aortic valve.
3 = Ascending aorta.
4 = Brachiocephalic trunk.
5 = Bronchus of the accessory lobe of the right lung.
6 = Bronchus of the caudal lobe of the left lung.
7 = Bronchus of the cranial lobe of the left lung.
8 = Bronchus of the caudal lobe of the right lung.
9 = Bronchus of the cranial lobe of the right lung.
10 = Bronchus of the middle lobe of the right lung.
11 = Cardiac sphincter.
12 = Caudal vena cava.
13 = Cranial vena cava.
13’ = Cranial mediastinal lymph node.
14 = Cutaneus trunci muscle.
15 = Deltoid muscle.
16 = Descending aorta.
17 = Descending duodenum.
18 = Diaphragm (18’ = left crus; 18’’ = right crus).
19 = Eighth thoracic vertebra.
20 = Eleventh thoracic vertebra.
21 = Esophagus.
22 = Fifth thoracic vertebra.
23 = First thoracic vertebra.
24 = Fourth thoracic vertebra.
25 = Gallbladder.
25’ = Bile duct.
26 = Hepatic artery.
27 = Hepatic vein.
28 = Iliocostal muscle (lumbar portion).
29 = Iliocostal muscle (thoracic portion).
30 = Infraspinatous muscle.
31 = Intercostal vein.
32 = External intercostal muscle.
33 = Internal intercostal muscle.
34 = Interventricular septum of the heart.
35 = Latissimus dorsi muscle.
36 = Left atrioventricular (mitral) valve of the heart.
37 = Left atrium of the heart.
38 = Left auricle of the heart.
39 = Left axillary artery.
40 = Left axillary vein.
41 = Left brachiocephalic vein.
42 = Left common carotid artery.
43 = Left coronary vessels.
44 = Left costocervical trunk.
45 = Left costocervical vein.
46 = Left external jugular vein.
47 = Left internal thoracic artery.
48 = Left internal thoracic vein.
49 = Left lung, caudal lobe.
50 = Left lung, cranial lobe.
51 = Left principal bronchus.
52 = Left pulmonary artery.
53 = Left pulmonary vein.
54 = Left subclavian artery.
55 = Left subclavian vein.
56 = Left ventricle of the heart.
57 = Levator muscle of rib.
58 = Liver.
59 = Longissimus muscle (cervical portion).
60 = Longissimus muscle (thoracic and lumbar portion).
61 = Long muscle of the neck.
62 = Manubrium of sternum.
63 = Multifidous muscle (thoracic portion).
64 = Ninth thoracic vertebra.
65 = Nuchal ligament.
65’ = Supraspinal ligament.
66 = External oblique abdominal muscle.
67 = Pectoralis muscle (deep portion).
68 = Pectoralis muscle (superficial portion).
69 = Pleural cavity.
70 = Portal vein.
71 = Pulmonary trunk.
72 = Quadrate lumbar muscle.
73 = Straight abdominal muscle.
73’ = Straight thoracic muscle.
74 = Rhomboid muscle (cervical portion).
75 = Rhomboid muscle (thoracic portion).
76 = Rib.
77 = Right atrioventricular (tricuspidal) valve of the heart.
78 = Right atrium of the heart.
79 = Right auricle of the heart.
80 = Right axillary artery.
81 = Right axillary vein.
82 = Right azygos vein.
83 = Right brachiocephalic vein.
84 = Right common carotid artery.
85 = Right costocervical trunk.
86 = Right costocervical vein.
87 = Right external jugular vein.
88 = Right internal thoracic artery.
89 = Right internal thoracic vein.
90 = Right lung, accessory lobe.
91 = Right lung, caudal lobe.
92 = Right lung, cranial lobe.
93 = Right lung, middle lobe.
94 = Right principal bronchus.
95 = Right pulmonary artery.
96 = Right pulmonary vein.
97 = Right subclavian artery.
98 = Right subclavian vein.
99 = Right ventricle of the heart.
100 = Scalenus muscle (dorsal part).
101 = Scapula.
102 = Second thoracic vertebra.
103 = Semispinal muscle of the head (biventer muscle).
104 = Semispinal muscle of the head (complexus muscle).
105 = Dorsal serrate muscle.
106 = Ventral serrate muscle.
107 = Seventh cervical vertebra.
108 = Seventh thoracic vertebra.
109 = Sixth cervical vertebra.
110 = Sixth thoracic vertebra.
111 = Spinal cord.
112 = Spinal muscle (cervical portion).
113 = Spinal muscle (thoracic portion).
114 = Splenius muscle.
115 = Sternothyroid and sternohyoid muscle.
116 = Sternum.
116’ = Sternal lymph node.
117 = Stomach (117’= Fundus; 117’’ = Corpus; 117’’’= Pylorus).
118 = Subscapular muscle.
119 = Supraspinatous muscle.
120 = Tenth thoracic vertebra.
121 = Major teres muscle.
122 = Third thoracic vertebra.
123 = Trachea.
124 = Tracheal bifurcation.
124’ = Tracheobroncheal lymph node.
125 = Transverse thoracic muscle.
126 = Trapezius muscle (cervical portion).
127 = Trapezius muscle (thoracic portion).
128 = Triceps muscle of the forearm (long head).
129 = Twelfth thoracic vertebra.
130 = Vertebral artery.
131 = Vertebral vein.

be discerned. In 1 dog, however, the lobar bronchus of the accessory lobe of the right lung could not be discerned. Large intrathoracic vessels such as the descending aorta, caudal vena cava, and major pulmonary arteries and veins could be identified in all instances. Of the heart and liver only contours were visible. The presence of air in the esophagus and in cardia and fundus of the stomach allowed the position of these organs to be determined on CT images. However, it was impossible to see the cardiac sphincter and all parts of the stomach in any dog.

DISCUSSION

Results of our study indicate that the use of anatomic sections is helpful for identifying a large number of thoracic structures that are visible on CT images of the canine thorax. Only nerves and small vessels could not be discerned. Anatomic images made in our study matched closely with corresponding CT images, except for the more caudal position of the scapulae on CT images. This indicates that the forelimbs were less extended during CT examination than during the freezing process.

Dogs are routinely positioned in sternal (ventral) recumbency to prevent recumbency-induced pulmonary atelectasis. [4,27,30] Dogs with severe hydrothorax are scanned twice; once in ventral recumbency and once in dorsal recumbency. [27] For a complete examination of the lungs, it is recommended to scan the patient in various positions, depending on the area of interest, because atelectasis and gravitational pulmonary-flow differences may alter the density of the dependent lung. Assisted suspended inspiration may also be needed to better assess overall lung density.[32]

Thoracic CT images were evaluated by use of a lung and a soft tissue (mediastinal) setting. A lung window consists of a broad window width (1000 to 2000 HU) centered around a negative value (-600 to –700 HU). This allows the lung parenchyma to appear gray. A mediastinal window consists of a narrow window width (300 to 400 HU) centered on soft tissues (40 to 50 HU).[32] Various structures of the respiratory tract were most distinct on the lung window. Still, for detection of pathologic processes, the lungs should be evaluated with lung and mediastinal windows to avoid missing lesions excluded by window settings.[32]

In our study the various parts of the heart could not be identified on soft tissue CT images and the details of the lungs could not be defined on lung window CT images as a result of motion artifacts.

Because thoracic CT investigations were performed on living dogs, cardiovascular movements could not be avoided. Applying intermittent positive-pressure ventilation to the lungs decreased motion artifacts caused by irregular or fast respiration of each dog. Computed tomographic images were taken during the expiratory pause of dogs as described by Henninger et al.[29] Hyperventilation is another method that has been described for decreasing respiratory movements during performance of intrathoracic biopsies.[25] Use of newer scanning equipment such as helical (spiral) computed tomography, could also minimize these motion artifacts.[2,19,20,30,32] In the past few years, high-resolution computed tomography (HRCT) has been found useful for evaluation of the lungs and for diagnosis of a variety of pulmonary diseases.[9,15,18,30,32,50] HRCT allows structures as small as 0.2mm to be visualized, gives a detailed display of lobular and sublobular anatomy and allows a better assessment of parenchymal detail than conventional CT. However the examination time is long and the radiation burden inherent in HRCT is considerable. Therefore, conventional CT of the lungs should still be used for routine indications and HRCT should be reserved for particular circumstances. [11]

Until now some information has been published[3,27,29,30,32] on the use of computed tomography for pulmonary evaluation in animals. Nevertheless, applications of pulmonary computed tomography in dogs and cats appear to be similar to those in humans and the role of computed tomography for diagnostic and investigative studies of the heart and lungs will likely progress as access to better equipment improves.[32]

A number of vessels identified on anatomic sections could not be discerned on corresponding CT images. Intravascular administration of contrast media might be helpful in identification of vascular structures on soft tissue CT images.[29] In humans, computed tomography following an IV bolus of contrast medium has replaced arteriography for the diagnosis of most intrathoracic vascular lesions.[11] Intravascular contrast agents are also useful in defining the extent of mediastinal masses and their relation to delicate structures such as major vessels or the heart and to enhance the pleura.[4,21,29,32] Intravenous contrast enhancement of the heart allows the atria and chambers to become readily visible and a rough estimation of chamber wall thickness can be made.[29] Subsequently a definitive diagnosis of pericardial effussion becomes also possible.[22] In our study, IV administration of contrast medium was not used because the aim was to describe plain CT images made by standard procedures.

Thoracic CT is more and more routinely used in veterinary medicine. In the future its use in animals as a diagnostic and preoperative tool for detection of thoracic diseases and as a guide for performing thoracic biopsies will undoubtedly still evolve.[1] Results of our study indicate that CT images provide detailed information on most structures of the canine thorax. Therefore our description of CT anatomy of the canine thorax could be used for evaluation of CT images of dogs with thoracic disease.

---

[a] Tidwell A, Johnson K. Applications of CT guided biopsy in small animals (abstr). Vet Radiol Ultrasound 1998;39:238.

[b] Domitor, Orion Corp, Espoo, Finland.

[c] Pentothal, Abbott Laboratories, North Chicago, Ill.

[d] Fluothane, Zeneca, Wilmington, Del.

[e] CT-scanner Pace Plus, GE Medical Systems, Milkauwee, Wis.

[f] X-ray film, Fuji Photo Film Co, Tokyo, Japan.

[g] T-61, Hoechst Roussel Vet GmbH, Unterschleiβheim, Germany.

[h] Electric band saw, Eureka, Savioli Lelio Snc, Coriano, Italy

REFERENCES

1. Jost G, Sagel S, Stanley R, et al. Computed tomography of the thorax. Radiology 1978;126:125-136.

2. Fike J, Druy E, Zook B, et al. Canine anatomy as assessed by computerized tomography. Am J Vet Res 1980;41:1823-1832.

3. Spann D, Sellon R, Thrall D, et al. Computed tomographic diagnosis: use of computed tomography to distinguish a pulmonary mass from alveolar disease. Vet Radiol Ultrasound 1998;39:532-535.

4. Stickle R, Hathcock J. Interpretation of computed tomographic images. Vet Clin North Am Small Anim Pract 1993;23:417-435.

5. Breyer R, Karstaedt N, Mills S, et al. Computed tomography for evaluation of mediastinal lymph nodes in lung cancer: correlation with surgical staging. Ann Thorac Surg 1984;38:215-220.

6. Brown L, Muhm J. Computed tomography of the thorax: current perspectives. Chest 1983;83:806-813.

7. Goldwin R, Heitzman E, Proto A. Computed tomography of the mediastinum: normal anatomy and indications for the use of CT. Radiology 1977;124:235-241.

8. Jaffe C. Computed tomography evaluation of abscesses. Connecticut Medicine 1981;45:291-295.

9. Kazerooni E. High-resolution CT of the lungs. Am J Roentgenol 2001;177:501-519.

10. Knisely B, Kuhlman J. Radiographic and computed tomography (CT) imaging of complex pleural disease. Crit Rev Diagn Imag 1997;38:1-58.

11. Mootoosamy I, Reznek R. Computed tomography scanning of the thorax. Br J Hosp Med 1993;50:95-106.

12. Müller H, van Kaick G, Lullig H, et al. Indications for computerized tomography of the lungs and mediastinum. Prax Klin Pneumol 1981;35:213-219.

13. O’Donovan P, Eng P. Pleural changes in malignant pleural effusions: appearance on computed tomography. Cleve Clin J Med 1994;61:127-131.

14. Poon P, Bronskill M, Henkelman R, et al. Mediastinal lymph node metastases from bronchogenic carcinoma detection with MR imaging and CT. Radiology 1987;162:651-656.

15. Primack S, Remy-Jardin M, Remy J, et al. High-resolution CT of the lung: pitfalls in the diagnosis of infiltrative lung disease. Am J Roentgenol 1996;167:413-418.

16. Rotte K, Angerstein W. The application of computed tomography in the diagnosis of thoracic diseases. Z Erkrank Atm Org 1980;154:271-282.

17. Siegelman S, Khouri N, Leo F, et al. Solitary pulmonary nodules: CT assessment. Radiology 1986;160:307-312.

18. Swensen S, Aughenbaugh G, Douglas W, et al. High-resolution CT of the lungs: findings in various pulmonary diseases. Am J Roentgenol 1992;158:971-979.

19. Uffmann M, Prokop M. Multislice-CT der Lunge: Technik und Klinische Anwendungen. Radiologe 2001;41:240-247.

20. Waters D, Coakley F, Cohen M, et al. The detection of pulmonary metastases by helical CT: a clinicopathologic study in dogs. J Comput Assist Tomogr 1998;22:235-240.

21. Westra D, Verbeeten B. Indications for computerized tomography of the thorax. Ned Tijdschr Geneeskd 1983;127:617-621.

22. Wong B, Lee K, Mac Arthur R. Diagnosis of pericardial effusion by computed tomography. Chest 1982;81:177-181.

23. Zerhouni E, Stitik F. Controversies in computed tomography of the thorax: the pulmonary nodule-lung cancer staging. Radiol Clin North Am 1985;23:407-426.

24. Garbagnati F, Lutman R, Valvassori L, et al. Nonpulmonary thoracic biopsy. Eur J Radiol 1989;9:214-216.

25. Tidwell A, Johnson K. Computed tomography-guided percutaneous biopsy in the dog and cat: description of technique and preliminary evaluation in 14 patients. Vet Radiol Ultrasound 1994;35:445-456.

26. Ahlberg N, Hoppe F., Kelter U, et al. A computed tomographic study of volume and x-ray attenuation of the lungs of Beagles in various body positions. Vet Radiol 1985;26;43-47.

27. Burk R. Computed tomography of thoracic diseases in dogs. J Am Vet Med Assoc 1991;199:617-621.

28. Chen Q, Klein J, Gamsu G, et al. High-resolution computed tomography of the mammalian lung. Am J Vet Res 1992;53:1218-1224.

29. Henninger W. Use of computed tomography in the diseased feline thorax. J Small Anim Pract 2003;44:56-64.

30. Morandi F, Mattoon J, Lakritz J, et al. Correlation of helical and incremental high-resolution thin-section computed tomographic imaging with histomorphometric quantitative evaluation of lungs in dogs. Am J Vet Res 2003;7:935-944.

31. Ottesen N, Moe L. An introduction to computed tomography in the dog. Eur J Comp Anim Pract 1998;8:29-36.

32. Schwarz L, Tidwell A. Alternative imaging of the lung. Clin Techn Small Anim Pract 1999;14:187-206.

33. Tidwell A. Diagnostic pulmonary imaging. Problems. Vet Med 1992;4:239-264.

34. Tidwell A. Uses of computed tomography in cardiopulmonary disease. In: Bonagura JD (ed): Kirk: Current Veterinay Therapy XIII. Philadelphia, PA: Saunders, 2000;709-710.

35. Walker M, Hartsfield S, Matthews N, et al. Computed tomography and blood gas analysis of anesthetized bloodhounds with induced pneumothorax. Vet Radiol Ultrasound 1993;34:93-98.

36. De Haan C, Papageorges M, Kraft S. Radiographic Diagnosis. Vet Radiol 1991;32:75-77.

37. Douglass J, Berry C, Thrall D, et al. Radiographic features of aortic bulb/valve mineralization in 20 dogs. Vet Radiol Ultrasound 2003;44:20-27.

38. Essman S, Hoover J, Bahr R. An intrathoracic malignant peripheral nerve sheat tumor in a dog. Vet Radiol Ultrasound 2002;43:255-259.

39. Punto L, Nevalainen T, Wiljasalo S, et al. Computed tomography of aspiration pneumonia in a dog. Vet Radiol 1984;25:43-45.

40. Schwarz T, Sullivan M, Stork C, et al. Aortic and cardiac mineralization in the dog. Vet Radiol Ultrasound 2002;43:419-427.

41. Samii V, Biller D, Koblik P. Normal cross-sectional anatomy of the feline thorax and abdomen: comparison of computed tomography and cadaver anatomy. Vet Radiol Ultrasound 1998;39:504-511.

42. Smallwood J, Healey W. Computed tomography of the thorax of the adult Nubian goat. Vet Radiol 1982;23:135-143.

43. Smallwood J, George T. Anatomic atlas for computed tomography in the mesaticephalic dog: thorax and cranial abdomen. Vet Radiol Ultrasound 1993;34:65-84.

44. Feeney D, Fletcher T, Hardy R. Atlas of correlative imaging anatomy of the normal dog. Ultrasound and computed tomography. Philadelphia: WB Saunders Co, 1991.

45. Polgar M, Probst A, Sora M, et al. Plastination of whole-body slices : a new aid in cross-sectional anatomy, demonstrated for thoracic organs in dogs. Wiener Tierärztl Monatsschr 2003;90:45-52.

46. Zook B, Hitzelberg R, Bradley E. Cross-sectional anatomy of the Beagle thorax. Vet Radiol 1989;30:277-281.

47. Done S, Goody P, Evans S, et al. Chapter 5 : The thorax. In: Done S, Goody P, Evans S, et al. eds. Color atlas of veterinary anatomy, Volume 3. London: Mosby, 1999;1-59.

48. Popesco P. Volume II Trunk. In : Atlas of topographical anatomy of the domestic animals. Philadelphia: WB Saunders Co, 1977.

49. World Association of Veterinary Anatomists (WAVA). Nomina Anatomica Veterinaria. 4th ed. Ithaca, NY: International Committee on Veterinary Gross Anatomical Nomenclature, 1994;1-198.

50. Gruden J, Webb R, Warnock M. Centrilobular opacities in the lung on High-Resolution CT: Diagnostic considerations and pathologic correlation. Am J Roentgenol 1994;162:569-574.

2.1.2. Thoracoscopic anatomy of dogs positioned in lateral recumbency

Lieve M. De Rycke*, DVM; Ingrid M. Gielen*, DVM, MSc;
Bernadette Van Ryssen*, DVM, PhD; Henri van Bree*, DVM, PhD;
Paul J. Simoens**, DVM, PhD; Ingeborg Polis, DVM ***

*Department of Medical Imaging, Faculty of Veterinary Medicine, Ghent University,
Salisburylaan 133, 9820 Merelbeke, Belgium.

**Department of Morphology, Faculty of Veterinary Medicine, Ghent University,
Salisburylaan 133, 9820 Merelbeke, Belgium.

*** Department of Small Animal Medecine, Faculty of Veterinary Medicine,
Ghent University, Salisburylaan 133, 9820 Merelbeke, Belgium

Adapted from :

De Rycke LM, Gielen IM, Van Ryssen B, van Bree H, Simoens PJ, Polis I. Thoracoscopic anatomy of dogs positioned in lateral recumbency. *J Am Anim Hosp Assoc* 2001;37:543-548.

SUMMARY

In four healthy, adult male German shepherd dogs, thoracoscopy was performed to provide a detailed description and illustration of the endoscopic anatomy of the normal intrathoracic structures of dogs. The dogs were anesthetized and placed in left or right lateral recumbency. The cannula and the endoscope were advanced into the thoracic cavity via entry of the free upper side in the dorsal third of the eighth intercostal space. Most intrathoracic structures of the left and right hemithorax were endoscopically visible. During the four thoracoscopic procedures, endoscopic photographs were taken and are illustrated in this paper.

A sound knowledge of the anatomy of intrathoracic structures is a prerequisite for diagnostic and therapeutic thoracoscopy.

INTRODUCTION

Thoracoscopy is an accurate and practical technique for diagnosis and surgical management of intrathoracic pathologies. The technique is minimally invasive and allows a rapid postoperative recovery. Disadvantages are the expensive equipment and the need for technical training of the surgeon. Contraindications to thoracoscopy are profuse bleeding and hemodynamic instability.

In human surgery, thoracoscopy is a rapidly expanding area. It is used for diagnosis of diseases and traumatic injuries involving the pleura, lungs, esophagus, heart, pericard, diaphragm, lymph nodes and vertebrae[1-5]. Biopsies of lungs and lymph nodes, for diagnosis of diffuse lung diseases or for staging of lung cancer, can be taken under thoracoscopic guidance. Thoracoscopic biopsies are also possible for extrapulmonary tissues such as vertebral bodies, thoracic wall and mediastinal masses, and pleura[6-8] .
Thoracoscopy is not only a diagnostic tool, but can also be used for minimal invasive thoracic surgery such as lung lobectomy or lung wedge resection in cases of lung disease, neoplasia and bullae (bullectomy); drainage of empyema, hemothorax and spinal abcesses; esophageal myotomy or esophagectomy in case of neoplasia; fenestration of the pericard or pericardectomy in case of pericardial effusion; ligation of patent ductus arteriosus and vascular ring-anomaly; thymectomy in the setting of myasthenia gravis; resection of benign thymic, pericardial and bronchogenic cysts; resection of neurogenic mediastinal tumors; sympathectomy in case of palmar hyperhidrosis and parietal pleurectomy in case of malignant pleural effusion[8-23]. Thoracoscopy is also used for surgical treatment of traumatic thoracic injuries; diaphragmatic hernia; bronchopleural fistulas; chylothorax; spontaneous pneumothorax and herniated intervertebral discs[3,5,24-26].

Until now, the application of the technique in veterinary medicine is limited to experimental studies and direct observation of the pleural cavity and intrathoracic structures, collection of pleural fluid, repair of diaphragmatic hernias, and obtaining of biopsy specimens of lungs in horses[27-30] and dogs[31-36]. Some surgical interventions by means of thoracoscopy have been reported in dogs including ligation of the thoracic duct, correction of persistent right aortic arch, pericardectomy, lung lobectomy, ligation of a patent ductus arteriosus, and fenestration of thoracic intervertebral discs [37-48]. There is still much to learn about indications, side-effects, advantages, disadvantages, complications and contraindications of veterinary thoracoscopy. Moreover, before performing thoracoscopy a good knowledge of the intrathoracic anatomy is required.

The purpose of the present study was to describe and illustrate the endoscopic anatomy of the normal intrathoracic structures in four healthy dogs.

MATERIALS AND METHODS

Thoracoscopy was performed on 4 adult, male, clinically healthy Shepherd dogs owned by the University of Ghent, Faculty of Veterinary Medicine, Department of Medical Imaging. The animals weighed between 25 and 33 kg.

The animals had fasted for 12 to 24 hours prior to the procedure. After positioning the dogs in left (n=2) or right (n=2) lateral recumbency thoracoscopy was performed via the free upper side.

All thoracoscopic examinations were performed under a surgical plane of anesthesia.

The animals were premedicated with fentanyl (0.005-0.01 mg/kg, IV) and droperidol (0.25 - 0.5 mg/kg, IV). Anesthesia was induced with propofol (4-6 mg/kg, IV) and maintained on isoflurane vaporized in 100% oxygen using a conventional tracheotube. Lactated Ringer’s solution (10 ml/kg/h) was administered intravenously throughout the procedure. Heart rate and blood oxygenation were monitored by pulse-oximetry and CO2ET by capnography. A catheter was inserted into the femoral artery for analysis of Pa O2 and Pa CO2.

The skin was clipped over the entire upper thoracic wall. After aseptic preparation the surgical site was draped and a 1 cm long dorsoventral skin incision was made in the dorsal third of the 8th intercostal space. The skin incision was continued through the intercostal muscles. A 10-mm cannula was advanced through the incision into the thoracic cavity. To establish a pneumothorax and to collapse the lung lobes in the associated hemithorax, a high-flow, pressure-limited insufflating device was connected to the cannula and carbondioxide was insufflated (4 l / min) until an intrathoracic pressure of 3 mm Hg was achieved. Positive-pressure ventilation (10-15 ml/kg) was given to the other lung.

Subsequently either a 10 mm, 0°-view angle or a 5 mm, 25°-view angle endoscope connected to a 300W xenon light source and video camera was introduced through the cannula. Through a second cannula placed in the 4th intercostal space a hand-shaped tool was inserted to manipulate the lunglobes.

Thoracoscopic photographs were taken. After completing the examination the lungs were reexpanded by overinsufflation of oxygen under direct visualisation through the endoscope and the instrumentation was removed. Afterwards, the chest wall incisions were closed with one suture (vicryl®) in the superficial fascia and one suture (vicryl®) in the skin. For the next 24 hours post - thoracoscopy the dogs were observed for signs of hemorrhage or hypotension by monitoring mucosal membrane color, capillary refill time, pulse and respiratory rates. No complications were encountered.

RESULTS

The lateral surface of the lungs covered by pulmonary pleura were easily to evaluate. The pulmonary pleura adheres tightly to the surface of the lungs and is normally smooth and shiny. With endoscopic magnification, close-up observation permitted clear visualisation of superficial lung alveoli. On the left side of the thorax both the cranial and caudal lobes of the left lung were observed. The cranial lobe is devided into cranial and caudal parts by a shallow cardiac notch (Fig. 1). On the right side of the thorax the cranial, middle and caudal lobes of the right lung were inspected. The accessory lobe of the right lung lies medially to the caudal lobe and is therefore unapproachable for the endoscope. The interlobar fissures were evaluated by displacement of adjacent pulmonary tissue by the hand-shaped tool.

The costal pleura covering the inner surface of the lateral thoracic wall was inspected. The ribs, sternum, intercostal muscles as well as the intercostal blood vessels and nerves that run caudal to each rib were easily perceptible (Fig 1). The m. longus colli lies craniodorsally in the thorax and ventral to the bodies of the first six thoracic vertebrae (Fig. 2). The sympathetic trunk was visible as a white strand lateral to the vertebral bodies (Fig. 3).

The thoracic surface of the diaphragm is covered by the transparent diaphragmatic pleura and describes active movements which were observable (Fig. 4). The diaphragm is composed of a central tendinous part and a peripheral muscular part. On the border between both parts the phrenic

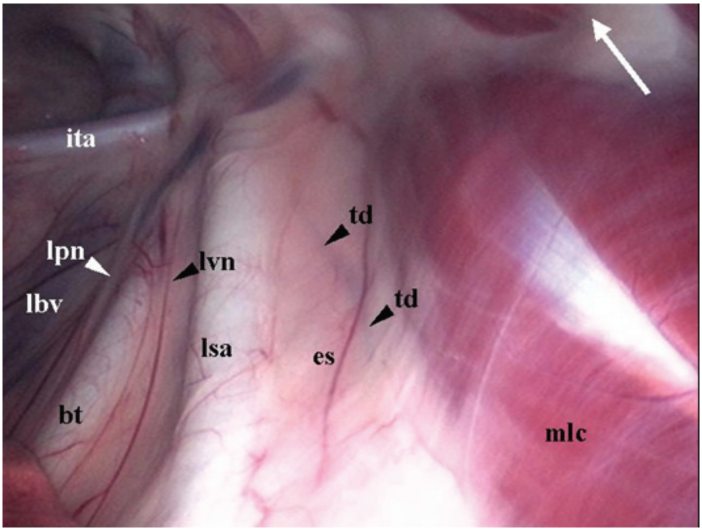

Figure 1 - Normal endoscopic appearance of the cranial mediastinum in the left hemithorax with the endoscope directed cranially. (The white arrow points to the head of the animal.) Key : bt=brachiocephalic trunk; es=esophagus; ita=internal thoracic artery; lbv=left brachiocephalic vein; lpn=left phrenic nerve; lsa=left subclavian artery; lvn=left vagal nerve; mlc=m. longus colli; td=thoracic duct

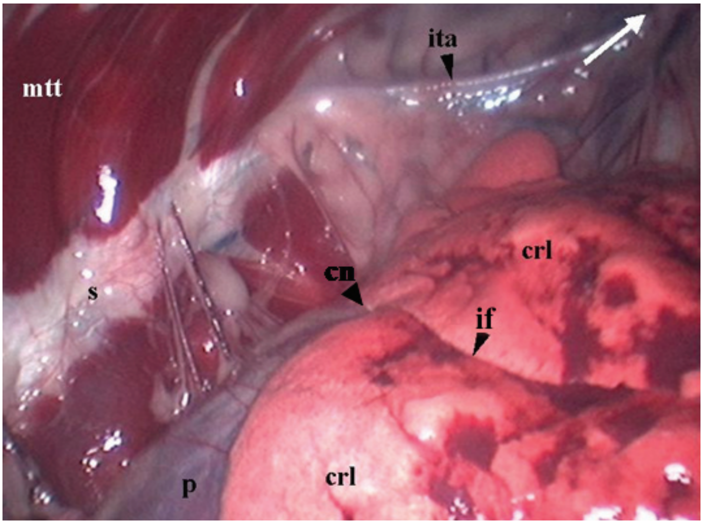

Figure 2 - Normal endoscopic appearance of the left lung after iatrogenic pulmonary collapse. (The white arrow points to the head of the animal.) Key : cn=cardiac notch; crl=cranial lung lobe; if=intralobar fissure; ita=left internal thoracic artery; mtt=m. transversus thoracis; p=pericardium; s=sternum

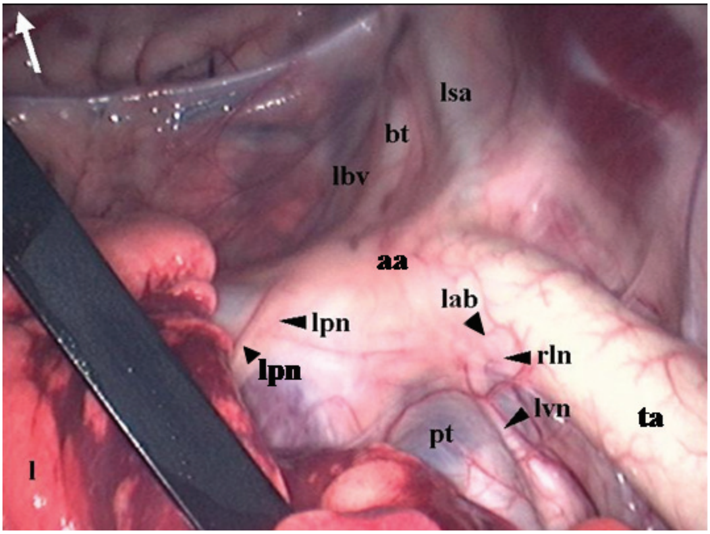

Figure 3 - Normal endoscopic appearance of the heart base in the left hemithorax. (The white arrow points to the head of the animal.) Key : aa=aortic arch; bt=brachiocephalic trunk; l=left lung (retracted); lab=ligamentum arteriosum (Botalli); lbv=left brachiocephalic vein; lsa=left subclavian artery; lpn=left phrenic nerve; lvn=left vagal nerve; pt=pulmonary trunk; rln=recurrent laryngeal nerve; ta=thoracic aorta

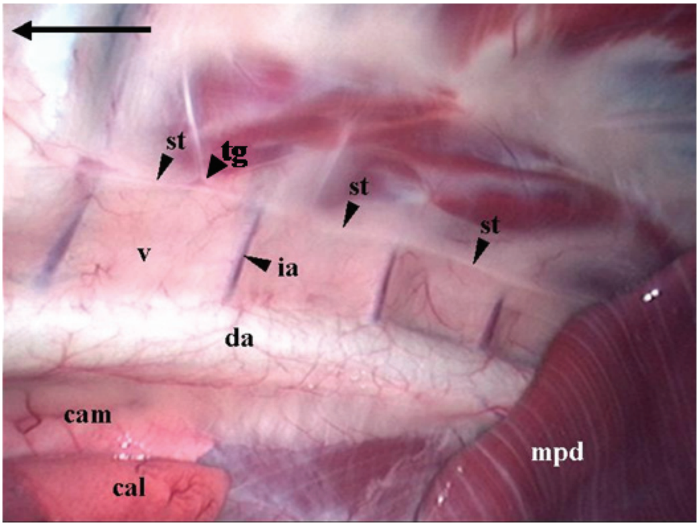

Figure 4 - Normal endoscopic appearance of the thoracic vertebrae in the left hemithorax. (The black arrow points to the head of the animal.) Key : cal=caudal lung lobe; cam=caudal mediastinum; da=descending aorta; ia=intercostal artery; mpd=muscular part of diaphragm; st=sympathetic trunk; tg=thoracic ganglion; v=vertebral body

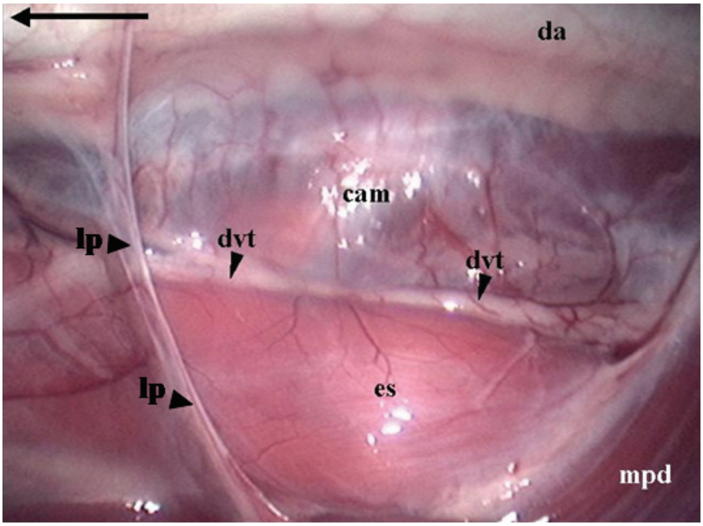

Figure 5 - Normal endoscopic appearance of the caudal mediastinum in the left hemithorax with the endoscope directed caudodorsally. (The black arrow points to the head of the animal.) Key : cam=caudal mediastinum; da=descending aorta; dvt=dorsal vagal trunk; es=esophagus; lp=ligamentum pulmonale; mpd=muscular part of the diaphragm

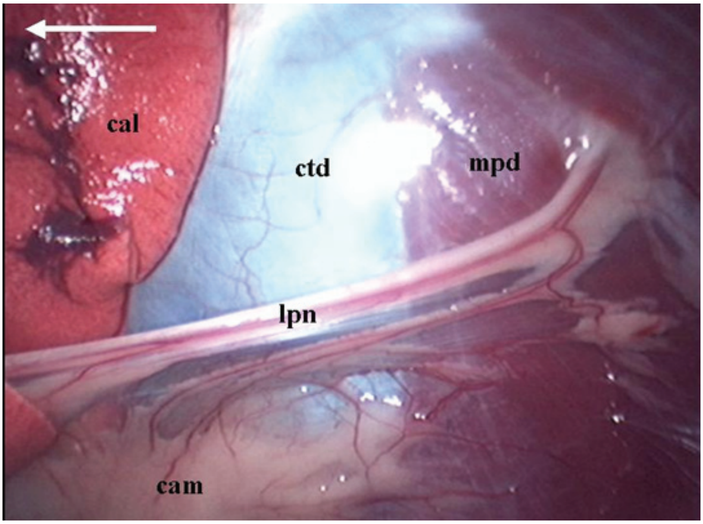

Figure 6 - Normal endoscopic appearance of the diaphragm in the left hemithorax with the endoscope directed caudally. (The white arrow points to the head of the animal.) Key : cal=caudal lung lobe; cam=caudal mediastinum; ctd=central tendon of the diaphragm; lpn=left phrenic nerve; mpd=muscular part of the diaphragm

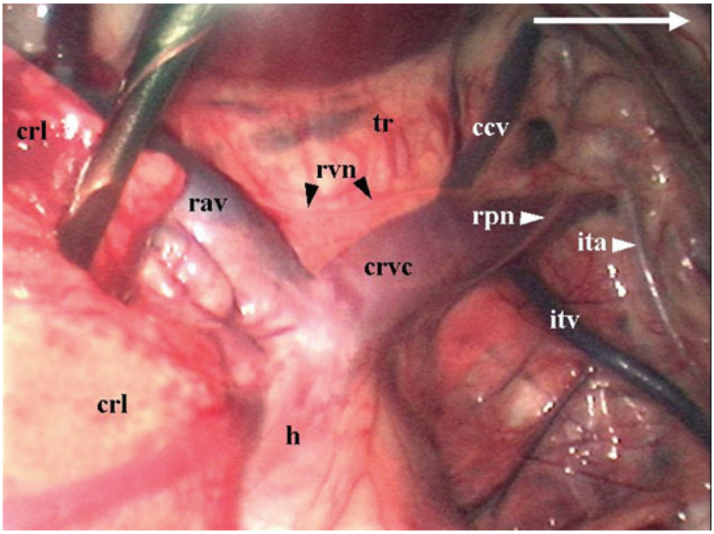

Figure 7 - Normal endoscopic appearance of the cranial mediastinum in the right hemithorax. (The white arrow points to the head of the animal.) Key : ccv=right costocervical vein; crl=cranial lung lobe; crvc=cranial vena cava; h=heart (covered by pericardium); ita=internal thoracic artery; itv=internal thoracic vein; rav=right azygos vein; rpn=right phrenic nerve; rvn=right vagal nerve; tr=trachea

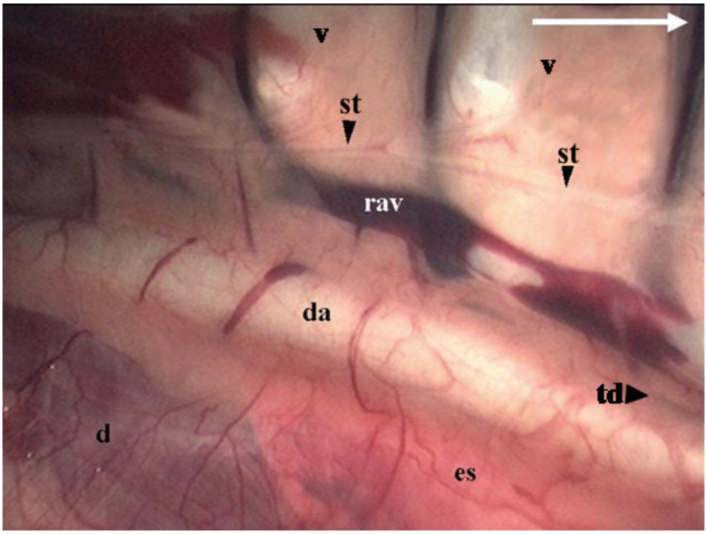

Figure 8 - Normal endoscopic appearance of the vertebrae and the caudal mediastinum in the right hemithorax.
(The white arrow points to the head of the animal.) Key : d=diaphragm; da=descending aorta; es=esophagus; rav=right azygos vein (+intercostal veins); st=sympathetic trunk; td=thoracic duct; v=vertebra

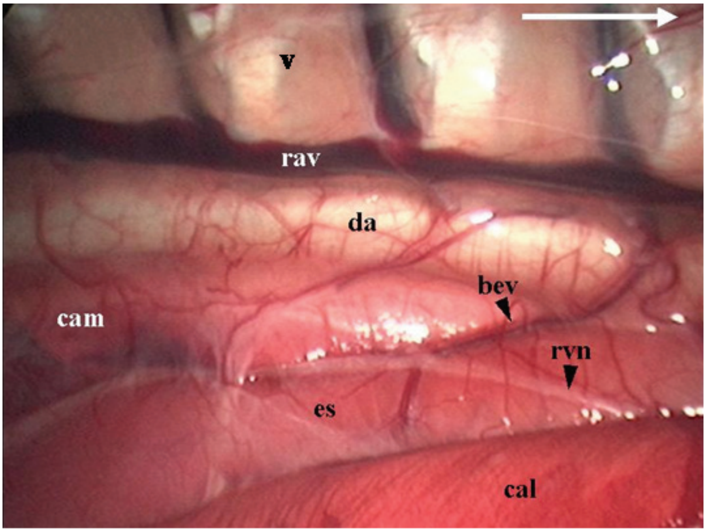

Figure 9 - Normal endoscopic appearance of the vertebrae and caudal mediastinum in the right hemithorax. (The white arrow points to the head of the animal.) Key : bev=bronchoesophageal vein; cal=caudal lung lobe; cam=caudal mediastinum; da=descending aorta; es=esophagus; rav=right azygos vein (+intercostal veins); rvn=right vagal nerve; v=vertebra

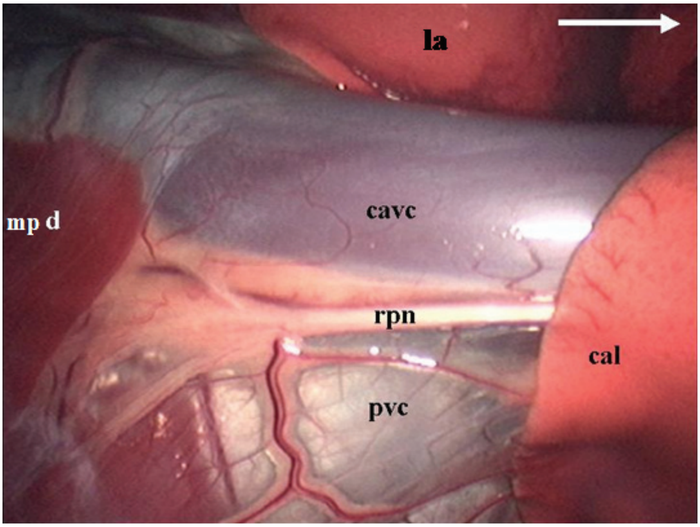

Figure 10 -Normal endoscopic appearance of the plica venae cavae in the right hemithorax with the endoscope directed caudally. (The white arrow points to the head of the animal.) Key : cal=caudal lung lobe; cavc=caudal vena cava; la=lobus accessorius of the right lung; mpd=muscular part of the diaphragm; pvc=plica venae cavae; rpn=right phrenic nerve

nerves were noticed, penetrating into the diaphragm (Fig 4). The left phrenic nerve was also perceptible coursing across the pericardiac surface (Fig. 5). The right phrenic nerve was visible in the cranial mediastinum lateral to the cranial vena cava, and caudal to the heart in the plica venae cavae (Fig. 6,7).

Cardiac movements were seen through the pericardium, which is opaque and sometimes covered by fat. The best way to approach the pericardium is from the left thoracic cavity (Fig. 1). From this side the thoracic part of the descending aorta was also observable ventral to the vertebral bodies (Fig. 3). After displacement of the cranial lobe of the left lung by using a hand-shaped tool, the ascending aorta and the pulmonary trunk became visible (Fig. 5). In between both vessels the ligamentum arteriosum (Botalli) and the left recurrent laryngeal nerve, which is a branch of the vagal nerve, were defined (Fig. 5). The left vagal nerve was observable coursing across the pericardiac surface at the base of the aorta (Fig. 5). The right vagal nerve runs dorsal to the cranial vena cava and crosses the right azygos vein medially (Fig. 8).

In the cranial mediastinum blood vessels and several adjacent structures were located and defined. The esophagus and trachea were endoscopically visible in each hemithorax (Fig. 9).

In the left hemithorax the left subclavian artery and left brachiocephalic vein and their branches were perceptible (Fig. 2). The thoracic duct is located craniodorsal to the heart and, cranial to the 5th thoracic vertebra, on the left lateral surface of the esophagus and (Fig. 9).

On the right side of the thorax the azygos vein and the cranial vena cava were seen in the cranial mediastinum (Fig. 10). The right azygos vein lies upon the lateral surface of some thoracic vertebral bodies. The thoracic duct was defined caudal to the 6th thoracic vertebra between the descending aorta and the azygos vein. After displacing the cranial lobe of the right lung the broncho-esophageal vein that runs into the azygos vein was inspected at the level of the 7th thoracic vertebra (Fig. 10). Caudal to the heart the caudal vena cava was visible in the plica venae cavae of the right hemithorax (Fig. 7).

All intrathoracic structures that are visible endoscopically are listed in table 1.

	LEFT	RIGHT
thoracic wall and organs :		
thoracic inlet	+	+
thoracic vertebrae	+	+
diaphragm	+	+
heart	+	+
oesophagus	+	+
trachea	+	+
lung	+	+
m. transversus thoracis	+	+
m. longus colli	+	+
mm. intercostales interni	+	+
vessels and nerves :		
ascending aorta	+	
descending aorta	+	+
pulmonary trunk	+	
left subclavian artery/vein	+	
brachiocephalic vein	+	
internal thoracic artery/vein	+	+
intercostal vessels	+	+
cranial vena cava		+
caudal vena cava		+
right azygos vein		+
broncho-esophageal vein		+
phrenic nerves	+	+
sympathic trunk	+	+
vagal nerve	+	+
recurrent laryngeal nerve	+	
thoracic duct	+	+
ligament or ductus arteriosus (Botalli)	+	

TABLE 1 : Intrathoracic structures visible endoscopically

DISCUSSION

In human medicine, thoracoscopy has proven its value for diagnosis and management of different thoracic pathologies. Many traditional open procedures have now been replaced by minimally invasive surgical techniques. In humans as well as in animals, postoperative pain, morbidity, mortality, cost and duration of hospitalization associated with thoracoscopy is less than that with thoracotomy[4,46,48-52]. Smaller incisions result in improved cosmesis and fewer postoperative complications such as wound infection, hypothermia, dehiscence, bleeding, seroma and hernia formation[37,47,48]. Disadvantages of the new technology are the specialized and expensive equipment and the need for operator experience, which is a major consideration in performing thoracoscopic operations successfully[47]. Before performing the technique a good knowledge of the thoracic anatomy, the equipment, the operation techniques and the most suitable access route is a prerequisite. The endosurgical procedures can be more time-consuming compared with thoracotomy[41]. Although, the speed of thoracoscopic interventions will improve with the experience of the operator[37]. Other limitations of thoracoscopy are the small size of some of the patients[37].

In veterinary medicine the primary indication for thoracoscopy is for the evaluation of intrathoracic pathology when less invasive methods do not provide sufficient information[4,33]. Evaluating and obtaining tissue from intrathoracic masses, obtaining lung biopsie and evaluating patients with pleural effusion (as the pleural space can be visually inspected and pleural fluid and tissue can be obtained to be evaluated diagnostically) are significant indications.[4,31,34-36] Staging of neoplastic disease and preoperative evaluation of lesion resectability are other indications[4].
In dogs therapeutic interventions such as drainage of empyema or spinal abcesses, oesophageal myotomy, hernioplasty, surgical treatment of bronchopleural fistulas, spontaneous pneumothorax and traumatic thoracic injuries are potential indications for the operative thoracoscopy[47].

The 10 mm, 0°-view angle and 5 mm, 25°-view angle endoscopes used in this study were very adequate evaluating intrathoracic structures. Using two telescopes with different viewing angles decreases the likelihood of missing a lesion which is ‘around the corner’[4].
There is no specific rule that states where the telescope needs to be inserted, however it should be placed so that it and the instruments that may be inserted, are not parallel or close to each other[4].
Endoscopic examination via the 8th intercostal space with the dog in lateral recumbency made it possible to see most intrathoracic structures, although other positions of the endoscope or the animal could result in better imaging certain structures such as the accessory lobe of the right lung, which was not visible in our study. A ventral approach of the endoscope with the dog in dorsal recumbency could solve this problem. Displacement of lung tissue by means of a hand-shaped tool was required for observation of structures such as the ascending aorta, the pulmonary trunk, the ligamentum arteriosum (Botalli) and the recurrent laryngeal nerve.

Complications that are associated with thoracoscopy are pneumothorax, hemorraghe, cutaneous emphysema, subcutaneous hematoma, infections of the skin or pleural cavity[31,33]. In the dogs used in this study, no post-operative complications were noticed.

Veterinary operative thoracoscopy is still in the developmental stage but the trend toward minimally invasive surgery will certainly escalate in the next years. The images of thoracoscopic anatomy in dogs that are discussed in this study may be a guide for the operator in performing thoracoscopic surgery.

ACKNOWLEDGMENTS

The authors acknowledge the assistance of Prof. Dr. Ferguson from the Veterinärmedizinische Fakultät of Leipzig (Germany) and Prof. Dr. Van Raemdonck from the Department of Thoracic Surgery, University Clinic Gasthuisberg (Leuven, Belgium).

REFERENCES

1. Daniel T. Diagnostic thoracoscopy for pleural disease. Ann Thorac Surg 1993;56:639-40.

2. Hsu CP, Hanke I, Douglas JM. Diagnostic video-assisted thoracoscopic procedures. Ann Surg 1995;222: 626-31.

3. Graeber G, Jones D. The role of thoracoscopy in thoracic trauma. Ann Thorac Surg 1993;56:646-8.

4. Jones BD. Is thoracoscopy useful ? Proc 15th ACVIM Forum 1996:351.

5. Vermassen F, De Roose J. Thoracoscopische diagnose en therapie. Tijds Geneesk 1994;50:1698-1703.

6. Ferguson M. Thoracoscopy for diagnosis of diffuse lung disease. Ann Thorac Surg 1993;56:694-6.

7. Naruke T, Asamura H, Kondo H, et al. Thoracoscopy for staging of lung cancer. Ann Thorac Surg 1993;56:661-3.

8. Naunheim K. Video thoracoscopy for masses of the posterior mediastinum. Ann Thorac Surg 1993;56:657-8.

9. Cohen Z, Shinar D, Levi I, et al. Thoracoscopic upper thoracic sympathectomy for primary palmar hyperhidrosis in children and adolescents. J Pediatr Surg 1995;30:471-473.

10. Dowling R, Keenan R, Ferson P, et al. Video-assisted thoracoscopic resection of pulmonary metastases. Ann Thorac Surg 1993;56:772-5.

11. Harvey J, Erdman C, Beattie E. Early experience with videothoracoscopic hydrodissection pleurectomy in the treatment of malignant pleural effusion. J Surg Oncol 1995;59:243-245.

12. Hazelrigg S, Mack M, Landreneau R, et al. Thoracoscopic pericardiectomy for effusive pericardial disease. Ann Thorac Surg 1993;53:792-5.

13. Hazelrigg S, Landreneau R, Mack M, et al. Thoracoscopic resection of mediastinal cysts. Ann Thorac Surg 1993;56:659-60.

14. Hillardal G, Gustafsson G, Wegenius G, et al. Large emphysematous bullae. Successful treatment with thoracoscopic technique using fibrin glue in poor-risk patients. Chest 1995;107:1450-53.

15. Hurley J, Subarreddy K, McCarthy J, et al. Video-assisted thoracic surgery for delayed pericardial effussion post-CABG. Chest 1994;106:1617-19.

16. Kennedy A, Snyder C, Ashcraft K, et al. Comparison of muscle-sparing thoracotomy and thoracoscopic ligation for the treatment of patent ductus arteriosus. J Pediatr Surg 1998;33:259-261.

17. Kirby T, Rice T. Thoracoscopic lobectomy. Ann Thorac Surg 1993;56:784-6.

18. Lewis R. The role of video-assisted thoracic surgery for carcinoma of the lung: wedge resection to lobectomy by simultaneous individual stapling . Ann Thorac Surg 1993;56:762-8.

19. LoCicero J. Thoracoscopic management of malignant pleural effusion. Ann Thorac Surg 1993;56:641-3.

20. Lupoglazoff J, Laborde F, magnier S, et al. Fermeture du canal artériel par vidéothoracoscopie chez 45 enfants. Arch Mal Cœur 1995;88:705-10.

21. Nezu K, Kushibe K, Tojo T, et al. Thoracoscopic wedge resection of blebs under local anesthesia with sedation for treatment of a spontaneous pneumothorax. Chest 1997;111:230-35.

22. Sugarbaker D. Thoracoscopy in the management of anterior mediastinal masses. Ann Thorac Surg 1993;56:653-6.

23. Wakabayashi A. Thoracoscopic technique for management of giant bullous lung disease. Ann Thorac Surg 1993;56:708-12.

24. Ferguson M. Thoracoscopy for empyema, bronchopleural fistula, and chylothorax. Ann Thorac Surg 1993;56:644-5.

25. Liu H, Lin P, Hsieh M, et al. Thoracoscopic surgery as a routine procedure for spontaneous pneumothorax. Chest 1995;107:559-62.

26. Schippers E, Tittel A, Truong S, et al. Videothoracoskopische Therapie des Spontanpneumothorax. Technik und erste Ergebnisse. Chirurg 1994;65:722-725.

27. Hendrickson DA, Wilson DG. Instrumentation and techniques for laparascopic and thoracoscopic surgery in the horse. Vet Clin North Am Eq Pract 1996;12:235-59.

28. Mackey VS, Wheat JD. Endoscopic examination of the equine thorax. Eq vet J 1985;17:140-2.

29. Malone E, Farnsworth K, Lennox T, et al. Thoracoscopic-assisted diaphragmatic hernia repair using a thoracic rib resection.

30. Vachon A, Fischer A. Thoracoscopy in the horse: diagnostic and therapeutic indications in 28 cases. Equine Vet J 1998;30-175-178.

31. Chabchoub A, Mathlouthi A, Kacem S, et al. Thoracoscopie chez le chien (travail expérimental) : Intérêt dans le diagnostic des affections pleurales canines. Rec Méd Vét 1992;168:9-15.

32. Faunt K, Cohn L, Jones B,et al. Cardiopulmonary effects of bilateral hemithorax ventilation and diagnostic thoracoscopy in dogs. Am J Vet Res 1998;59:1494-1498.

33. Faunt K, Jones B, Turk J, et al. Evaluation of biopsy specimens obtained during thoracoscopy of lungs of clinically normal dogs. Am J Vet Res 1998;59:1499-1502.

34. Kovak J, Ludwig L, Bergman P, et al. Use of thoracoscopy to determine the etiology of pleural effusion in dogs and cats: 18 cases (1998-2001). J AmVet Med Assoc 2002;221:990-994.

35. McCarthy TC, McDermaid ShL. Thoracoscopy. Vet Clin North Am Small Anim Pract 1990;20:1341-52.

36. McCarty T. Diagnostic thoracoscopy. Clin Tech Small Anim Pract 1999;14:213-219.

37. Borenstein N, Behr L, Chetboul V, et al. Minimally invasive patent ductus arteriosus occlusion in 5 dogs. Vet Surg 2004;33:309-313.

38. Brugmans F, Thiele S, Koehler L. Minimaal invasieve chirurgie door middel van laparascopische en thoracoscopische technieken. Vlaams Dierg Tijds 1996;65:72-81.

39. Dupre G, Corlouer J, Bouvy B. Thoracoscopic pericardectomy performed without pulmonary exclusion in 9 dogs. Vet Surg 2001;30:21-27.

40. Garcia F., Prandi D, Pena T, et al. Examination of the thoracic cavity and lung lobectomy by means of thoracoscopy in dogs. Can Vet J 1998;39:285-91.

41. Isakow K, Fowler D, Walsh P. Video-assisted thoracoscopic division of the ligamentum arteriosum in two dogs with persistent right aortic arch. J Am Vet Med Assoc 2000;217:1333-1336.

42. Jackson J, Richter K, Launer D. Thoracoscopic partial pericardectomy in 13 dogs. J Vet Intern Med 1999;13:529-533.

43. MacPhail C, Monnet E, Twedt D. Thoracoscopic correction of persistent right aortic arch in a dog; J Am Anim Hosp Assoc 2001;37:577-581.

44. Radlinsky M, Mason D, Biller D, et al. Thoracoscopic visualization and ligation of the thoracic duct in dogs. Vet Surg 2002;31:138-146.

45. Remedios AM, Steinacher S, Furgeson JF, et al. Laparoscopic and thoracoscopic fenestration of the thoracolumbar intervertebral discs (T11 - L7) in dogs. Vet Surg 1995;24:439.

46. Remedios AM, Walsh PJ, Furgeson JF. Thoracoscopic pericardectomy in dogs : Preliminary findings. Proc 3rd Int Laparosc Course Vet 1996.

47. Remedios AM, Ferguson JF. Minimally Invasive Surgery : Laparascopy and Thoracoscopy in Small Animals. Comp Cont Educ Vet Pract 1996;18(11):1191-9.

48. Walsh P, Remedios A, Ferguson J, et al. Thoracoscopic versus open partial pericardectomy in dogs : comparison of postoperative pain and morbidity. Vet Surg, 1999;28:472-479.

49. Bensard D, McIntyre R, Waring B, eta al. Comparison of video thoracoscopic lung biopsy to open lung biopsy in the diagnosis of interstitial lung disease. Chest 1993;103:765-770.

50. Ferson P, Landrenear R, Dowling R, et al. Comparison of open versus thoracoscopic lung biopsy for diffuse infiltrative pulmonary disease. J Thorac Cardiovasc Surg 1993;106:194-199.

51. Landreneau R, Hazelrigg S, Mack M, et al. Postoperative pain-related morbidity: video-assisted thoracic surgery versus thoracotomy. Ann Thorac Surg 1993;56:1285-1289.

52. Weatherford D, Stephenson J, Taylor S, et al. Thoracoscopy versus thoracotomy : indications and advantages. Am Surg 1995;61:83-86.

2.1.3 CT of the normal canine thorax versus thoracoscopy in the dog : anatomic comparison

Lieve M. De Rycke, DVM

Department of Medical Imaging, Faculty of Veterinary Medicine,
Ghent University, Salisburylaan 133, 9820 Merelbeke, Belgium

INTRODUCTION

Recommendations regarding treatment and prognosis should be based on the most accurate morphologic and etiologic diagnosis obtainable by diagnostic techniques. Clinicians dealing with dogs with thoracic disorders have a variety of diagnostic techniques at their disposal[1]. The standard approach should be to start with the less invasive and less risky procedure and proceed to the more complicated, more intrusive evaluation. After a thorough history, physical examination and laboratory studies, x-rays of the thorax must be performed. Depending on the findings, other techniques such as **computed tomography**, magnetic resonance imaging, ultrasonography, angiography or scintigraphy may follow [2,3].

When these procedures have failed to delineate the problem or the therapeutic course, an invasive approach must follow. Thoracocentesis or a pleural biopsy may be performed in cases of pleural disease or intrapleural fluid. Bronchoscopic examination followed by bronchial or pulmonary lavage or biopsy could be indicated in dogs with intrapulmonary or endobronchial disease processes. Depending on the findings, an extrapulmonary CT-guided or a pulmonary fluoroscopic needle biopsy could be accomplished[3,4].

If the above approaches reveal mediastinal, pleural, pulmonary or hilar masses, pericardial fluid or pleural fluid that can not be completely removed, a more invasive endothoracic procedure is indicated. Either **thoracoscopy** or open thoracotomy can be used for diagnosis of intrathoracic disorders. Both techniques make the direct visualisation of the lesion possible, while biopsies can be taken and samples for bacterial and fungal cultures can be obtained. The thoracoscopic approach is far less invasive than thoracotomy and leads to a much lower morbidity and mortality[3,5]. In some cases, evaluation and diagnosis can be followed by minimally invasive thoracic surgery performed by means of thoracoscopy.

RESULTS

Table 1 lists the intrathoracic structures that are visible by each technique. The results are based on former investigations *(see chapter 2.1.1 and 2.1.2).*

	THORACOSCOPY	CT
thoracic wall		
intervertebral disc	+	+
mm. intercostales interni	+	+
m. longus colli	+	+
m. transversus thoracis	+	+
pleura	+	-
rib	+	+
sternum	+	+
thoracic inlet	+	+
thoracic vertebrae	+	+
thoracic structures		
diaphragm	+	-
mediastinum	(+)	+
oesophagus	+	+
pleural cavity	+	+
plica venae cavae	+	-
spinal cord	-	+
vessels		
aortic arch	$+^{l}$	+
ascending aorta	$+^{l}$	+
descending aorta	+	+
left and right axillary arteries	-	-
left and right axillary veins	-	+
right azygos vein	$+^{r}$	+
brachiocephalic trunc	-	+
left brachiocephalic vein	$+^{l}$	+
right brachiocephalic vein	-	+
broncho-esophageal vein	$+^{r}$	-
left and right common carotid arteries	-	+
left costocervical trunc	-	+
right costocervical trunc	-	-
left costocervical vein	-	+
right costocervical vein	$+^{r}$	-
left and right external jugular veins	-	+
intercostal vessels	+	-
left and right internal thoracic arteries	+	+
left and right internal thoracic veins	+	+
left and right pulmonary arteries	-	+
left and right pulmonary veins	-	+
pulmonary trunk	$+^{l}$	+
left subclavian artery	$+^{l}$	+
right subclavian artery	-	+
left and right subclavian veins	-	+
cranial vena cava	$+^{r}$	+
caudal vena cava	$+^{r}$	+
vertebral artery	-	-
vertebral vein	-	-
thoracic duct	+	-
ligament or ductus arteriosus (Botalli)	$+^{l}$	-

	THORACOSCOPY	CT
nerves		
intercostal nerves	+	-
phrenic nerves	+	-
recurrent laryngeal nerve	$+^{l}$	-
sympathic trunk	+	-
vagal nerve	+	-
heart		
left atrium	-	-
left auricle	-	-
left ventricle	$+^{l}$	-
left atrioventricular (mitral) valve	-	-
right atrium	-	-
right auricle	-	-
right ventricle	$+^{r}$	-
right atrioventricular (tricuspidal) valve	-	-
interventricular septum	-	-
pericardium	+	-
left coronary vessels	-	-
trachea and lungs		
trachea	+	+
tracheal bifurcation	-	+
left principal bronchus	-	+
right principal bronchus	-	+
left lung		
- cranial lobe	$+^{l}$	$+^{lw}$
- cranial lobe bronchus	-	$+^{lw}$
- caudal lobe	$+^{l}$	$+^{lw}$
- caudal lobe bronchus	-	$+^{lw}$
right lung		
- cranial lobe	$+^{r}$	$+^{lw}$
- cranial lobe bronchus	-	$+^{lw}$
- accessory lobe	-	$+^{lw}$
- accessory lobe bronchus	-	$+^{lw}$
- middle lobe	$+^{r}$	$+^{lw}$
- middle lobe bronchus	-	$+^{lw}$
- caudal lobe	$+^{r}$	$+^{lw}$
- caudal lobe bronchus	-	$+^{lw}$
lymph nodes		
cranial mediastinal lymph node	-	+
sternal lymph node	-	+
tracheobroncheal lymph node	-	+

TABLE 1 : Intrathoracic structures visible by thoracoscopy and by computed tomography (^{l} = only visible in the left hemithorax, ^{r} = only visible in the right hemithorax, ^{lw} = only visible on lung window setting)

Intrathoracic structures that were not visible on CT-images but were easily observed by thoracoscopy include the parietal and visceral pleura, pericardium, heartbase with ligamentum arteriosum (Botalli), thoracic duct, plica venae cava and several intrathoracic nerves *(see table 1).* On the other hand, visualization of the spinal cord, mediastinum and several vessels was difficult or impossible by thoracoscopy, but easy by CT examination. The lymphnodes could only be seen by computed tomography.

The aspect of the several lung lobes (except for the accessory lung lobe) could be inspected by thoracoscopy, while the inner details were visible on the CT images at lung window setting. The several parts of the heart could not be observed during thoracoscopy due to the surrounding pericardium and were impossible to identify on the CT images as a result of motion artifacts.

CONCLUSIONS

Thoracoscopy as well as CT examination reveal most of the intrathoracic anatomical information and can be used for diagnosing thoracic pathologies. The choice will mainly depend on the clinical history of the animal and the results of former investigations. The fact that thoracoscopy has therapeutic possibilities will also influence the final choice of diagnostic technique.

REFERENCES

1. Bauer T, Thomas W. Pulmonary Diagnostic Techniques. Vet Clinic North Am Small Anim Pract 1983;13:273-298.

2. Esposito G. Diagnosis of mediastinal masses and principles of surgical tactics and techniques for their treatment. Semin Pediatr Surg 1999;8:54-60.

3. Raymond A. Chapter 5 : Indications and Advantages of Thoracoscopy. In: Raymond A, ed. *Thoracoscopy for surgeons: diagnostic and therapeutic*. New York: Igaku-Shoin, 1995;1-271.

4. Garbagnati F, Lutman R, Valvassori L, et al. Nonpulmonary thoracic biopsy. Europ J Radiol 1989;9:214-216.

5. McCarthy TC, McDermaid ShL. Thoracoscopy. Vet Clin North Am Small Anim Pract 1990;20:1341-52.

Cross-sectional anatomy of the

LIMBS

3.1. The Elbow

The next two chapters concern the investigation of the elbow joint of the clinically normal dog. In the first chapter (chapter 3.1.1) the computed tomographic examination of the elbow is described. The second chapter (chapter 3.1.2) briefly handles the magnetic resonance of this joint and gives a comparison between the results of the 2 techniques, CT and MR. .

However, all figures (anatomic, CT and MR sections) of the elbow joint are combined in figure 2 of the first chapter (chapter 3.1.1) to make a visual comparison easier and simple.

3.1.1. Computed tomography of the elbow joint in clinically normal dogs

Lieve M. De Rycke*, DVM; Ingrid M. Gielen*, DVM, MSc;
Henri van Bree*, DVM, PhD; Paul J. Simoens**, DVM, PhD

*Department of Medical Imaging, Faculty of Veterinary Medicine, Ghent University,
Salisburylaan 133, 9820 Merelbeke, Belgium.

**Department of Morphology, Faculty of Veterinary Medicine, Ghent University,
Salisburylaan 133, 9820 Merelbeke, Belgium.

Adapted from :

De Rycke LM, Gielen IM, van Bree H, Simoens PJ. Computed tomography of the elbow joint in clinically normal dogs. *Am J Vet Res* 2002;63:1400-1407.

SUMMARY

Objective-To use computed tomography (CT) to provide a detailed description of elbow joint structures in clinically normal dogs

Animals- 6 clinically normal adult mixed-breed dogs weighing 24 to 37 kg and one 12-month-old Labrador Retriever weighing 27 kg.

Procedure -To perform computed tomography of both elbow regions, dogs were anesthetized and placed in lateral recumbency. One- and 2-mm contiguous slices were obtained by use of a third generation computed tomographic scanner. Good resolution and anatomical detail were acquired from the computed tomographic images by use of a bone (window width = 3500 Hounsfield units; window level = 500 Hounsfield units) and soft tissue setting (window width = 400 Hounsfield units; window level = 66 Hounsfield units). After euthanasia, the forelimbs from the Labrador Retriever were removed and frozen in water at –18 °C. Elbow joints were sectioned into approximately 1-mm thick slab sections by use of an electric planer. Anatomic sections were photographed and compared with the corresponding CT images. Computed tomographic reconstructions of the elbow joint were created in sagittal and dorsal planes.

Results- Structures on the computed tomographic images were matched with structures in the corresponding anatomic sections. The entire humero-radioulnar joint surface could be evaluated on the reconstructed images in the sagittal and dorsal plane.

Conclusions and clinical Relevance- Computed tomographic images provide full anatomic detail of the bony structures of the elbow joint in dogs. Muscles, large blood vessels and nerves can also be evaluated. These results could be used as a basis for evaluation of computed tomographic images of the forelimbs of dogs with elbow joint injuries.

INTRODUCTION

The elbow joint in dogs is a complex and compound joint with multiple articulations : the humeroradial joint, the humeroulnar joint and the proximal radioulnar joint. Though its radiographic anatomy and gross anatomical appearance have been investigated in detail,[1-3] the information acquired has limitations, primarily as a result of superimposition of the radial head over the medial coronoid process and the tight fit between the humerus and the trochlear notch of the ulna. Therefore the radiographic diagnosis of elbow lesions including medial coronoid process fragmentation and joint incongruity, can be challenging, and an exploratory arthrotomy has been advocated as a reasonable diagnostic option by some authors.[4,5] Computed tomography (CT) has a high accuracy for the diagnosis of a fragmented coronoid process (FCP) and associated changes, and may be useful when findings on survey radiographs are negative.[6-12] The advantages of CT over conventional radiography include the following : depiction of detailed cross-sectional anatomy without distraction from superimposed structures, thereby decreasing the complexity of the image, variation in gray scale formats and enhanced contrast resolution and computer reconstruction of multiplanar images.[11-15]

In human medicine CT is an established diagnostic tool. In humans with osteochondrosis dissecans, intra-articular fragments, complex intra-articular fractures and, subchondral bone sclerosis, CT is useful and expedient for precise diagnosis, and it helps to identify subtle subchondral lucencies and the presence of loose bodies.[13-16] The knowledge of the anatomy of the elbow joint on computer tomographic images is necessary to provide accurate interpretation and to describe abnormalities that may be present. The purpose of the study presented here was to provide a detailed description of the elbow joint in clinically normal dogs, as revealed by CT. The results of this CT study were subsequently compared to the results of a MR investigation of the canine elbow (see chapter 3.1.2).

MATERIALS AND METHODS

Animals- Six healthy mature mixed breed dogs weighing 24 to 37 kg and one 12-month-old Labrador Retriever weighing 27 kg were used for our study. Prior to use in our study, the dogs had their elbow joints physically and radiographically examined. Three radiographic views were obtained: the neutral and flexed mediolateral view and the craniocaudal view. No abnormalities were found on any radiograph.

Computed tomography- Dogs were sedated using fentanyl (0.005 to 0.01 mg/kg, IV) and droperidol [a] (0.25 to 0.5 mg/kg, IV) and then anesthetized with thiopental sodium[b] (8 mg/kg, IV). After intubation, anesthesia was maintained with halothane. Dogs were positioned in left lateral recumbency on the computed tomographic scanning table with the elbow joints parallel and extended cranially. The heads of the dogs were pulled back to the lateral side to scan both elbow joints in the gantry. Wedge sponges were placed between both elbow joints to avoid rotation. This position allows a perfect symmetry and comparison of both elbows at the same level. A lateral survey view was made by a third generation CT scanner[c] to confirm correct positioning. On a craniocaudal survey view, computed tomographic scans were performed from the top of the olecranon to 3 cm distal to the elbow joint and parallel to the humeroradial joint space.

Two-millimeter thick contiguous views were obtained from the most proximal part of the ulna to 3 cm distal to the radial head. However in the region of the radioulnar joint, 1-mm thick contiguous views were obtained. Individual images were reviewed by use of a bone setting (window width = 3500 Hounsfield units; window level = 500 Hounsfield units) and a soft tissue setting (window width = 400 Hounsfield units; window level = 66 Hounsfield units). Settings for the computed tomographic image technique were as follows : 120 kV and 100 mA. Image acquisition time was approximately 10 minutes. Images from all 7 dogs were formatted on x-ray film[d] and evaluated.

Comparison of CT and anatomic images - All 6 dogs recovered from anesthesia. The Labrador Retriever was euthanatized for reasons not associated to orthopedic conditions. The forelimbs of the Labrador Retriever were removed, and frozen at –18 °C with the elbow joints in extension. Subsequently, the frozen elbow joints were removed from the capitulum and trochlea of the humerus down to the proximal portion of radius and ulna. Without thawing, these specimens were embedded in water, stored at –18°C until the surrounding water was frozen, and sectioned into approximately 1-mm thick slab sections (parallel to the humeroradial joint space) by use of an electric planer.[e] All anatomic sections were photographed and matched with a corresponding computed tomographic image (bone setting) on the basis of appearance. From this collection, 10 representative matched pairs of the right elbow joint were selected from proximal to distal regions.

Bony and soft tissues were identified on the anatomic sections by comparing all features with a dissected right elbow region of a large-breed dog that had been euthanatized for reasons unrelated to forelimb lameness. The identified structures were subsequently located on the corresponding computed tomographic images (both bone and soft tissue settings), and afterwards the list of identified structures was evaluated on the computed tomographic images of the 6 other dogs. The nomenclature used for designating all structures was in accordance with official anatomic terms.[17] Computed tomography-based reconstructions of the elbow joint in a sagittal and dorsal plane were made to determine whether an evaluation of the entire joint surface could be performed without superimposition of any bony structures.

RESULTS

The 10 selected levels of the right elbow joint of the Labrador Retriever were determined on a craniocaudal computed tomographic survey view (Fig 1). A comparison was made between the computed tomographic images (bone and soft tissue-settings) and the cut-surface of the corresponding anatomic sections of the right elbow joint (Fig 2).

Figure 1– Craniocaudal survey view of the elbow joint of a clinically normal dog indicating the levels (A through J) at which computed tomographic images were obtained.

On the proximal anatomic sections (Fig 2, rows A through F) several osseous, muscular, tendinous, vascular and nervous structures could be identified. Bony structures included the distal portion of the humerus with the lateral and medial parts of the humeral condyle, the lateral and medial epicondyle, the radial, olecranon and supratrochlear fossa, and the proximal part of the ulna with the olecranon and olecranon tuber, the anconeal process, and the trochlear notch. A number of soft tissue structures, including 9 muscles, were visible on the proximal anatomic sections. Four major blood vessels (3 veins and 1 artery) and 3 nerves could be identified on all sections. The olecranon ligament (row C), the lateral and medial collateral ligaments and the elbow joint capsule were also identified (rows E and F). On the soft-tissue setting, computed tomographic images all of these structures and 1 supplementary muscle, namely the cleidobrachialis muscle were visible. Only the olacranon ligament could not been detected. All previously mentioned bony structures could be identified at the bone setting (rows A through F).

Bony structures that were visible on the more distal anatomic sections (Fig 2, rows G through J) included the proximal portions of the radius and ulna with the lateral and medial coronoid processes, the radial notch and the ulnar tuberosity. Compared with the more proximal located anatomic sections, the tendons of the triceps brachii muscle were absent, the brachialis muscle and biceps brachii muscle were disappearing and five additional muscles could be identified. The distal anatomic sections of the elbow joint (Fig 2, rows H through J) revealed the median vein, formed by the anastomosis of the brachial vein and the median cubital vein, and the median artery which is the continuation of the brachial artery. In addition the anular ligament of the radius (row H) and the antebrachial interosseous membrane (row J) were visible. On the computed tomographic images at the soft tissue setting, the same osseous and soft tissue structures could also be identified, except for the anular ligament of the radius and the antebrachial interosseous membrane. All bony structures that were seen on the anatomic sections were visible on the computed tomographic images at the bone setting.

Sagittal and dorsal reconstructions were made of the right elbow joint of the Labrador Retriever (Fig 3). The sagittal images were reconstructed in the lateral compartment of the joint and through the central ridge of the trochlear notch. All images allowed a thorough evaluation of the shape of the trochlear notch and the congruity of the 3 joint spaces.

For the other 6 dogs, all osseous structures mentioned for the Labrador Retriever could be seen on the computed tomographic images at the bone setting. Similarly, all bony, muscular, nervous and vascular structures that could be identified on the computed tomographic images at the soft-tissue


21
20
24
2
2
3
7
19
17
23
H
rf
of
25
1
ot
ot
ot
16
A
a
Cran.
Med.
Lat.
H
of
ot
ot
ot
Caud.
b
4
21
20
2
3
7
24'
24"
19
17
23
H
7
25
1
ot
ot
ot
16
c
20
2
2
7
19
17
H
of
1
ot
16
d

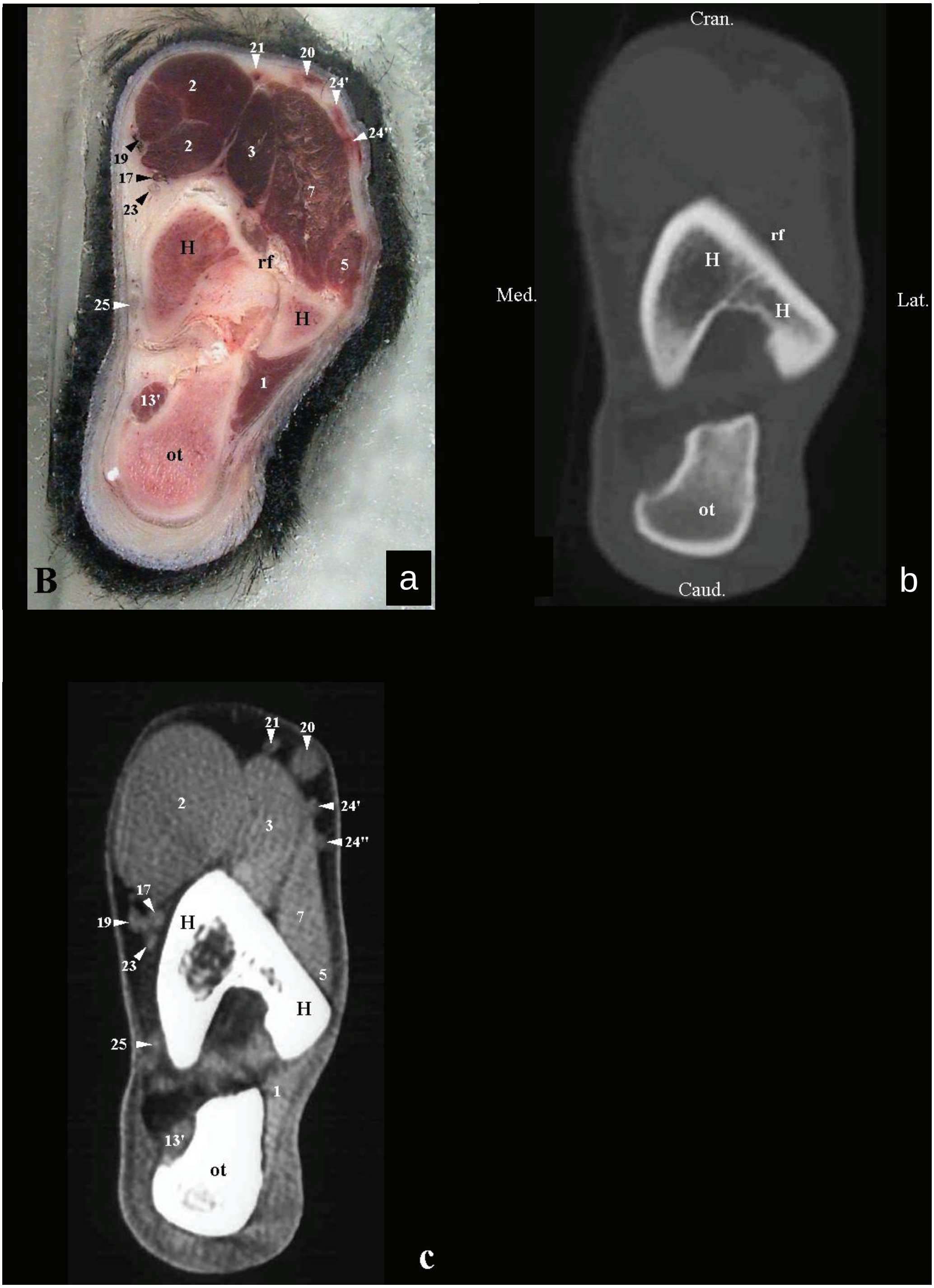
B
a
21
20
24'
24''
2
2
3
7
5
19
17
23
H
rf
H
25
1
13'
ot
Cran.
Med.
Lat.
Caud.
rf
H
H
ot
b
21
20
24'
24''
2
3
17
19
H
7
23
5
H
25
1
13'
ot
c

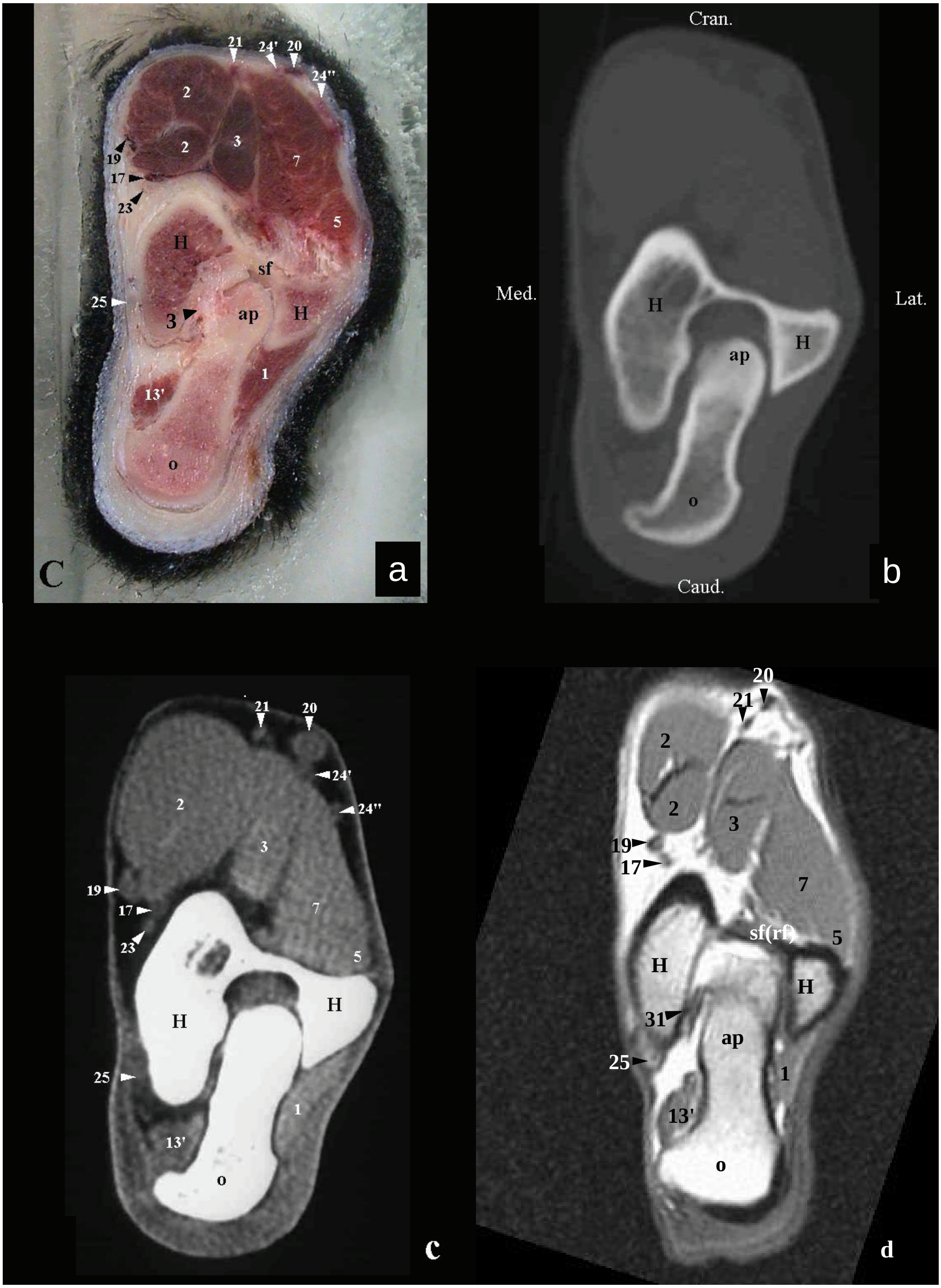
21
24'
20
24''
2
2
3
7
19
17
23
5
H
sf
25
3
ap
H
1
13'
o
C
a
Cran.
Med.
H
ap
H
Lat.
o
Caud.
b
21
20
24'
24''
2
3
19
17
7
23
5
H
H
25
1
13'
o
c
20
21
2
2
3
19
17
7
sf(rf)
5
H
H
31
ap
25
1
13'
o
d

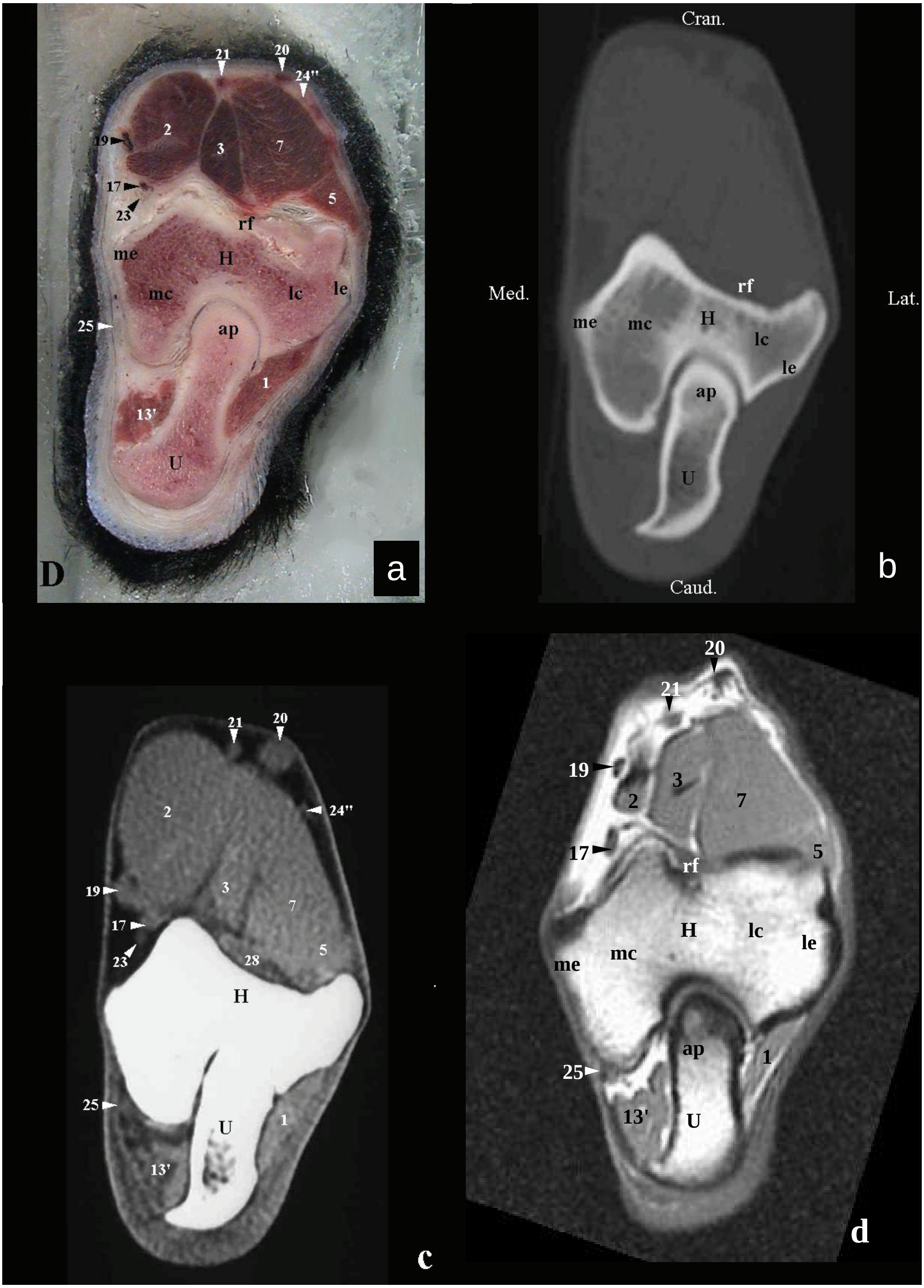
21
20
24"
19
2
3
7
17
23
5
rf
me
H
mc
lc
le
25
ap
1
13'
U
D
a
Cran.
Med.
Lat.
rf
me
mc
H
lc
le
ap
U
Caud.
b
21
20
24"
2
19
3
7
17
23
28
5
H
25
U
1
13'
c
20
21
19
3
2
7
17
5
rf
H
lc
le
me
mc
ap
25
1
13'
U
d

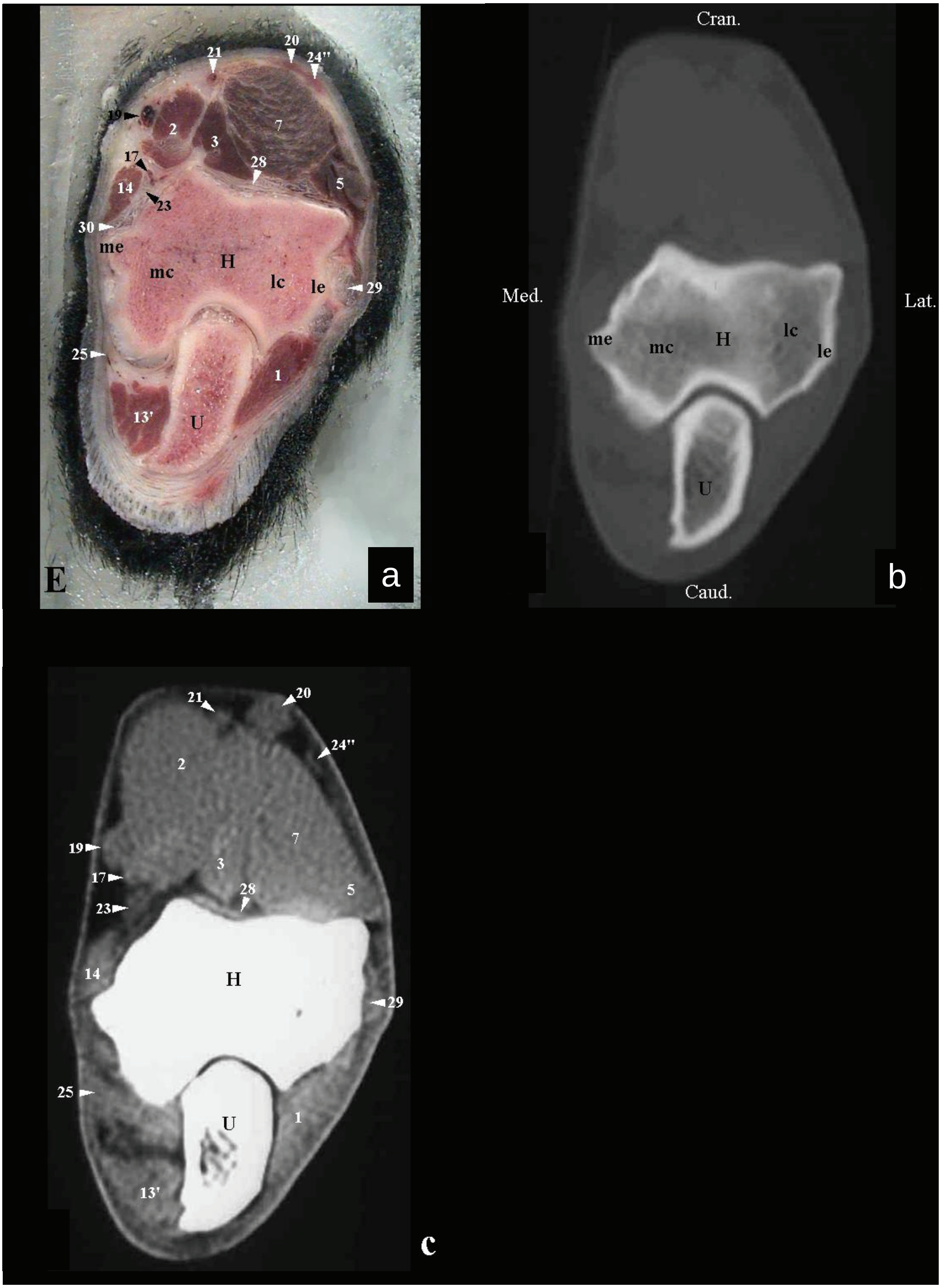
E
21
20
24''
19
2
3
7
17
28
14
5
23
30
me
mc
H
lc
le
29
25
1
13'
U
a
Cran.
Med.
Lat.
me
mc
H
lc
le
U
Caud.
b
21
20
24''
2
19
7
3
17
28
5
23
14
H
29
25
U
1
13'
c

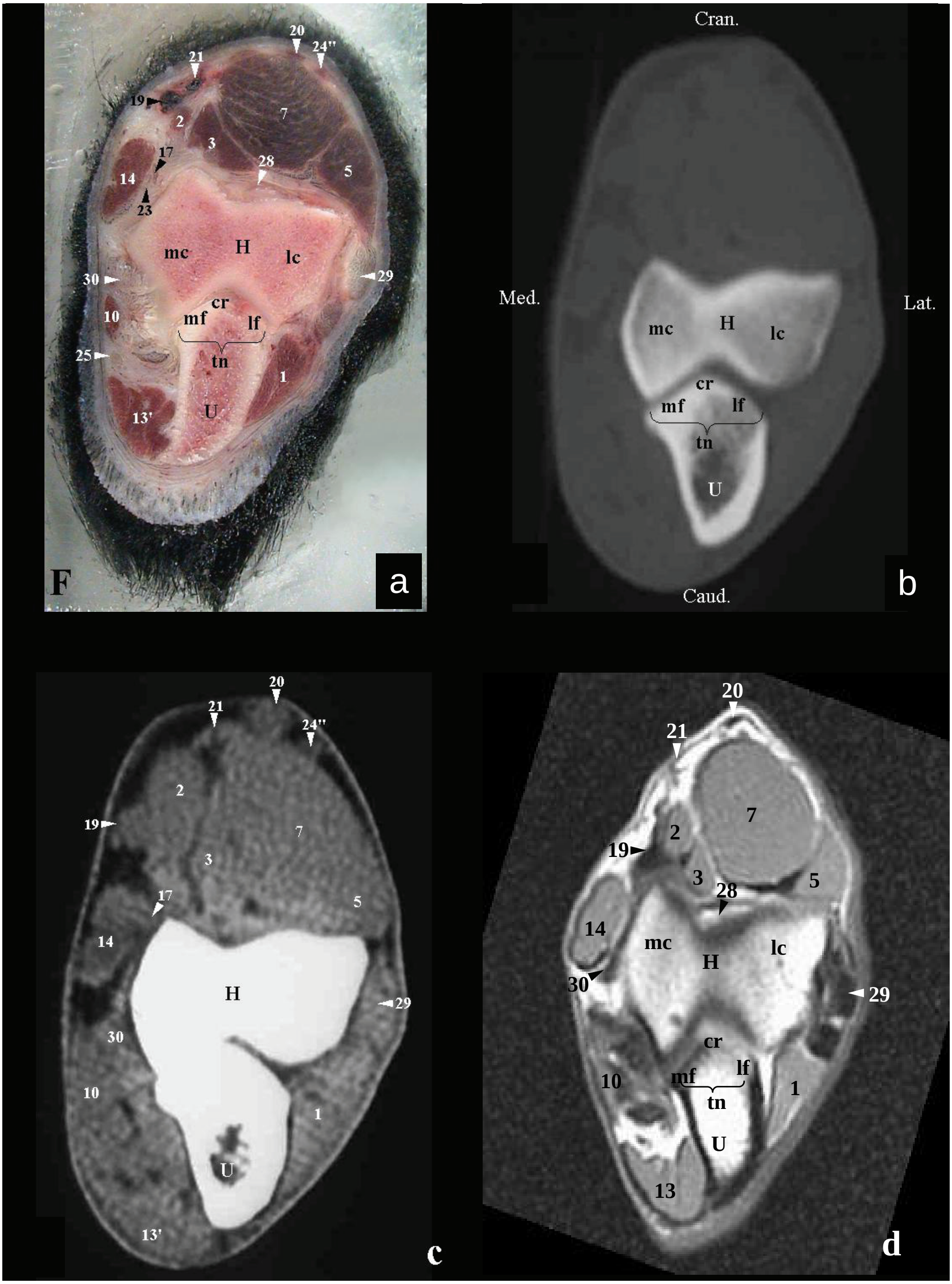
20
24''
21
19
2
7
3
17
28
5
14
23
mc
H
lc
30
29
cr
10
mf
lf
tn
25
1
13'
U
F
a
Cran.
Med.
Lat.
mc
H
lc
cr
mf
lf
tn
U
Caud.
b
20
21
24''
2
19
7
3
17
5
14
H
29
30
10
1
U
13'
c
20
21
7
2
19
3
28
5
14
mc
H
lc
30
29
cr
lf
mf
10
tn
1
U
13
d


20
24"
21
19
7
2
3
17
14
5
23
mcp
R
U
11
29
lcp
10
8
25
13
1
U
13'
G
a
Cran.
Med.
R
Lat.
H
lcp
U
Caud.
b
20
24"
21
7
19
2
5
14
3
17
R
29
11
U
8
10
1
13
13'
c
20
7
19
2
3
5
14
H
R
29
11
l cp
8
U
10
13
1
13'
d

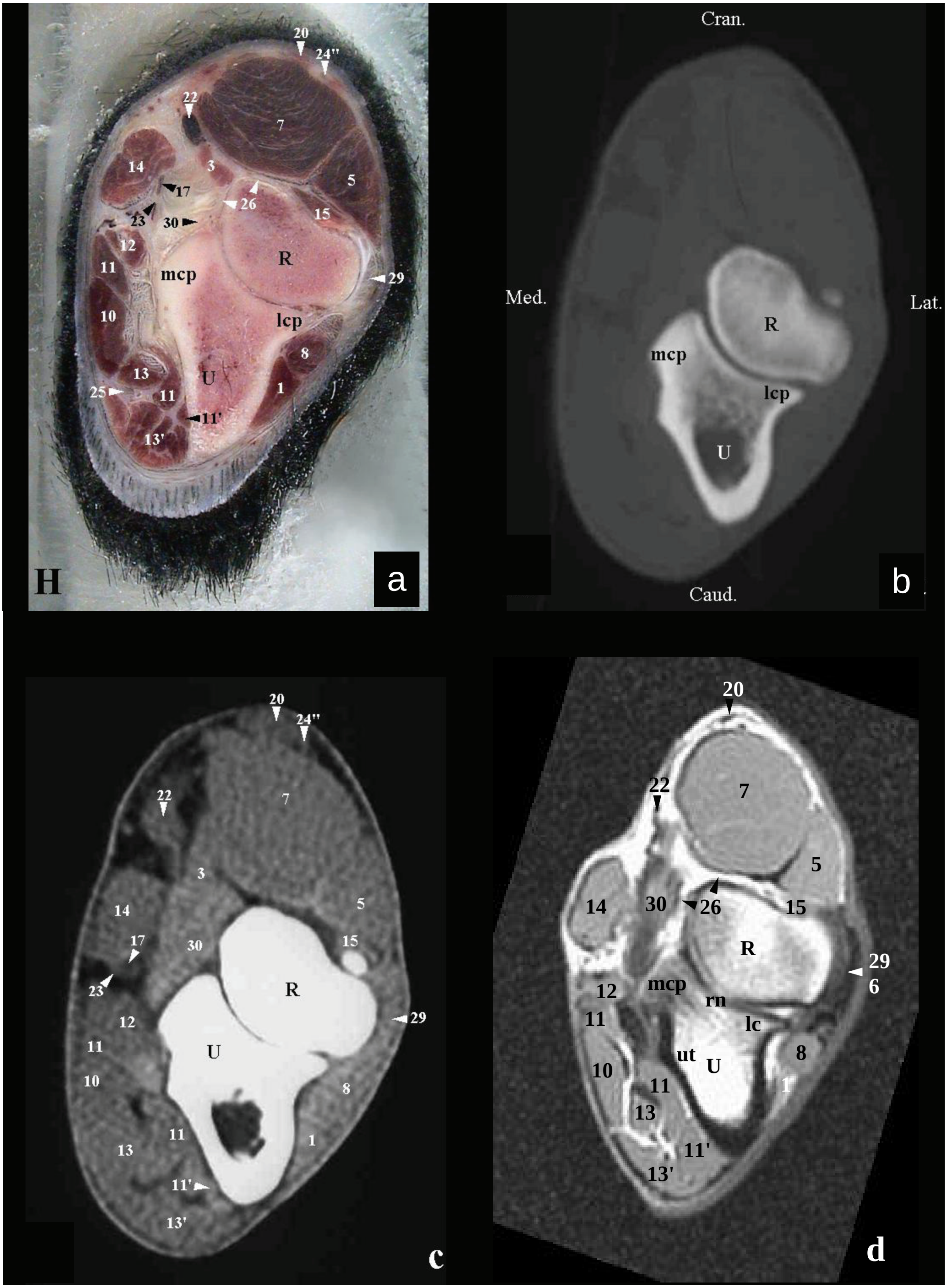
H
a
20
24"
22
7
14
3
5
17
26
15
23
30
12
R
11
mcp
29
10
lcp
8
13
U
25
11
1
11'
13'
b
Cran.
Med.
Lat.
Caud.
R
mcp
lcp
U
c
20
24"
22
7
3
14
5
17
30
15
23
R
29
12
11
U
10
8
11
13
1
11'
13'
d
20
22
7
5
14
30
26
15
R
29
6
12
mcp
rn
11
lc
ut
8
10
U
11
1'
13
11'
13'

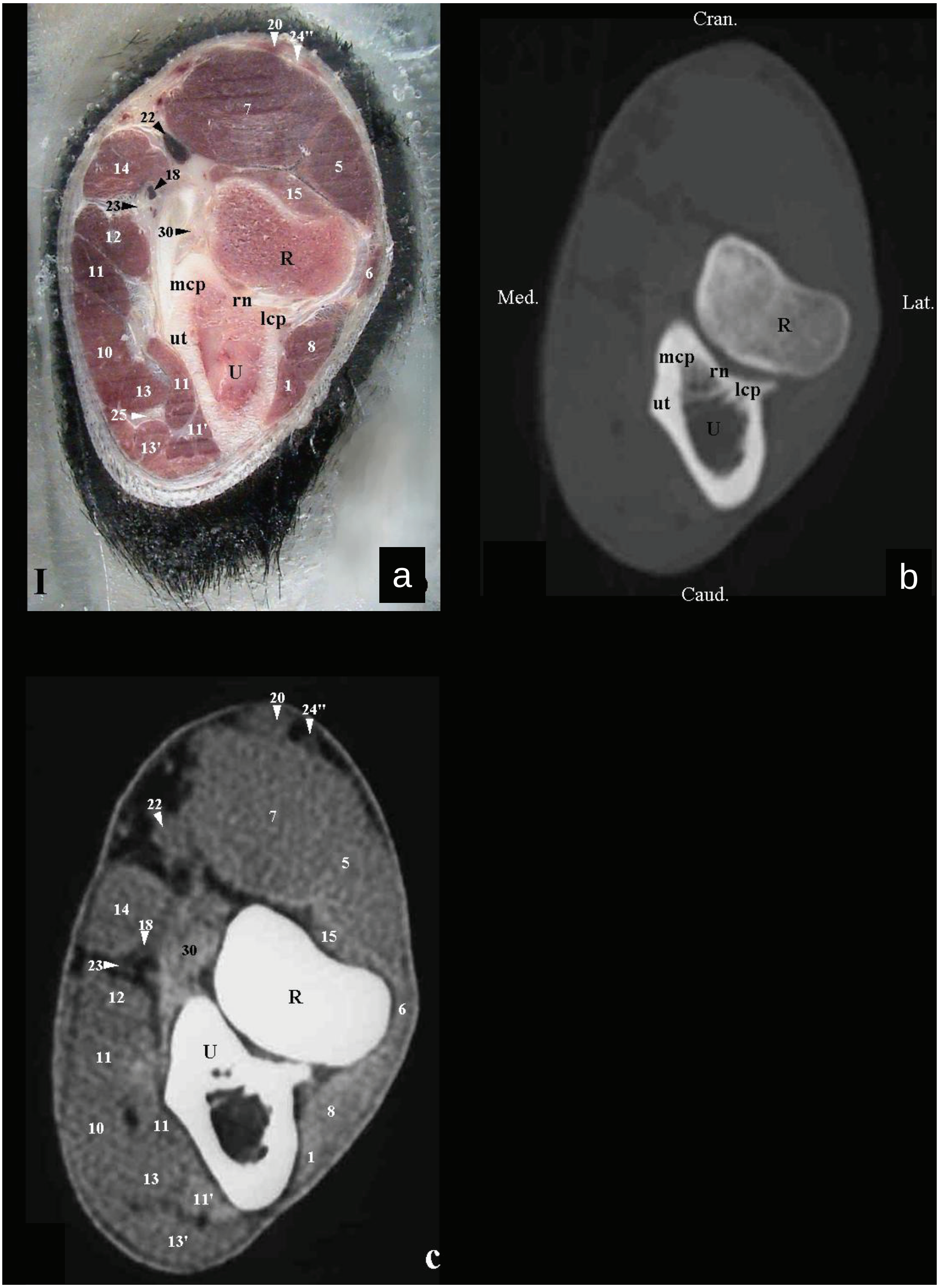
I
a
20
24''
22
7
14
18
5
15
23
30
12
R
11
6
mcp
rn
lcp
ut
10
8
U
13
11
1
25
11'
13'
b
Cran.
Med.
Lat.
Caud.
R
mcp
rn
lcp
ut
U
c
20
24''
22
7
5
14
18
30
15
23
12
R
6
U
11
8
10
11
1
13
11'
13'

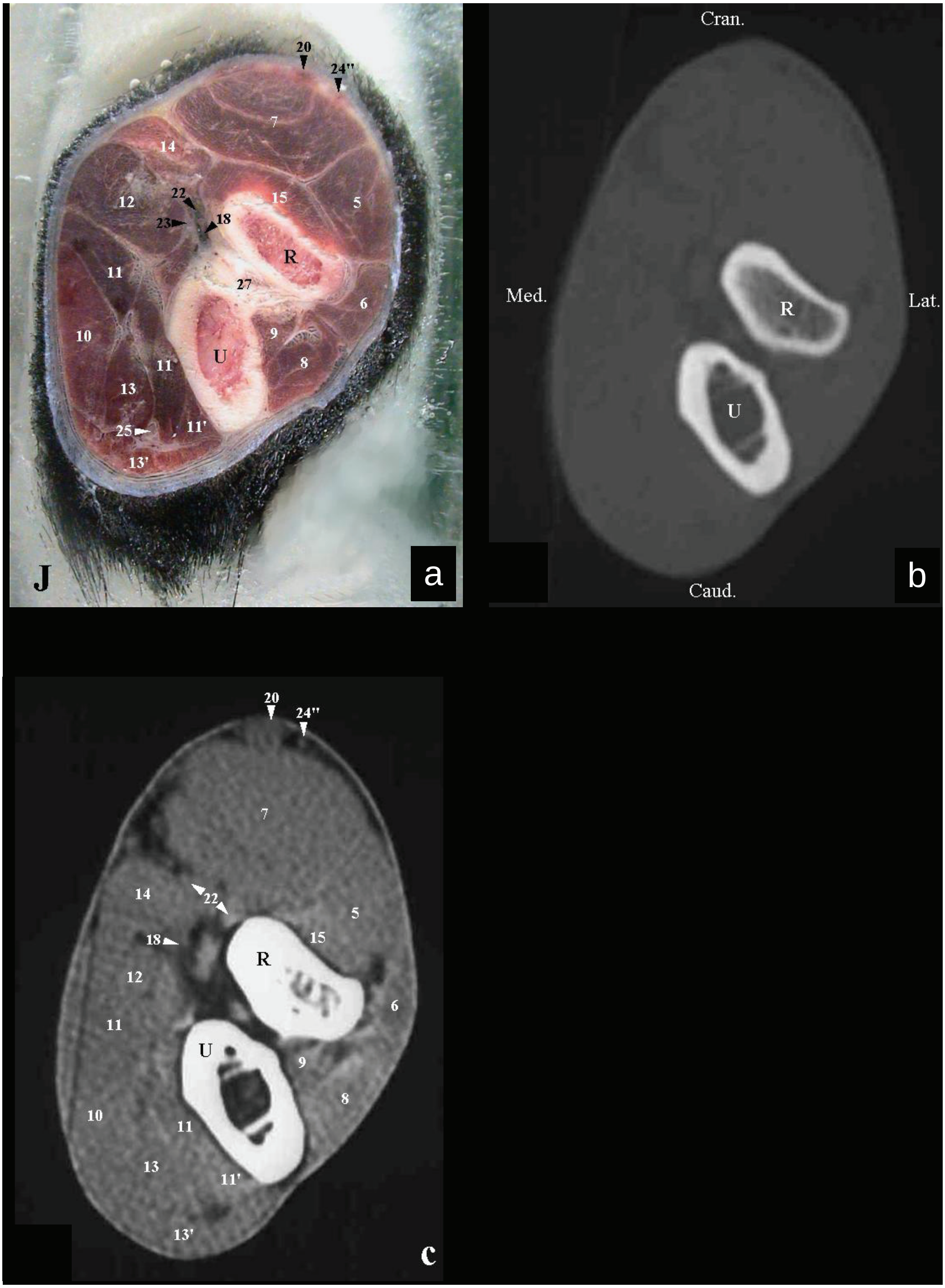
20
24''
7
14
12
22
23
18
15
5
R
11
27
6
10
9
U
11
8
13
25
11'
13'
J
a
Cran.
Med.
R
Lat.
U
Caud.
b
20
24''
7
14
22
5
18
15
R
12
6
11
U
9
8
10
11
13
11'
13'
c

Figure 2 – Transverse anatomic sections (top left), computed tomographic images (bone image, top right ; soft-tissue image, bottom left) and T1-weighted MR images (TR = 500msec, TE= 12msec; bottom right) of a right elbow joint of a clinically normal Labrador Retriever. Images were obtained at levels A through J as illustrated in figure 1. Caud = Caudal. Med = Medial. Lat = Lateral. Cran = cranial.

1 = Anconeus muscle.
2 = Biceps brachii muscle.
3 = Brachialis muscle.
4 = Cleidobrachialis muscle.
5 = Extensor digitorum communis muscle.
6 = Extensor digitorum lateralis muscle.
7 = Extensor carpi radialis muscle.
8 = Extensor carpi ulnaris muscle.
9 = Abductor digiti I muscle.
10 = Flexor digitorum superficialis muscle.
11 = Flexor digitorum profundus muscle (11 = caput humerale, 11’ = caput ulnare).
12 = Flexor carpi radialis muscle.
13 = Flexor carpi ulnaris muscle (13 = caput humerale, 13’ = caput ulnare).
14 = Pronator teres muscle.
15 = Supinator muscle.
16 = Triceps brachii muscle (tendons).
17 = Brachial artery.
18 = Median artery.
19 = Brachial vein.
20 = Cephalic vein.
21 = Median cubital vein.
22 = Median vein.
23 = Median nerve.
24 = Radial nerve (24’= medial superficial branch, 24’’= lateral superficial branch).
25 = Ulnar nerve.
26 = Anular ligament of radius.
27 = Antebrachial interosseous membrane.
28 = Cubital joint capsule (fibrous membrane).
29 = Lateral collateral ligament (proximal, undivided part).
30 = Medial collateral ligament (proximal, undivided part).
31 = Olecranon ligament.
H = Humerus.
lc = Lateral part of humeral condyle.
le = Lateral epicondyle.
mc = Medial part of humeral condyle.
me = Medial epicondyle.
of = Olecranon fossa.
rf = Radial fossa.
sf = Supratrochlear foramen.
R = Radius.
U = Ulna.
ap = Anconeal process.
lcp = Lateral coronoid process.
mcp = Medial coronoid process.
o = Olecranon.
ot = Olecranon tuber.
rn = Radial notch.
tn = Trochlear notch (cr = central ridge, mf = medial flange, lf = lateral flange).
ut = Ulnar tuberosity.

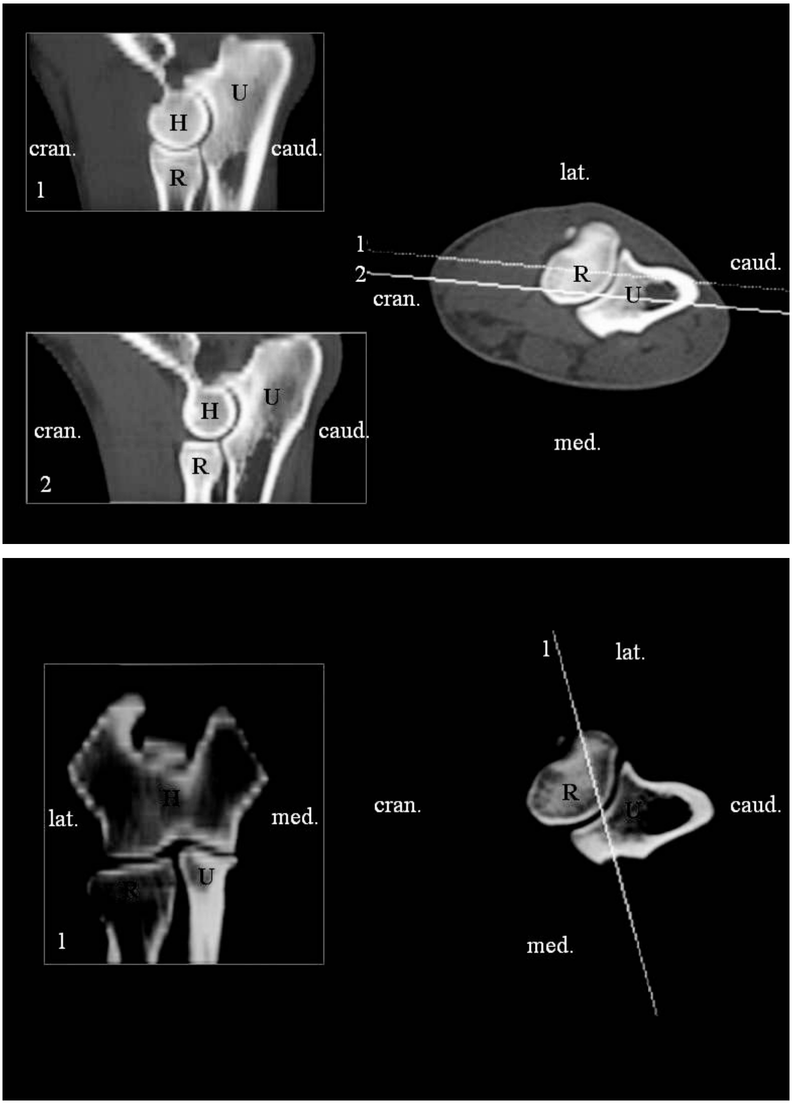

Figure 3 – Sagittal (top) and dorsal (bottom) reconstructions from computed tomographic images of the right elbow joint of a Labrador Retriever euthanized for reasons unrelated to the musculoskeletal system. See Figure 2 for key.

setting for the Labrador Retriever were also noticed on the computed tompographic images at the soft-tissue setting for the 6 mixed-breed dogs. In 2 dogs, however, the median artery could not be identified.

DISCUSSION

Lameness referable to the elbow joint is a common finding among young, rapidly growing large- to giant-breed dogs. It can be caused by several developmental conditions including FCP, osteochondritis dissecans (OCD) of the medial part of the humeral condyle, ununited anconeal process, articular anomaly, or joint incongruity.[5,18-22] Of these developmental conditions, FCP is most common. [5,20,22-24] They all lead to secondary degenerative joint disease (DJD), loss of range of motion and possible lameness as the animal ages.[21,22,25-27]

It has been stressed that early diagnosis is essential for the successful treatment of FCP and OCD.[5,21,23,25-31] Besides the clinical signs, the diagnosis is mostly made on the basis of the radiographic examination of the patients. Unfortunately, the radiographic findings may not be conclusive, and in most instances, the lesions can only be indirectly diagnosed by the appearance of secondary osteophytes. These osteophytes are signs of a secondary DJD and they do not appear until the dog is about seven to eight months old.[5,12,21,25-29] The ideal situation, however, would be that FCP, OCD, or both within the elbow joint could be directly diagnosed before the radiographic appearance of DJD changes, which are signs of joint damage. Moreover, in some dogs with radiographic changes suggestive of FCP, grossly normal appearing joints can be found at surgery, and in those cases unnecessary arthrotomies are performed.[4,32,33]

For these reasons, imaging techniques that provide a direct observation of the medial coronoid process and other joint structures would greatly improve the accuracy of preoperative diagnosis of FCP and would contribute to the early diagnosis of this condition. Magnetic resonance imaging has been described as being useful in the detection of FCP, especially in instances of nonmineralised cartilaginous fragments that cannot be seen on computed tomographic images.[34] Although arthroscopic techniques to evaluate elbow structures of clinically normal dogs are described [35] and the possible arthroscopic changes are reported [36], this technique is more invasive than CT and can only evaluate the surface of the lesions.

Although some information on computed tomographic images of the elbow joint in dogs exists [37] and a number of reports have been published on the clinical application of CT in elbow disorders [6,8,33,38] a detailed description of the computed tomographic anatomy of that region in clinically normal dogs is lacking. With the increasing availability of CT for the veterinary profession [7,11] its application in elbow disease will undoubtedly increase and such a description is useful to detect and evaluate pathologic changes.

In the published reports on CT of the elbow joints in dogs[6,8,11,14,16,33,38] no definite protocol has been described on the positioning of the dog. We had excellent results with the positioning in lateral recumbency with the elbow joints parallel and extended cranially. The head of the dog was pulled back to the lateral side in order to scan only both elbow joints in the gantry. This positioning allowed us to scan both elbows in perfect symmetry at the same time and made comparison of both joints at the same level possible. Avoiding supplementary tissue within the gantry increases the quality of the images because beam-hardening can be avoided.[39]

The results of our study indicate that by use of CT not only bony structures can be evaluated but that with the correct window settings a detailed observation of muscular, tendinous, vascular, and even some nervous structures is possible. By studying the axial computed tomographic images, the complexity of the radiographic images can be reduced, although some familiarization with this type of imaging is necessary. Use of CT offers the advantage of evaluating the medial coronoid process and the medial part of the humeral condyle in detail and without superimposition of bony structures. From reports on the arthroscopic findings in FCP [36] it is obvious that besides fragmentation of the medial coronoid process there are other pathologic entities in that area including chondromalacia. Fragmentation of the coronoid process is easy to recognise on computed tomographic images but the computed tomographic appearance of other conditions is yet unknown. The exact and objective evaluation of the area of the medial coronoid process requires the study of grossly normal structures to compare with pathologic conditions.

From studying the sagittal and dorsal reconstructions, the entire humero-radioulnar joint surface could be studied, as well as the intimate relation of the 3 bony structures (ie, humerus, ulna, and radius) composing the complex elbow joint. In the evaluation of incongruity, the information gained by CT could be more objective than findings obtained by radiography of which the evaluation is always somewhat subjective also as a result of superimposition. Major incongruity is easy to evaluate radiographically but minor incongruity can be hard to recognise. The situation becomes even more complicated as some degree of incongruity has been proven to be normal in humans [40] and animals. [1] For the detection of minor incongruity comparative studies on clinically normal dogs are also prerequisite.

The major disadvantage of CT is the requirement of general anaesthesia and the purchase and maintenance costs of the equipment. The overall examination time of 10 minutes, however, is acceptable especially if the computed tomographic examination can be combined with the eventual arthroscopic or surgical procedure.

[a] Thalamonal, Janssen Pharmaceutics, Beerse, Belgium
[b] Pentothal, Abbott Laboratories, North Chicago, Ill.
[c] CT-scannner Pace Plus, GE Medical Systems, Milkauwee, Wis.
[d] Fuji Photo Film Co, Ltd, Tokyo, Japan
[e] Electric planer, Black and Decker, Berkshire, England

REFERENCES

1. Wind A. Elbow incongruity and developmental elbow diseases in the dog : Part I. J Am Anim Hosp Assoc 1986;22:711-724.

2. Flückiger M. Ellbogendysplasie (ED) beim Hund. Schweiz Arch Tierheilk 1992;261-270.

3. Miyabayashi T, Takiguchi M, Schrader S, et al. Radiographic anatomy of the medial coronoid process of dogs. J Am Anim Hosp Assoc 1995;31:125-132.

4. Voorhout G, Hazewinkel H. Radiographic evaluation of the canine elbow joint with special reference to the medial humeral condyle and the medial coronoid process. Vet Radiol 1987;5:158-165.

5. Fox S,Walker A. Identifying and treating the primary manifestations of osteochondrosis of the elbow. Vet Med 1993;132-146.

6. Carpenter L, Schwarz P, Lowry J, et al. Comparison of radiologic imaging techniques for diagnosis of fragmented medial coronoid process of the cubital joint in dogs. J Am Vet Med Assoc 1993;203:78-83.

7. Kippenes H, Johnston G. Diagnostic imaging of osteochondrosis. Vet Clin North Am Small Anim Pract 1998;28:137-160.

8. Reichle J, Park R, Bahr A. Computed tomographic findings of dogs with cubital joint lameness. Vet Radiol Ultrasound 2000;41:125-130.

9. Hornof W, Wind A, Wallack S, et al. Canine elbow dysplasia. Vet Clin North Am Small Anim Pract 2000;2:257-266.

10. Boulay J. Fragmented medial coronoid process of the ulna in the dog. Vet Clin North Am Small Anim Pract 1998;1:51-73.

11. Stickle R, Hathcock J. Interpretation of computed tomographic images. Vet Clin North Am Small Anim Pract 1993;23:417-435.

12. Lewis D, Parker R, Hager D. Fragmented medial coronoid process of the canine elbow. Compend Cont Ed : Small Animal 1989;11:703-715.

13. Berquist T, Trigg D. The Elbow. In : Berquist T, ed. Imaging atlas of orthopedic Appliances and Prosthesis. New York: Raven Press Ltd.,1995;751-814.

14. Newberg A. Computed tomography of joint injuries. Radiol Clin North Am 1990;2:445-460.

15. Miller T. Imaging of elbow disorders. Orthop Clin North Am 1999;1:21-36.

16. Garniek A, Morag B, Yaffe B, et al. True sagittal CT scanning of the elbow. J Computer Assisted Tomography 1995;19(6):1012-1013.

17. World Association of Veterinary Anatomists (WAVA). In: Nomina Anatomica Veterinaria. 4th ed. Ithaca, NY: International Committee on Veterinary Gross Anatomical Nomenclature 1994;1-198.

18. Mason T, La Velle R, Skipper S, et al. Osteochondrosis of the elbow joint in young dogs. J Small Anim Pract 1980;21:641-656.

19. Wind A, Packard M. Elbow incongruity and developmental diseases in the dog: Part I. J Am Anim Hosp Assoc 1986;22(6):711-724.

20. Wind A, Packard M. Elbow incongruity and developmental diseases in the dog: Part II. J Am Anim Hosp Assoc 1986;22(6):725-730.

21. Denny HR. The canine elbow. I. Developmental conditions. Br Vet J 1987;143:1-20.

22. Guthrie S. Use of a radiographic scoring technique for the assessment of dogs with elbow osteochondrosis. J Small Anim Pract 1989;30:639-644.

23. Grondalen J. Arthrosis with special reference to the elbow joint of young rapidly growing dogs. II. Nord Med Vet 1979;31:69-75.

24. Grondalen J. Arthrosis in the elbow joint of young rapidly growing dogs. III. Nord Med Vet 1979;31:520-527.

25. Grondalen J, Grondalen T. Arthrosis in the elbow joint of young rapidly growing dogs: a pathoanatomical investigation. Nord Vet Med 1981;33:1-16.

26. Ollson S. The early diagnosis of fragmented coronoid process. J Am Vet Med Assoc 1983;184:799-805.

27. Henry W. Radiographic diagnosis and surgical management of fragmented medial coronoid process in dogs. J Am Vet Med Assoc 1984;184:799-805.

28. Berzon J, Quick C. Fragmented coronoid process : anatomical, clinical, and radiographic considerations with case analyses. J Am Anim Hosp Assoc 1980;16:241-251.

29. Hazewinkel H, Voorhout G. Examination and treatment of ununited medial coronoid process in dogs. Tijdschr Diergeneesk 1986;111(24):1234-1245.

30. Guthrie S, Buckland-Wright J, Vaughan L. Microfocal radiography as an aid to the diagnosis of canine elbow osteochondrosis. J Small Anim Pract 1991;32:503-508.

31. Walde I, Tellhelm B. Fragmented medial coronoid process of the ulna (FCP) and osteochondrosis dissicans (OCD) of the canine elbow and hock joint: A review of literature, diagnosis and therapy. Wien Tierärztl Monatsschr 1991;78:414-421.

32. Grondalen J. Arthrosis in the elbow joint of the young rapidly growing dogs. VI. Interrelation between clinical, radiographical and pathoanatomical findings. Nord Vet Med 1982;34:65-75.

33. Braden T, Stickle R, Dejardin L, et al. The use of computed tomography in fragmented coronoid disease: a case report. Veterinary and Comparative Orthopedaedics and Traumatology 1994;7:40-44.

34. Snaps F, Balligand M, Saunders J, et al. Comparison of radiography, magnetic resonance imaging, and surgical findings in dogs with elbow dysplasia. Am J Vet Res 1997;58:1367-1370.

35. Van Ryssen B, van Bree H, Veyt P. Arthroscopy of the shoulder joint in the dog. J Am Anim Hosp Assoc 1993;29:101-105.

36. Van Ryssen B, van Bree H. Arthroscopic findings in 100 dogs with elbow lameness. Vet Rec 1997;140:362.

37. Assheuer J, Sager M. Elbow joint. In: Assheuer J, Sager M, eds. MRI and CT atlas of the dog. Berlin: Blackwell Science 1997;210-227.

38. Reichle J, Snaps F. The elbow. Clin Techn Small Anim Pract 1999;3:177-186.

39. Seeram E. Image Quality. In : Seeram E, ed. Computed Tomography : physical principles, clinical applications, and quality control. Pennsylvania: W.B. Saunders Company 1994;173-197.

40. Eckstein F, Löhe F, Schulte E. Physiological incongruity of the humero-ulnar joint : a functional principle of optimized stress distribution acting upon articulating surfaces ? Anat Embryol 1993;188:449-455.

3.1.2. Magnetic Resonance Imaging of the Elbow Joint of the Normal Dog.

Lieve M. De Rycke, DVM

Department of Medical Imaging, Faculty of Veterinary Medicine,
Ghent University, Salisburylaan 133, 9820 Merelbeke, Belgium

SUMMARY

Objective-To use magnetic resonance imaging (MR) to provide a detailed description of elbow joint structures in clinically normal dogs

Animals- 1 clinically normal 12-month-old Labrador Retriever weighing 27 kg.

Procedure- Immediately after the CT examination of the elbow joints *(see chapter 3.1.1)* and under the same anesthesia, MR of the elbow joints was performed in the Labrador Retriever. A commercially available MR equipment[a] was used. The animal was kept in the same position as used on the CT scanning table (lateral recumbency with the elbow joints parallel and extended cranially and the head pulled back to the lateral side). Transverse T1-weighted images (TR = 500msec, TE = 12msec) were obtained with a slice thickness of 3 mm from the top of the olecranon to 3 cm distal to the elbow joint and parallel to the humeroradial joint space. After euthanasia, anatomic sections of the elbow were made as descibed in chapter 3.1.1 and compared with the corresponding MR images. Subsequently the MR images were compared to the corresponding CT images *(chapter 3.1.1).*

Results- All bony structures that were visible on the anatomic sections could be identified on the MR images. From the soft tissue structures visible on the anatomic and CT soft tissue sections sections, only the median artery and nerve and the radial nerve could not be located on the MR images. On the other hand the anular ligament and of the radius and the olecranon ligament were very distinct on the MR images and unidentifiable on the CT images. In general, vessels and soft tissue structures such as muscles and ligaments were more clearly visible on the MR-images compared to the CT images.

Conclusions and clinical Relevance- MR images provide anatomic detail of bony and soft tissue structures of the elbow joint in dogs. These results could be used as a basis for evaluation of MR images of the forelimbs of dogs with elbow joint injuries and developmental or degenerative conditions, especially nonmineralized cartilaginous MCP.

INTRODUCTION

Magnetic resonance imaging (MR) has been proved to be very useful in humans to examine synovial joints, most notably the knee[1-4]. Although computed tomography (CT) is superior for cortical bone imaging, advantages of MR for the musculoskeletal system include : absence of ionising radiation, direct multiplanar imaging, and an imaging signal directly from the bone marrow, subchondral bone and cartilage[5]. MR has high soft tissue contrast resolution that provides visualization of ligaments, the joint capsule, menisci, and synovial fluid [6-11].

In recent years, MR has been used to a limited extent to diagnose orthopedic conditions in small animals.[12-14]. In a number of reports, investigators have documented the use of IV contrast injection and MR arthrography in diagnosing cartilage abnormalities in canine joints[15-17].

MR and CT have both proved to be quite useful in the diagnosis of canine elbow disorders. CT provides a detailed assessment of the medial coronoid process (MCP), radial incisure, anconeal process and trochlear notch of the ulna, the humeral condyle, elbow joint congruity and osteoarthrosis[18]. MR readily differentiates the various conditions associated with canine elbow dysplasia, and appears to be superior to CT for identifiying nonmineralized cartilaginous MCP. Improved visualization of other cartilage abnormalities such as humeral condylar osteochondrosis /osteochondritis dissecans (OC/OCD) or wear lesions will likely occur as MR imaging sequences for the elbow are continually refined[18].

A complete MR examination of the elbow joint should include sagittal, dorsal, and transverse plane images to encompass the entire joint [18]. In order to make an accurate interpretation of these images a thorough knowledge of the anatomy of the elbow joint on MR images is necessary. The purpose of this chapter was to provide a description of the elbow joint in clinically normal dogs, as revealed by MR and to make a comparison between the results of the CT study *(see chapter 3.1.1*) and this MR study of the canine elbow.

MATERIAL AND METHODS

Immediately after the CT examination of the elbow joints *(see chapter 3.1.1)* and under the same anesthesia, MR of the elbow joints was performed in the Labrador Retriever used in the previous study. A commercially available MR equipment[a] was used. The animal was kept in the same position as used on the CT scanning table (lateral recumbency with the elbow joints parallel and extended cranially and the head pulled back to the lateral side). Transverse T1-weighted images (TR = 500msec, TE = 12msec) were obtained with a slice thickness of 3 mm from the top of the olecranon to 3 cm distal to the elbow joint and parallel to the humeroradial joint space. T1-weighted images were preferred for the good anatomical resolution. Acquisition matrix was 256 x 256.

The anatomical sections of the elbow joints of the Labrador Retriever *(see chapter 3.1.1)* were compared to the corresponding transverse MR images.

From the collection of matched MR and anatomical images, 6 representative pairs were selected from the proximal to distal regions of the elbow (Figure 2 chapter 3.1.1). The identified structures on the anatomical sections *(see chapter 3.1.1)* were subsequently located on the corresponding MR images. Subsequently the MR images were compared to the corresponding CT images (Fig. 2 chapter 3.1.1).

RESULTS

All bony structures that were visible on the anatomic sections could be identified on the MR images. From the soft tissue structures visible on the anatomic sections, only the median artery and nerve and the radial nerve could not be located on the MR images.

All structures identified on the soft tissue setting CT images could be identified on the MR images, except for the median artery and nerve and the radial nerve. On the other hand the anular ligament and of the radius and the olecranon ligament were very distinct on the MR images and unidentifiable on the CT images. In general, vessels and soft tissue structures such as muscles and ligaments were more clearly visible on the MR-images compared to the CT images.

These results are also listed in Table 1

TABLE 1	CT	MR
Bony structures		
H = Humerus	+	+
lc = Lateral part of humeral condyle	+	+
le = Lateral epicondyle	+	+
mc = Medial part of humeral condyle	+	+
me = Medial epicondyle	+	+
of = Olecranon fossa	+	+
rf = Radial fossa	+	+
sf = Supratrochlear foramen	n	+
R = Radius	+	+
U = Ulna	+	+
ap = Anconeal process	+	+
lcp = Lateral coronoid process	+	+
mcp = Medial coronoid process	+	+
o = Olecranon	+	+
ot = Olecranon tuber	+	+
rn = Radial notch	+	+
tn = Trochlear notch	+	+
cr = central ridge	+	+
mf = medial flange	+	+
lf = lateral flange	+	+
ut = Ulnar tuberosity	+	+
Soft tissue structures		
1 = Anconeus muscle	+	+
2 = Biceps brachii muscle	+	+
3 = Brachialis muscle	+	+
4 = Cleidobrachialis muscle	+	n
5 = Extensor digitorum communis muscle	+	+
6 = Extensor digitorum lateralis muscle	+	+
7 = Extensor carpi radialis muscle	+	+
8 = Extensor carpi ulnaris muscle	+	+
9 = Abductor digiti I muscle	+	n
10 = Flexor digitorum superficialis muscle	+	+
11 = Flexor digitorum profundus muscle	+	+
11 = humeral head	+	+
11’ = ulnar head	+	+
12 = Flexor carpi radialis muscle	+	+
13 = Flexor carpi ulnaris muscle	+	+
13 = humeral head	+	+
13’ = ulnar head	+	+
14 = Pronator teres muscle	+	+
15 = Supinator muscle	+	+
16 = Triceps brachii muscle (tendons)	+	+
17 = Brachial artery	+	+
18 = Median artery	+	--
19 = Brachial vein	+	+
20 = Cephalic vein	+	+
21 = Median cubital vein	+	+
22 = Median vein	+	+
23 = Median nerve	+	--
24 = Radial nerve	+	--
24’= medial superficial branch	+	--
24’’= lateral superficial branch	+	--

TABLE 1	CT	MR
25 = Ulnar nerve	+	+
26 = Anular ligament of radius	--	+
27 = Antebrachial interosseous membrane	--	n
28 = Cubital joint capsule (fibrous membrane)	+	+
29 = Lateral collateral ligament (proximal, undivided part)	+	+
30 = Medial collateral ligament (proximal, undivided part)	+	+
31 = Olecranon ligament	--	+

TABLE 1 : Structures of the canine elbow visible on CT and MR scans. (n= not present in the selected views)

CONCLUSION

MR images provide anatomic detail of bony and soft tissue structures of the elbow joint in dogs. Muscles, ligaments, large blood vessels and some nerves are very distinct and can easily be evaluated. On the T1-weighted images, the cortical bone is presented by a band of signal void, ligaments and tendons image with a low signal intensity, whereas adjacent muscle or hyaline articular cartilage demonstrates an intermediate signal intensity. Yellow or fatty marrow generates increased signal intensity.

The choice between CT or MR for elbow patologies will depend on the suspected lesion. CT is superior for cortical bone imaging, while MR provides a better visualization of ligaments, joint capsule, synovial fluid and cartilage abnormalities. MR appears to be superior for identifying nonmineralized cartilaginous MCP.

These results could be used as a basis for evaluation of MR images of the forelimbs of dogs with elbow joint injuries and developmental or degenerative conditions, especially nonmineralized cartilaginous MCP.

[a] Symphony, Siemens A.G., Erlangen, Germany

REFERENCES

1. De Smet AA, Fisher DR, Graf BK, et al. Osteochondrosis dissecans of the knee: Value of MR imaging in determining lesion stability and the presence of cartilage defects. Am J Roentgenol 1990;155:549-553.

2. Hayes CW, Conway FW. Evaluation of articular cartilage: Radiographic and cross-sectional imaging techniques. Radiographics 1992;12:409-428.

3. Heron CW, Calvert PT. Three-dimensional gradient echo MR imaging of the knee: comparison with arthroscopy in 100 patients. Radiology 1992;183:839-844.

4. Hodler J, Berthiaume MJ, Scheitzer ME, et al. Knee joint hyaline cartilage defects: A comparative study of MR imaging and anatomic sections. J Comput Assist Tomogr 1992;16:597-603.

5. Tyrrel RL, Guckert K, Pathria M, et al. Fast three-dimensional MR imaging of the knee: Comparison with arthroscopy. Radiology 1988;166:865-872.

6. Bjsrkengren AG, Alroiwaith A, Linstrand A, et al. Spontaneous osteonecrosis of the knee: value of MR imaging in determining prognosis. Am J Roentgenol 1990;154:331-336.

7. Bloem JL, Reiser MF, Vanel D. Magnetic resonance contrast agents in the evaluation of musculoskeletal system. Magn Reson 1990;6:136-163.

8. König H, Sauter R, Deimlich M, et al. Cartilage disorders: Comparison of spin-echo chess, and flash sequence MR images. Skel Radiol 1987;164:753-758.

9. Mink JH, Deutsh AL. Occult cartilage and bones injuries of the knee: detection, classification and assessment with MR imaging. Radiology 1989;170:823-829.

10. Solomon SL, Totty WG, Lee JK, et al. MR imaging of the knee: Comparison of the three-dimensional FISP and two-dimensional spin-echo pulse sequences. Radiology 1989;173:739-742.

11. Tervoven O, Dietz MJ, Carmichael SW, et al. MR imaging of knee hyaline cartilage: Evaluation of two- and three- dimensional sequences. J Magn Reson Imag 1993;3:663-668.

12. Snaps F, Balligand M, Sauders J, et al. Comparison of radiography, magnetic resonance imaging, and surgical findings in dogs with elbow dysplasia. Am J Vet Res 1997;58:1367-1370.

13. Van Bree H, Degryse H, van Ryssen B, et al. Pathologic correlations with magnetic resonance images of osteochondrosis lesions in canine shoulders. J Am Vet Med Assoc 1993;202:1099-1105.

14. Widmer WR, Buckwalter KA, Braunstein EM, et al. Radiographic and magnetic resonance imaging of the stifle joint in experimental osteoarthrosis of dog. Vet Radiol Ultrasound 1994;35:371-383.

15. Snaps F, Saunders J, Park R, et al. Comparison of spin-echo, gradient echo, and fat saturation MRI sequence. Vet Radiol Ultrasound 1998;39:518-523.

16. Snaps F, Park R, Suanders J, et al. Magnetic resonance arthroscopy of the cubital joint in dogs affected with fragmented medial coronoid processes. Am J Vet Res 1999;60:190-193.

17. Van Bree H, van Ryssen B, Degryse H, et al. Magnetic resonance arthrography of the scapulohumeral joint in dogs, using gadopentetate dimeglumine. Am J Vet Res 1995;56:286-288.

18. Reichle J, Snaps F. The elbow. Clin Techn Small Anim Pract 1999;3:177-186.

3.2. The Tarsus

The next two chapters concern the investigation of the tarsal joint of the clinically normal dog. In the first chapter (chapter 3.2.1) the computed tomographic examination of the tarsus is described. The second chapter (chapter 3.2.2) briefly handles the magnetic resonance of this joint and gives a comparison between the results of the 2 techniques, CT and MR. .

However, all figures (anatomic, CT and MR sections) of the tarsal joint are combined in figure 2 of the first chapter (chapter 3.2.1) to make a visual comparison easier and simple.

3.2.1. Computed tomography of the tarsal joint in clinically normal dogs

Lieve M. De Rycke*, DVM; Ingrid M. Gielen*, DVM, MSc;
Henri van Bree*, DVM, PhD; Paul J. Simoens**, DVM, PhD

*Department of Medical Imaging, Faculty of Veterinary Medicine, Ghent University,
Salisburylaan 133, 9820 Merelbeke, Belgium.

**Department of Morphology, Faculty of Veterinary Medicine, Ghent University,
Salisburylaan 133, 9820 Merelbeke, Belgium.

Adapted from :

Gielen IM, De Rycke LM, van Bree H, Simoens PJ. Computed tomography of the tarsal joint in clinically normal dogs. *Am J Vet Res* 2001;62:1911-1915.

SUMMARY

Objective—To use computed tomography to provide a detailed description of tarsal joint structures in clinically normal dogs.

Animals—6 clinically normal adult mixed-breed dogs weighing 25 to 35 kg and one 12-month-old Bullmastiff weighing 65 kg.

Procedure—To perform computed tomography (CT) of both tarsal regions, dogs were anesthetized and placed in ventral recumbency. One and 2mm thick contiguous slices were obtained, using a third generation CT scanner. Individual images were reviewed, using bone (window width = 3500 Hounsfield units; window level = 500 Hounsfield units) and soft tissue (window width = 400 Hounsfield units; window level = 66 Hounsfield units) settings. After euthanasia, the hind limbs from the Bullmastiff were removed and frozen at –18 C. Tarsal joints were sectioned into approximately 1-mm thick slab sections using a cryomicrotome. Anatomic sections were photographed and compared with the corresponding CT images. CT reconstructions of the tarsocrural joint were created in sagittal and dorsal planes.

Results—Structures on the CT images were matched with structures in the corresponding anatomic sections. The entire tarsocrural joint surface could be evaluated on the reconstructed images in the sagittal and dorsal planes.

Conclusions and Clinical Relevance—CT images provide full anatomic detail of the bony structures of the tarsal joint in dogs. Tendons and large blood vessels can also be seen. These results can be used as a basis for evaluation of computed tomographic images of dogs with tarsal joint injuries.

INTRODUCTION

The tarsal joint in dogs is a compound and complex joint, and although there is a detailed study[1] on the radiographic anatomy of the tarsocrural joint, radiographic evaluation of this region remains difficult because of superimposition of various bony structures, including the distal portion of the tibia and fibula, talus, calcaneus, tarsal, and metatarsal bones. Therefore, the radiographic diagnosis of tarsal lesions, including tarsocrural osteochondrosis, can be challenging, and arthrotomy has been advocated as a reasonable diagnostic option by some authors.[2-5] Computed tomography (CT) offers several advantages over conventional radiography, including the following: elimination of superimposed structures, thereby decreasing the complexity of the image; variation in gray scale formats, which can enhance observation of specific structures; and reconstruction in multiple anatomic planes.[6]

In humans medicine, CT is indicated in situations where detailed information is needed to make a precise diagnosis or to define a tarsal injury more accurately.[7-9] In instances of complex intra-articular fractures, subchondral bone sclerosis, and other subchondral bone lesions such as osteochondrosis of the talus, CT is a useful expedient for the diagnosis and may indicate the exact size and location of the lesion.

To provide accurate interpretation of CT images and to recognize abnormalities that may be found, knowledge of the anatomy of the tarsal joint in clinically normal dogs is a prerequisite. The aim of the study presented here was to provide a detailed description of the tarsal joint in clinically normal dogs, as revealed by use of CT. The results of this CT study were subsequently compared to the results of a MR investigation of the canine tarsus (see chapter 3.2.2).

MATERIALS AND METHODS

Animals- Six healthy adult mixed-breed dogs weighing 25 to 35 kg and one 12-month-old Bullmastiff weighing 65 kg were used for our study. Prior to the study, tarsal joints of each dog were physically and radiographically examined. The following 6 radiographic views were obtained: a fully extended and fully flexed mediolateral, a plantarodorsal, a 30° plantarolateraldorsomedial and 30° plantaromedial-dorsolateral and a flexed dorsoplantar skyline view. No abnormalities were found on any radiograph.

Computed tomography- Dogs were sedated using medetomidine hydrochloride[a] (40 to 50 μg/kg of body weight, IM), and anesthetized with thiopental sodium[b] (8 mg/kg, IV). After intubation, anesthesia was maintained with halothane. Dogs were positioned in ventral recumbency on the CT scanning table with the tarsal joints in extension. This position allows a perfect symmetry and comparison of both tarsi at the same level. Lateral and plantarodorsal survey views were obtained, using a third generation CT scanner[c] to confirm correct positioning. On the plantarodorsal survey view, CT scans were performed from the distal portion of the tibia and fibula to the proximally located metatarsal bones and parallel to the tarsocrural joint space.

Two millimeter thick contiguous slices were obtained from the most proximal part of the calcaneus to 1 cm distal to the tarsometatarsal joint. However, in the region of the tarsocrural joint, 1-mm thick contiguous views were obtained. Individual images were reviewed using a bone setting (window width = 3500 Hounsfield units; window level = 500 Hounsfield units) and a soft tissue setting (window width = 400 Hounsfield units; window level = 66 Hounsfield units). Settings for the CT image technique were as follows 120 kVp and 100 mA. Image acquisition time was approximately 10 minutes. Images from all 6 dogs were formatted on x-ray film[d] and evaluated.

Comparison of CT and anatomic images- All 6 dogs recovered from anesthesia. The Bullmastiff was euthanatized after CT for reasons unrelated to orthopedic conditions. After euthanasia, the hind limbs of this dog were removed and frozen at –18 C with the tarsal joints in extension. The tarsal joints from the distal portion of the tibia and fibula to the distal portion of the talus and calcaneus were embedded in carboxymethylcellulose and sectioned into approximately 1-mm-thick slab sections, using a large specimen cryomicrotome.[e] All anatomic sections were photographed and matched with a corresponding CT image (bone setting) on the basis of appearance. From this collection, 12 representative matched pairs of the right tarsal joint were selected from proximal to distal regions. Bony structures and soft tissues were identified on the anatomic sections by comparing all features with a dissected tarsal joint of a large-breed dog that had been euthanatized for reasons unrelated to orthopedic conditions. The identified structures were subsequently located on the corresponding CT images (both bone and soft tissue settings) and afterwards, the list of identified structures was evaluated on the CT images of the 6 other dogs. The nomenclature used for designating all structures was in accordance with official anatomic terms.[10] Using data from the transverse slices, images can be produced in other planes using computer reformatting. Computed tomography-based reconstructions of the tarsocrural joint in a sagittal and dorsal plane were made to determine whether an evaluation of the entire joint surface could be performed without superimposition of any bony structures.

RESULTS

The plantarodorsal survey view of the 17 selected levels of the right tarsal joint of the Bullmastiff was obtained (Fig 1). CT images (bone and soft tissue settings) and the cut surface of the corresponding anatomic sections of the right tarsal joint of the Bullmastiff were compared (Fig 2 and 3).

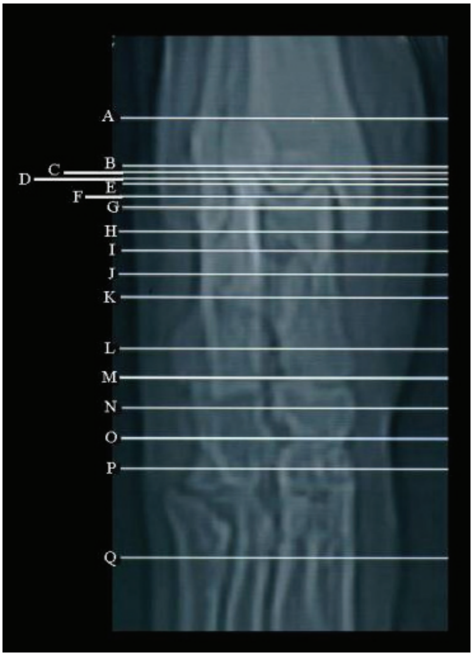

Figure 1 - Plantarodorsal survey view of the tarsal joint of a clinically normal dog indicating the levels (A through Q) at which computed tomographic (CT) images were obtained

Most of the bony, tendinous, and vascular structures were visible on the proximally located anatomic sections (Fig. 2, rows A through E). Osseous structures included the distal portion of the tibia and fibula with the pertaining malleoli, the talus and trochlea tali ridges, and the tuber calcanei. Additionally, tendons of 7 muscles could be identified on the anatomic sections. Five major blood vessels (4 veins and 1 artery) were readily visible on all sections. All of these structures were also visible on the soft tissue-setting CT images except for the rami caudales of the vena saphena lateralis and vena saphena medialis. On the bone setting CT images, only the previously mentioned bony structures could be identified.

On the distally located anatomic sections (Fig 2, rows F through L), bony structures that could be identified included the distal portion of the tibia and fibula with the pertaining malleoli, the talus and calcaneus with a prominent sustentaculum tali, or the collum tali and calcaneus. Soft-tissue structures were almost identical to those described for the proximally located anatomic sections, except that the tendons of the peroneus longus muscle and extensor digitorum lateralis muscle crossed over and, therefore changed positions, the talocalcaneous interosseous ligament was visible, and the extensor digitorum brevis muscle was observed. Distally, the dorsal region of anatomic sections of the tarsal joint contained only a single superficial vein, formed by the fusion of the rami craniales of the saphena lateralis vein and the saphena medialis vein. Except for the extensor digitorum brevis muscle, these osseous and soft-tissue structures were also visible on the soft-tissue setting CT images. In contrast with the more proximal anatomic sections, the rami caudales of the saphena lateralis and saphena medialis veins could be located. On the bone-setting CT images, all bony structures seen on the anatomic sections could be identified.

Analysis of CT images made at the most distal levels (Fig 3) revealed the talus, calcaneus, and os tarsi centrale; the os tarsi centrale and os tarsale quartum; the os tarsale secundum, tertium, and quartum; the os tarsale primum, secundum, tertium, and quartum; or metatarsals II, III, IV, and V.

Sagittal and dorsal reconstructions were made of the right tarsocrural joint of the Bullmastiff (Fig 4). The sagittal images allowed a thorough evaluation of the lateral and medial parts of the tarsocrural joint including the lateral and medial ridge. On the dorsal reconstructions, the tarsocrural joint could be evaluated from the dorsal to plantar surface in detail.

For the other 6 dogs, all osseous structures mentioned for the Bullmastiff could be seen on the bone-setting CT images. Similarly, all bony, tendinous, and vascular structures that could be identified on the soft tissue-setting CT images of the Bullmastiff were also noticed on the soft-tissue setting CT images of the 6 mixed-breed dogs. Additionally, in 4 dogs, the rami craniales of the saphena

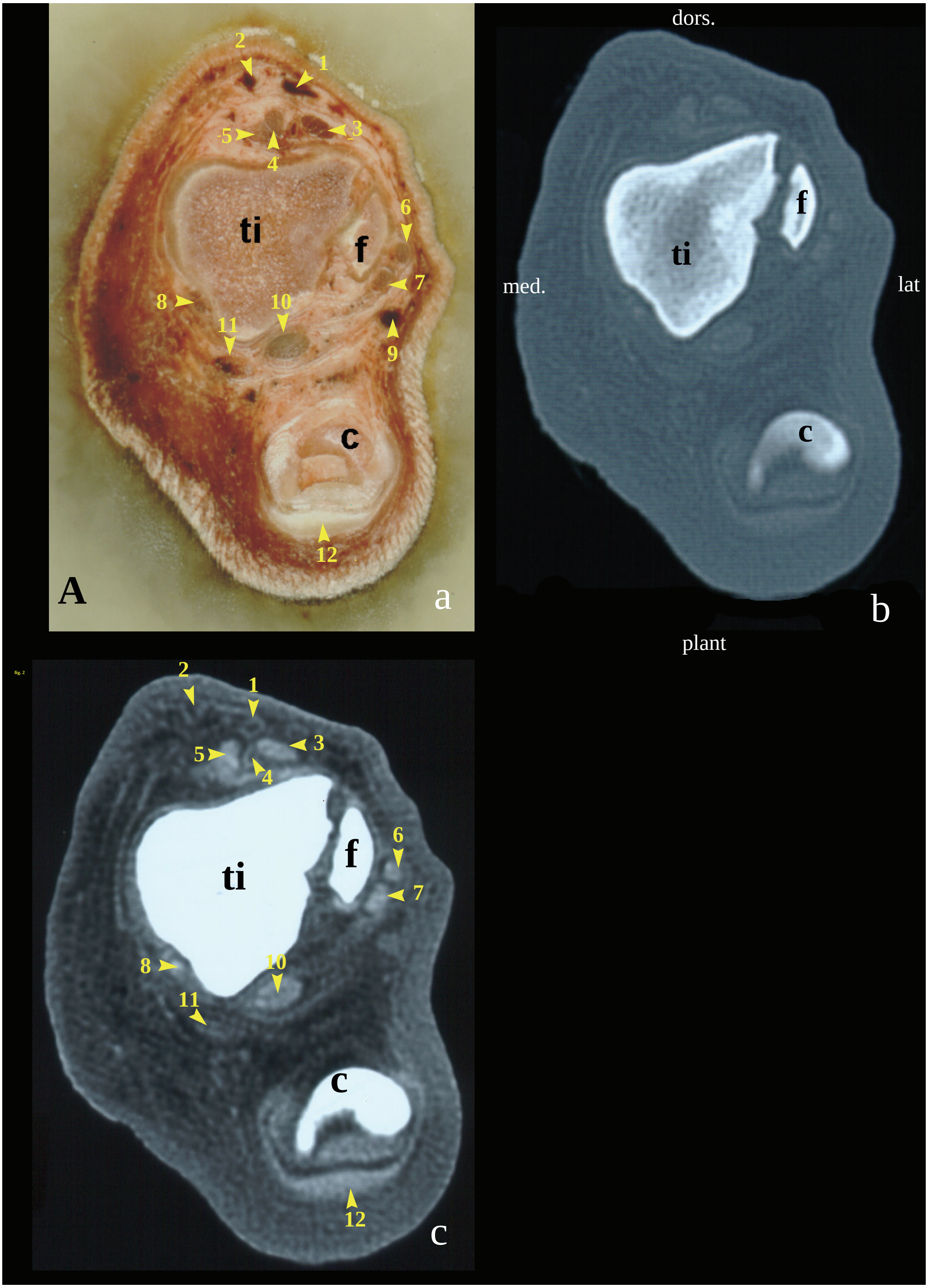
A
a
2
1
5
4
3
ti
f
6
7
8
10
11
9
c
12
dors.
med.
lat
plant
b
fig. 2
c

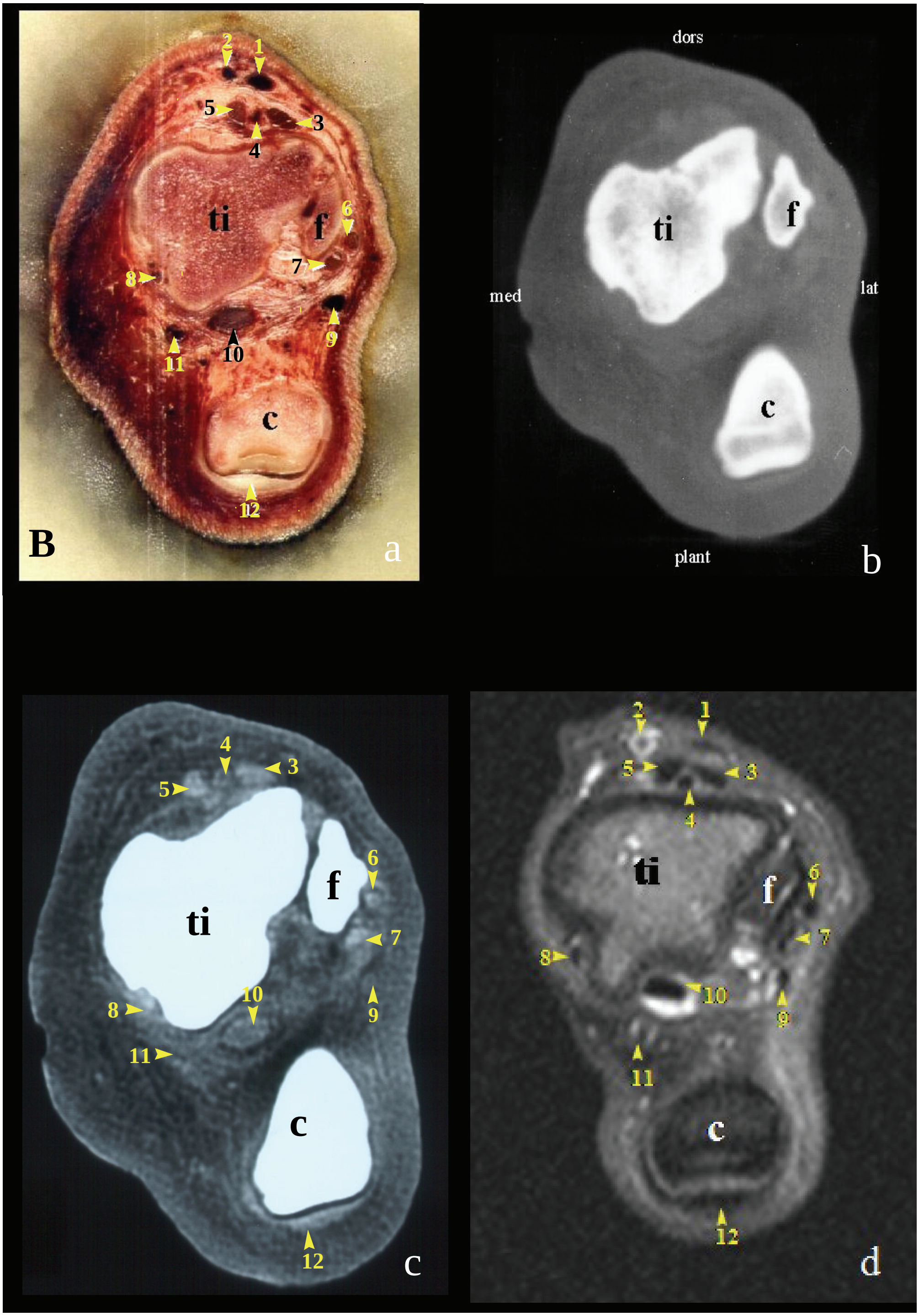
B
a
2
1
5
3
4
ti
f
6
7
8
9
10
11
c
12
b
dors
med
lat
plant
ti
f
c
c
4
3
5
ti
f
6
7
8
10
9
11
c
12
d
2
1
5
3
4
ti
f
6
7
8
10
9
11
c
12

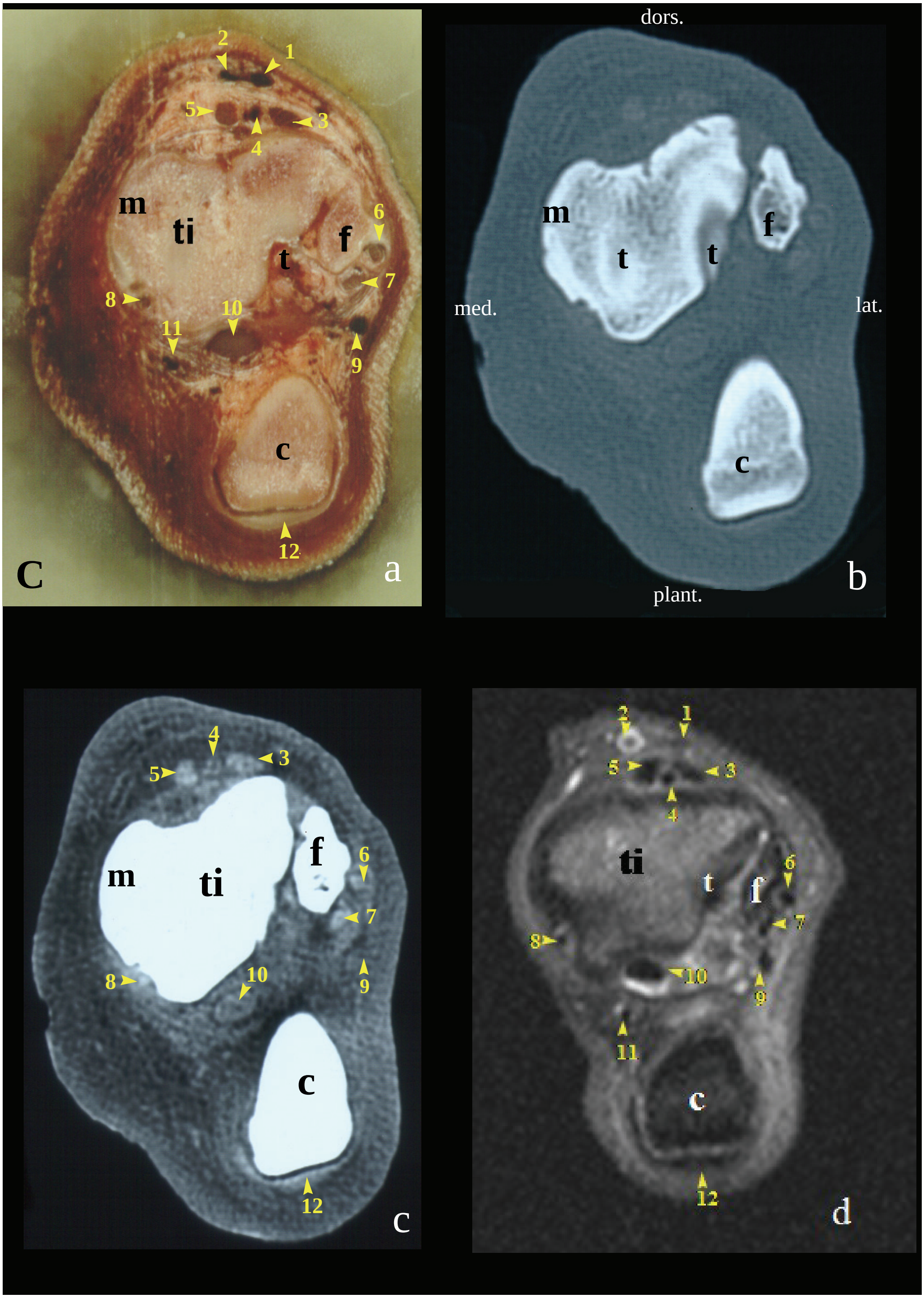
C
2
1
5
3
4
m
ti
t
f
6
7
8
10
11
9
c
12
a
dors.
m
t
t
f
med.
lat.
c
plant.
b
4
5
3
m
ti
f
6
7
8
10
9
c
12
c
2
1
5
3
4
ti
t
f
6
8
7
10
9
11
c
12
d

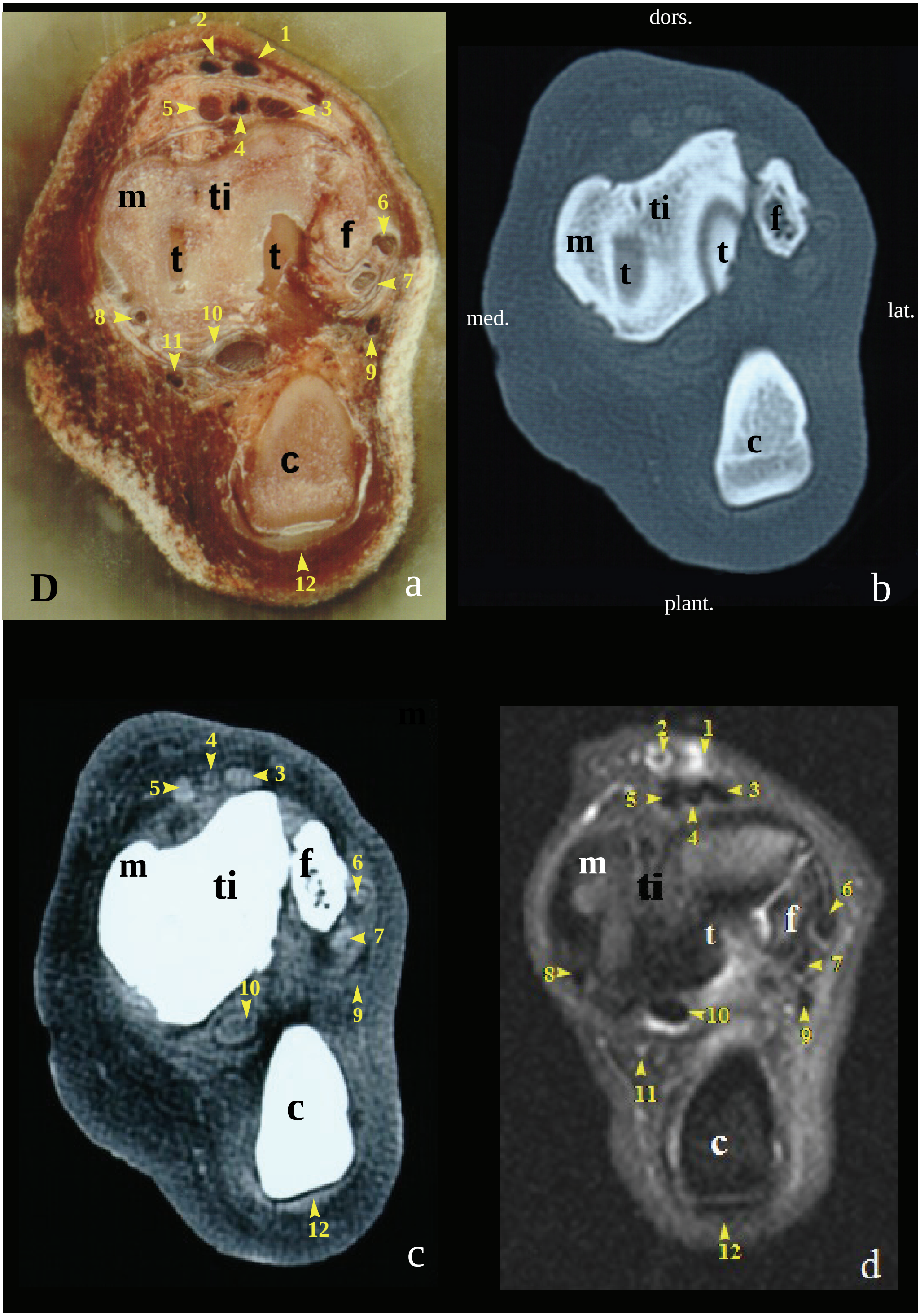
2
1
5
3
4
m
ti
6
t
t
f
7
8
10
11
9
c
D
12
a
dors.
ti
f
m
t
t
med.
lat.
c
plant.
b
m
4
3
5
m
ti
f
6
7
10
9
c
12
c
2
1
5
3
4
m
ti
6
t
f
8
7
10
9
11
c
12
d

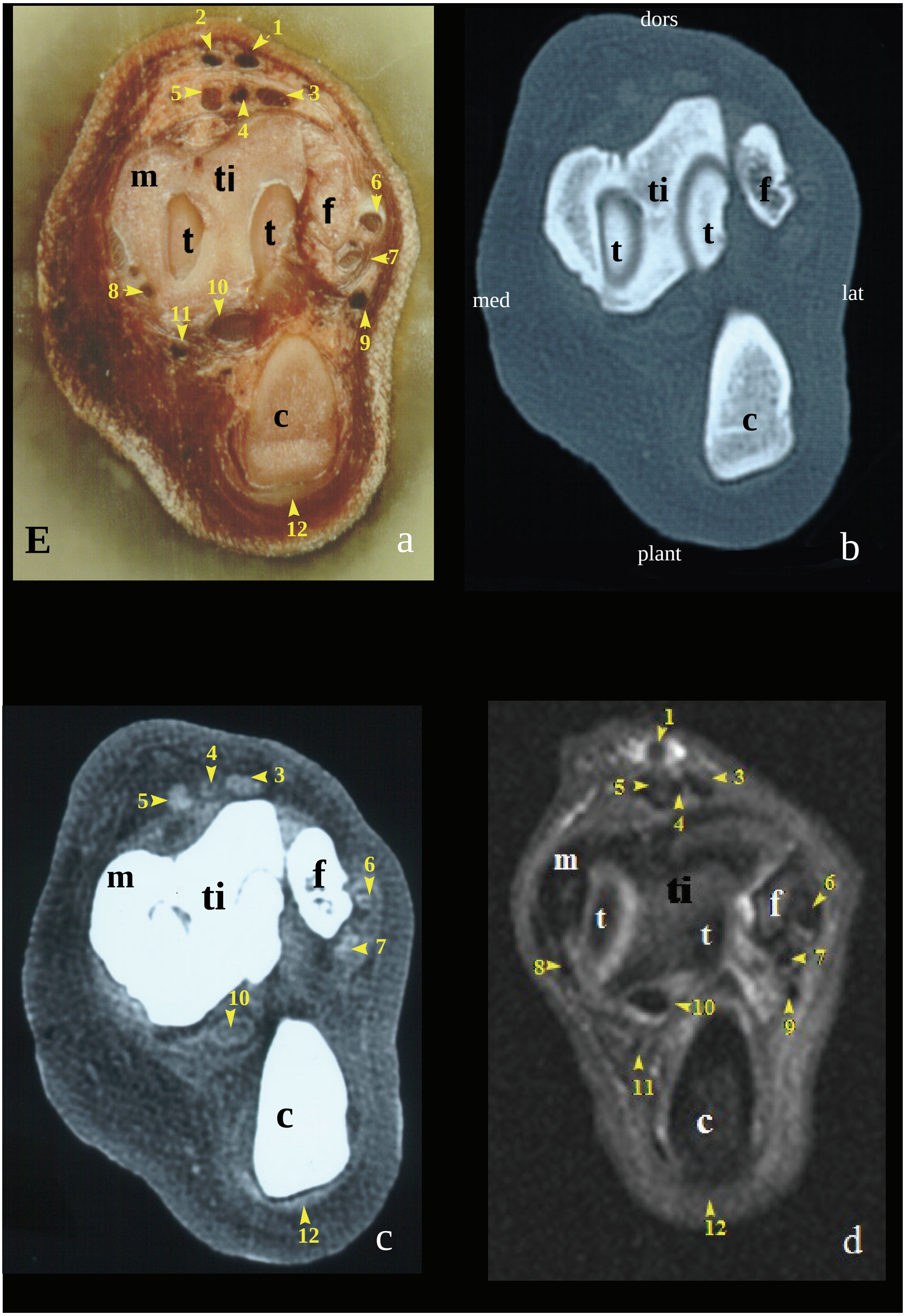
2
1
5
3
4
m
ti
6
f
t
t
7
8
10
11
9
c
E
12
a
dors
ti
f
t
t
med
lat
c
plant
b
4
3
5
m
f
6
ti
7
10
c
12
c
1
5
3
4
m
ti
6
t
f
t
8
7
10
9
11
c
12
d

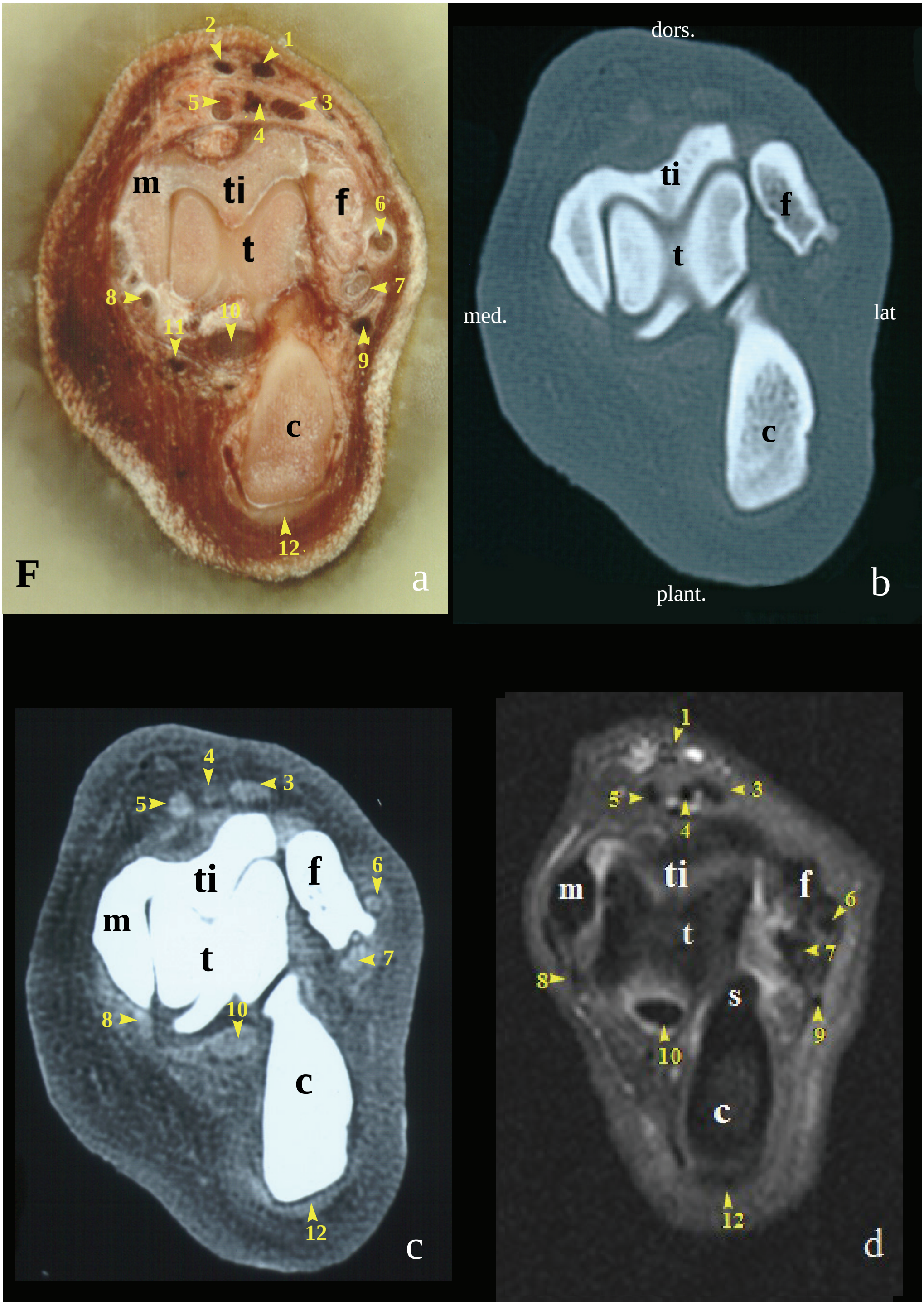
F
a
1
2
3
4
5
6
7
8
9
10
11
12
m
ti
t
f
c
b
dors.
med.
lat
plant.
ti
t
f
c
c
1
3
4
5
6
7
8
10
12
m
ti
t
f
c
d
1
3
4
5
6
7
8
9
10
12
m
ti
t
f
s
c

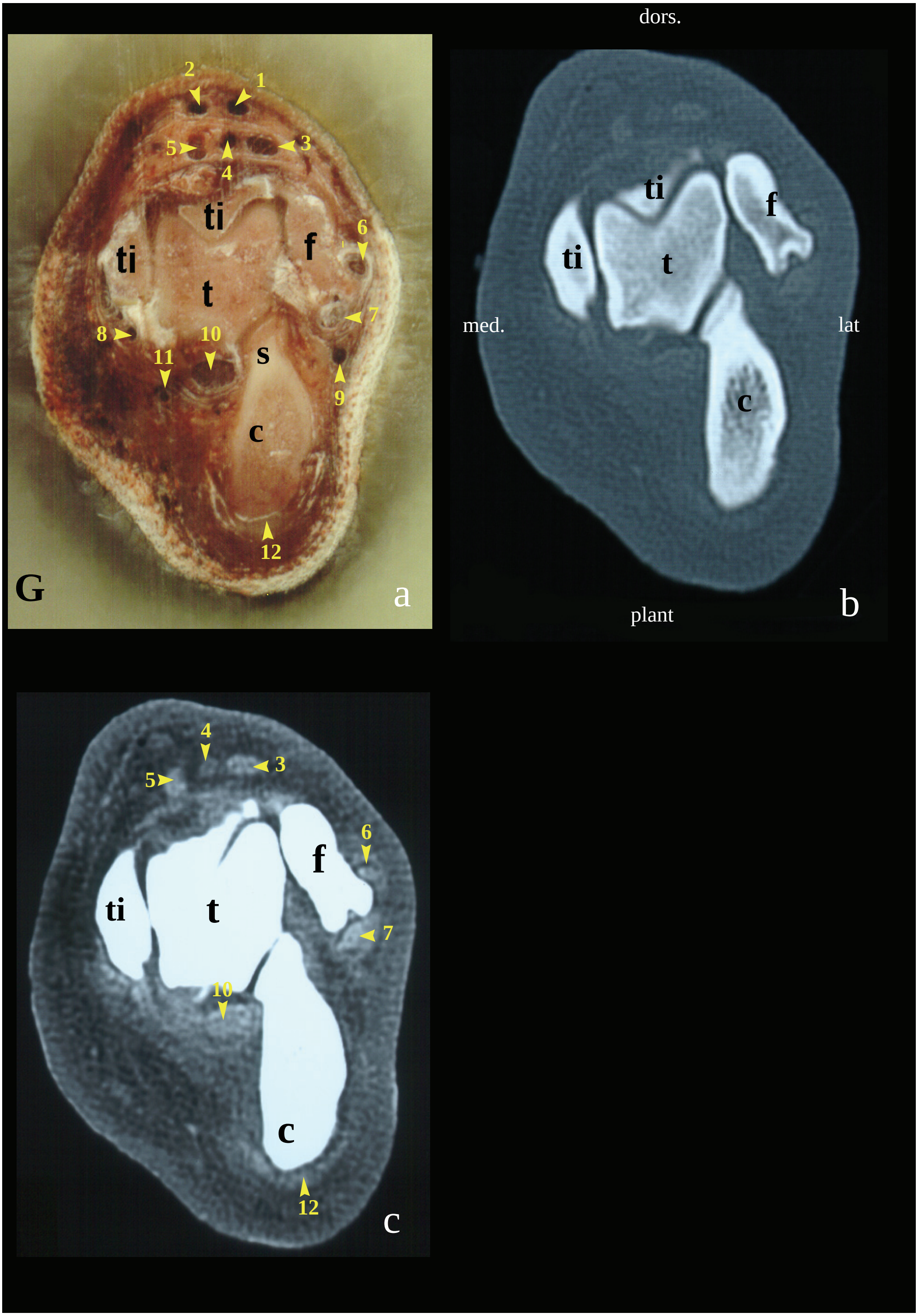
dors.
2
1
5
4
3
ti
ti
f
6
t
7
8
10
s
11
9
c
12
G
a
ti
f
ti
t
med.
lat
c
plant
b
4
3
5
6
f
ti
t
7
10
c
12
c

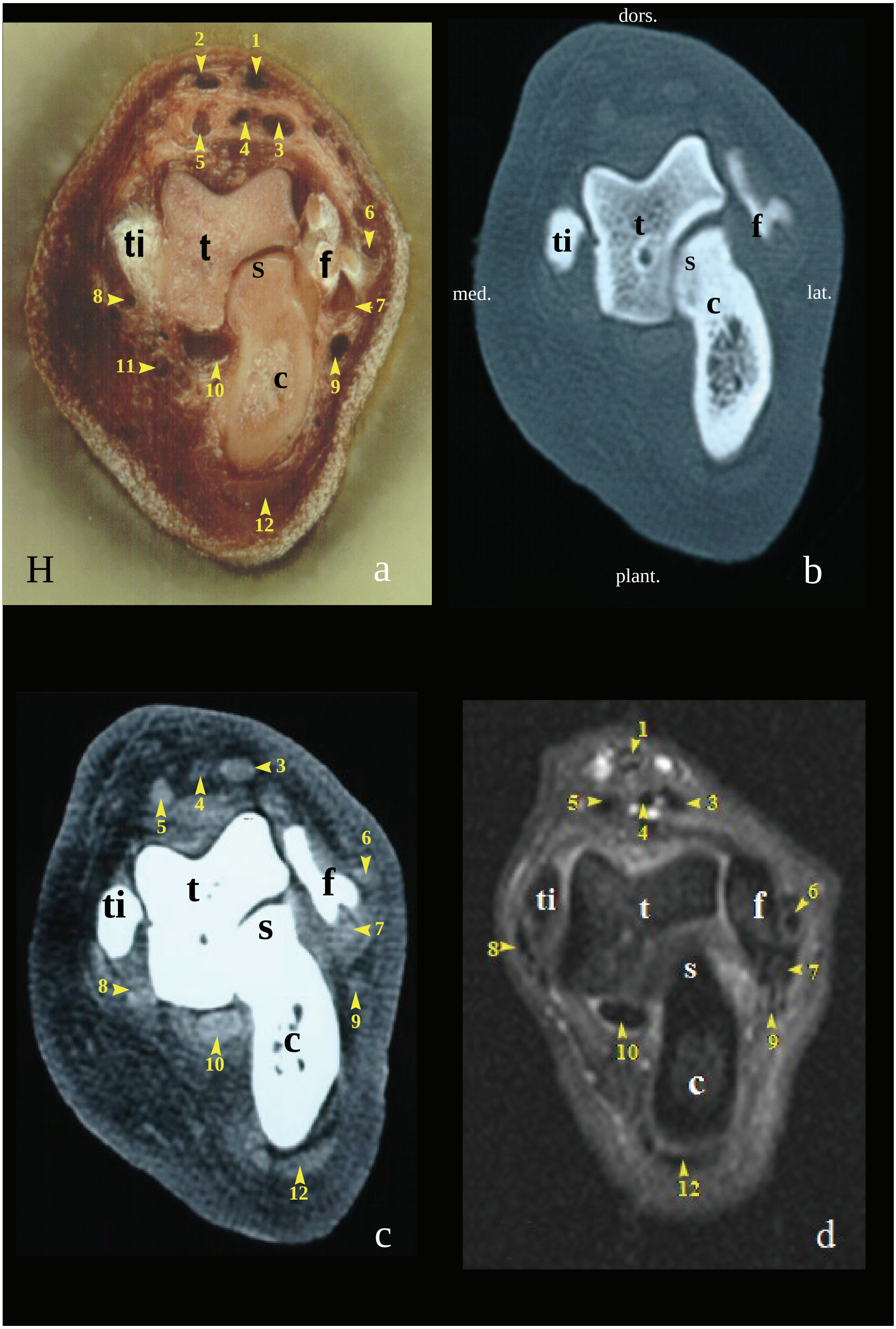
2
1
5
4
3
6
ti
t
s
f
8
7
11
10
c
9
12
H
a
dors.
ti
t
f
s
med.
c
lat.
plant.
b
3
4
5
6
ti
t
f
s
7
8
9
c
10
12
c
1
5
3
4
ti
t
f
6
8
s
7
10
9
c
12
d

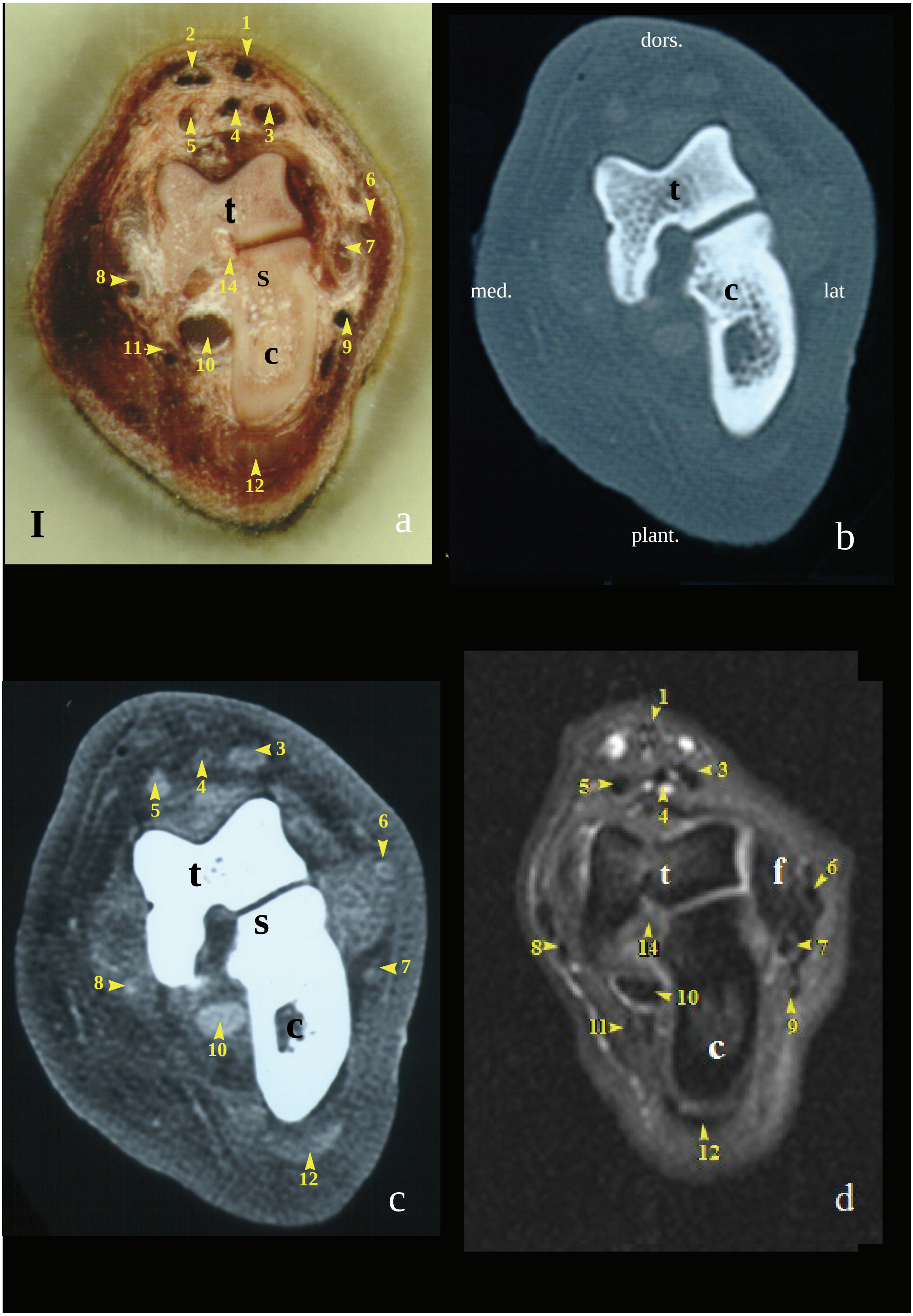
1
2
3
4
5
6
7
8
9
10
11
12
14
t
s
c
I
a
dors.
med.
lat
plant.
b
3
4
5
6
7
8
10
12
t
s
c
c
1
3
5
4
t
f
6
8
14
7
10
11
9
c
12
d

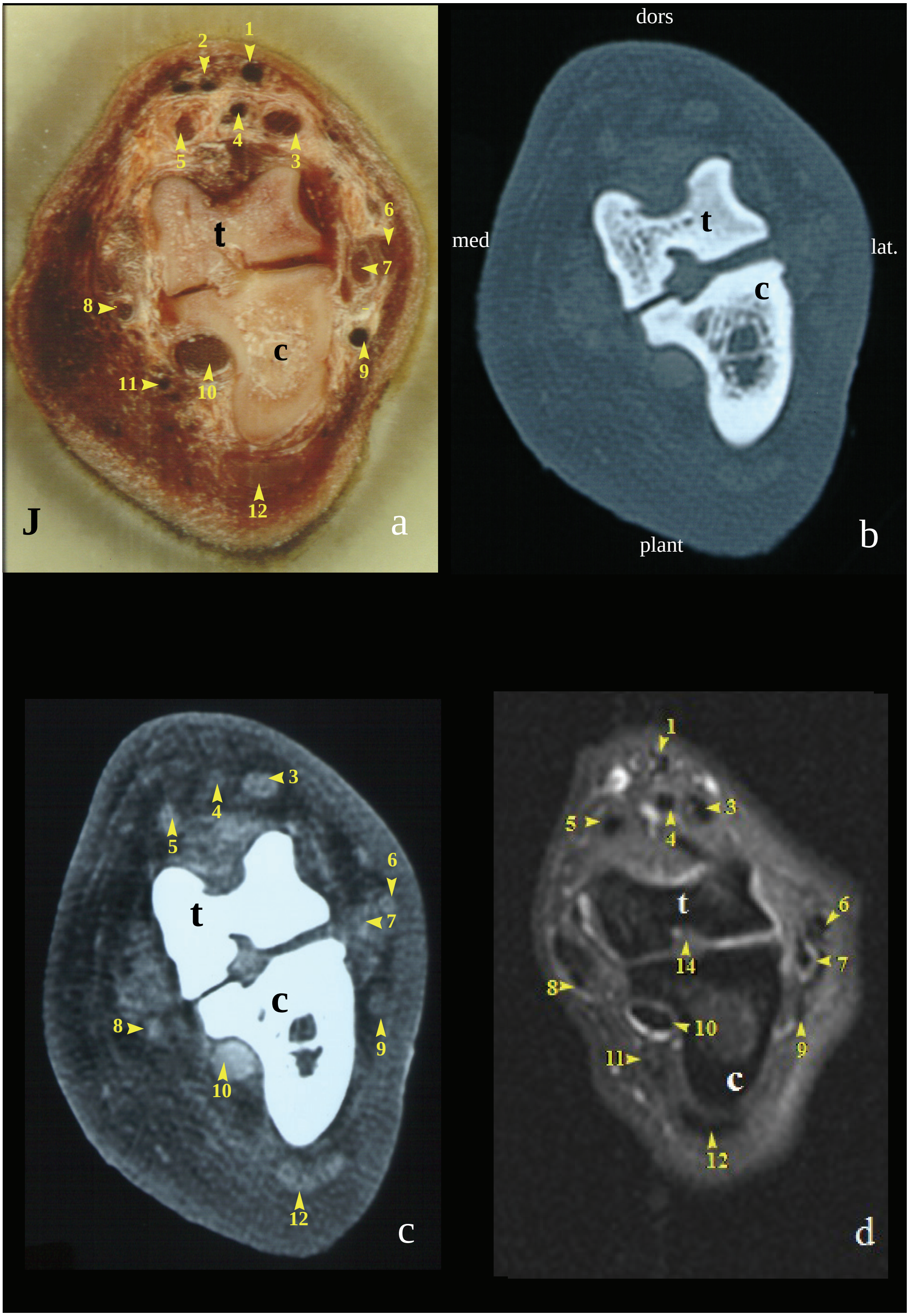
1
2
4
5
3
t
6
7
8
c
9
11
10
12
J
a
dors
med
t
lat.
c
plant
b
3
4
5
6
t
7
c
8
9
10
12
c
1
3
5
4
t
6
14
7
8
10
11
9
c
12
d

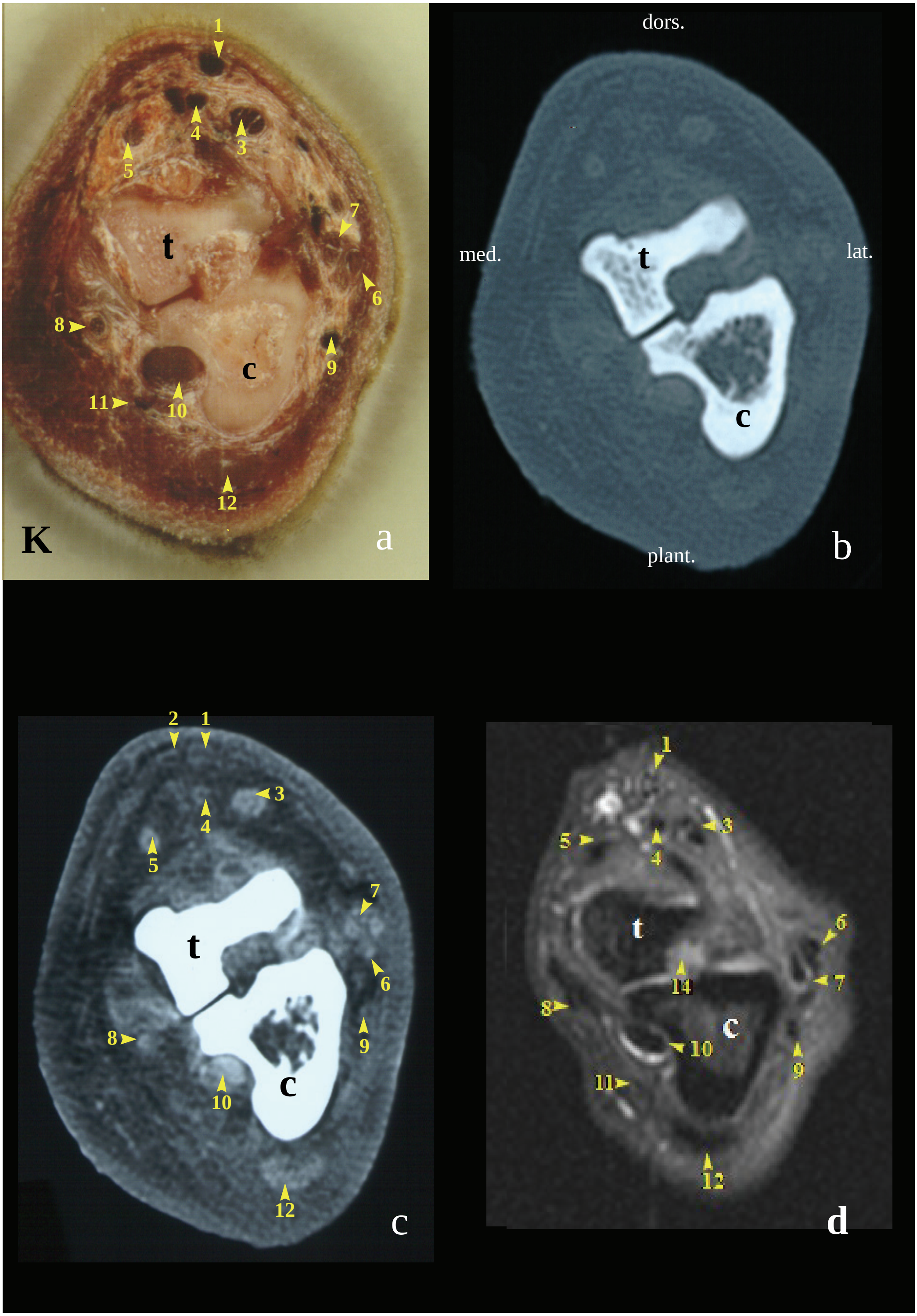
1
4
3
5
7
t
6
8
c
9
11
10
12
K
a
dors.
med.
t
lat.
c
plant.
b
2
1
3
4
5
7
t
6
8
9
c
10
12
c
1
5
3
4
6
t
14
7
8
c
10
9
11
12
d

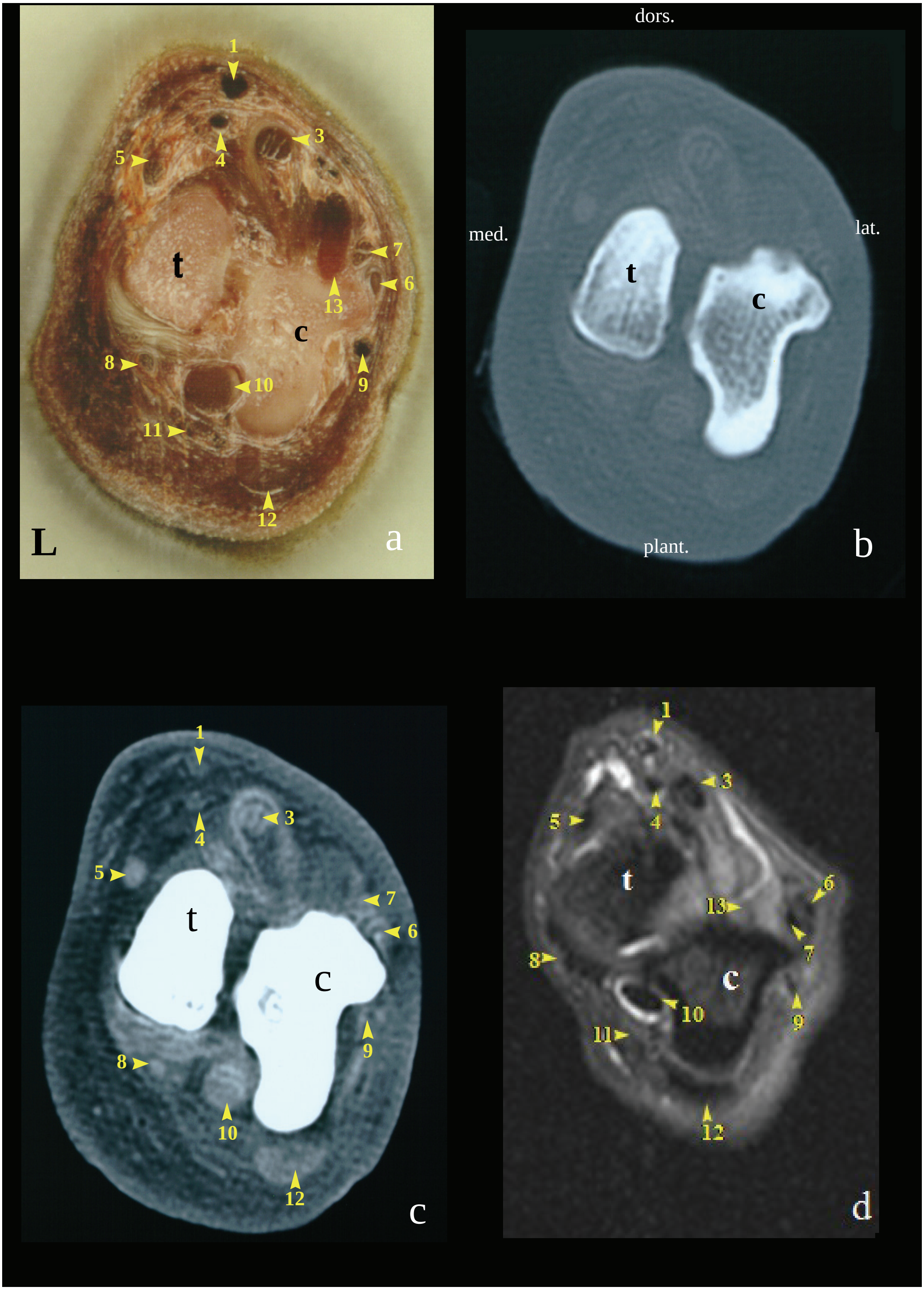
1
5
4
3
t
7
6
13
c
8
10
9
11
12
L
a
dors.
med.
lat.
t
c
plant.
b
1
3
4
5
t
7
6
c
8
9
10
12
c
1
3
5
4
t
6
13
8
7
c
10
11
9
12
d

Figure 2—Transverse anatomic sections (top left), corresponding CT images (top right, bone image; bottom left, soft tissue image) and combined T2-proton density MR images (TE = 3500msec, TE = 84msec; bottom right) of the tarsal joint of a clinically normal dog obtained at levels A through L as illustrated in figure 1. Plant = Plantar. Med = Medial. Lat = Lateral. Dors = Dorsal

1 = Ramus cranialis of the vena saphena lateralis.
2 = Ramus cranialis of the vena saphena medialis.
3 = Extensor digitorum longus muscle.
4 = Tibialis cranialis artery.
5 = Tibialis cranialis muscle.
6 = Peroneus (fibularis) longus muscle.
7 = Extensor digitorum lateralis muscle.
8 = Flexor digitorum medialis muscle.
9 = Ramus caudalis of the vena saphena lateralis.
10 = Flexor digitorum lateralis muscle.
11 = Ramus caudalis of the vena saphena medialis.
12 = Flexor digitorum superficialis muscle.
13 = Extensor digitorum brevis muscle.
14 = Talocalcaneal interosseous ligament (*ligamentum talocalcaneum interosseum*).
c = Calcaneus.
f = Fibula.
m = Malleolus medialis.
s = sustentaculum tali.
se = Os tarsale secundum.
t = Talus.
ti = Tibia.

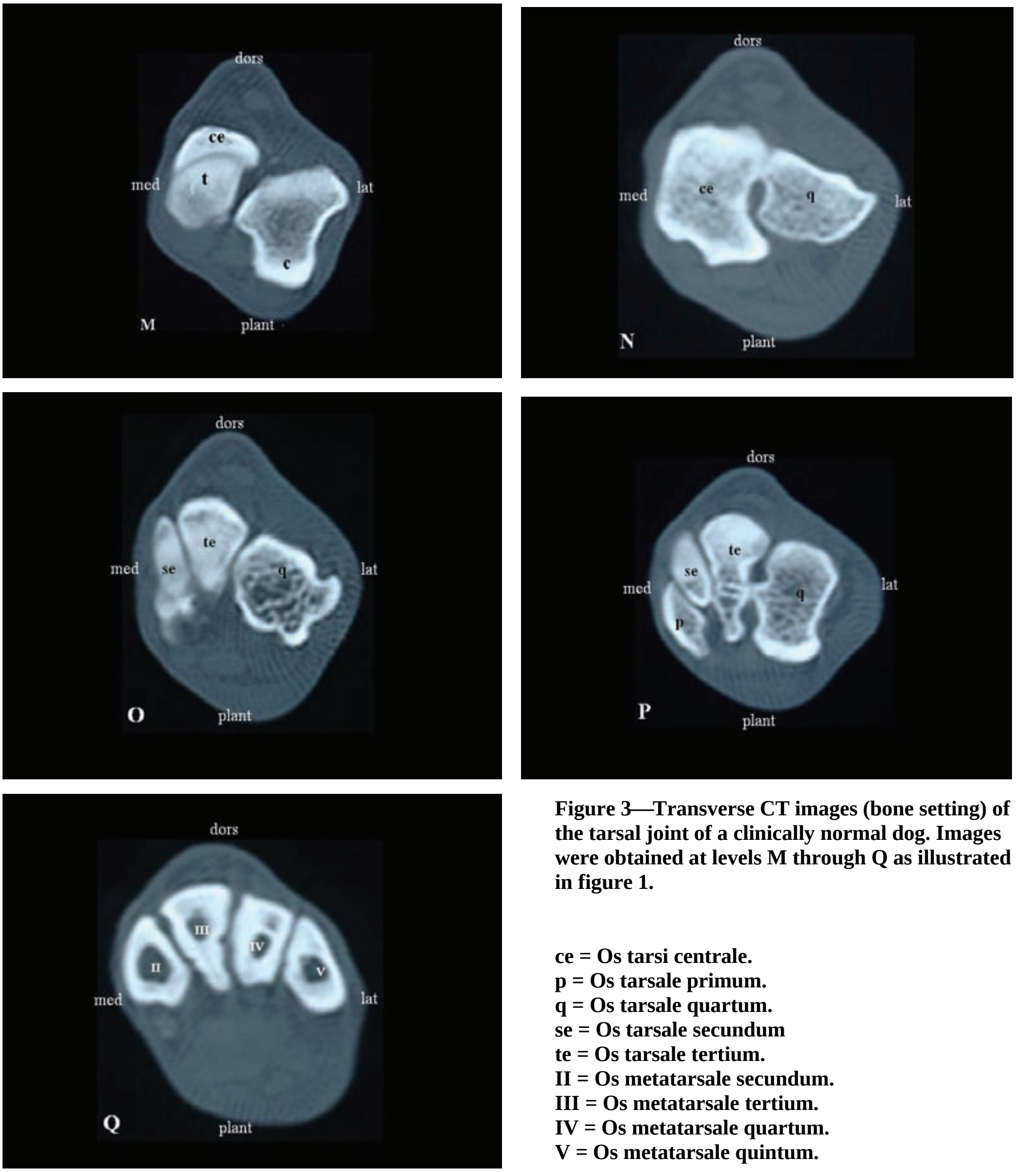

Figure 3—Transverse CT images (bone setting) of the tarsal joint of a clinically normal dog. Images were obtained at levels M through Q as illustrated in figure 1.

ce = Os tarsi centrale.
p = Os tarsale primum.
q = Os tarsale quartum.
se = Os tarsale secundum
te = Os tarsale tertium.
II = Os metatarsale secundum.
III = Os metatarsale tertium.
IV = Os metatarsale quartum.
V = Os metatarsale quintum.

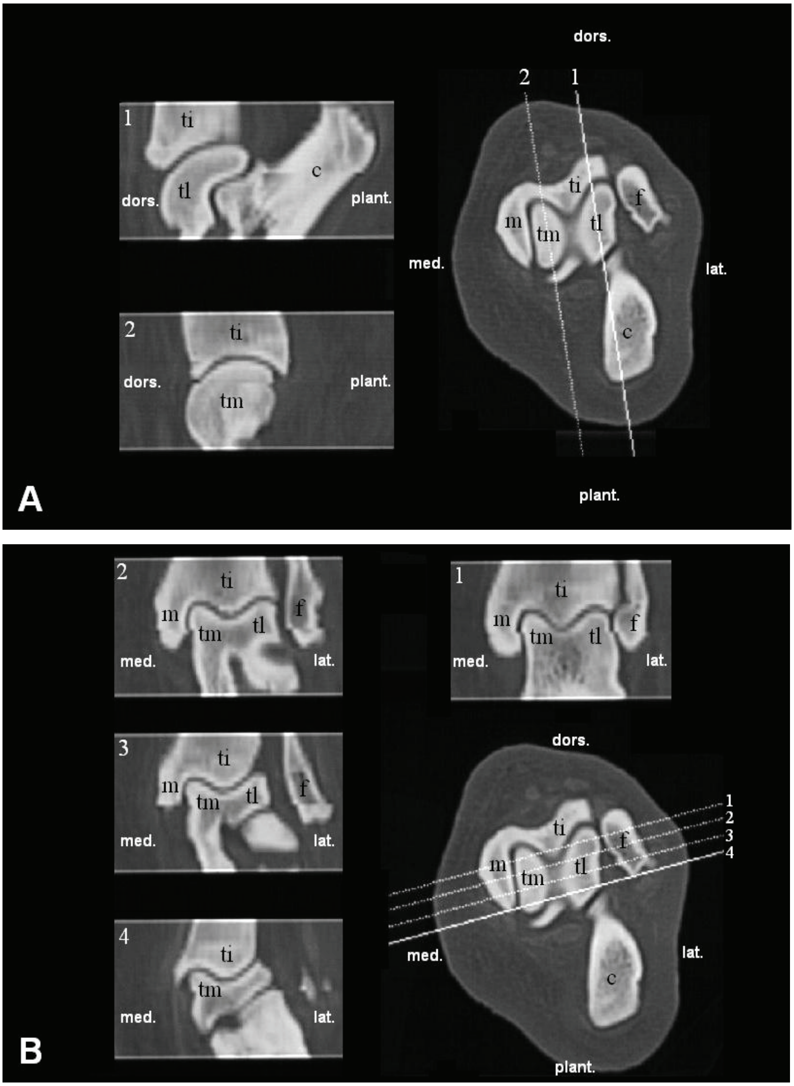

Figure 4——Sagittal (A) and dorsal (B) reconstructions from CT images of the right tarsocrural joint of a Bullmastiff euthanatized for reasons unrelated to the musculoskeletal system.
tl = Lateral ridge of talus. tm = medial ridge of talus. *See* figures 2 and 3 for remainder of key.

lateralis and saphena medialis veins were distinct, and in 1 of these dogs, the rami caudales of both veins were also visible. In another dog, however, the tendons of the peroneus longus and extensor digitorum longus muscles could not be identified.

DISCUSSION

Although some information on CT of the tarsal joint in dogs exists,[11] a detailed description of imaging in clinically normal dogs is lacking. The results of our study indicate that not only is a detailed evaluation of the bony structures of the tarsal joint in dogs possible but that, by adjusting the window and making use of the varying gray scale formats, many soft tissues, including tendons and vascular structures, can be viewed as well. The complexity of the radiographic image caused by superimposition of bony structures can be overcome by studying the axial CT images of the tarsal joint, although some familiarization with this type of imaging is necessary. By studying the sagittal and dorsal reconstructions, the entire tarsocrural joint surface (ie, the lateral and medial tarsal ridge and also the dorsal and plantar surfaces) can be evaluated. These results suggest that CT could be of use in the diagnosis of tarsocrural osteochondrosis, especially when the lateral ridge is involved and superimposition of the calcaneus over the lateral tarsocrural compartment hinders fragment detection. Moreover, CT could be of use in determining the therapeutic strategy for tarsocrural osteochondrosis.

Using CT, the exact localization, size, and number of fragments may be determined in dogs with tarsocrural osteochondrosis. The location of the fragments on the trochlear ridge, especially on the lateral part, can be diverse, but this information is useful for the orthopedic surgeon who wants to use a minimal exposure technique to remove the fragments.[1,12] A disruption of the collateral ligament complex following an arthrotomy could create postsurgical instability and, thus, may compromise the long-term prognosis of affected dogs following surgical treatment.[13] For arthroscopic treatment of these lesions, exact location is prerequisite knowledge, because various arthroscopic approaches must be performed depending on the location of the fragments. The number and size of the fragments is also important information for determining whether fragments should be removed or repaired. Osteoarthritic changes may progress because of instability or incongruity of the joint following removal of a large fragment.[14] Several authors[2,13,15,16] claim that the reattachment of osteochondrosis fragments would be preferable to removal, especially when the lateral talar ridge is involved and traumatic fragmentation with avulsion of the short collateral ligaments has been identified.

Computed tomography could also be of use in instances of complex tarsal fractures where the same problem of superimposition of the surrounding bony structures exists and could provide information contributing to adequate treatment. Another application for CT of the tarsal joint is for detection of subchondral sclerosis, which can be done by measuring the difference in density between cortical and spongy bone. In instances of sclerosis, the density of the spongy bone is increased. Changes in cortical thickness can also be measured.

Computed tomography is becoming more readily available to veterinarians than in the past and is becoming more commonly used for the diagnosis of orthopaedic disorders in small animals.[17,18] Major disadvantages of the technique include cost and the need for general anesthesia. The examination time is, with the type of scanner used in our study, about 10 minutes, which is acceptable. Obtaining 6 radiographic views of the tarsal joint is more time consuming, and in some countries, general anesthesia is obligatory for radiation safety reasons.[1] If access to additional software for multiplanar reconstruction is not available, evaluation is limited to the axial images. This requires more time to evaluate the true extent of possible lesions. Still, the information gained from only the transverse images is worthwhile.

ACKNOWLEDGEMENT

We are very grateful to Janssen Pharmaceutics (Beerse, Belgium) for the collaboration and the use of the cryomicrotome.

[a] Domitor, Orion Corporation, Espoo, Finland.
[b] Pentothal, Abott Laboratories, North Chicago, Ill.
[c] CT-scanner Pace Plus, GE Medical Systems, Milwaukee, Wis.
[d] Fuji Photo Film Co., Ltd., Tokyo, Japan.
[e] Jung Cryomacrocut CM 3600, Leica Microsystems Nussloch Gmbh, Nussloch, Germany.

REFERENCES

1. Carlisle CH., Reynolds KM. Radiographic anatomy of the tarsocrural joint of the dog. J Small Anim Pract 1990; 31:273–279.

2. Beale BS, Goring RL, Herrington J, Dee J, Conrad K. A prospective evaluation of four surgical approaches to the talus of the dog used in the treatment of osteochondritis dissecans. J Am Anim Hosp Assoc 1991;27:221–229.

3. Fitch RB, Beale BS. Osteochondrosis of the canine tibiotarsal joint. Vet Clin North Am, Small Anim Pract 1998; 28:95–113.

4. Johnson KA, Howlett CR, Pettit GD. Osteochondrosis in the hock joint in dogs. J Am Anim Hosp Assoc 1980; 16:103–113.

5. Montgomery RD, Hathcock JT, Milton JL, Fitch RB. Osteochondritis dissecans of the canine tarsal joint.Compend Cont Educ Pract Vet 1994; 16:835–845.

6. Drost WT, Love NE, Berry CR. Comparison of radiography, myelography and computed tomography for the evaluation of canine vertebral and spinal cord tumors in sixteen dogs. Vet Radiol Ultrasound 1996; 37:28–33.

7. Newberg AH. Computed tomography of joint injuries. Radiol Clin North Am 1990; 28:445–460.

8. Zinman C, Reis ND, Osteochondritis dissecans of the talus : use of the high resolution Computed Tomography Scanner. Acta Orthop Scand 1982; 53:697–700.

9. Zinman C, Wolfson N, Reis ND. Osteochondritis dissecans of the dome of the talus. J Bone Joint Surg 1988; 70:1017–1019.

10. World Association of Veterinary Anatomists (WAVA). In: Nomina Anatomica Veterinaria, 4th ed. Zurich and Ithaca, N.Y: International Committee on Veterinary Gross Anatomical Nomenclature, 1994; 1-198.

11. Assheuer J, Sager M. Tarsal joint and paw. In: Assheuer J, Sager M. MRI and CT atlas of the dog. Berlin: Blackwell Science, 1997; 288–295.

12. Van Ryssen B, van Bree H. Arthroscopic evaluation of osteochondrosis lesions in the canine hock joint : a review of two cases. J Am Anim Hosp Assoc 1992; 28:295–299.

13. Smith M, Vasseur P, Morgan J. Clinical evaluation of dogs after surgical and nonsurgical management of osteochondritis dissecans of the talus. J. Am Anim Hosp Assoc 1985; 187:31–35.

14. Brinker WO, Piermattei DL, Flo GL. Diagnosis and Treatment of Orthopedic Conditions of the Hindlimb. In: Brinker WO, Piermattei DL, Flo GL, 3rd ed. Small animal orthopedics and fracture repair. Philadelphia, Pennsylvania: WB Saunders Co, 1997; 607–655.

15. Van Ee R, Gibson K, Roberts E. Osteochondritis dissecans of the lateral ridge of the talus in a dog. J Am Vet Med Assoc 1988; 193:1284–1286.

16. Sjösström L, Håkanson N. Traumatic injuries associated with the short lateral collateral ligaments of the talocrural joint of the dog. J Small Anim Pract 1994; 35:163–168.

17. Stickle RL, Hathcock JT. Interpretation of computed tomographic images. Vet Clin North Am ,Small Anim Pract 1993; 23:417–435.

18. Kippenes H, Johnston G. Diagnostic imaging of osteochondrosis. Vet Clin North Am, Small Anim Pract 1998; 28:137–160.

3.2.2. Magnetic resonance imaging of the tarsal joint of the normal dog.

Lieve M. De Rycke, DVM

Department of Medical Imaging, Faculty of Veterinary Medicine,
Ghent University, Salisburylaan 133, 9820 Merelbeke, Belgium

SUMMARY

Objective—To use magnetic resonance imaging (MR) to provide a detailed description of tarsal joint structures in clinically normal dogs.

Animals—1 clinically normal 12-month-old Bullmastiff weighing 65 kg

Procedure— Immediately after the CT examination of the tarsal joints *(see chapter 3.2.1)* and under the same anesthesia, MR of the tarsal joints was performed in the Bullmastiff using a 1.5 Tesla closed MR equipment[a]. The animal was kept in the same position as used on the CT scanning table (ventral recumbency with the tarsal joints in extension). A series of transverse combined T2 - proton density images (TR =3500msec, TE = 84msec) were obtained with a slice thickness of 3mm from the distal portion of the tibia and fibula to the proximally located metatarsal bones and parallel to the tarsocrural joint space. After authanasia, anatomic sections of the tarsus were performed as described in chapter 3.2.1 and compared with the corresponding MR images. Afterwards a comparison with the corresponding CT images was made (chapter 3.2.1).

Results— All bony and soft tissue structures that were visible on the anatomic sections could be identified on the MR images.

All structures identified on the soft tissue setting CT images could be identified on the MR images. In addition the talocalcaneal interosseous ligament and the extensor digitorum brevis muscle could be located on the MR images. In general, most blood vessels and tendons were much more clearly visible on the MR images compared to the CT images.

Conclusions and Clinical Relevance— MR images provide anatomic detail of bony and soft tissue structures of the tarsal joint in dogs.

These results could be used as a basis for evaluation of MR images of dogs with tarsal joint injuries.

INTRODUCTION

Magnetic resonance imaging (MR) is used routinely for the diagnosis of injuries of the musculoskeletal system in humans because of its superb soft tissue contrast[1]. The image resolution of ligaments, tendons, articular cartilage, subchondral bone and other soft-tissue structures surrounding joints, along with the ability to image in multiple planes has made MR the preferred imaging modality for diagnosis of traumatic, degenerative and inflammatory diseases of joints in humans[2].

Although few veterinarians currently have the equipment available, MR as a major diagnostic tool in veterinary medicine is increasing. Several studies have investigated MR of the orthopedic system of the horse and the dog. MR of the normal equine carpus, stifle, tarsus and foot has been described [3-9]. Furthermore, MR of normal and pathologic models of the canine shoulder, carpal and stifle joints has been published [10-17]. However, similar studies of the canine tarsal joint have not been reported. The purpose of this chapter was to describe the normal MR anatomy of the canine hock and to make a comparison with the corresponding CT images.

MATERIAL AND METHODS

Immediately after the CT examination of the tarsal joints *(see chapter 3.2.1)* and under the same anesthesia, MR of the tarsal joints was performed in the Bullmastiff using a 1.5 Tesla closed MR equipment[a]. The animal was kept in the same position as used on the CT scanning table (ventral recumbency with the tarsal joints in extension). A series of transverse combined T2 -proton density images (TR =3500msec, TE = 84msec) were obtained with a slice thickness of 3mm from the distal portion of the tibia and fibula to the proximally located metatarsal bones and parallel to the tarsocrural joint space.

The anatomical sections of the tarsal joints of the Bullmastiff *(see chapter 3.2.1)* were compared to the corresponding transverse MR images. The structures identified on the anatomical sections *(see chapter 3.2.1)* were subsequently located on the corresponding MR images.

From the collection of matched MR and anatomical images, 10 representative pairs were selected from the proximal to distal regions of the tarsal joint (Figure 2 chapter 3.2.1). Afterwards a comparison with the corresponding CT images was made (Figure 2 chapter 3.2.1).

RESULTS

All bony and soft tissue structures that were visible on the anatomic sections could be identified on the MR images.
All structures identified on the soft tissue setting CT images could be identified on the MR images. In addition the talocalcaneal interosseous ligament and the extensor digitorum brevis muscle could be located on the MR images. In general, most blood vessels and tendons were much more clearly visible on the MR images compared to the CT images.

These results are also listed in Table 1

TABLE 1	**CT**	**MR**
Bony structures		
c = Calcaneus	+	+
ce = Os tarsi centrale	+	+
f = Fibula	+	+
m = Malleolus medialis	+	+
p = Os tarsale primum	+	n
q = Os tarsale quartum	+	n
s = sustentaculum tali	+	+
se = Os tarsale secundum	+	n
t = Talus	+	+
te = Os tarsale tertium	+	n
ti = Tibia	+	+
II = Os metatarsale secundum	+	n
III = Os metatarsale tertium	+	n
IV = Os metatarsale quartum	+	n
V = Os metatarsale quintum	+	n
Soft tissue structures		
1 = Cranial branch of the vena saphena lateralis	+	+
2 = Cranial branch of the vena saphena medialis	+	+
3 = Extensor digitorum longus muscle	+	+
4 = Tibialis cranialis artery	+	+
5 = Tibialis cranialis muscle	+	+
6 = Peroneus (fibularis) longus muscle	+	+
7 = Extensor digitorum lateralis muscle	+	+
8 = Flexor digitorum medialis muscle	+	+

TABLE 1	CT	MR
9 = Ramus caudalis of the vena saphena lateralis	+	+
10 = Flexor digitorum lateralis muscle	+	+
11 = Ramus caudalis of the vena saphena medialis	+	+
12 = Flexor digitorum superficialis muscle	+	+
13 = Extensor digitorum brevis muscle	--	+
14 = Talocalcaneal interosseous ligament	--	+

TABLE 1 : Structures of the canine tarsal joint visible on CT and MR scans. (n= not present in the selected views)

CONCLUSION

MR images provide anatomic detail of bony and soft tissue structures of the tarsal joint in dogs. Muscles, tendons, ligaments, large blood vessels are very distinct and easier to evaluate compared to the CT images. On this proton-density images, the cortical bone generates a low signal. The brighter signal of articular cartilage is not distinguishable from synovial fluid. Yellow and fatty marrow, muscles and tendons demonstrate a low signal intensity.

The choice between CT or MR for diagnosing tarsal pathologies will mainly depend on the kind of suspected lesion. CT provides more detail of the cortical bone, while MR is superior for recognizing abnormalities of the joint capsule, ligaments, cartilage and subchondral bone.

These results could be used as a basis for evaluation of MR images of dogs with tarsal joint injuries.

[a] Symphony, Siemens A.G., Erlangen, Germany.

REFERENCES

1. Peterfy C, Linares R, Steinbach L. Recent advances in magnetic resonance imaging of the musculoskeletal system. Radiol Clin North Am 1994;32:291-311.

2. Blaik M, Hanson R, Kincaid S et al. Low-field magnetic resonance imaging of the equine tarsus: normal anatomy. Vet Radiol Ultrasound 2000;41:131-141.

3. Kaser B, Sartoretti-Schefer S, Weiss R. Computed tomography and magnetic resonance imaging of the normal equine carpus. Vet Radiol Ultrasound 1994;35:457-461.

4. Denoix JM, Crevier N, Roger B, et al. Magnetic resonance imaging of the equine foot. Vet Radiol Ultrasound 1993;34:405-411.

5. Holcombe S, Bertone A, Biller D et al. Magnetic resonance imaging of the equine stifle. Vet Radiol Ultrasound 1995;36:119-125.

6. Kleiter M, Kneissl S, Stanek C et al. Evaluation of magnetic resonance imaging techniques in the equine digit. Vet Radiol Ultrasound 1999;40:15-22.

7. Martinelli M, Kuriashkin I, Carragher B et al. Magnetic resonance imaging of the equine metacarpophalangeal joint: three dimensional reconstruction and anatomic analysis. Vet Radiol Ultrasound 1997;38:193-199.

8. Park R, Nelson T, Hoopes J. Magnetic resonance imaging of the normal equine digit and metacarpophalangeal joint. Vet Radiol 1987;28:105-116.

9. Ruohoniemi M, Kärkkäinen M, Tervahartiala P. Evaluation of the variably ossified collateral cartilages of the distal phalanx and adjacent anatomic structures in the Finnhorse with computed tomography and magnetic resonance imaging. Vet Radiol Ultrasound 1997;38,344-351.

10. Baird D, Hathcock J, Rumph P et al. Low-field magnetic resonance imaging of the canine stifle joint: normal anatomy. Vet Radiol Ultrasound 1998;39:87-97.

11. Baird D, Hathcock J, Kincaid S, et al. Low-field magnetic resonance imaging of early subchondral cyst-like lesions in induced cranial ligament deficient dogs. Vet Radiol Ultrasound 1998;39:167-173.

12. Baird D, Kincaid S, Hathcock J, et al. Effect of hydration on signal intensity of gelatin phantoms using low-field magnetic resonance imaging: possible application in osteoarthritis. Vet Radiol Ultrasound 1999;40:27-35.

13. Banfield C, Morrison W. Magnetic resonance arthrography of the canine stifle joint: technique and applications in eleven military dogs. Vet Radiol Ultrasound 2000;41:200-213.

14. Fitch R, Wilson E, Hathcock J et al. Radiographic, computed tomograpic and magnetic resonance imaging evaluation of a chronic long digital extensor tendon avulsion in a dog. Vet Radiol Ultrasound 1997;38:177-181.

15. Nordberg C, Johnson K. Magnetic resonance imaging of normal canine ligaments. Vet Radiol Ultrasound 1998;39:128-136.

16. Van Bree H, Degryse H, van Ryssen B, et al. Pathologic correlations with magnetic resonance images of osteochondrosis lesions in canine shoulders. J Am Vet Med Assoc 1993;202:1099-1105.

17. Widmer WR, Buckwalter KA, Braunstein EM, et al. Radiographic and magnetic resonance imaging of the stifle joint in experimental osteoarthrosis of dog. Vet Radiol Ultrasound 1994;35:371-383.

A thorough knowledge of the normal cross-sectional anatomy of the body is most essential for interpretation of CT and MR, as the radiologist is confronted with detailed anatomical cross-sections instead of two-dimensional “shadow pictures” seen on radiographs. These new developments have caused difficulties when evaluating CT and MR images, because the knowledge of the normal conventional anatomy and radiographic anatomy was not longer sufficient for recognising structural abnormalities in diseased animals.

Since CT and MR have become more available to veterinarians, several articles devoted to the cross-sectional normal anatomy of specific body regions have been published[1-4]. The idea for comparing normal cross-sectional anatomy to normal CT or MR images is not original[5-14]. These articles and books have been most helpful in performing this work, however they have not alleviated the prevailing great need for more detailed investigations on the normal cross-sectional anatomy as seen on CT and MR images. Based on the perception that a color atlas comparing the normal cross-sectional anatomy to the CT and MR anatomy would be supportive in the interpretation of the increasing numbers of cross-sectional images, several CT and MR images were obtained in transversal planes of clinical important regions of the canine body. Taking advantage of the MR characteristics of depicting soft tissue in great detail and in superior spatial resolution, and combining the MR scans with CT pictures of the same region showing the calcium containing structures, the basis for an unique atlas has been created. The various regions are illustrated using a sufficient number of transverse CT and MR scans and all anatomical structures depicted on the images were labelled in great detail. The regions of the canine body selected for this work were chosen based on their clinical importance, particularly the frequency of pathologies associated with these regions.

Interpretation of the findings on CT and MR images is a prerequisite to establish a precise diagnosis in clinical cases. Besides the use of this atlas, interpretation of CT and MR images can also be simplified by comparing with the opposite side. Furthermore, strictly standardised positioning produces symmetric images, making interpretation much easier. On the transverse images, structures can also be identified by examining adjacent transverse images. The scanned structure can thus be followed as it appears and disappears in relation to recognisable surrounding organs.

The CT images were performed on a third generation CT scanner[a]. Dependant on the region, soft tissue window (brain, thorax, elbow, tarsus), bone window (nasal cavities, elbow, tarsus) or lung window (thorax) settings were used. This CT scanning technique allows a slice thickness of 1 mm resulting in slices with an increased signal/noise ratio[15]. Such thin slices are very effective for examination of small lesions and small organs. An increase in mAs can compensate for image noise associated with narrow slice collimation which can be very interfering. Thin slices however require long scan times, which result in high doses of anaesthesia and radiation and increases the cooling time for the thermal tube of this third generation scanner. Thick slices have a large scanning area and low noise but also have a large partial volume effect[15]. Slice thicknesses of 2 mm for the brain, 5 mm for the nasal cavities, 5 mm for the thorax, and 2 mm for the joints were used.

Most generators support a wide range of exposure techniques from 80 to 140 kilovolts (kV) and 30 to 500 milliamperes (mA)[16]. A high kV is always used to ensure adequate penetration, and for very dense objects to minimise beam hardening. The choice of milliamperes seconds (mAs) depends on the selected kV and slice thickness. High mAs will increase image detail because it reduces image noise, but radiation dose and tube cooling time increases [15,17]. In our investigations 120 kVp and 130 mAs were used. The choosen scan time was 3 seconds. A longer scan time may result in improved image detail, but may cause motion artefacts (including respiratory motion) and can eventually cause x-ray tube heating[18].

The MR studies were performed using a 1.5 closed Tesla MR unit[b]. In general, T1-weighted images provide superior tissue contrast and anatomic detail, while T2-weighted images are more sensitive to demonstrate fluid (e.g. CSF), edema and inflamed tissues which show increased signal intensity. Proton-density images are balanced T1- and T2-images.

For the present study (chapter 1.1.2), T1-weighted images were chosen as they demonstrate very well the over-all morphology of the brain. On the other hand, the difference between the gray and white matter is indistinct and almost similar to CT. T2-weighted images are highly sensitive in detecting pathologic processes affecting the brain parenchyma[16,19]. Vascular structures show signal void in all regular T1- and T2-weighted and proton-density images. The appearance of vessels can be changed by applying a special technique of magnetic resonance angiography[16].

When evaluating the nasal cavities and paranasal sinuses with MR, the standard protocol includes transverse and dorsal T1- and T2-weighted images[16]. In the present study, also proton density images were performed. Cortical bone and air are not well depicted on the MR-images. In contrast, the mucosal covering of the nasal cavities and sinuses is distinct on both T1- and T2-weighted images due to the intermediate signal intensity. Low viscosity secretions (in case of sinusitis) appear as hypointense on T1-weighted images and hyperintense on T2-weighted images. For mucous secretions with higher viscosity, the signal intensity on T2-weighted images decreases. A fungal sinusitis is characterized by a low signal intensity on T1-weighted images and a signal void on T2-weighted images. This is due to the presence of paramagnetic metals (iron and manganese present in Aspergillus colonies)[19]. The signal intensity of nasal tumors on MR images is dependent on the nature of the neoplasm[19].

For the examination of the elbow joint, T1-weighted images were chosen for the good anatomical resolution. Proton density images were selected for the tarsus, as T1- and T2-weighted images were not available. For the musculoskeletal system in general, cortical bone generates a low signal on all pulse sequences. Yellow or fatty bone marrow generates increased signal intensity on T1-weighted acquisitions. Signal intensity decreases with progressive T2 weighting[20,21]. Collagen-containing ligaments and tendons image with low signal intensity, whereas adjacent muscle or hyaline articular cartilage demonstrates an intermediate signal intensity on a T1-weighted image[21]. Cortical bone is presented by a void signal on T1-weighted images[20]. On T2-weighted sequences the bright signal of the articular cartilage is not distinguishable from synovial fluid[20].

For most of the CT and MR images in this work, no intravenous contrast medium was administered, as the aim was to describe plain images made by standard procedures. Only for the CT study of the canine brain, contrast medium was applied, but the post-contrast images were not used as they differed little from the pre-contrast images. For detection of brain pathologies however, the use of contrast medium is routine. Postcontrast CT and MR images enhance the pituitary gland, dural structures such as the falx cerebri and the tentorium cerebelli, arterial structures and the choroid plexuses of the lateral, third, and fourth ventricles[16,22].

The CT and MR examinations of the nasal cavities were also performed on plain images, as the use of intravenous contrast medium has not been shown to aid in the recognition of anatomical structures[16]. IV contrast medium can be useful in nasal cavities with pathologic changes to enable differentiation between fluid and soft tissue or to define more accurately the nature of an abnormal soft-tissue structure[23,24]. The use of contrast medium in MR examinations has been proposed as a method for differentiating sinunasal neoplasms from inflammatory masses[25].

For the CT images of the thorax, no IV contrast medium was injected. When performing CT of the diseased thorax, an IV bolus of contrast medium is very useful in the diagnosis of intrathoracic vascular lesions, for defining the extent of mediastinal masses and their relation to structures such as major vessels or the heart, and to enhance the pleura and heart[26-30].

The CT and MR studies of the elbow and tarsal joints were also made by means of plain images. The indications for CT-arthrography include detecting cartilaginous intrasynovial loose bodies and synovial abnormalities, and assessing the cartilaginous surfaces[31]. The requirement of intraarticular contrast in MR is not necessary as synovial fluid has a bright signal intensity on T2-weighted images and the articular hyaline cartilage can be selectively highlighted on fast scan sequences[21].

The judicious use of CT and MR requires a working knowledge of the utility and pitfalls of their application in the diagnosis of various disorders in each region of the body.

CT and MR have many applications in detecting brain pathologies. However, each imaging modality has its limitations. The limitations of CT include a poor resolution in changes involving the white matter, artefacts which may significantly degrade the images through the region of the fourth ventricle, and the need for a large amount of intravenous contrast when defining intracranial masses or evaluating the vascular component of the lesions[19]. All these factors are obviated with MR. MR allows imaging in all three orthogonal (saggital, dorsal and transversal) planes. The resolution of the gray and white matter is better than with CT and the vascular anatomy can be evaluated with noninvasive, magnetic resonance angiography (MRA). The limitation of MR is primarily related to the difficulty in recognizing fresh hemorrhage, mineral deposition from flow-related artifacts, and subtle changes involving the osseous structures[19].

MR offers some advantages over CT scans when imaging pathologic conditions of the nasal cavities and paranasal sinuses. In contrast to CT, MR allows not only differentiation between the nasal mucosa and other soft tissues or fluid, but is able to map the extent of a mass or inflammatory process into either the orbit or intracranial cavities[16]. For this purpose, the multiplanar capabilities of MR are unsurpassed. In addition, the signal characteristics of a sinunasal mass may help to distinguish inflammatory from neoplastic sinonasal diseases[32-34] . If the mass is neoplastic, this ability allows for better surgical and radiation planning. In contrast, the bony architecture or destruction will be more clearly visible on the CT images.

CT is particularly effective in evaluating trauma, soft tissue and bony lesions, infection and degenerative disorders of the musculoskeletal system. CT is especially useful in the assessment of small joints that require thin section evaluation. CT provides high bone detail in cross-sectional display. Reformatting capabilities and three-dimensional display of CT are functions that facilitate the understanding of complex anatomy and spatial relationships. The drawbacks to CT include the use of ionizing radiation and the narrow range of soft tissue contrast. Nonorthogonal imaging capabilities result in a loss of resolution when reformatting cross-sectional images. Routine use of thin-section CT images to increase the resolution of reformatted images is not practical in studies of large anatomic structures[21]. MR allows for direct multiplanar imaging of the appendicular joints in nonorthogonal planes and can differentiate fat, fluid, muscle, tendon, cartilage, neurovascular structures and cortical bone in both normal and pathologic states[20,21]. The ability to noninvasively image and characterize early changes in bone marrow, subchondral bone, and cartilage provides a more precise evaluation in patients presenting trauma, infection, and neoplasia. MR is limited in that the identification of small soft tissue or joint calcification is inferior to that of CT. For imaging of the bony cortex, cortical edge detail of CT is superior to MR. MR requires more detailed imaging protocols adapted to both anatomy and pathology; often these must be joint specific[21]. Furthermore, MR is limited in that it has a greater sensitivity to motion than CT[21].

For the study of the thorax, we choose to compare the results of the CT examination with those of thoracoscopy, as MR of the thorax has little applications in veterinary medicine at present. In human medicine, MR has a clear advantage over other imaging modalities when evaluating cardiac and vascular disorders of the thorax, but its role in the evaluation of parenchymal lung disease is limited[16]. Obstacles to lung imaging include respiratory motion and magnetic susceptibility effects caused by air-tissue interfaces. For imaging mediastinal abnormalities, MR has also two potential disadvantages compared to CT, namely its low potential to demonstrate calcification and its poor spatial resolution[16]. Rapid evolution of MR technology suggests that some of these problems may be overcome in the near future. Assessment of chest wall disease and peridiaphragmatic processes, which do not suffer as much from respiratory or magnetic susceptibility artifacts, already benefits from the multiplanar capabilities of MR and its improved soft tissue contrast[16].

To obtain the anatomic slices described in the present study different techniques have been used. For the fixed brain a stainless-steel knife was sufficient to make 5-mm thick transverse sections. The same knife was used to cut the decalcified and fixed nasal cavities and paranasal sinuses. Because of its much bigger size, the frozen thorax was cut into 10-mm thick slices by use of an electic bandsaw[c]. For the anatomic sections of the frozen elbow joint an electic planer[d] was choosen as the cryomicrotome[e] technique used to section the frozen tarsus was too time-consuming and not available in our department.

The great need for a clear CT and MR atlas in our department was the motivation for this work. In the future, other regions of the canine body such as the knee, hip, carpal joint and the abdomen will be investigated in a similar way, in order to complete this comparative atlas.

[a] CT-scanner Pace Plus, GE Medical Systems, Milwaukee, Wis.
[b] MR Unit Symphony, Siemens A.G., Erlangen, Germany.
[c] Electric band saw, Eureka, Savioli Lelio Snc, Coriano, Italy
[d] Electric planer, Black and Decker, Berkshire, England
[e] Jung Cryomacrocut CM 3600, Leica Microsystems Nussloch Gmbh, Nussloch, Germany.

REFERENCES

1. Done S, Goody P, Evans S, et al. In: Done S, Goody P, Evans S, et al. eds. *Color Atlas of Veterinary Anatomy, Volume 3*. London: Mosby, 1999.

2. Polgar M, Probst A, Sora M, et al. Plastination of whole-body slices : a new aid in cross-sectional anatomy, demonstrated for thoracic organs in dogs. Wiener Tierärztl Monatsschr 2003;90:45-52.

3. Zook B, Hitzelberg R, Fike J, et al. Anatomy of the Beagle in cross-section: Head and neck. Am J Vet Res 1981;42:844-849.

4. Zook B, Hitzelberg R, Bradley E. Cross-sectional anatomy of the Beagle thorax. Vet Radiol 1989;30:277-281.

5. Arencibia A, Vazquez JM, Jaber R, et al. Magnetic resonance imaging and cross sectional anatomy of the normal equine sinuses and nasal passages. Vet Radiol Ultrasound 2000;41:313-319.

6. Blaik M, Hanson R, Kincaid S, et al. Low-field magnetic resonance imaging of the equine tarsus: normal anatomy. Vet Radiol Ultrasound 2000;41:131-141.

7. Feeney D, Fletcher T, Hardy R. Atlas of correlative imaging anatomy of the normal dog. Ultrasound and computed tomography. Philadelphia: WB Saunders Co, 1991.

8. Fike J, Druy E, Zook B, et al. Canine anatomy assisted by computerized tomography. Am J Vet Res 1980;41:1823-1832.

9. George T, Smallwood J. Anatomic atlas for computed tomography in the mesaticephalic dog : head and neck. Vet Radiol Ultrasound 1992;33:217-240.

10. Jones J, Cartee R, Bartels J. Computed tomographic anatomy of the canine lumbosacral spine. Vet Radiol Ultrasound 1995;36:91-99.

11. Lonosky JH, Abbott LC, Kuriashkin IV. Computed tomography of the normal feline nasal cavity and paranasal sinuses. Vet Radiol Ultrasound 1997;38:251-258.

12. Samii V, Biller D, Koblik P. Normal cross-sectional anatomy of the feline thorax and abdomen: comparison of computed tomography and cadaver anatomy. Vet Radiol Ultrasound 1998;39:504-511.

13. Smallwood J, George T. Anatomic atlas for computed tomography in the mesaticephalic dog : Caudal abdomen and pelvis. Vet Radiol Ultrasound 1992;33:143-167.
14. Smallwood J, George T. Anatomic atlas for computed tomography in the mesaticephalic dog: thorax and cranial abdomen. Vet Radiol Ultrasound 1993;34:65-84.

15. Azemoto S, Gono M, Tetsuya H, et al. ABCs of CT Scan. Internal education publication GE Medical systems 1995;14.

16. Haaga J, Lanzieri C, Gilkeson R. In : CT and MR imaging of the whole body, 4th edition. Haaga J, et al., eds. Missouri : Mosby Inc., 2003; p5,92-93,383,558-559,838,937.

17. Seeram E. Computed tomography of the head, neck and spine. In : Wilke J. (ed). Computed tomography: physical principles, clinical applications, and quality control, second edition, WB Saunders, Philadelphia, USA 2001, pp 325-340.

18. Stickle R, Hathcock J. Interpretation of computed tomographic images. Vet Clin North Am: Small Anim Pract 1993;23:417-429.

19. Lee H., Rao K, Zimmerman R. In : Cranial MRI an CT, 4th edition. Howard Lee S, Roa K, Zimmerman R, eds. McGraw-Hill, 1999, pp834, 840-850.

20. Drayer B, Burger P, Dawrin R, et al. MRI of brain iron. Am J Neuroradiol 1986;7:373-380.

21. Firooznia H, Golimbu C, Rafii M, et al. In : MRI and CT of the musculoskeletal system. Firooznia H, et al., eds. Missouri : Mosby Inc, 1992; p574.

22. Moss A, Gamsu G, Genant H. In : Computed tomography of the body with magnetic resonance imaging, 2nd edition. Genant H, ed. Philadelphia : WB Saunders Company 1992.

23. Love N, Fisher P, Hudson L. The computed tomographic enhancement pattern of the normal canine pituitary gland. Vet Radiol Ultrasound 2000;41:507-510.

24. Park R, Beck E, LeCouteur R. Comparison of computed tomography and radiography for detecting changes induced by malignant nasal neoplasia in dogs. J Am Vet Med Assoc 1992;201:1720-1724.

25. Thrall D, Robertson I, McLeod D, et al. A comparison of radiographic and computed tomographic findings in 31 dogs with malignant nasal cavity tumors. Vet Radiol 1989;30:59-66.

26. Lanzieri C, Shah M, Krauss D, et al. Use of Gd-DTPA enhanced MRI for differentiating mucoceles from neoplasms in the paranasal sinuses. Radiology 1991;178:425-428.

27. Stickle R, Hathcock J. Interpretation of computed tomographic images. Vet Clin North Am Small Anim Pract 1993;23:417-435.

28. Westra D, Verbeeten B. Indications for computerized tomography of the thorax. Ned Tijdschr Geneesk 1983;127:617-621.

29. Wong B, Lee K, Mac Arthur R. Diagnosis of pericardial effusion by computed tomography. Chest 1982;81:177-181.

30. Henniger W. Use of computed tomography in the diseased feline thorax. J Small Anim Pract 2003;44:56-64.

31. Schwarz L, Tidwell A. Alternative imaging of the lung. Clin Techn Small Anim Pract 1999;14:187-206.

32. Singsong R, Feldman F, Rosenberg Z. Elbow joint : assessment with double contrast CT-arthrography. Radiology 1986;160:167-173.

33. Som P, Dillon W, Fullerton G, et al. Chronically obstructed sinonasal sectretions observations on T1 and T2 shortening. Radiology 1989;172:515-520.

34. Som P, Dillon W, Sze G, et al. Benign and malignant sinonasal lesions with intracranial extension: Differentiation with MRI. Radiology 1989;172:763-766.

35. Som P, Shapiro M, Biller H, et al. Sinonasal tumors and inflammatory tissues: Differentiation with MRI. Radiology 1988;167:803-808.

This study presents the cross-sectional anatomy of several clinically important regions of the normal canine body. Labeled gross anatomical sections are used to identify a wide range of structures on corresponding CT and MR images. This detailed comparative description is intended to serve as an atlas for clinicians, allowing an optimal interpretation of CT and MR images of dogs affected with pathologies - except for disorders that transform the normal anatomy of a region severly by their size or invasive growth.

In the first chapter CT and MR images of two regions of the head namely the brain and the nasal cavities including the paranasal sinuses, were examined.

To perform CT and MR of the brain, 4 shepherd dogs were anesthetized and placed in ventral recumbency. For CT, 2-mm thick pre- and post-contrast transversal slices were made, ranging from the cribriform plate of the ethmoid bone to the cranial part of the atlas, using a soft-tissue setting. MR of the brain was performed in one of the dogs that was kept in the same position as used on the CT scanning table. Transverse, 4-mm thick T1-weighted and T2-weighted MR images were obtained from the same regions of the head.

Afterwards, one of the dogs was euthanatized and the brain was prepared, fixed, embedded in gelatine and sectioned into 5-mm-thick transversal slices. The anatomic sections were photographed and numerous structures of the canine brain and the various parts of the ventricular system were identified.

Most of these structures could also be located on the corresponding CT images, by the use of landmarks such as adjacent radiolucent cerebrospinal fluid and bony structures. Unfortunately, it was not possible to distinguish some parts of the telencephalon, such as the internal capsule and hippocampal gyrus, nor some structures of the diencephalon, including the optic tract, epiphysis, infundibulum and the tuber cinereum. From the mesencephalon, the interpeduncular fossa, red nucleus, and the substantia nigra were not identifiable. At the level of the metencephalon the cerebellar white matter, floccular lobe and the middle cerebellar peduncle could not be localized. Some structures of the medulla oblongata including the medial ventral fissure, pyramids and the central canal were impossible to distinguish, and neither were the choroid plexuses of the lateral and fourth ventricles. On the CT images, the bony and soft tissue structures surrounding the brain were additionally labeled.

Most of the brain structures that were visible on the anatomic sections could be identified on the MR images, except for some parts of the diencephalon such as the epiphysis, hypophysis with

infundibulum and the mamillary body, probably because these structures were not present in any of the sections. The mesencephalic red nucleus and substantia nigra could not been located on the MR images and neither was the cerebellar white matter.

When comparing the MR images of the brain with the corresponding CT images, all brain structures and surrounding soft tissue structures could be much better visualized with MR. Moreover, several brain structures such as the internal capsule, optic tract, hippocampal gyrus, rostral and caudal collicle, interpeduncular fossa, brachium of the pons, median ventral fissure, floccular lobe, pyramid of the medulla oblongata and the choroid plexuses of the fourth and lateral ventricles could be located on the MR images and were unidentifiable on the CT images. Only the bony structures of the skull, and in particular the foramina, fossae, canals and sulci, were more distinct on the CT images compared to the MR images.

These results could be used as a basis for evaluation of CT and MR images of the brain of dogs affected with pathologies.

Two dogs were used to perform CT and MR of the nasal cavities and paranasal sinuses. The first dog was anesthetized and positioned in ventral recumbency for both examinations. For CT, 5-mm thick transversal slices from the caudal part of the frontal sinuses to the nostrils were made using a bone setting. The same dog underwent a MR examination and transversal T1-weighted, T2-weighted and proton density MR sequences were performed. The second dog was positioned in dorsal recumbency with the head perpendicular to the table to obtain dorsal images and the same CT and MR protocols were used.

At the end of the examinations, both dogs were euthanatized and the skulls were, after preparation and decalcification, embedded in gelatine and sectioned into 5-mm thick transversal slices. Each anatomic section was compared with the corresponding CT and MR images, and all recognizable structures were labeled on all images. The various facial bones that form the wall of the nasal cavities as well as most parts of the nasal cavities, such as the nasal conchae, septa, meatuses and all endo- and ectoturbinates, could easily be identified on the anatomic sections. The medial and lateral parts of the frontal sinuses and the maxillary recess were also visible. Additionally, several adjacent structures that remained on the skull were labeled.

On the CT scans it was also possible to identify various structures of the nasal cavities and paranasal sinuses, except for the dorsal, middle and ventral nasal meatuses and some of the ectoturbinates. It was less obvious to distinguish a number of surrounding soft-tissue structures on the CT scans.

On the MR scans, the facial bones could not be identified, but most of these could be located due to their void signal. In contrast, the conchae, conchal septa, and turbinates -except for some of the ectoturbinates- were well imaged because of their distinct mucosal covering. The surrounding soft-tissue structures were clearly visible on MR scans, especially when compared to the CT scans. Considering these results, CT and MR images provide consistent evaluation of all structures of the nasal cavities and paranasal sinuses. In conclusion, both techniques could be useful for evaluation of nasal diseases.

In the second chapter of this study the anatomy of the thorax was described as revealed by CT and by thoracoscopy, followed by a comparison between both techniques.

For CT examination of the thorax, 4 dogs were anesthetized and positioned in ventral recumbency. Transversal CT images from the thoracic inlet to the diaphragm were made with a slice thickness of 5-mm and reviewed by use of soft tissue and lung settings. One dog was euthanatized and frozen, and the thorax was subsequently sectioned at 10-mm thick intervals. For each anatomic slice, a corresponding CT image was searched for, and anatomic structures were matched.

On the anatomic sections, the various intrathoracic parts of the respiratory tract and the different lung lobes were clearly visible. Major blood vessels could also readily be seen in the cranial mediastinum and thoracic cavity. Other intrathoracic structures, such as the heart with its chambers and valves, esophagus, lymph nodes and muscles were easily to distinguish, and so were the various parts of the thoracic wall and the surrounding tissues.

Most of the previously mentioned structures of the thorax could be identified on CT images at the soft tissue setting, except for the different parts of the heart, some vessels, the nuchal ligament, diaphragm, the various lobes of the lungs and the lobar bronchi. On CT images obtained at the lung setting, only the parts of the respiratory tract and some large vessels were distinct. Only contours of the heart and liver only were visible, and the presence of air in the esophagus and in the cardia and fundus of the stomach revealed the position of these organs.

For thoracoscopy, 4 dogs were anesthetized and placed in left or right lateral recumbency. The endoscope was advanced in the thoracic cavity via the free upper side and photographs were taken.

A large number of endoscopically visible intrathoracic structures of the left and right hemithorax were identified.

On both sides, the pulmonary and costal pleura, the diaphragm, the heart surround by pericardium and the various parts of the thoracic wall, including nerves and vessels, were easily perceptible. In the cranial mediastinum, the esophagus and trachea could be located in each hemithorax.

In the left hemithorax, the cranial and caudal lobes of the left lung were observed and large blood vessels, such as the ascending and descending aorta and the pulmonary trunk were visible. At the heart base, the ligamentum arteriosum (Botalli) and the left recurrent laryngeal nerve were defined, while the left vagal and phrenic nerves were observable coursing across the pericardiac surface. In the cranial mediastinum the thoracic duct, the left subclavian artery and left brachiocephalic vein and their branches were perceptible.

On the right side of the thorax the cranial, middle, and caudal lobes of the right lung could be evaluated. Caudal to the heart, the caudal vena cava and right phrenic nerve were visible in the plica venae cavae. In the cranial mediastinum, the azygos vein, cranial vena cava, right vagal and phrenic nerves, the broncho-esophageal vein and the thoracic duct were seen.

Afterwards the 2 techniques for examination of the thorax were compared. Intrathoracic structures that were not visible on CT-images but easily observed by thoracoscopy included the parietal and visceral pleura, pericardium, heartbase with ligamentum arteriosum (Botalli), thoracic duct, plica venae cavae and several intrathoracic nerves. On the other hand, visualization of the spinal cord, lymphnodes, mediastinum and several vessels was difficult or impossible by thoracoscopy, but easy when using CT examination.

The surface morphology of the different lung lobes (except for the accessory lung lobe) could be inspected by thoracoscopy, while the inner details were visible on the CT images at lung window setting. The various parts of the heart could not be observed during thoracoscopy due to the surrounding pericardium and were impossible to identify on the CT images as a result of motion artefacts.

In conclusion, thoracoscopy as well as CT examination of the thorax revealed a wide range of the intrathoracic anatomical information and can be used for diagnosing thoracic pathologies. The choice between both techniques will mainly depend on the clinical history of the animal and the results of former investigations. The fact that thoracoscopy has therapeutic possibilities will also influence the final choice of diagnostic technique.

In the third chapter of this work, the CT and MR anatomy of two appendicular regions, i.e., the elbow and tarsus, were described and compared.

To perform CT of the elbow regions, 7 dogs were anesthetized and placed in lateral recumbency. One- and 2-mm thick slices were obtained, ranging from the top of the olecranon to 3 cm distal to the elbow joint, in parallel planes to the humeroradial joint space. Images were reviewed using a bone and soft tissue setting and CT reconstructions of the elbow joint were made in sagittal and dorsal planes. MR of the elbow joints was performed in one of the dogs (a Labrador retriever) that was kept in the same position as on the CT scanning table. Transversal 3-mm thick T1-weighted and T2-weighted images were obtained from the same regions as mentioned above. After the examinations, the Labrador retriever was euthanatized and the forelimbs were removed and frozen. The elbow joints were sectioned into approximately 1-mm thick slab sections, which were photographed and compared with corresponding CT and MR images.

On the anatomic sections several osseous, muscular, tendinous, vascular and nervous structures could be identified. On the CT images at the soft tissue setting, the same osseous and soft tissue structures could be identified, except for the anular ligament of the radius and the antebrachial interosseous membrane. All bony structures that were seen on the anatomic sections were also visible on the CT images at the bone setting and the entire humero-radioulnar joint surface could be evaluated on the reconstructed CT images.

On the MR images, all anatomic structures that were visible on the anatomic sections could be identified, except for the median artery and nerve, and the radial nerve. Subsequently, the MR images were compared to the corresponding CT images at the soft tissue setting and, except for the median artery and nerve and the radial nerve, the same structures were defined. On the other hand, the anular ligament of the radius was very distinct on the MR images and unidentifiable on the CT images.

Most of the anatomic structures of the elbow joint are recognizable on the CT and MR images. Consequently this compilation could be used as an atlas for evaluation of CT and MR images of the forelimbs of dogs with elbow joint injuries and developmental or degenerative conditions.

For CT examination of both tarsal regions, 7 dogs were anesthetized and placed in ventral recumbency. Transverse, 1- and 2-mm slices were obtained from the most proximal part of the calcaneus to 1 cm distal to the tarsometatarsal joint, using bone and soft tissue settings. Afterwards,

CT reconstructions of the tarsocrural joint were created in sagittal and dorsal planes. MR of the tarsal joints was performed in one of the dogs that was kept in the same position as mentioned above. Transverse, T1-weighted and T2-weighted images were obtained with a slice thickness of 3 mm. After euthanasia, the hind limbs of one of the dogs were removed and frozen and the tarsal joints were sectioned into approximately 1-mm thick slices. Anatomic sections were photographed and compared with the corresponding CT and MR images.

Most of the bony, tendinous, and vascular structures were visible on the anatomic sections and all of these structures were also perceptible on the soft tissue setting CT images, except for the extensor digitorum brevis muscle and the talocalcaneal interosseus ligament. On the bone setting CT images, only the previously mentioned bony structures could be identified. The entire tarsocrural joint surface could be evaluated on the reconstructed CT images in the sagittal and dorsal planes. All bony and soft tissue structures visible on the anatomic sections could be identified on the MR images. When comparing the MR images to the corresponding soft tissue CT images, the same structures as well as the talocalcaneal interosseous ligament and the extensor digitorum brevis muscle could be located on the MR images. In general, most blood vessels and tendons were more clearly visible on the MR images compared to the CT images.

This detailed atlas of the tarsal joint formed an excellent anatomical basis for clinicians to evaluate CT and MR images of dogs affected with tarsal joint injuries.

The findings of the present study, together with the results of additional prospective investigation of other regions of the canine body such as the knee, hip, carpal joint and the abdomen, offer a comparative and multidisciplinary atlas with useful applications in clinical veterinary medicine.

Dit werk beschrijft en illustreert dwarse anatomische doorsneden van verschillende klinisch belangrijke lichaamszones van de normale hond. Gelabelde anatomische snedes worden gebruikt om alle strukturen op de corresponderende CT- en MR-beelden te identificeren. Deze gedetailleerde, vergelijkende beschrijving kan dienst doen als atlas voor de prakticus, daar het een optimale interpretatie van CT- en MR-beelden van honden met pathologische afwijkingen mogelijk maakt.

In het eerste hoofdstuk worden de CT- en MR-beelden bestudeerd van twee craniale gebieden, namelijk de hersenen en de neusgangen inclusief de paranasale sinussen.

Om CT- en MR-studies van de hersenen uit te voeren, werden 4 herdershonden verdoofd en in rugligging gepositioneerd. Tijdens het CT-onderzoek werden 2-mm dikke, pre-en postcontrast dwarse snedes gemaakt vanaf de lamina cribrosa van het zeefbeen tot het craniale gedeelte van de atlas, hierbij gebruik makende van een weke delenvenster. Eén van de honden onderging vervolgens MR-onderzoek waarbij dezelfde positie als voor het CT-onderzoek werd behouden. Dwarse, 4-mm dikke T1-gewogen en T2-gewogen MR-beelden werden gemaakt van dezelfde zone van de schedel als bij het CT-onderzoek.

Eén van de honden onderging euthanasie, waarna de hersenen werden vrijgeprepareerd, gefixeerd, ingebed in gelatine en in 5-mm dikke, dwarse schijven gesneden met een mes. De anatomische doorsnedes werden gefotografeerd en een groot aantal hersenstrukturen en verschillende delen van het ventrikelsysteem werden geïdentificeerd.

De meeste van deze strukturen konden teruggevonden worden op de CT-beelden, gebruik makende van oriëntatiepunten zoals radiolucent cerebrospinaalvocht en de omgevende beenderige weefsels. Helaas was het niet mogelijk om sommige onderdelen van het telencephalon te onderscheiden, meer bepaald de capsula interna en de gyrus hippocampi, noch sommige strukturen van het diencephalon waaronder de tractus opticus, epiphysis, infundibulum en tuber cinereum. Van het mesencephalon waren de fossa intercruralis, nucleus ruber en substantia nigra niet identificeerbaar, en ter hoogte van het metencephalon konden de substantia alba van het cerebellum, de flocculus en de pedunculus cerebellaris medius niet worden gelokaliseerd. Sommige strukturen van de medulla oblongata zoals de fissura mediana ventralis, de pyramis en het canalis centralis van de medulla spinalis waren onmogelijk te onderscheiden, evenmin als de plexus choroidei van de laterale en vierde ventrikels. Op de CT-beelden werden ook de beenderige en weke weefsels rondom de hersenen benoemd.

Bijna alle hersenstrukturen die zichtbaar waren op de anatomische beelden konden worden geïdentificeerd op de MR-beelden, met uitzondering van sommige onderdelen van het diencephalon zoals de epiphysis, hypophysis met infundibulum en het corpus mamillare. Het onvermogen om deze strukturen terug te vinden, was waarschijnlijk te wijten aan het feit dat deze laatste net niet in één van de snedes aanwezig waren. De nucleus ruber en substantia nigra van het mesencephalon konden eveneens niet gelokaliseerd worden, evenmin als de substantia alba van het cerebellum. Wanneer de MR-beelden vergeleken worden met de corresponderende CT-beelden kan worden besloten dat alle hersenstrukturen en de omgevende zachte weefselstrukturen veel beter zichtbaar zijn op de MR-beelden. Daarenboven konden verschillende strukturen van de hersenen zoals de capsula interna, tractus opticus, gyrus hippocampi, colliculi rostrales et caudales, brachium pontis, fissura mediana ventralis, lobus floccularis, pyramis (ter hoogte van de medulla oblongata) en de plexus choroidei van de laterale en vierde ventrikels gemakkelijk worden gelokaliseerd op de MR-beelden, terwijl ze onherkenbaar waren op de CT-beelden. Alleen de beenderen van de schedel, met in het bijzonder de foramina, fossae, canales en sulci, waren veel duidelijker op de CT-beelden vergeleken met de MR-beelden.

Deze resultaten kunnen gebruikt worden als een basis voor evaluatie van CT- en MR-beelden van de hersenen van honden met pathologieën van het centraal zenuwstelsel.

Twee herdershonden werden gebruikt voor de CT- en MR-onderzoeken van de neusholte en paranasale sinussen. De eerste hond werd verdoofd en in rugligging geplaatst voor beide onderzoeken. Tijdens het CT-onderzoek werden 5-mm dikke dwarse snedes gemaakt vanaf het caudaal gedeelte van de frontale sinussen tot aan de neusgaten. Nadien werden deze CT-beelden afgedrukt op een botvenster. De hond onderging vervolgens een MR-onderzoek, waarbij T1-gewogen, T2-gewogen en proton-densiteit MR-beelden werden bekomen. Voor de tweede hond werd hetzelfde protocol gevolgd, met die uitzondering dat het dier in rugligging werd gepositioneerd met de kop loodrecht op de tafel teneinde dorsale beelden te bekomen.

Op het einde van de onderzoeken ondergingen beide honden euthanasie en de schedels werden vrijgeprepareerd, ontkalkt, in gelatine ingebed en daarna met een mes in 5-mm dikke plakken gesneden. Elke anatomische doorsnede werd vergeleken met de corresponderende CT- en MR-beelden en alle herkenbare strukturen werden gelabeld op alle beelden. De verschillende schedelbeenderen die de wand van de neusgangen vormen en de meeste onderdelen van de neusholte zoals de conchae nasales, de septa, meatussen en alle endo- en ectoturbinalia, konden gemakkellijk geïdentificeerd worden op de anatomische figuren. De mediale en laterale delen van de frontale sinussen en de recessus maxillaris waren eveneens zichtbaar. Daarnaast werden ook verschillende omgevende strukturen van het hoofd aangeduid.

Op de CT-beelden was het bovendien mogelijk om een groot aantal strukturen van de neusgangen en paranasale sinussen te identificeren, met uitzondering van de dorsale, middelste en ventrale meatus en enkele van de ectoturbinalia. Ook een deel van de omgevende weke weefselstrukturen kon niet onderscheiden worden.

Op de MR-beelden was het moeilijk om de verschillende schedelbeenderen te identificeren, doch de meeste konden worden gelokaliseerd aan de hand van hun 'leeg' signaal. In tegenstelling tot de beenderen waren de conchae, de conchale septa en de turbinalia –met uitzondering van enkele ectoturbinalia- gemakkelijk te onderscheiden dankzij het dunne laagje bedekkende mucosa. Ook de omgevende weke weefselstrukturen waren zeer duidelijk zichtbaar op de MR-beelden, zeker wanneer vergeleken wordt met de CT-beelden.

Deze resultaten laten toe te besluiten dat de CT- en MR-beelden een nauwkeurige lokalisatie van alle strukturen van de neusgangen en paranasale sinussen mogelijk maken. Bijgevolg kunnen beide technieken nuttig zijn voor het evalueren van neusaandoeningen.

In het tweede hoofdstuk van dit proefschrift werd de anatomie van de thorax beschreven zoals die gevisualiseerd wordt door CT en thoracoscopie. Vervolgens werd een vergelijkende studie tussen beide technieken gemaakt.

Voor CT-onderzoek van de thorax werden vier honden verdoofd en in rugligging gepositioneerd. Dwarse, 5 mm dikke CT-beelden werden gemaakt vanaf de borstingang tot aan het diafragma en werden bekeken gebruik makende van een weke delenvenster en een longvenster. Eén hond werd geëuthanaseerd en ingevroren, waarna de bevroren thorax in schijven van 10 mm dikte werd gezaagd. Bij elke anatomische snede werd een corresponderend CT-beeld gezocht en de anatomische strukturen werden vergeleken.

Op de anatomische snedes waren de verschillende intrathoracale delen van het ademhalingsstelsel en de longlobben gemakkelijk zichtbaar. Ook de grote bloedvaten in de borstholte en in het craniale mediastinum konden eenvoudig worden geïdentificeerd. Andere intrathoracale strukturen zoals het hart met zijn kamers en kleppen, de slokdarm, lymfeknopen en spieren waren eveneens eenvoudig te lokaliseren, evenals de verschillende delen van de thoraxwand en de omgevende weefsels. De meeste van de hierboven vermelde strukturen van de thorax konden geïdentificeerd worden op de CT-beelden met weke delenvenster, met uitzondering van de verschillende onderdelen van het hart, sommige bloedvaten, het ligamentum nuchae, het diafragma, de longlobben en de lobaire bronchen. Op de CT-beelden met longvenster waren alleen de verschillende delen van het ademhalingsstelsel zichbaar en sommige grote bloedvaten. Van het hart en de lever konden alleen de contouren worden waargenomen, terwijl de positie van de slokdarm en van de cardia en fundus van de maag werd aangegeven door de aanwezigheid van lucht.

Voor thoracoscopie werden 4 honden verdoofd en in linker of rechter zijligging geplaatst. De endoscoop werd in de borstholte ingebracht via de bovenliggende zijde en ondertussen werden endoscopische foto’s genomen. Een groot aantal intrathoracale structuren van de linker en rechter hemithorax waren endoscopisch zichtbaar.
Aan beide zijden waren de pulmonaire en costale pleura, het diafragma, het hart met pericardium en de onderdelen van de borstwand met de daarop verlopende zenuwen en bloedvaten gemakkelijk te onderscheiden. Zowel in de rechter als linker borstholte was het mogelijk om de slokdarm en trachea te lokaliseren in het craniale mediastinum.
In de linker borstholte werden de craniale en caudale longlobben bekeken en ook de grote bloedvaten zoals de aorta ascendens, aorta descendens en truncus pulmonalis. Aan de hartbasis waren het ligamentum arteriosum Botalli en de nervus laryngeus recurrens duidelijk zichbaar, terwijl de linker nervus vagus en nervus phrenicus gelokaliseerd konden worden ter hoogte van het pericardium. In het craniale mediastinum werden de ductus thoracicus, de arteria subclavia sinistra en de vena brachiocephalica sinistra met hun takken geïdentificeerd.
In de rechter borstholte was het mogelijk om de craniale, middelste en caudale longlobben te evalueren en caudaal van het hart waren de vena cava caudalis en de rechter nervus phrenicus zichtbaar in de plica venae cavae. In het rechter craniale mediastinum konden daarenboven de vena azygos, vena cava cranialis, rechter nervus vagus en nervus phrenicus, vena broncho-esophagea en de ductus thoracicus worden bekeken.

Nadien werden deze beide technieken voor het onderzoek van de thorax met elkaar vergeleken. Tot de intrathoracale strukturen die niet zichtbaar bleken op de CT-beelden maar eenvoudig te lokaliseren waren met thoracoscopie behoorden onder andere de pariëtale en viscerale pleura, het pericardium, de hartbasis met het ligamentum arteriosum Botalli, de ductus thoracicus, de plica venae cavae en verschillende intrathoracale zenuwen. Daarentegen was de identificatie van het ruggenmerg, lymfeknopen, mediastinum en verschillende bloedvaten moeilijk tot onmogelijk via thoracoscopie maar eenvoudig via CT-onderzoek. Het uitwendig oppervlak van de verschillende longlobben (met uitzondering van de lobus accessorius) kon tijdens thoracoscopie bekeken worden, terwijl de inwendige details zichtbaar waren op de CT-beelden met longvenster. De onderdelen van het hart waren niet te onderscheiden tijdens het thoracoscopisch onderzoek mede door het ondoorzichtbare pericardium, maar ook op de CT-beelden was dit ten gevolge van bewegingsartefacten niet mogelijk.

Zowel thoracoscopie als CT van de thorax bieden een grote hoeveelheid aan intrathoracale anatomische informatie en kunnen gebruikt worden voor de diagnose van thoraxaandoeningen. De keuze tussen beide technieken zal vooral afhangen van de klinische voorgeschiedenis van het dier en van de resultaten van reeds gedane onderzoeken. Het feit dat thoracoscopie ook therapeutische mogelijkheden heeft, zal mede de definitieve keuze van de diagnostische techniek bepalen.

In het derde hoofdstuk van deze studie werd de CT- en MR-anatomie van twee regio’s van de ledematen, namelijk de elleboog en de sprong, bestudeerd. Daarbij werden, voor elk gewricht, beide technieken met elkaar vergeleken.

Om het CT-onderzoek van de ellebogen uit te voeren, werden zes honden verdoofd en in zijligging geplaatst. Dwarse, 1 en 2 mm dikke CT-snedes werden bekomen vanaf de top van het olecranon tot 3 cm distaal van het ellebooggewricht en parallel met de humeroradiale gewrichtsspleet. De beelden werden bekeken gebruik makende van een botvenster en een weke delenvenster, en bijkomend werden sagittale en dorsale CT-reconstructies van het ellebooggewricht gemaakt. MR-onderzoek van de ellebogen werd uitgevoerd bij één van de honden (een Labrador retriever) waarbij het dier in dezelfde positie werd gehouden als tijdens het CT-onderzoek. Dwarse, 3 mm dikke, T1-gewogen en T2-gewogen beelden werden gemaakt van dezelfde regio als hierboven vermeld. Na de onderzoeken onderging de Labrador retriever euthanasie, waarna beide voorpoten werden verwijderd en ingevroren. Vervolgens werden de ellebogen in ongeveer 1 mm dikke schijfjes gesneden, gefotografeerd en vergeleken met de corresponderende CT- en MR-beelden.

Op de anatomische beelden waren verschillende beenderen, spieren, pezen, bloedvaten en zenuwen zichtbaar.

Dezelfde strukturen waren te identificeren op de CT-beelden met weke delenvenster, met uitzondering van het ligamentum anulare van de radius en de membrana interossea antebrachii.

Alle beenderige strukturen die gelokaliseerd waren op de anatomische beelden konden ook worden aangeduid op de CT-beelden met beenvenster, en het volledige humero-radiaal gewrichtsoppervlak kon geëvalueerd worden op de CT-reconstructies.

Alle strukturen zichtbaar op de anatomische beelden waren ook aanwezig op de MR-beelden; alleen de arteria mediana, nervus medianus en nervus radialis konden niet gelokaliseerd worden. Vervolgens werden de MR-beelden vergeleken met de corresponderende CT-beelden met weke delenvenster. Met uitzondering van de hogervermelde leidingen, die niet zichtbaar waren op de MR-beelden, werden dezelfde strukturen onderscheiden. Anderzijds was het ligamentum anulare van de radius zeer duidelijk op de MR-beelden en onmogelijk te identificeren op de CT-beelden.

De meeste anatomische strukturen van het ellebooggewricht zijn herkenbaar op CT- en MR-beelden. Bijgevolg kunnen deze resultaten gebruikt worden als een naslagwerk voor de beoordeling van CT- en MR-beelden van de ellebogen van honden met letsels en ontwikkelingsstoornissen of degeneratieve aandoeningen van dit gewricht.

Om het CT-onderzoek van de sprongen uit te voeren, werden zes honden verdoofd en in rugligging gepositioneerd. Dwarse, 1 en 2 mm dikke CT-snedes werden bekomen vanaf het meest proximale punt van de calcaneus tot 1 cm distaal van het tarsometatarsaal gewricht, gebruik makende van een botvenster en een weke delenvenster. Nadien werden CT-reconstructies gemaakt van het tarsocruraal gewricht in sagittale en dorsale vlakken. Het MR-onderzoek van de tarsi werd uitgevoerd bij één van de honden waarbij het dier in dezelfde positie werd gehouden als op de CT-tafel. Dwarse T1-gewogen en T2-gewogen beelden werden gemaakt met een dikte van 3 mm. Na euthanasie van één van de honden werden de achterpoten verwijderd en ingevroren, waarna de spronggewrichten in 1 mm dikke schijfjes werden gesneden. Vervolgens werden de anatomische doorsnedes gefotografeerd en vergeleken met de corresponderende CT- en MR-beelden.

Alle beenderen, pezen en bloedvaten zichtbaar op de anatomische snedes werden gelabeld. Deze strukturen werden eveneens teruggevonden op de CT-beelden met weke delenvenster, met uitzondering van de musculus extensor digitorum brevis en het ligamentum talocalcaneum interosseum. Op de CT-beelden met botvenster konden alleen de beenderen worden benoemd, terwijl het volledige tarsocrurale gewrichtsvlak kon worden geëvalueerd op de sagittale en dorsale CT-reconstructies.

Alle beenderige en zachte weefselstrukturen die zichtbaar waren op de anatomische beelden, werden ook onderscheiden op de MR-beelden. Wanneer deze laatste werden vergeleken met de

corresponderende CT-beelden, konden niet alleen dezelfde strukturen gelokaliseerd worden op de MR-beelden, maar tevens ook de musculus extensor digitorum brevis en het ligamentum talocalcaneum interosseum. In het algemeen waren bloedvaten en pezen duidelijker te zien op de MR- beelden in vergelijking met de CT-beelden.
Deze gedetailleerde atlas van het tarsaalgewricht leent zich als een uitstekende anatomische basis voor de evaluatie van CT- en MR-beelden van honden met letsels van de sprong.

De bevindingen van deze studie, samen met de resultaten van bijkomende toekomstige onderzoeken van andere lichaamszones van de hond, zoals de knie, de heup, de carpus en het abdomen, bieden een vergelijkende en multidisciplinaire atlas die van groot nut kan zijn in de klinische diergeneeskunde.

Een doctoraat maken leek mij altijd een onbereikbare droom, temeer daar ik na 2 jaar voltijds assistente aan de vakgroep Morfologie gekozen had voor een eigen praktijk. Wel bleef ik als deeltijds assistente practica anatomie en histologie geven. Prof. P. Simoens bood mij de kans om daarnaast verder wetenschappelijk onderzoek te verrichten en publicaties te maken, wat ik ook met groot enthousiasme aanvaardde. Met zijn goede raad en opbouwende kritiek leidde hij mijn schrijfsels in goede banen. Zijn nimmer afnemend enthousiasme was voor mij een enorme stimulans. Ook toen ik naar de vakgroep Medische Beeldvorming overstapte, kon ik voor mijn publicaties verder op zijn steun en advies rekenen. Voor dit alles en het feit dat hij als mede-promotor voor dit doctoraat wou optreden, ben ik hem zeer dankbaar.

Gedurende mijn periode als assistente Morfologie was er ook een hechte samenwerking met Prof. H. van Bree. Mijn opgedane anatomische kennis was een enorme hulp voor onze onderzoeksprojecten, die – dankzij mijn ‘schrijversopleiding’ - resulteerden in enkele publicaties omtrent echografie. Later, als assistente op de vakgroep Medische Beeldvorming had ik de mogelijkheid om mij te verdiepen in de interpretatie van CT-beelden. Ondertussen opperde Prof. Van Bree het idee om hieromtrent een doctoraat te maken. Dankzij zijn overtuigingskracht en zijn geloof in mijn ‘kunnen’ is mijn droom dan ook werkelijkheid geworden. De lovende woorden van mijn diensthoofd en tevens promotor smoorden steeds al mijn twijfels. Met zijn goede ideeën en scherpe kijk op zaken legde hij de basis van dit werk. Ik dank hem voor het vertrouwen dat hij in mij had en voor de vrijheid die hij me gaf, zodat ik zelfstandig en op eigen tempo dit werk kon vervolmaken.

Elke woensdag dit doctoraat verder opbouwen was dan ook geen opgave voor mij maar iets waar ik elke week naar uitkeek. Een bijkomende stimulans was de aanwezigheid van mijn toffe collega’s, in het bijzonder van Dr. Ingrid Gielen. Door samen in eenzelfde bureau te werken, elkaar te helpen en moed in te spreken, en daarnaast nog eens samen te paard onze gepijnigde hersenen te laten uitwaaien aan zee, werd zij meer een vriendin dan medewerkster. Ik bewonder haar belangloze inzet voor de dienst en haar internationale uitstraling. Dankzij haar bijdrage, voornamelijk bestaande uit talrijke CT- en MR-beelden, is dit werk tot stand gekomen. Ik ben haar zeer dankbaar en hoop dat onze samenwerking ook in de toekomst produktief, en vooral ontspannen en plezierig mag blijven.

Mijn dank gaat ook uit naar Prof. em. F. Verschooten. Ik heb hem leren kennen als een man met enerzijds sterke principes en anderzijds vaderlijke bezorgdheid. Zijn wijsheid, en niet alleen op wetenschappelijk vlak, vervulde mij met groot respect. Ik was dan ook verheugd dat hij mij als assistente wou aannemen en hoop dat hij dit doctoraat als een teken van dank wil beschouwen.

Ook dank aan Dr. Jimmy Saunders voor de leuke samenwerking die ‘wortel schoot’ ten tijde van zijn doctoraat. De wederzijdse hulp afgewisseld met een prettige babbel was de aanzet tot een verdere vriendschap. Ik kijk op naar zijn wetenschappelijke kennis, de inzet voor zijn werk en zijn volharding om een doel te bereiken. Ik dank hem ten zeerste voor zijn inbreng in dit doctoraat en zijn begeleidende hulp.

Mijn andere collega’s van de vakgroep, met name Dr. Annemie Van Caelenberg, Dr. Barbara Vandevelde, Prof. Bernadette van Ryssen, Dr. Frank Coopman, Marleen Goethals en Claudine Van Sante wil ik bedanken voor het creëren van de toffe werksfeer en voor de welgemeende interesse in mijn persoon en werk.

Met Marnix Verdonck heb ik ettelijke uren aan de computer doorgebracht. Hij stond steeds klaar om me te helpen met het bewerken van de beelden van dit doctoraat. Ook leerde hij mij omgaan met verschillende computerprogramma’s zoals Thumbs en Paint, zodat ik wat onafhankelijker van hem werd. Als multivalente technieker nam hij ook alle foto’s van de anatomische snedes en ontwierp zelfs een speciale zaag om de hersenen te snijden. Daartussen vond hij ook altijd tijd voor een grapje. Kortom, zonder hem was ik verloren. Erg bedankt voor je hulp en immer opgewekt humeur, Marnix!

Patrick Vervaet van de Vakgroep Morfologie wil ik niet alleen danken voor het versnijden van de anatomische stukken maar ook voor zijn vriendschap die sinds onze samenwerking in de snijzaal morfologie niet meer stuk kan.

Dr. Ingeborg Polis dank ik voor de samenwerking tijdens de thoracoscopieën. Studenten Olaf Thas en Sofie Van de Meervenne voor hun thesissen die het voorbereidend werk voor mijn publicaties vereenvoudigden.

Verder ben ik de andere leden van de begeleidings- en examencommissie Dr. J Vandevenne en Prof. Dr. H. Waibl zeer erkentelijk. Hun kritische commentaren en hun nauwkeurig verbeterwerk leverden een grote bijdrage bij het tot stand komen van dit werk. Dr. Vandevenne wil ik daarnaast danken voor het uitvoeren van de MR onderzoeken.

En dan mijn lieve ouders die mij al hun hele leven koesteren en stimuleren, en mij een onbezorgde jeugd en alle kansen om te studeren gaven. De wens -die ik als kind reeds had- om dierenarts te worden, hebben zij helpen vervullen. Mentaal en fysiek hebben ze me steeds gesteund. Nachtenlang bleef mijn moeder wakker bij haar studerende dochter, omdat ze wist dat haar aanwezigheid mij de moed gaf voor het volgende examen. Mijn vader gaf me daarnaast ook de financiële steun die nodig was om als pas afgestudeerde een eigen praktijk te starten. Met hard werken probeer ik hen een stuk van mijn enorme dankbaarheid te tonen. Dit doctoraat beschouw ik dan ook als een eerbetoon aan hen die dit allemaal mogelijk maakten.

En natuurlijk wil ik ook Johan danken. Mijn man en tevens beste vriend die mij een stabiele relatie gaf en de ruimte om mijn dromen op werkvlak te realiseren. Ik kreeg daarenboven zijn onvoorwaardelijke liefde én twee schatten van kindjes : Manon en Héloïse. Ook de steun en interesse van mijn schoonouders, zus, schoonzus, schoonbroers en onze vele vrienden en vriendinnen waren een hart onder de riem. Zij allen maken het leven zo veel aangenamer.
Het geluk in mijn privéleven gaf me de energie om aan dit doctoraat te werken en weerspiegelt zich elke dag in mijn beroep als dierenarts, een beroep dat ik met steeds toenemend plezier, overtuiging en voldoening uitoefen.
Lieve

Lieve De Rycke werd geboren op 17 april 1966 te Brugge. Na het behalen van het diploma hoger secundair onderwijs aan het Onze-Lieve-Vrouw-Hemelvaart-Instituut te Brugge begon zij in 1984 met de studie Diergeneeskunde aan de Universiteit Gent. Gedurende haar laatste studiejaar begeleidde ze de practica anatomie als leerling-assistente bij de vakgroep Morfologie van de Huisdieren. Aan dezelfde vakgroep voltooide zij haar eindestudiewerk "European Brown Hare Syndrome in België" waarmee ze de Norden-Wetenschappelijke prijs won. In 1990 behaalde ze het diploma van Doctor in de Diergeneeskunde met grote onderscheiding.

Onmiddellijk daarna trad zij als assistente in dienst bij de Vakgroep Morfologie van de Huisdieren waar zij het onderricht van de practica anatomie en histologie verzorgde. Daarnaast startte ze een eigen praktijk Kleine Huisdieren te Brugge. Daar haar interesse eveneens uitging naar de medische beeldvorming was zij vanaf 1995 ook aktief als navorser bij de Vakgroep Medische Beeldvorming van de Huisdieren. In 1999 stopte ze haar aktiveiten bij de vakgroep Morfologie en werd zij bij de vakgroep Medische Beeldvorming aangenomen als 20% assistente. Gedurende de laatste jaren heeft zij zich verdiept in het anatomisch interpreteren van CT-beelden van de hond, wat heeft geleid tot dit proefschrift.

Lieve De Rycke is auteur of mede-auteur van 13 publicaties in internationale en nationale tijdschriften en nam aktief deel aan verschillende nationale en internationale congressen.

PUBLICATIONS

L. De Rycke.
Het European Brown Hare Syndrome.
Zoogdier 1990;3: 14-17.

P. Simoens.,L. De Rycke, F. Verschooten.
Leeftijdsbepaling van hazen (*Lepus europaeus*) door middel van het skelet en het gebit. Vlaams Diergeneeskundig Tijdschrift 1992;61: 73-84 (21 fig.)

L. De Rycke, P. Simoens, H. Lauwers.
Morfologische basis van portosystemische shunts bij de hond.
Vlaams Diergeneeskundig Tijdschrift 1995;64:163-172.

L. De Rycke, H. van Bree.
Echografisch begeleide bioptname van abdominale organen bij kleine huisdieren: een literatuuroverzicht.
Vlaams Diergeneeskundig Tijdschrift 1996;65:135-144.

L. De Rycke, H. van Bree, P. Simoens.
Ultrasound- guided tissue-core biopsy of liver, spleen and kidney in normal dogs.
Veterinary Radiology and Ultrasound 1999;40:294-299.

I. Gielen, L. De Rycke, B. Van Ryssen, H. van Bree.
Die Thoracoscopie beim Hund.
Kleintier Medizin, 1999;3:114-117.

L. De Rycke, I. Gielen, I. Polis, B. Van Ryssen, H. van Bree, P. Simoens.
Thoracoscopic anatomy of dogs positioned in lateral recumbency.
Journal of American Animal Hospital Association 2001;37:543-548.

I.Gielen, L. De Rycke, H. van Bree, P. Simoens.
Computed tomography (CT) of the tarsal joint in clinically normal dogs.
American Journal of Veterinary Research 2001;62:1911-1915.

I. Polis, F. Gasthuys, I. Gielen, B. Van Ryssen, H. van Bree, H. Laevens, L. De Rycke.
The efffects of intrathoracic pressure during continuous two-lung ventilation for thoracoscopy on the cardiorespiratory parameters in sevoflurane anaesthetized dogs.
Journal of Veterinary Medicine A 2002;49:113-120.

L. De Rycke, I. Gielen, H. Van Bree, P. Simoens.
Computed tomography of the elbow joint in clinically normal dogs.
American Journal of Veterinary Research 2002;63:1400-1407.

L. De Rycke, J. Saunders, I. Gielen, H. van Bree, P. Simoens.
Magnetic resonance imaging, computed tomography, and cross-sectional views of the anatomy of normal nasal cavities and paranasal sinuses in mesaticephalic dogs.
American Journal of Veterinary Research 2003;64:1093-1098.

L. De Rycke, I. Gielen, P. Simoens, H. van Bree.
Computed tomography and cross sectional anatomy of the normal canine thorax.
American Journal of Veterinary Research 2005;66:512-524.

L. De Rycke, I. Gielen, S. Van Meervenne, P. Simoens, H. van Bree.
Computed tomography and cross sectional anatomy of the normal canine brain.
American Journal of Veterinary Research 2005;66: 1743-1756.

COMMUNICATIONS/PROCEEDINGS PRESENTED DURING INTERNATIONAL SCIENTIFIC MEETINGS

L. De Rycke, P. Simoens, H. Lauwers.
Portosystemic shunts in the dog.

Proceedings fourteenth Congress of the European Society of Veterinary Pathology.
1996, p76.

H. van Bree, I. Gielen, L. De Rycke, B. Van Ryssen.
Computerized tomography (CT) of the canine tarsal joint.
Proceedings 3e Berliner Kleintiersymposium, Erkrankungen der Hintergliedmasse und Therapie, 7-8 november 1998, Berlin University, Germany, p 94-95.

I. Gielen, I. Polis, B. Van Ryssen, L. De Rycke, H. van Bree.
Thoracoscopie beim Hund : Material, Technik und normale Anatomie.
Berliner Kleintierforum, Endoscopie Seminar I, 22-23 Juni 2002, Kleintierklinik der FU, Universität Berlin, Berlin, Deutschland.

COMMUNICATIONS/ABSTRACTS PRESENTED DURING INTERNATIONAL SCIENTIFIC MEETINGS

L. De Rycke, P. Simoens, H. Lauwers.
The dentition of the European hare (*Lepus europaeus*).
150 Years of Veterinary Education in Turkey, Ankara, Cappadocia, Istanbul, 1992, p141.

P. Simoens, L. De Rycke, H. Lauwers.
Postnatal development of the teeth of the European Hare.
19th Congress of the European Association of Veterinary Anatomists, Ghent & Antwerp, 1992, p59.

I. Gielen, L. De Rycke, T. Declercq, H. van Bree.
Computerized tomography (CT) of the normal canine tarsal joint.
5th annual Conference of the EAVDI, August 26-28, 1998, Bälsta, Zweden, p31.
Veterinary Radiology and Ultrasound 1999;40:190.

I. Gielen, L. De Rycke, B. Van Ryssen, H. Van Bree.
Thoracoscopy: normal intrathoracic anatomy in the dog.

5th International Workshop in Videoscopic Surgery for Veterinarians, Norderstedt, Duitsland, 9-11 november 1998.

L. De Rycke, I. Gielen, B. Van Ryssen, H. van Bree, P. Simoens.
Canine thoracoscopic anatomy.
8th Annual Scientific Meeting of the European College of Veterinary Surgeons, Bruges, Belgium, 2-4 july 1999, p108-109.

L. De Rycke, J. Saunders, I. Gielen, H. van Bree, P. Simoens.
Computerized tomography (CT) and magnetic resonance (MR) anatomy of the normal canine nasal cavity and frontal sinuses.
9th EAVDI (European Association of Veterinary Diagnostic Imaging) Annual Conference, Archena (Murcia), Spain, 24-27 July 2002, p100.
Veterinary Radiology and Ultrasound 2003;44:233.

L. De Rycke, J. Saunders, I. Gielen, H. van Bree, P. Simoens.
Computerized tomography (CT) and magnetic resonance (MR) anatomy of the normal canine elbow.
9th EAVDI (European Association of Veterinary Diagnostic Imaging) Annual Conference, Archena (Murcia), Spain, 24-27 July 2002, p101.
Veterinary Radiology and Ultrasound 2003;44,233.

L. De Rycke, I. Gielen, H. van Bree, P. Simoens.
Computerized tomography (CT) of the normal canine thorax.
11th EAVDI (European Association of Veterinary Diagnostic Imaging) Annual Conference, Ghent, Belgium, 8-11 September 2004, p116.

A. Van Caelenberg, I. Gielen, F. Pasmans, A. Martel, L. De Rycke, H. van Bree.
Computerized tomography (CT) anatomy of the normal chelonian.
11th EAVDI (European Association of Veterinary Diagnostic Imaging). Annual Conference, Ghent, Belgium, 8-11 September 2004, p110.